

Galaxy Evolution in the Fors Deep Field



Armin Gabasch

GALAXY EVOLUTION IN THE FORS DEEP FIELD

Ph.D. Thesis

at the Faculty of Physics
of the
Ludwig-Maximilian University Munich

submitted by

Armin Gabasch

Munich, October 2004

1. Evaluator: Prof. Dr. Ralf Bender
2. Evaluator: Dr. Peter Schücker

Date of the oral exam: 22 December 2004

Es irrt der Mensch, solang' er strebt

– Johann Wolfgang von Goethe

*to my parents, brother and sister –
for their endless support*

Contents

List of Figures	xiii
List of Tables	xvi
Zusammenfassung	xviii
1 Introduction	1
1.1 The early Universe	1
1.1.1 Basic concepts	1
1.2 Structure formation	3
1.2.1 The cosmic microwave background	3
Matter-radiation equality	3
Photon decoupling and recombination	4
Analyzing the cosmic microwave background	4
1.2.2 The dark age	5
1.2.3 Reionization and the first stars	6
Formation of the first stars	6
Reionizing the IGM	8
1.3 Galaxy evolution	8
1.3.1 Theoretical framework for galaxy evolutions	8
Monolithic collapse model	9
Hierarchical clustering	9
1.3.2 Observational evidence for galaxy evolutions	10
Surveys and their distance determinations	11
Restframe galaxy luminosity function	12
Star formation rate	13
Clustering	14
1.4 Outline of the thesis	15
2 The FORS Deep Field	17
2.1 Introduction	18
2.2 Field selection	18
2.3 Observations	19
2.4 Optical data reduction	21
2.4.1 Basic reduction	21

2.4.2	Image stacking	24
2.4.3	Calibration	25
2.5	NIR data reduction	26
2.6	Basic properties of the co-added images	26
2.7	Source detection and photometry	26
2.8	Photometric catalog	31
2.8.1	Compilation of the photometric catalog	31
2.8.2	Contents of the photometric catalog	32
2.9	Galaxy number counts	35
2.10	z- and 835nm-band	38
3	The evolution of the luminosity functions: I. The blue bands	39
3.1	Introduction	40
3.2	The FORS Deep Field	41
3.3	I selection versus K selection	42
3.4	Photometric redshifts	42
3.5	Luminosity functions	46
3.5.1	The method	46
3.5.2	The slope of the luminosity function	47
3.5.3	The restframe luminosity functions	47
3.6	Parameterizing the evolution of the luminosity function	51
3.7	Comparison with literature	55
3.8	Comparison with model predictions	56
3.9	Summary and conclusions	56
3.10	Appendix of Chapter 3	60
3.10.1	Schechter parameters	60
3.10.2	Comparison with literature	65
UV bands	65
SDSS bands (u' , g' , $^{0.1}u$, $^{0.1}g$)	69
B-band	73
3.10.3	Confidence levels for the slope	74
4	The evolution of the luminosity functions: II. The red bands	75
4.1	Introduction	75
4.2	Luminosity functions in the r' , i' , and z' bands	75
4.2.1	The slope of the luminosity function	76
4.2.2	The redshift evolution of the luminosity functions	77
4.3	Parameterizing the evolution of the luminosity function	81
4.4	Comparison with literature	85
4.5	Comparison with model predictions	91
5	LF redshift evolution as a function of SED type	93
5.1	Introduction	93
5.2	Galaxy classification	93
5.3	Type-dependent luminosity function	95

5.4	Appendix of Chapter 5	97
6	The SFR history in the FORS Deep and GOODS South Fields	111
6.1	Introduction	112
6.2	Data sets	112
6.3	The Star Formation Rate	115
6.4	Conclusions	117
7	Evolution of the stellar mass density and dust correction	119
7.1	Introduction	119
7.2	The stellar mass density from the SFR up to $z \sim 4.5$	119
7.3	Tight constraint to the mean dust correction	121
8	Summary and concluding synthesis	123
8.1	Summary	123
8.2	Concluding synthesis	126

List of Figures

1.1	WMAP all-sky image	5
1.2	Mass fluctuations and collapse thresholds in cold dark matter models	7
1.3	The observed cumulative <i>number</i> of galaxies between $1 < z < 3$	10
2.1	Palomar Digitized Sky Survey (DSS) plots of the FDF	19
2.2	Cosmic ray rejection	22
2.3	I-band difference image of the PR and the final reduction.	23
2.4	Histogram of the weighting factors α and difference image for the R-band	25
2.5	The FDF in the I-band from FORS observations	28
2.6	Pixel-value histograms for the I-band image at various analysis stages	29
2.7	Detection file of SExtractor for a $1' \times 1'$ region of the northern part of the FDF	31
2.8	Galaxy number counts in the U & B bands	36
2.9	Galaxy number counts in the g & R bands	36
2.10	Galaxy number counts in the I & J bands	37
2.11	Galaxy number counts in the Ks-band	37
2.12	Fringe-pattern extracted from the z-band image	38
3.1	Color-magnitude relation for K_s -selected objects of the HDF-S	42
3.2	Comparison of spectroscopic and photometric redshifts in the FDF	43
3.3	Histogram of the reduced χ^2 and the photometric redshift errors	44
3.4	Absolute B magnitudes and redshift number distribution of the FDF galaxies	44
3.5	Luminosity functions at 2800 \AA	48
3.6	Luminosity functions in the g' -band	49
3.7	1σ and 2σ confidence levels in Schechter parameter space for different redshift bins	51
3.8	1σ and 2σ confidence levels of the evolution parameters a and b	52
3.9	Redshift evolution of M^* and ϕ^* for g' , u' and the UV bands	53
3.10	Comparison of the FDF luminosity function with Steidel <i>et al.</i> (1999)	54
3.11	Comparison of the FDF luminosity function with Wilson <i>et al.</i> (2002)	54
3.12	Comparison of the B-band FDF LF with model predictions of Kauffmann <i>et al.</i> (1999)	57
3.13	Comparison of the B-band FDF LF with model predictions of Menci <i>et al.</i> (2002)	58
3.14	Luminosity functions at 1500 \AA	60
3.15	Luminosity functions in the u' -band	61
3.16	Luminosity functions in the B -band	62
3.17	Comparison of the FDF luminosity function with Sullivan <i>et al.</i> (2000)	65
3.18	Comparison of the FDF luminosity function with Wolf <i>et al.</i> (2003)	66

3.19	Comparison of the FDF luminosity function with Kashikawa <i>et al.</i> (2003)	67
3.20	Comparison of the FDF luminosity function with Poli <i>et al.</i> (2001)	68
3.21	Comparison of the FDF LF with Iwata <i>et al.</i> (2003) and Ouchi <i>et al.</i> (2004a)	69
3.22	Comparison of the u' -band FDF LF with Blanton <i>et al.</i> (2001) and Blanton <i>et al.</i> (2003)	70
3.23	Comparison of the g' -band FDF LF with Blanton <i>et al.</i> (2001) and Blanton <i>et al.</i> (2003)	71
3.24	Comparison of the FDF luminosity function with Poli <i>et al.</i> (2003)	72
3.25	1σ and 2σ confidence levels of $M^* - \alpha$ in Schechter parameter space	74
4.1	Luminosity functions in the r' -band	78
4.2	Luminosity functions in the i' -band	79
4.3	Luminosity functions in the z' -band	80
4.4	Luminosity functions as given by Blanton <i>et al.</i> (2001) for the r' , i' , and z' bands	81
4.5	Confidence levels of the parameters a and b in the r' , i' and z' bands	82
4.6	Relative evolution of M^* with redshift	83
4.7	Relative evolution of ϕ^* with redshift	83
4.8	Comparison of the FDF LF with Lin <i>et al.</i> (1996) and Lin <i>et al.</i> (1997)	87
4.9	Comparison of the FDF luminosity function with Brown <i>et al.</i> (2001)	87
4.10	Comparison of the FDF luminosity function with Wolf <i>et al.</i> (2003)	89
4.11	Comparison of the FDF luminosity function with Chen <i>et al.</i> (2003)	90
4.12	Comparison of the FDF luminosity function with Shapley <i>et al.</i> (2001)	90
4.13	Comparison of the R-band FDF LF with model predictions of Kauffmann <i>et al.</i> (1999)	91
4.14	Comparison of the I-band FDF LF with model predictions of Kauffmann <i>et al.</i> (1999)	92
5.1	SEDs grouped according to their spectral type	94
5.2	Sérsic index as a function of SED type	95
5.3	Luminosity function per SED type grouped by the 1500 \AA filter	98
5.4	Luminosity function per SED type grouped by the 2800 \AA filter	99
5.5	Luminosity function per SED type grouped by the u' -band	100
5.6	Luminosity function per SED type grouped by the g' -band	101
5.7	Luminosity function per SED type grouped by the r' -band	102
5.8	Luminosity function per SED type grouped by the i' -band	103
5.9	Luminosity function per SED type grouped by the z' -band	104
5.10	Luminosity function per SED type grouped by <i>redshift</i> : $0.45 < z \leq 0.85$	105
5.11	Luminosity function per SED type grouped by <i>redshift</i> : $0.85 < z \leq 1.31$	106
5.12	Luminosity function per SED type grouped by <i>redshift</i> : $1.31 < z \leq 1.91$	107
5.13	Luminosity function per SED type grouped by <i>redshift</i> : $1.91 < z \leq 2.61$	108
5.14	Luminosity function per SED type grouped by <i>redshift</i> : $2.61 < z \leq 3.81$	109
5.15	Luminosity function per SED type grouped by <i>redshift</i> : $3.81 < z \leq 4.51$	110
6.1	Absolute UV-band magnitude vs. redshift of a B, I and K selected catalog	114
6.2	SFR as a function of redshift of a B, I, I+B and K selected catalog	116
7.1	Redshift evolution of the stellar mass fraction from the SFR uncorrected for dust	120
7.2	Dust corrected redshift evolution of the mass fraction in stars from the SFR	121
8.1	Comparison of the luminosity function in the UV, g' , i' , and K bands	127

8.2	Evolution parameters a and b as a function of waveband	128
8.3	Evolution parameters b and ξ as a function of waveband and luminosity densities . .	129
8.4	Restframe K-band luminosity density and mean K-band mass-to-light ratio	130
8.5	Hierarchical clustering vs. monolithic collapse model	132

List of Tables

1.1	Basic and derived cosmological parameters	6
2.1	Characteristics of the FORS Deep Field	20
2.2	Observing log of the FDF observations	20
2.3	Overview of the photometric observations	27
2.4	Excerpt from the FDF object catalog	34
2.5	Photometric properties of the z- and 834nm-band	38
3.1	Galaxy distribution in the FDF for the redshift intervals used for computing the luminosity function in the blue bands	45
3.3	Slope α of the luminosity functions for the different wavebands as determined from an error-weighted fit to the data	47
3.2	Slope of the luminosity function for all wavelengths and all redshifts as derived from 3-parameter Schechter fits	50
3.4	Evolution parameters a, b, M_0^* , and ϕ_0^* according to Eq. (3.1)	53
3.5	Schechter parameter for the LF at 1500 Å	63
3.6	Schechter parameter for the LF at 2800 Å	63
3.7	Schechter parameter for the LF in the u'-band	63
3.8	Schechter parameter for the LF in the g'-band	64
3.9	Schechter parameter for the LF in the B-band	64
4.1	Galaxy distribution in the FDF for the redshift intervals used for computing the luminosity function in the red bands	76
4.2	Slope of the luminosity function for all wavelengths and all redshifts as derived from 3-parameter Schechter fits	77
4.3	Slope α of the luminosity functions for the different wavebands as determined from an error-weighted fit to the data	77
4.4	Schechter parameter for the LF in the r'-band	78
4.5	Schechter parameter for the LF in the i'-band	79
4.6	Schechter parameter for the LF in the z'-band	80
4.7	Evolution parameters a, b, M_0^* , and ϕ_0^* according to Eq. (3.1) for <i>Case 1</i>	84
4.8	Evolution parameters a, b, M_0^* , and ϕ_0^* according to Eq. (3.1) for <i>Case 2</i>	84
4.9	Evolution parameters a, b, M_0^* , and ϕ_0^* according to Eq. (3.1) for <i>Case 3</i>	85
7.1	Evolution parameters β and ρ_*^0 of the mass density	122

Zusammenfassung

In dieser Dissertation wird die Entwicklung von Galaxien innerhalb eines sehr großen Zeitraums (90% des Alters des Universums) anhand sehr tief belichteter Aufnahmen des sogenannten *FORS Deep Field* (FDF) untersucht. Homogenität und Größe des Datensatzes erlauben eine gründliche Analyse der Galaxienentwicklung, ohne großen systematischen Effekten zu unterliegen. Nachdem in Kapitel 1 ein Überblick der Kosmologie sowie der Strukturbildung und der bis dato beobachteten Entwicklungen von Galaxien gegeben wurde, werden in Kapitel 2 die Eigenschaften des FDFs diskutiert. Dabei wird der Objekt-Katalog, der über 8000 Galaxien und photometrische Informationen in 9 Filtern enthält, vorgestellt. In Kapitel 3 werden mögliche Auswahleffekte aufgrund des im I-Band ($\sim 8000 \text{ \AA}$) selektierten Kataloges diskutiert und die Güte der Entfernungsbestimmung, welche auf photometrischen Rotverschiebungen basiert, beschrieben ($\Delta z / (z_{spec} + 1) \leq 0.03$). Basierend auf diesen photometrischen Rotverschiebungen wird in Kapitel 3 und Kapitel 4 die Entwicklung der Anzahldichte von Galaxien pro Magnitude und Volumen, also der Leuchtkraftfunktion (LF), in Abhängigkeit der Rotverschiebung analysiert. Die LF der Galaxien entwickelt sich im UV viel stärker als im sichtbaren bzw. nah-infraroten Licht. Ein Vergleich mit der lokalen LF ergibt, daß die Galaxienpopulation im frühen Universum im Mittel im UV viel heller (\sim Faktor 10), die Gesamtanzahl dagegen wesentlich niedriger (\sim Faktor 10) gewesen ist. Im optischen bleibt dieser Trend nachweisbar. Ein Vergleich mit LF-Ergebnissen von anderen Himmelsdurchmusterungen zeigt eine sehr gute Übereinstimmung mit deren Ergebnissen. Aufgrund der tiefen Belichtung des FDFs ist es zudem möglich, auch noch sehr schwache Galaxien in die Analyse mit einzubeziehen und dadurch die Steigung der Leuchtkraftfunktion, d.h. das Verhältnis von schwachen zu hellen Galaxien, deutlich besser zu bestimmen. Ein Vergleich mit Vorhersagen theoretischer Galaxienentwicklungs-Modelle zeigt eine gute Übereinstimmung bei kleiner Rotverschiebung. Mit zunehmender Entfernung nehmen jedoch die Unterschiede zu. Um die Beiträge von einzelnen Galaxienpopulationen zur LF zu untersuchen, wird der Objekt-Katalog in Kapitel 5 in vier typische Populationen aufgeteilt: von frühen Typen mit praktisch keiner Sternentstehung bis hin zu Typen mit extremer Sternbildung. Die jeweilige LF wird in den verschiedenen Rotverschiebungsbereichen mit der Gesamt-LF verglichen. Der unterschiedliche Beitrag dieser Subpopulationen zur Gesamt-LF in den verschiedenen Filtern und bei verschiedenen Rotverschiebungen erklärt auf natürliche Weise die Änderung der Steigung der LF als Funktion der Wellenlänge. In Kapitel 6 wird die Entwicklung der Sternentstehungsrate, d.h. wieviel stellare Masse pro Jahr und Volumen bei welcher Rotverschiebung gebildet wird, untersucht. Dazu wird jeweils ein FDF B, I, (I+B) und GOODS (Great Observatories Origins Deep Survey) K selektierter Galaxien-Katalog analysiert. Es wird gezeigt, daß die Sternentstehungsrate bis $z \sim 1.5$ ansteigt, um dann bis $z \sim 4$ konstant zu bleiben. Bei noch höherer Rotverschiebung scheint sie wieder abzunehmen. Dieser Trend ist weitgehend unabhängig vom Selektionsband. Aus der Sternentstehungsrate wird in Kapitel 7 die Entwicklung der stellaren Massendichte als Funktion der Rotverschiebung berechnet. Unter der Annahme, daß die mittlere Staubkorrektur im UV weitgehend unabhängig von der Rotverschiebung ist, steigt die stellare Masse zw. $z \sim 4$ und $z \sim 0.5$ um einen Faktor ~ 10 an. Ein Vergleich mit der Massendichte in der Literatur ermöglicht es uns außerdem eine mittlere Staubkorrektur von 2.5 ± 0.2 für den UV-Fluß abzuleiten. In Kapitel 8 werden die Ergebnisse nochmals zusammengefasst. Ein Vergleich mit Vorhersagen theoretischer Galaxienentwicklungs-Modelle basierend auf monolithischen Kollaps und hierarchischer Strukturbildung zeigt zudem, daß letztere meist besser mit integralen Beobachtungsgrößen wie der Leuchtkraftdichte übereinstimmen. Es gibt jedoch bei allen Modellen Probleme bei manchen detaillierten Vorhersagen wie zum Beispiel bei der Entwicklung der LF.

Chapter 1

Introduction

1.1 The early Universe

In this section we introduce the basic concepts as well as the predictions of the standard cosmological model focusing mainly on the consequences for galaxy evolution. A detailed descriptions of the mathematical framework of the standard cosmological model can be found for example in Kolb & Turner (1990), Peebles (1993), Padmanabhan (1993) and Peacock (1999) (see also Narlikar & Padmanabhan, 2001, for a review).

1.1.1 Basic concepts

The standard cosmological model is based on two assumptions:

1. The large-scale structure of the universe is determined by gravitational interactions and can be described by Einstein's theory of gravity.
2. The distribution of matter in the universe is isotropic and homogeneous at sufficiently large scales.

These two assumptions are very powerful. The first assumption requires the geometry of the universe to be determined via Einstein's Field Equations. The Field Equations connect the energy (and therefore the mass) distribution in space to its geometrical properties (curvature). The second assumption implies that the large-scale geometry can be described by the Robertson–Walker metric. In spherical coordinates (r, θ, ϕ) the Robertson–Walker metric reads:

$$ds^2 = c^2 dt^2 - a(t)^2 \left(\frac{dr^2}{1 - kr^2} + r^2 (d\theta^2 + \sin^2(\theta) d\phi^2) \right) \quad (1.1)$$

with the dimensionless scalefactor $a(t) = \frac{R(t)}{R_0}$, where $R(t)$ and R_0 are the expansion parameters at time t and t_0 . The Robertson–Walker metric is the most general metric for the space–time distance between two events in a homogenous universe. Depending on the value of k the universe is *open* ($k < 0$), *flat* ($k = 0$) or *closed* ($k > 0$) corresponding to a negatively curved, flat or positively curved space time. With the Robertson–Walker metric, Einstein's equations become

$$\ddot{a} = -\frac{4\pi G a}{3} \left(\rho + 3\frac{p}{c^2} \right) + \frac{1}{3} \Lambda c^2 a \quad (1.2)$$

$$\dot{a}^2 = \frac{8\pi G\rho}{3}a^2 + \frac{1}{3}\Lambda c^2 a^2 - kc^2 \quad (1.3)$$

Eq. (1.2) and Eq. (1.2) are also called the Friedmann-Lemaitre equations. Here ρ is the matter density, p the pressure and Λ the cosmological constant. The ratio $\frac{\dot{a}(t)}{a(t)}$ describing the expansion of the universe is defined as the *Hubble constant*:

$$H(t) = \frac{\dot{a}(t)}{a(t)} \quad (1.4)$$

The value of the *Hubble constant* today ($t = t_0$) is usually written as $H_0 \equiv H(t_0)$. At present time, the proportionality constant H_0 has a value of $71 \pm 3 \text{ km s}^{-1} \text{ Mpc}^{-1}$ (Spergel *et al.*, 2003). Furthermore it is convenient to introduce a dimensionless constant h defined as $H_0 \equiv h 100 \text{ km s}^{-1} \text{ Mpc}^{-1}$. Sometimes also $H_0 \equiv h_{100} 100 \text{ km s}^{-1} \text{ Mpc}^{-1}$ or $H_0 \equiv h_{70} 70 \text{ km s}^{-1} \text{ Mpc}^{-1}$ is used to define H_0 .

Introducing the Hubble constant allows us to rewrite the second Friedman equation in the following form:

$$\frac{H^2(z)}{H_0^2} = \Omega_m(1+z)^3 - \frac{kc^2}{R_0^2 H_0^2}(1+z)^2 + \Omega_\Lambda \quad (1.5)$$

where we have introduced

$$\Omega_m = \frac{8\pi G}{3H_0^2}\rho, \quad \text{and} \quad \Omega_\Lambda = \frac{\Lambda c^2}{3H_0^2} \quad (1.6)$$

as well as the cosmological redshift z . The latter is defined as:

$$z = \frac{\lambda_o - \lambda_e}{\lambda_e} \quad (1.7)$$

where λ_e is the rest-frame wavelength of the emitted radiation, and λ_o is the observed wavelength. Please note that the redshift z is related to the scale factor a by

$$1 + z = \frac{a_0}{a} = \frac{1}{a} \quad (1.8)$$

where a_0 denotes the scalefactor at the present time (defined as unity). As the Friedman equations are second-order differential equations one needs to specify a and \dot{a} at some instant in time (e.g. at the current epoch $t = t_0$) in order to solve them. Therefore, once H_0 , Ω_m , and Ω_Λ , (see Eq. 1.5) as well as the equation of state connecting the density ρ and pressure p (see Eq. 1.2) is known, it is possible to determine not only ρ as a function of the scale factor a , but also a as a function of time t . Therefore it is not surprising that it is a major task in modern cosmology to derive those parameters as precisely as possible.

At this point it is worth mentioning that although astronomers can measure H_0 , Ω_m and Ω_Λ (as we will see later) the relationship between ρ and p has to be provided by particle physic as well as by atomic physics. Therefore it is necessary to combine the knowledge of astronomers, atomic, nuclear and particle physicist in order to make substantial advances in astrophysics.

As shown before, the geometry of the universe is completely determined if the equation of state at all energies is known, and the present values of H_0 , and the individual Ω_i are specified. Ω_i are the contributions of the different energy densities due to matter (Ω_m), vacuum energy / cosmological

constant (Ω_Λ), radiation (Ω_r) and curvature (Ω_k) to the total energy density in the universe that drives the expansion. Combining the Eqs. (1.3) and (1.4) yields

$$1 = \frac{8\pi G\rho}{3H^2} + \frac{c^2\Lambda}{3H^2} - \frac{kc^2}{a^2H^2} \quad (1.9)$$

with

$$\Omega_k = -\frac{kc^2}{a^2H^2} \quad (1.10)$$

translates into:

$$1 = \Omega_m + \Omega_r + \Omega_\Lambda + \Omega_k \quad (1.11)$$

1.2 Structure formation

In order to produce the inhomogeneities seen in the local universe, it is necessary to assume that the universe in its early state contains small deviations from homogeneity in the energy density. If this density perturbations are small, they can be described and evolved forward in time by an unambiguous procedure (see for example Padmanabhan, 1993, for details). The evolution of the density fluctuations with time are a very powerful tool to better understand structure formation. A comparison between the observed structure in the universe and the predicted density fluctuations show that, beside baryons, we need an additional contribution to Ω_m . This can be seen as follows. Let us assume, that Ω_m is exclusively dominated by baryons. Then, for adiabatic fluctuations and strong coupling between photons and baryons at high redshift ($z > 1500$) due to Thomson scattering, the perturbations of the baryonic density follow the relation

$$\delta_B = \frac{\Delta\rho_B}{\bar{\rho}_B} \simeq 3 \frac{\Delta T}{T} \quad (1.12)$$

As at the time of recombination ($z \simeq 1100$), we have

$$\frac{\Delta T}{T} \simeq 10^{-5} \quad \Rightarrow \quad \delta_B < 5 \cdot 10^{-5} \quad (1.13)$$

and therefore we would expect only (as $\delta_k \propto (1+z)^{-1}$ for $\Omega = 1, \Lambda = 0$)

$$\delta_B(t = t_0) < 0.1 \quad (1.14)$$

which is in contrast to the large inhomogeneities observed in the local universe. *Therefore, in a pure baryonic universe galaxies cannot form.* On the other hand, dark matter, which does not couple to photons, would allow tiny fluctuations to grow for a long time before the baryonic matter decouples from radiation (at the time of recombination). Later, after decoupling, the baryonic matter falls in the potential wells of dark matter and form the structures seen today. The signatures of these density fluctuations at the epoch of recombination are clearly visible in the Cosmic Microwave Background (CMB) and are discussed in Sect. 1.2.1

1.2.1 The cosmic microwave background

Matter-radiation equality

The early universe was radiation dominated, because the normal matter density ($p \ll \rho c^2$) scales with $\rho_m \propto R^{-3}$ whereas the radiation-like matter (photons plus neutrinos) scales with $\rho_r \propto R^{-4}$, if they don't interact (of course, radiation and matter are coupled by Thomson scattering, but if we take the thermodynamic approach one also gets $\frac{\rho_m}{\rho_r} \propto (1+z)^{-1}$). Therefore the universe must have been radiation dominated at some time in the past, when the densities of the matter and radiation crossed over. As we also approximately know the present day energy density due to radiation ($\rho_r \approx 9 \times 10^{-34} \text{ g cm}^{-3}$) and due to the normal matter ($\rho_m \approx 1.88 \times 10^{-29} \Omega_m h^2 \text{ g cm}^{-3}$) the redshift, and the temperature of equal matter and radiation energy are given by:

$$1 + z_{eq} \equiv R_0/R_{eq} = 2.32 \times 10^4 \Omega_m h^2 \quad (1.15)$$

$$T_{eq} = T_0(1 + z_{eq}) = 5.50 \Omega_m h^2 \text{ eV} \quad (1.16)$$

Newest measurements of Spergel *et al.* (2003) determines the redshift of matter-radiation equality to $z_{eq} = 3233^{+194}_{-210}$.

Photon decoupling and recombination

Because of the interactions between photons and electrons in the early universe matter and radiation where in good thermal equilibrium. As the universe expands and the mean free path of the photons became larger than the Hubble distance H^{-1} , the density of free electrons became too low to sustain thermal contact. As a consequence matter and radiation decoupled.

The equilibrium abundance of the free electrons (determined by the Saha equation) depends on the temperature. If we define recombination as the point when 90% of the electrons have combined with protons, the recombination occurred at $z_{rec} \approx 1100$ (1089 ± 1 , Spergel *et al.*, 2003). The photons emitted from the last-scattering surface (Surface of Last Scatter) at z_{rec} are now seen in the CMB.

Analyzing the cosmic microwave background

The CMB radiation was first observed in 1965 by Penzias & Wilson (1965). It corresponds to the remnant radiation of the Big Bang emitted at z_{rec} from the last-scattering surface. The COBE (Cosmic Background Explorer) satellite measured the temperature spectrum with high precision. The CMB radiation (as measured with COBE) is a blackbody spectrum with a temperature of $T = 2.728 \pm 0.002 \text{ K}$ (Fixsen *et al.*, 1996) with only very small deviations. Although the deviations from a perfect blackbody spectrum are very small and in the order of only $\frac{\Delta T}{T} \simeq 10^{-5}$ they are very important. Because the temperature fluctuations in the CMB are connected to density fluctuations at the epoch of recombination they are relevant for all structure formation models. Recently the Wilkinson Microwave Anisotropy Probe (WMAP) (Spergel *et al.*, 2003, and references therein) provided high precision maps for the temperature fluctuations (see Fig. 1.1).

Three physical processes are responsible for the origin of the temperature fluctuations:

- On large angular scales ($\theta \sim 10^\circ$) the dominant source of fluctuations is the *Sachs–Wolfe effect* due to the gravitational potential fluctuations at the last scattering surface. This is simply due to

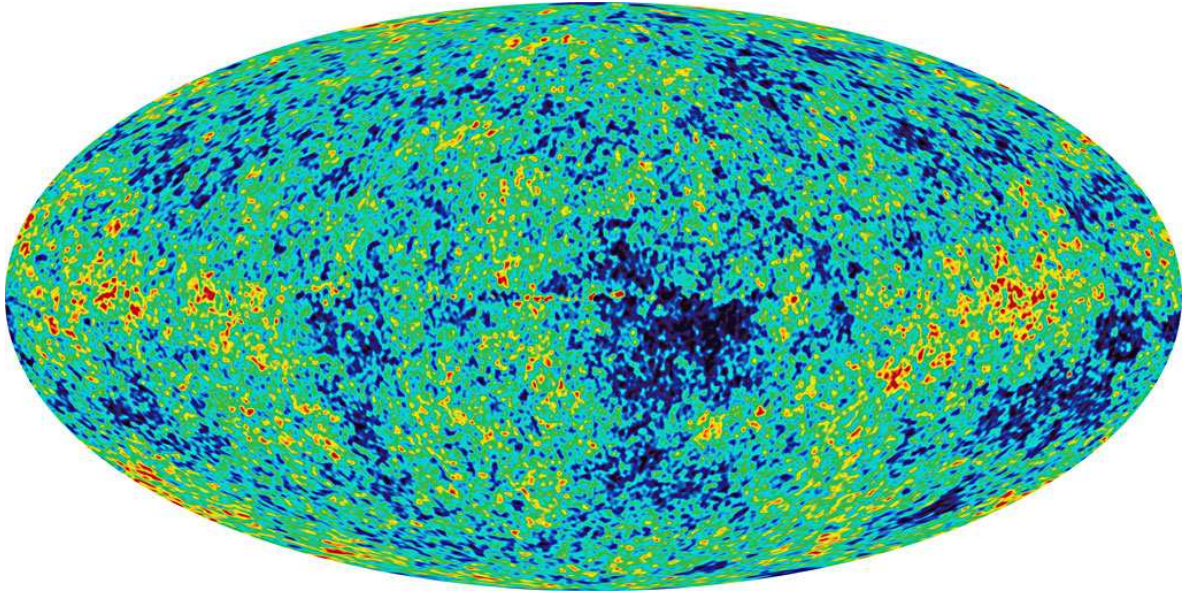


Figure 1.1: All-sky image of the temperature fluctuations in the Cosmic Microwave Background as measured by *WMAP* (Spergel *et al.*, 2003).

the fact that photons gain (or lose) energy when they escape from over-dense (or under-dense) regions (gravitational redshift).

- On *intermediate scales* ($\theta \sim 1^\circ$) the baryonic perturbations oscillate, which can be observed as *acoustic peaks* in the angular spectrum of CMB fluctuations.
- On *small angular scales* ($\theta < 1^\circ$) the oscillations are damped, mainly by the process called *Silk damping* (photon diffusion suppresses small-scale perturbation).

It turns out that the form of the angular power spectrum is strongly dependent on the cosmological parameters (Spergel *et al.*, 2003). Therefore Spergel *et al.* (2003) combined data of *WMAP*, CBI (Cosmic Background Imager), ACBAR (Arcminute Cosmology Bolometer Array Receiver), 2dFGRS (2dF Galaxy Redshift Survey) and Lyman α forest data and was able to derive very accurate values for most of the cosmological parameters as h , Ω_m , Ω_Λ , etc. An excerpt of the results derived by Spergel *et al.* (2003) is presented in Table 1.1.

1.2.2 The dark age

The period of time between the last scattering of the CMB radiation (by the homogeneous plasma) and the formation of the first stars is also known as the Dark Age of the universe (see Barkana & Loeb, 2001; Miralda-Escudé, 2003, for reviews). The universe would then have appeared completely dark (for human eyes) as the temperature dropped and the blackbody radiation of the CMB shifted to the infrared. On the other hand the small fluctuations generated in the early universe grow over time (due to gravitational instability) and lead to the formation of galaxies and large scale structure observed today. Structure formation in cold dark matter models proceeds hierarchically: At early times, most

Table 1.1: Basic and derived cosmological parameters as published by Spergel *et al.* (2003)^a

	Mean and 68% Confidence Errors
Hubble Constant	$h = 0.71^{+0.04}_{-0.03}$
Baryon Density	$\Omega_b h^2 = 0.0224 \pm 0.0009$
Matter Density	$\Omega_m h^2 = 0.135^{+0.008}_{-0.009}$
Optical Depth	$\tau = 0.17 \pm 0.06$
Baryon Density/Critical Density	$\Omega_b = 0.044 \pm 0.004$
Matter Density/Critical Density	$\Omega_m = 0.27 \pm 0.04$
Age of the Universe	$t_0 = 13.7 \pm 0.2$ Gyr
Reionization Redshift ^b	$z_r = 17 \pm 4$
Decoupling Redshift	$z_{dec} = 1089 \pm 1$
Redshift of Matter/Radiation Equality	$z_{eq} = 3233^{+194}_{-210}$

^aFit to the *WMAP*, CBI (Cosmic Background Imager), ACBAR (Arcminute Cosmology Bolometer Array Receiver), 2dFGRS and Lyman α forest data

^bAssumes ionization fraction, $x_e = 1$

of the dark matter is concentrated in low-mass halos, and these halos continuously accrete mass and merge to form high-mass halos (see also Sect. 1.3.1).

Bound objects form out of the primordial density fluctuations when they reach the so called non linear regime i.e. the density fluctuations reach an amplitude near unity ($\frac{\Delta\rho}{\rho} \sim 1$). This happens first on small spatial scales and later on larger and larger scales. During the dark age the linear fluctuations grow in proportion to the scale factor $(1+z)^{-1}$ when matter dominates the energy density of the universe i.e. for $1 \lesssim z \lesssim 3500$. Therefore at relatively low redshift ($10 \lesssim z \lesssim 20$) primordial density fluctuations had grown enough for the dark matter halos of about $10^4 \mathcal{M}_\odot$ to collapse. As the dynamical collapse of a dark matter halo can be solved analytically only in cases of a particular symmetry it is done by numerical simulations. In Fig. 1.2 we show the mass scale for different models at which a 1σ fluctuation is just collapsing for different redshifts ($z = 0, 2, 5, 10, 20, 30$). The figure has been taken from Barkana & Loeb (2001). From the point where the blue horizontal lines crosses the red solid line one can infer, e.g., that at $z = 5$ a 1σ fluctuation on a mass scale of $2 \times 10^7 \mathcal{M}_\odot$ will collapse. One can also clearly see from the figure, that at local redshift structures between $10^{13} \mathcal{M}_\odot$ and $10^{14} \mathcal{M}_\odot$ start to collapse out of a 1σ fluctuation. This mass range corresponds to present day massive galaxy clusters.

Once the halo mass reach the Jeans mass of the gas (at the virialized temperature and density of the intergalactic medium) the gas can follow the collapse of the dark matter halos. Shortly after the first stars were formed and the dark age ended.

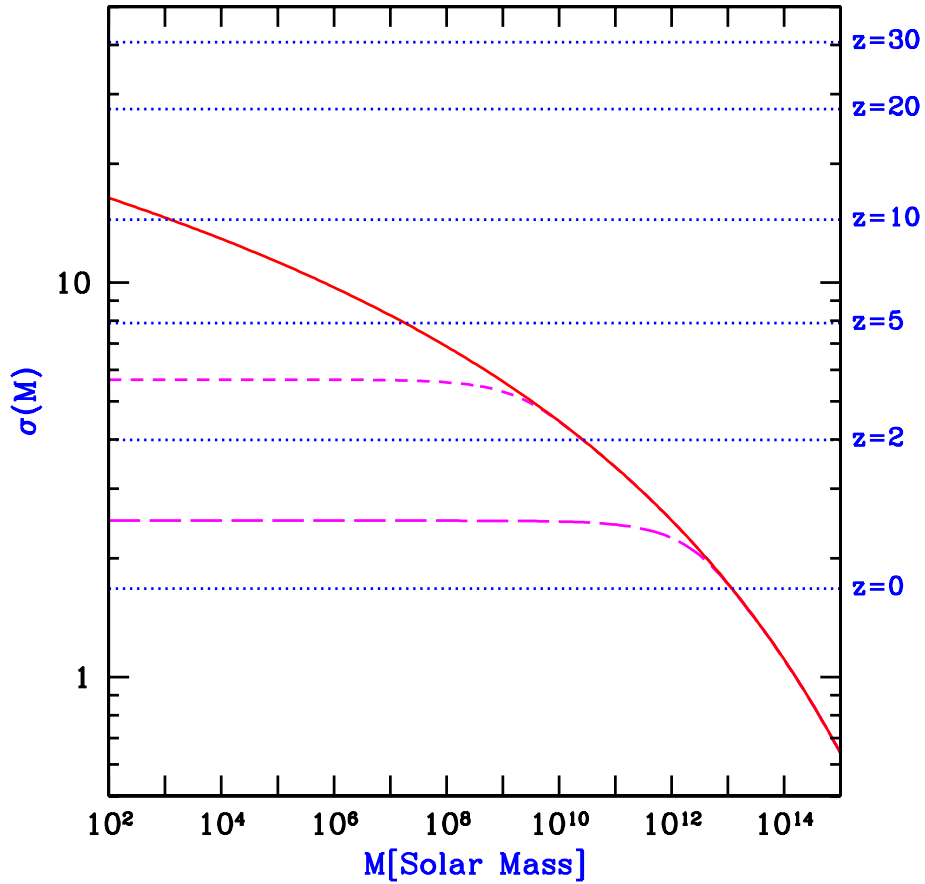


Figure 1.2: Mass fluctuations and collapse thresholds in cold dark matter models as published in Barkana & Loeb (2001). The horizontal dotted lines show the value of the extrapolated collapse overdensity $\delta_{\text{crit}}(z)$ at the indicated redshifts. Also shown is the value of $\sigma(M)$ for a Λ CDM model with $\Omega_m = 0.3$ (solid curve), as well as $\sigma(M)$ for a power spectrum with a cutoff below a mass $M = 1.7 \times 10^8 \mathcal{M}_\odot$ (short-dashed curve), or $M = 1.7 \times 10^{11} \mathcal{M}_\odot$ (long-dashed curve). The intersection of the horizontal lines with the other curves indicate, at each redshift z , the mass scale (for each model) at which a 1σ fluctuation is just collapsing at z

1.2.3 Reionization and the first stars

Formation of the first stars

According to models of hierarchical structure formation the first stars (also known as Population III stars) should have formed in dark matter mini halos of mass $10^6 \mathcal{M}_\odot$ that collapsed at redshifts $z \approx 20 - 30$ (e.g. Couchman & Rees 1986; Yoshida *et al.* 2003; see also Bromm & Larson 2004 for a review). These systems correspond to $3\sigma - 4\sigma$ peaks of the primordial density fluctuations at that redshift (see also Fig. 1.2) and are sufficiently massive to contain dense gas clouds (Yoshida *et al.*, 2003).

Cooling of the gas is a basic ingredient of star formation. This is especially true in the absence of metals because only if the cooling timescale is shorter than the dynamical timescale of the system gas is able to cool and form stars. This enables us to derive the minimum halo mass ($\approx 10^6 M_{\odot}$) for a given redshift ($z \approx 20 - 30$) where the gas can cool.

The virial temperatures ($\propto 10^4 \text{K}$) in these low-mass halos ($T_{\text{vir}} \propto M^{2/3}(1+z)$; Barkana & Loeb 2001) are too low for efficient atomic hydrogen cooling. Therefore cooling can only be done by the means of molecular hydrogen (Oh & Haiman, 2002). Results of Bromm *et al.* (1999, 2001) show that the collapsing region forms a disk which fragments into many clumps. The clumps have a typical mass $\sim 10^2 - 10^3 M_{\odot}$. The slow cooling in these first objects (H_2 cooling) leads to the formation of these very massive stars. This mass scale corresponds to the Jeans mass for a temperature of $\sim 200 \text{K} - 500 \text{K}$ and the density $\sim 10^4 \text{cm}^{-3}$. Because of this high mass their lifetime is very short ($\sim 10^6$ years) but they produce a large amount of ionizing photons over a lifetime. Although it is not yet fully clear if Population III stars were the main source of ionizing photons during the reionization of the hydrogen in the universe at $z \sim 15$, they certainly play an important role.

When some of these massive stars end their lives in supernovae, they eject heavy elements. The next generation of stars can then be formed by cooling provided by heavy elements. This is much more effective and reduces the Jeans mass allowing the formation of low-mass stars.

Reionizing the IGM

As discussed in Sect. 1.2.1 the baryonic matter combined into atoms at $z \sim 1100$. Nevertheless the intergalactic matter must have been *reionized* before the present. The evidence comes from observations of the spectra of quasars. Photons emitted at wavelength shorter than $\text{Ly}\alpha$ (1216 Å) are scattered by atomic H when their wavelength is redshifted to the $\text{Ly}\alpha$ line. This suppression of the flux at wavelength shorter than $\text{Ly}\alpha$ is called the Gunn-Peterson trough. As quasars are very luminous and therefore can be observed up to very high redshift ($z \sim 6$) their absorption lines can be used to study the Gunn-Peterson trough as a function of z .

Quasars with redshifts of $z < 6$ do *not* show the Gunn-Peterson trough, but have flux also at wavelength shorter than $\text{Ly}\alpha$. Furthermore one also sees the flux absorbed only partially by intervening H clouds, known as the $\text{Ly}\alpha$ forest. Most of the intervening hydrogen between $z = 6$ and $z = 0$ must therefore be ionized and in equilibrium with a ionizing background produced by quasars and galaxies.

Although the FORS Deep Field is not deep enough to accurately constrain the star formation rate (SFR) and therefore the amount of ionizing photons between $z = 5$ and $z = 6$, we are able to follow the latter in the redshift interval $0.5 < z < 5$. We show in Chap. 6 precise measurements of the star formation rate. The SFR increases from low redshift up to $z \sim 1.5$ remaining approximately constant for $1.5 \leq z \leq 4$ and dropping by about 50% around $z = 4.5$, if dust corrections constant with redshift are assumed.

The situation changes very fast if we go to higher redshifts. Recently discovered quasars at $z \sim 6.4$ (e.g. White *et al.*, 2003) show a complete Gunn-Peterson trough indicating that the cosmic ionizing background changes at redshifts $z \sim 6$. Measurement of *WMAP* in combination with other data (Spergel *et al.*, 2003) were able to derive the redshift of reionization to $z_r = 17 \pm 4$. They mainly used the fact, that at the time of reionization most of the electrons were free electrons and able to scatter the CMB photons (Thompson scattering). The optical depth τ_e produced by the intergalactic medium therefore traces the ionization state of the intergalactic medium: the sooner reionization started, the

larger the value of τ_e . The large optical depth of $\tau = 0.17 \pm 0.06$ derived by Spergel *et al.* (2003) tells us, that a large fraction of the matter in the universe was already reionized at $z \sim 17$. Therefore, as at $z \sim 6$ nearly all the universe was ionized (see above) a large increase in the emitted ionizing radiation is required from $z \sim 6$ to $z \sim 17$. One possible source of the ionizing radiation could be the first stars. If the first stars that formed with no heavy elements were all massive (as it is expected, see above), they can produce a large amount of ionizing radiation.

1.3 Galaxy evolution

1.3.1 Theoretical framework for galaxy evolutions

There are two competing scenarios which try to describe the formation and evolution of galaxies. One theory is based on the *monolithic collapse model* and subsequent *pure luminosity evolution* of the galaxies. The second one describes galaxy evolution in the framework of *hierarchical clustering*. The main difference of the two models is the assembly of massive galaxies, i.e. the time or redshift when these massive galaxies have formed. A comparison of observations with the predicted redshift evolution of the stellar mass and luminosity density for the two scenarios are presented in Sec. 8.2.

Monolithic collapse model

In the monolithic collapse scenario elliptical and bulges formed at high redshift (e.g. $z_f \gtrsim 2.5$). They are the result of a violent burst of star formation which follows a monolithic collapse of a gas cloud (Eggen *et al.*, 1962; Sandage, 1986, 1990). They convert most of their gas into stars and loose a large part of the residual gas (after the main burst) by means of a galactic wind (Arimoto & Yoshii, 1987; Matteucci, 1994). The so called pure luminosity evolution starts after the violent burst simply because the stellar population ages. Please note that in the monolithic collapse model no interaction via merging is assumed.

Recent models of e.g. Pozzetti *et al.* (1996, 1998) divide the present day galaxy luminosity function into different Hubble types and describe the spectral evolution for each type using stellar population synthesis models (Tinsley 1980, modern version e.g. Bruzual & Charlot 1993). These models are tuned to reproduce well known properties of local galaxies. The age of most of the galaxy is set to a fixed redshift z_f and the evolution stems mainly from the different star formation rate histories adopted for the different Hubble types. Most of the models parameterize the time-evolution of the star formation rate (SFR) by the assumption $\text{SFR} \propto \exp(-t/\tau)$ where τ is the e-folding timescale. The (free parameter) τ is set to a value in order to reproduce the observed broad-band colors at $z \sim 0$. For the different Hubble types τ typically changes between 1/10 and 10 Gyr.

Hierarchical clustering

The hierarchical clustering scenario is based on the Press & Schechter (1974) structure formation theory. It assumes that galaxies are formed out of the primordial density fluctuations (see also Sect. 1.2) generated during inflation. Originally the Press & Schechter (1974) theory was developed to study the behavior of the dark matter. In a Λ cold dark matter dominated universe small dark matter halos collapse first (see Fig. 1.2) and form larger halos by merging. Moreover in this scenario baryonic matter follows dark matter in all merging processes, i.e the gas is mixed with the dark matter. After the dark

matter halos have collapsed stars can form out of the gas (see e.g. Cole *et al.*, 2000, and references therein).

In contrast to the monolithic collapse scenario small masses form first and massive spheroid are formed from several merging episodes triggering modest star formation (White & Rees, 1978; Kauffmann *et al.*, 1993; Baugh *et al.*, 1998).

To follow the evolution of the dark matter and baryons two different methods have been developed: the *semi-analytic models* (SAMs) (White & Rees, 1978; Kauffmann *et al.*, 1993; Cole *et al.*, 1994; Somerville & Primack, 1999; Kauffmann *et al.*, 1999; Poli *et al.*, 1999; Wu *et al.*, 2000; Cole *et al.*, 2000; Menci *et al.*, 2002, 2004) as well as simulations based on *smoothed-particle hydrodynamics* (SPH) (Davé *et al.*, 1999; Weinberg *et al.*, 2002; Nagamine, 2002; Nagamine *et al.*, 2004; Weinberg *et al.*, 2004).

The SPH simulations include the dynamics of the cooling gas in the calculations and solve the gravitational and hydrodynamical (gas) equations explicitly. Nevertheless, this approach is computationally very intensive and therefore the achieved resolution is still not suitable to resolve the formation and internal structure of individual galaxies.

The SAMs follow the evolution of the dark matter directly by N-body methods or using Monte Carlo techniques (in the framework of hierarchical clustering) while the evolution of the baryonic component is calculated by simple analytic models. Although SAMs do not suffer from resolution limitations, they have to use simplified recipes to describe the gas processes (gas cooling, photoionization, star formation, feedback processes, etc.). Nevertheless, a detailed comparison between SAM and SPH simulations by Pearce *et al.* (1999) and Benson *et al.* (2001) show good agreement.

As already mentioned, the main difference of the two scenarios (monolithic collapse and hierarchical clustering) is the redshift when massive galaxies have formed (see also e.g. Cimatti *et al.*, 2002b; Pozzetti *et al.*, 2003; Calura *et al.*, 2004, for a detailed comparison of the two models). The different predictions are very well illustrated in Fig. 1.3 taken from Cimatti *et al.* (2002b). The observed cumulative number of galaxies (from the K20 survey; Cimatti *et al.* 2002a) with $K_s \lesssim 20$ (Vega system) between $1 < z < 3$ and the corresponding poissonian $\pm 3\sigma$ confidence region is shown. As described in Chap. 7 the K-band is a very good tracer of the stellar mass and therefore galaxies bright in the K-band are also thought to be massive. The prediction of the PLE model of Pozzetti *et al.* (1996, 1998) denoted as PPLE as well as the predictions of the SAM of Menci *et al.* (2002) is also shown (see also Sec. 8.2). At redshift of about $z \sim 1.6$ nearly no massive galaxies are predicted by the SAM of Menci *et al.* (2002) whereas in the PLE models massive galaxies have already assembled at this redshift.

1.3.2 Observational evidence for galaxy evolutions

Observational constraints on galaxy formation have improved significantly over the last years and it has become possible to study the evolution of global galaxy properties up to very high redshifts.

Surveys and their distance determinations

Locally, the 2dF Galaxy Redshift Survey (2dFGRS; Colless *et al.* 2001), the Sloan Digital Sky Survey (SDSS; Stoughton *et al.* 2002) and the 2MASS survey (Jarrett *et al.*, 2000) have recently provided very large galaxy samples in various bands, from the blue U-band to the red K-band. Thanks to these superb datasets we are now able to assess very accurate local ($z \sim 0.1$) reference points for any kind

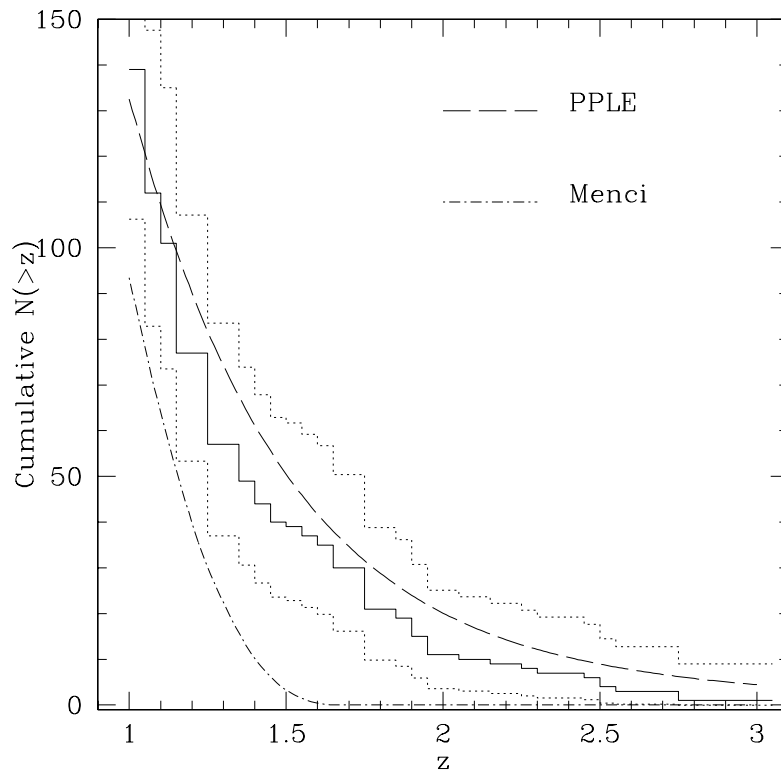


Figure 1.3: The observed cumulative *number* of galaxies with $K_s \lesssim 20$ (Vega) between $1 < z < 3$ (continuous line) and the corresponding poissonian $\pm 3\sigma$ confidence region (dotted lines). The figure has been taken from Cimatti *et al.* (2002b). The prediction of the PLE model of Pozzetti *et al.* (1996, 1998) (denoted as PPLE) as well as the predictions of the SAM of Menci *et al.* (2002) is also shown (see Cimatti *et al.*, 2002b, for details).

of measurements of the galaxy evolution like the luminosity function, the star formation activity, the spatial clustering of galaxies, the stellar population, the morphology, etc.

In the redshift range between $0.2 \lesssim z \lesssim 1$ pioneering work has been done in the context of the Canada France Redshift Survey (Lilly *et al.*, 1995a), the Autofib survey (Ellis *et al.*, 1996) and in the Canadian Network for Observational Cosmology survey (Yee *et al.*, 1996). They provide accurate distances and absolute luminosities by spectroscopic followup of optically selected galaxies, thus being able to probe basic properties of galaxies evolution. The K20-survey (Cimatti *et al.*, 2002a) as well as the MUNICS-survey (Drory *et al.*, 2001; Feulner *et al.*, 2003) extend the analysis of galaxy evolution into the near infrared regime (for $0.2 \lesssim z \lesssim 1.5$).

Because of historical difficulties in spectroscopically identifying galaxies in the redshift range $1.4 \lesssim z \lesssim 2.5$ ("redshift desert") from the ground, galaxies in that range are rare. It is not due to any intrinsic changes in the galaxy populations but simply due to observational difficulties. Only very recently it has been possible to overcome these limitations (see e.g. Steidel *et al.*, 2004) and interesting new results can be expected in the near future.

An important step to extend the analysis of galaxy evolution and to probe the properties of galaxies

up to the highest redshifts was the work of Steidel & Hamilton (1993) and Steidel *et al.* (1996). They used color selection to discriminate between low redshift and high redshift galaxies (see Giavalisco, 2002, for a review). The so called Lyman-break galaxies (LBGs, mainly starburst galaxies at high redshift) are selected by means of important features in the UV spectrum of star forming galaxies. One important feature is the Lyman continuum discontinuity at 912 Å (Lyman break) forming in the stellar atmospheres of massive stars. Furthermore the Lyman break is made more pronounced by the absorption of interstellar and intervening HI gas (Steidel *et al.*, 1995, 1999; Madau, 1995). Sources at high redshift are also subjected to a redshift dependent additional opacity by the intervening Ly α forest which dims the continuum between 912 Å and 1216 Å.

The next milestones in pushing the limiting magnitude for detectable galaxies to fainter and fainter limits were the space based Hubble Deep Field North (HDFN; Williams *et al.* 1996) and Hubble Deep Field South (HDFS; Williams *et al.*, 2000; Casertano *et al.*, 2000) (see Ferguson *et al.*, 2000, for a review). Although of a limiting field of view of about 5 arcmin² only, the depth of the HDFs allowed the detection of galaxies up to a redshift of 5 and even beyond.

In the past 5 years the space based HDFs were supplemented by more multi-band photometric surveys as the NTT SUSI deep Field (NDF; Arnouts *et al.* 1999b), the Chandra Deep Field South (CDFs; Arnouts *et al.* 2001), the William Herschel Deep Field (WHDF; McCracken *et al.* 2000; Metcalfe *et al.* 2001), the Subaru Deep Field/Survey (SDF; Maihara *et al.* 2001; Ouchi *et al.* 2003), the Great Observatories Origins Deep Survey (GOODS; Giavalisco *et al.* 2004b), the Ultra Deep Field (UDF and UDF-Parallel ACS fields; Giavalisco *et al.* 2004a; Bunker *et al.* 2004; Bouwens *et al.* 2004) and last but not least the FORS Deep Field (FDF; Heidt *et al.* 2003, see also Sect. 3.2).

Although the Lyman-break technique is very efficient in selecting high redshift galaxies (see Blaizot *et al.* 2004 for a detailed discussion) with a minimum of photometric data, it has the disadvantage that it does not sample galaxies homogeneously in redshift space and may select against certain types of objects. With the advent of more deep multi-band photometric surveys in the last years the photometric redshift technique (essentially a generalization of the drop-out technique) has increasingly been used to identify high-redshift galaxies. Several methods have been described in the literature to derive photometric redshifts (Baum, 1962; Koo, 1985; Brunner *et al.*, 1999; Fernández-Soto *et al.*, 1999; Benítez, 2000; Bender *et al.*, 2001; Le Borgne & Rocca-Volmerange, 2002; Firth *et al.*, 2003). Photometric redshifts are often determined by means of template matching algorithm (see Sect. 3.4 for a detail description) that applies Bayesian statistics and uses semi-empirical template spectra matched to broad band photometry. Redshifts of galaxies that are several magnitudes fainter than typical spectroscopic limits can be determined reliably with an accuracy of $\Delta z/(z_{spec} + 1)$ of 0.1 to 0.03.

Restframe galaxy luminosity function

One of the major task in extragalactic astronomy is to derive the galaxy luminosity function (number density per magnitude bin) in different bandpasses and for different redshifts. As the luminosity function is one of the fundamental observational tool the amount of work spend by different groups in deriving accurate luminosity functions was large. Based on either spectroscopic redshifts, drop-out techniques, or photometric redshifts, it has been possible to derive luminosity functions at different redshifts in the

- ultraviolet (UV): Treyer *et al.* (1998); Steidel *et al.* (1999); Cowie *et al.* (1999); Adelberger & Steidel (2000); Cohen *et al.* (2000); Sullivan *et al.* (2000); Ouchi *et al.* (2001); Poli *et al.*

(2001); Wilson *et al.* (2002); Wolf *et al.* (2003); Rowan-Robinson (2003); Kashikawa *et al.* (2003); Ouchi *et al.* (2003); Iwata *et al.* (2003); Gabasch *et al.* (2004b)

- blue bands: Lilly *et al.* (1995b); Heyl *et al.* (1997); Lin *et al.* (1997); Sawicki *et al.* (1997); Small *et al.* (1997); Zucca *et al.* (1997); Loveday *et al.* (1999); Marinoni *et al.* (1999); Fried *et al.* (2001); Cross & Driver (2002); Im *et al.* (2002); Marinoni *et al.* (2002); Norberg *et al.* (2002); Bell *et al.* (2004); de Lapparent *et al.* (2003); Liske *et al.* (2003); Poli *et al.* (2003); Pérez-González *et al.* (2003a); Gabasch *et al.* (2004b).
- red bands: Lin *et al.* (1996, 1997); Brown *et al.* (2001); Wolf *et al.* (2003); Chen *et al.* (2003); Shapley *et al.* (2001).
- Near-IR bands: Loveday (2000); Kochanek *et al.* (2001); Cole *et al.* (2001); Balogh *et al.* (2001); Drory *et al.* (2003); Huang *et al.* (2003); Feulner *et al.* (2003)

Pioneering work has been done by Lilly *et al.* (1995b) based on the Canada France Redshift Survey. Lilly *et al.* (1995b) find that the B-band luminosity function of red galaxies shows very little change in either number density or luminosity over the entire redshift range $0 \lesssim z \lesssim 1$. In contrast the luminosity function of blue galaxies shows substantial (~ 1 mag) evolution. This indicates that red, massive galaxies must have already been assembled at $z \sim 1$, whereas the still evolving blue sample are formed later. Poli *et al.* (2003) analyzed about 1700 galaxies from deep surveys (including the HDFs) to construct the B-band luminosity function up to redshift $\langle z \rangle \sim 3$. They found only little density evolution up to $z \sim 1$ and a moderate increase of the characteristic luminosity by ~ 0.6 mag in the range $0.4 \lesssim z \lesssim 1$. At $z \sim 2 - 3$ the luminosity function shows a brightening with respect to the local value in the order of about 1 mag (see Fig. 3.24).

In the UV Sullivan *et al.* (2000) derived the luminosity function based on about 433 UV-selected sources in the redshift range $0.15 < z \leq 0.4$. The analysis of Wolf *et al.* (2003, see Fig. 3.18), Kashikawa *et al.* (2003, see Fig. 3.19), Poli *et al.* (2001, see Fig. 3.20), and Steidel *et al.* (1999, see Fig. 3.10), extended the derivation to redshift $z \sim 3$. They all found a substantial brightening of the overall LF with increasing redshift and most of them also a decrease in number density.

It is not an easy task to discriminate between the luminosity evolution and density evolution of galaxies. This can be best seen if one analyzes the LF by means of a Schechter function (Schechter, 1976):

$$\Psi(L) = \frac{\phi^*}{L^*} \left(\frac{L}{L^*} \right)^\alpha \exp\left(-\frac{L}{L^*}\right) \quad (1.17)$$

where L^* is the characteristic luminosity, α the faint-end slope, and ϕ^* the normalization of the luminosity function. The corresponding equation in absolute magnitudes reads

$$\Psi(M) = \frac{2}{5} \phi^* \ln 10 10^{0.4(M^* - M)(1 + \alpha)} \exp\left(-10^{0.4(M^* - M)}\right) \quad (1.18)$$

The redshift evolution of the three free parameters of the Schechter function M^* , ϕ^* , and α can then be used to quantitatively describe the evolution in density and luminosity. Unfortunately the parameters are highly correlated (e.g. see Fig. 3.7 and Fig. 3.25) making it challenging to clearly separate the evolution of the different parameters (see also Andreon, 2004, for a discussion).

Iwata *et al.* (2003) as well as Ouchi *et al.* (2004a) extended the analysis to redshift $z \sim 4 - 5$ (see Fig. 3.21). Iwata *et al.* (2003) finds, that the luminosity function of LBG candidates at $z \sim 5$ did

not show a significant difference from those of LBGs at $z \sim 3$ and 4, though there might be a slight decrease in the fainter part. On the other hand Ouchi *et al.* (2004a) find that the number density of bright galaxies ($M_{1700} < -22$) decreases significantly from $z = 4$ to 5 and that the faint-end slope of the luminosity functions of LBGs may become steeper towards higher redshifts.

First attempts to derive the UV luminosity function even at redshift $z \sim 6$ and beyond are done by Bunker *et al.* (2004); Bouwens *et al.* (2004) and Yan & Windhorst (2004a). Bouwens *et al.* (2004) find that the shape of the LF is consistent with that found at lower redshift. Though a strong degeneracy is found between luminosity and density evolution, there seems to be a slightly decrease in density and also in luminosity (about 0.6 mag) if compared to the $z = 3$ LF of Steidel *et al.* (1999). The best fitting slope of the luminosity function on the other hand is rather uncertain extending from $\alpha = -1.15$ (Bouwens *et al.*, 2004) to $\alpha \sim -1.8$ (Yan & Windhorst, 2004a).

As at $z \sim 6$ we are approaching the time of reionization (see Sect. 1.2.3) the slope of the UV luminosity function starts to play an important role in identifying the sources responsible for the ionization of the IGM. This can be understood if one takes into account that the total luminosity density produced by integrating over the Schechter function is given by:

$$\mathcal{L} = \phi^* \times L^* \times \Gamma(2 - \alpha) \quad (1.19)$$

where Γ is the Γ -function. Thus, low luminosity galaxies are able to account for a large part of the UV photons given the number is sufficient (which implies a steep α). Recent results of Yan & Windhorst (2004b) show that to have the universe completely ionized at $z \sim 6$, the faint-end slope of the LF should be steeper than $\alpha = -1.6$, unless either the normalization of the LF or the clumping factor of the ionized hydrogen has been significantly underestimated.

Star formation rate

The global star formation rate history of the universe is a very basic ingredient when trying to understand at what time most of the mass locked in stars has been built up (see also Chap. 6 and Chap. 7). In the past different star formation rate indicators (e.g. see Hopkins *et al.*, 2001; Hopkins, 2004) are used to address the conversion from gas into stars. Based on about 4600 radio sources at 1.4 GHz Condon *et al.* (2002) measured the local SFR from the Uppsala Galaxy Catalog whereas Sadler *et al.* (2002) derived the SFR from the radio sources in the 2dF Galaxy Redshift Survey. The analyzed local 2dFGRS radio sources are a mixture of active galaxies (60 %) and star-forming galaxies (40 %).

Star formation up to $z \sim 1.2$ are derived by Hogg *et al.* (1998) and Teplitz *et al.* (2003) from the [O II] (3727 Å emission line) luminosity density. Teplitz *et al.* (2003) find that although the uncertainties involved are large, the evolution of the observed [O II] luminosity density is consistent with a $(1+z)^4$ evolution in global star formation since $z \sim 1$.

Hopkins *et al.* (2000), Tresse *et al.* (2002), and Pérez-González *et al.* (2003b), used observations of the $H\alpha$ Balmer line (6563 Å) to derive the SFR. Tresse *et al.* (2002) analyzed 33 field galaxies from the CFRS with redshifts between 0.5 and 1.1 to derive the SFR and compare the properties of this sample with the low-redshift sample of CFRS galaxies (at $z \sim 0.2$). They find, that the comoving $H\alpha$ luminosity density increases by a factor 12 from $z \sim 0.2$ to $z = 1.3$. Therefore their result is consistent with a $(1+z)^4$ evolution in global star formation at $z < 1.3$.

In order to trace the SFR to higher redshifts the flux emitted in the UV can be used. As galaxy luminosities measured in the ultraviolet are sensitive to the energy output of hot, short-living O and B type stars, for a given IMF the UV luminosity density is proportional to the instantaneous SFR

(Madau *et al.*, 1996, 1998). Although UV flux can be absorbed by dust and the total SFR depends on the initial mass function, this method allows to trace the SFR from the local universe up to very high redshift ($z \sim 6$). Pascarelle *et al.* (1998) and Madau *et al.* (1998) derived the SFR from the relatively small HDFN whereas Steidel *et al.* (1999) used the LBG-sample to derive the star formation rate. Recent work of Bouwens *et al.* (2003a), Iwata *et al.* (2003), Bunker *et al.* (2004), Giavalisco *et al.* (2004a), as well as Bouwens *et al.* (2004) extended this approach to redshift $z \sim 6$. Even though the absolute values slightly differ, they all confirm the picture, that the local star formation rate rises up to redshift of about $z \sim 1.5$ staying approximately constant for $1 \leq z \leq 4$ (if dust corrections constant with redshift are assumed). Even if recent results (e.g. Bouwens *et al.*, 2004) suggest a decrease in the SFR at redshift $z > 4$ this is still not yet clear.

The largest uncertainty in deriving the SFR from the luminosity density in the UV is dust correction. Therefore Hughes *et al.* (1998) used the deep submillimeter-wavelength ($850\mu\text{m}$) survey of the Hubble Deep Field to trace directly the emission from dust that has been warmed by massive star-formation activity. These so called SCUBA-sources appear to be galaxies in the redshift range $2 < z < 4$, which, assuming these objects have properties comparable to local dust-enshrouded starburst galaxies, implies a star-formation rate during that period about a factor of five higher than that inferred from the optical and ultraviolet observations.

Clustering

The clustering of galaxies has long been an essential testing ground for cosmological models and the theory of galaxy formation. The question of how the structures we see today have formed and developed, is still one of the most challenging ones in the field of cosmology. The advent of very large local redshift surveys as well as deep pencil beam surveys has led to measurements of increasing precision and detail. Galaxy clustering is usually measured by the spatial ($\xi(r)$) or angular ($\omega(\theta)$) two-point correlation function. The spatial correlation function is usually expressed by a power law:

$$\xi(r) = \left(\frac{r}{r_0}\right)^{-\gamma}, \quad (1.20)$$

where r is the spatial separation between two objects, r_0 is the correlation length, and γ is the slope of the power law. Therefore a large correlation length r_0 implies large clustering of the galaxies.

However, the values of r_0 and γ , depend on the luminosity, color, and type of the galaxies (Norberg *et al.*, 2001; Zehavi *et al.*, 2002). At the present epoch galaxies are highly clustered and the universe seems to be homogeneous only on the very largest scales. Jing *et al.* (2002), Zehavi *et al.* (2002), and Norberg *et al.* (2001) measured the clustering of galaxies in the PSCz, the SDSS and the 2dFGRS, respectively. The derived correlation length r_0 is of the order of $5 h_{100}^{-1} \text{Mpc}$.

At redshifts of about $z \sim 3$ Giavalisco & Dickinson (2001) and Giavalisco *et al.* (1998) report on the clustering properties of relatively bright Lyman break galaxies. They derived a correlation length r_0 for LBGs in the order of $4 h_{100}^{-1} \text{Mpc}$. The discovery that the clustering of Lyman-break galaxies is similar to that of L_* galaxies at $z = 0$, despite the weaker expected clustering of the underlying mass distribution, provides strong evidence that the bright galaxy population was highly *biased* at $z \approx 3$ (the bias parameter describes whether the clustering amplitude of the galaxies differs from that of the underlying dark matter). Combining the results of Ouchi *et al.* (2004b) with estimates for $z \approx 3$ LBGs in the literature show that the correlation length of $L \gtrsim L_*$ LBGs is almost constant ($\sim 5 h_{100}^{-1} \text{Mpc}$) in the redshift range $z \approx 3 - 5$. On the other hand the bias monotonically increases with redshift.

1.4 Outline of the thesis

This thesis is organized as follows. In Chap. 2 we present basic properties of the FORS Deep Field as the field selection, the photometric observations and the data reduction. We also describe the source catalog and discuss its properties.

In Chap. 3 accurate distances are derived for the galaxies based on the photometric redshift technique. We investigate possible selection effects, discuss the accuracy of the photometric redshifts and present the redshift distribution of the galaxies. Further we derive the evolution of the luminosity function (LF) in the restframe UV (1500 Å & 2800 Å), u' , B, and g' bands in the redshift range $0.5 < z < 5.0$. We also compare our results with observational results from the literature as well as with model predictions.

In Chap. 4 we extend all measurements and comparisons of Chap. 3 to the red r' , i' , and z' bands.

In order to determine the contribution of a typical SED type to the total LF we subdivide our galaxy sample into 4 different SED types and analyze the type-dependent LF evolution at all wavebands (UV $\rightarrow z'$) in Chap. 5.

The redshift evolution (out to $z \sim 5$) of the star formation rate derived from the total luminosity densities in the UV is presented in Chap. 6. In order to address the influence of selection effects we show and discuss the SFR derived from the FDF B, I, (I+B) and GOODS K selected catalogs.

In Chap. 7 we compare the redshift evolution of the stellar mass density as derived in the literature with the mass density computed from the star formation rate history presented in Chap. 6. This allows us to tightly constrain the mean amount of UV flux absorbed by dust and re-emitted in the far-infrared.

We summarize the thesis in Chap. 8 and compare the measured evolution of the luminosity and stellar mass density with predictions of the monolithic collapse and hierarchical clustering scenarios.

Chapter 2

The FORS Deep Field¹

Abstract. The FORS Deep Field project is a multi-color, multi-object spectroscopic investigation of a $\sim 7' \times 7'$ region near the south galactic pole based mostly on observations carried out with the FORS instruments attached to the VLT telescopes. It includes the QSO Q 0103-260 ($z = 3.36$). The goal of this study is to improve our understanding of the formation and evolution of galaxies in the young Universe. In this paper the field selection, the photometric observations, and the data reduction are described. The source detection and photometry of objects in the FORS Deep Field is discussed in detail. A combined B and I selected UBgRIJKs photometric catalog of 8753 objects in the FDF is presented and its properties are briefly discussed. The formal 50% completeness limits for point sources, derived from the co-added images, are 25.64, 27.69, 26.86, 26.68, 26.37, 23.60 and 21.57 in U, B, g, R, I, J and Ks (Vega-system), respectively. A comparison of the number counts in the FORS Deep Field to those derived in other deep field surveys shows very good agreement.

¹This chapter is a slightly modified and updated version of the article Heidt *et al.* (2003), co-authored by Armin Gabasch. Modified sections are highlighted by footnotes.

2.1 Introduction

Deep field studies have become one of the most powerful tools to explore galaxy evolution over a wide redshift range. One of the main aims of this kind of study is to constrain current evolutionary scenarios for galaxies, such as the hierarchical structure formation typical of Cold Dark Matter universes.

Undoubtedly, the Hubble Deep Field North (HDF-N, Williams *et al.* 1996) and follow-up observations with Keck were of particular importance to improve our knowledge of galaxy evolution in the redshift range $z = 1 - 4$ (see e.g. the contributions to the HDF symposium, 1998, ed. Livio *et al.*). The HDF-N is the deepest multi-color view of the sky made so far, with excellent resolution. A disadvantage of the HDF-N (and its southern counterpart, the Hubble Deep Field South (HDF-S, Williams *et al.* 2000) is a relatively small field of view (~ 5.6 arcmin²). Therefore, its statistical results may be affected by large-scale structure (Kajisawa & Yamada, 2001; Cohen, 1998) and by limitations due to small samples.

Following the pioneering work of Tyson (1988) several ground-based deep fields with a wide range of scientific goals, sizes, limiting magnitudes and resolutions have been initiated. Examples are the NTT SUSI Deep Field (NTTDF, Arnouts *et al.* 1999b), which has a size similar to the HDFs and sub-arcsecond resolution, but is a few magnitudes less deep than the HDFs, or the William Herschel Deep Field (WHTDF, Metcalfe *et al.* 2001 and references therein), which has a much larger field of view, a depth comparable to the HDFs, but lacks sub-arcsecond resolution. Other surveys, such as the Calar Alto Deep Imaging Survey (CADIS, Meisenheimer *et al.* 1998), are much shallower, but cover much larger areas (several 100 arcmin² in the case of CADIS) and are specifically designed to search for primeval galaxies in the redshift range $z = 4.6 - 6.7$.

The aim of the FORS Deep Field (FDF) is to merge some of the strengths of the deep field

studies mentioned above. The FDF program has been carried out with the ESO VLT and the FORS instruments (Appenzeller *et al.*, 1998) at a site that offers excellent seeing conditions and allows imaging to almost the depths of the HDFs. The larger field of view compared to the HDFs (about 4 times the combined HDFs) alleviates the problem of the large-scale structure and results in larger samples of interesting objects. Moreover, spectroscopic follow-up studies with FORS can make full use of the entire field. Using the FORS2 MXU-facility, up to ~ 60 spectra of galaxies (within 40 slitlets) in the FDF can be observed simultaneously.

In the present paper, the field selection of the FDF, the photometric observations and the data reduction are described. The first results have been described in Jäger *et al.* (1999). A source catalog (available electronically) based on objects detected in the B and I bands and containing 8753 objects in the FDF is described and its properties are discussed. This catalog supersedes a preliminary I-band selected catalog, which had been discussed by Heidt *et al.* (2001). Photometric redshifts obtained from the FDF will be discussed by Gabasch *et al.* (in prep.; see Bender *et al.* 2001 for preliminary results as well as Sect. 3.4). Spectroscopic follow-up observations of a subsample of the FDF galaxies have been started. Up to now, spectra of about 500 galaxies with redshifts up to $z \sim 5$ have been analyzed. Initial results have been described in Mehlert *et al.* (2001), Mehlert *et al.* (2002), Noll *et al.* (2001)² and Ziegler *et al.* (2002).

2.2 Field selection

A critical aspect for a deep field study is the selection of a suitable sky area. Since we intended to obtain a representative deep cosmological probe of the Universe, one condition was that the galaxy number counts were not influenced by galaxy clusters in the field. Moreover, the depth

²see also Noll *et al.* (2004)

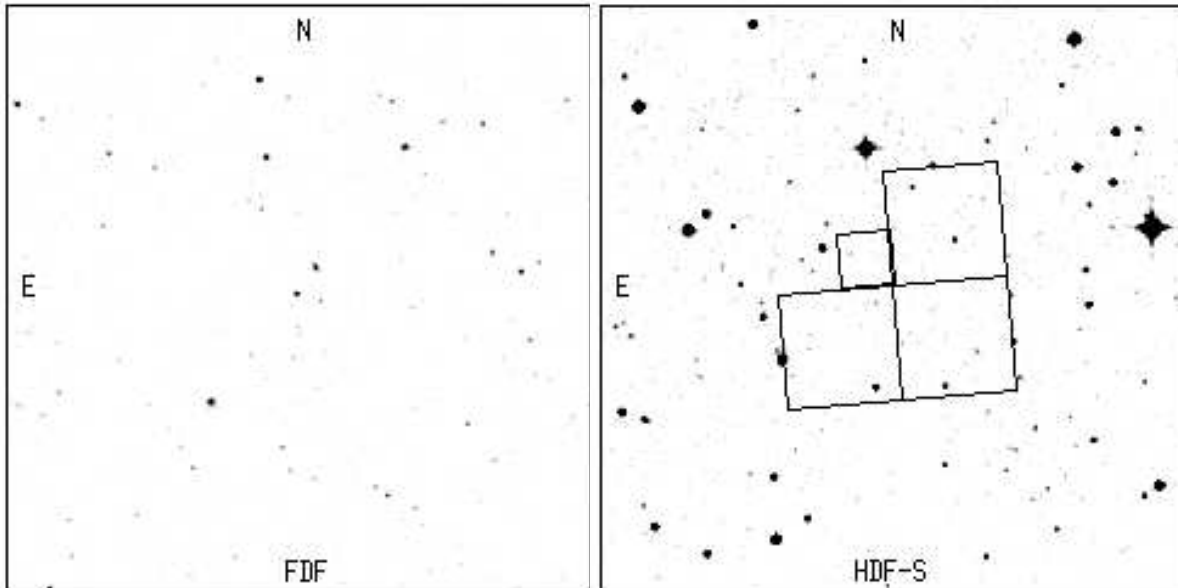


Figure 2.1: DSS plots of the FDF and of a field of the same size surrounding the HDF-S. Also indicated are the field boundaries of the HDF-S. Note the much lower surface density of bright foreground objects and the absence of bright stars in the FDF region.

of the images we wanted to achieve implies low galactic extinction ($E(B-V) < 0.02$ mag). For the same reason, the field had to be devoid of strong radio or x-ray sources (potentially indicating the presence of galaxy clusters at medium redshifts). On the other hand, we decided to include a radio-quiet QSO at high-redshift ($z > 3$) in order to study the IGM along the line-of-sight to the QSO as well as the QSO environment. To facilitate the observations in other wavebands, low HI column density ($< 2 \times 10^{20} \text{cm}^{-2}$) and low FIR cirrus emission was required. Moreover, stars brighter than 18th mag had to be absent to allow reasonably long exposures, to avoid saturation of the CCD and to minimize readout time losses. Because of the latter conditions, the HDF-S region was not suitable for our study. Additionally, stars brighter than 5th mag within 5° of the field had to be absent to avoid possible reflexes and stray-light from the telescope structure. Finally, the field had to have a good observability and, therefore, had to pass close to the zenith at the VLT site.

Due to these constraints, the south galactic

pole region was explored to find a suitable field. We started by selecting all the QSOs from the catalog of Veron-Cetty & Veron (1996) with $z > 3$ within 10° of the south galactic pole. This resulted in 32 possible field candidates. Next we did an extensive search in the literature from radio up to the x-ray regime (FIRST, IRAS maps, RASS etc.), checked visually the digitized sky survey and used the photometry provided by the COSMOS scans to select 4 promising field candidates containing a $z > 3$ QSO. For these 4 field candidates short test observations were carried out during the commissioning phase of FORS1, which showed that 3 of them were not useful (they either contained conspicuous galaxy clusters or, in one case, did not provide suitable guide stars for the active optics of the VLT). Finally, a field with the center coordinates $\alpha_{2000} = 1^{\text{h}}6^{\text{m}}3^{\text{s}}.6$, $\delta_{2000} = -25^\circ 45' 46''$ containing the QSO Q 0103-260 ($z = 3.36$, Warren *et al.* 1991) was chosen as the FDF. The characteristics of this field are summarized in Table 2.1.

Table 2.1: Characteristics of the FORS Deep Field

Field center	$1^{\text{h}}6^{\text{m}}3^{\text{s}}.6 - 25^{\circ}45'46''$ (2000)
mean $E(B - V)$	0.018
H I column density	$1.92 \times 10^{20} \text{cm}^{-2}$
Radio sources (NVSS)	none with flux > 2.5 mJy
IRASCirrus($100\mu\text{m}$)	0.035 Jy
Bright stars (< 5 mag)	none within 5°

Table 2.2: Observing log of the FDF observations

Tel./Inst.	Dates	Filters	Comments
FORS1/UT1	Aug. 13-17 1999	g, R	mostly non-phot.
FORS1/UT1	Oct. 6-13 1999	U, B, g, R, I	during 3 nights
FORS1/UT1	Nov. 3-6 1999	U, B, R, I	3×0.5 nights
FORS1/UT1	Dec. 2-6 1999	U, B, R, I	4×0.3 nights
FORS1/UT1	July/Aug. 2000	B, I	3.5 hours each
SofI/NTT	Oct. 25-28 1999	J, Ks	

2.3 Observations

Photometric observations using Bessel UBRI and Gunn g broad band filters were carried out with FORS1 at the ESO-VLT UT1 during 5 observing runs in visitor mode between August and December 1999. The data were complemented with some additional service-mode observations in the Bessel B and I filters with the same telescope in July and August 2000. Observing conditions were mostly photometric except for the August 1999 run, which was hampered by the presence of clouds and strong winds during some of the nights. In all cases a 2×2 k TEK CCD in standard resolution mode ($0''.2/\text{pixel}$, FOV $6'.8 \times 6'.8$), low gain and 4-port readout was used. The Gunn

g-filter was chosen instead of Bessel V in order to avoid the 5577 \AA night sky emission line, thus reducing the background significantly.

From the field-selection images taken with FORS1 it was known that twilight flatfields alone are not sufficient for a data reduction reaching very faint magnitudes. Therefore the images were taken in a jittered mode. A 4×4 grid with a spacing of $8''$ was adopted in order to maximize the use of the scientific images for flatfielding purposes on the one hand, and to minimize the loss of field-of-view on the other hand. The order of the individual observing positions was such that images with the largest separation were always taken first.

Exposure times for the individual frames were

set to 1200 sec in U, 515 sec in B and g, 240 sec in R and 300 sec in I. The seeing limit was initially set to $0''.5$ for B and I and $0''.8$ for the remaining filters. Unfortunately, it became clear after the first observing run that those seeing limits were too strict (mainly due to the La Niña phenomenon at that period) and could not be met within a reasonable amount of telescope time. Therefore the seeing limits were relaxed to $1''$ for U and g and $0''.8$ for the B-filter.

Due to the different seeing goals for each filter and varying seeing conditions during some of the nights, images in 3-5 filters were typically taken during each observing run. This resulted in somewhat longer exposure times on the summed images than initially anticipated (see section 2.6). Photometric standards from Landolt (1992) were taken at least once during each photometric night.

NIR observations of the FDF in the J and Ks bands were acquired using SofI at the ESO NTT during 3 photometric nights in October 1999. Since the field-of-view of SofI with the large field objective is $4'.94 \times 4'.94$ ($0''.292/\text{pixel}$) only and, thus, significantly smaller than the field-of-view offered by FORS1, the observations were split into 4 subsets to cover the entire FDF.

In order to have as similar observing conditions as possible for all subsets, the observations in both NIR filters were distributed evenly over the three nights. Always at least all four subsets were observed subsequently in one filter for 20 min. Each set of 20 min consisted of 20 exposures of 10×6 sec. The positions of the four subsets were chosen so as to cover the entire FDF as observed by FORS with a maximal overlap of the subsets, but to avoid the southernmost 100 pixels of the SofI camera, which show image degradation (see SofI manual). To allow a good sky subtraction, jittered images were taken. We used a random walk jitter pattern within a rectangular box of $22''$ border length centered on the central position of each subset. Photometric standard stars from Persson *et al.* (1998) were observed 3 times during each night to set the zero point.

In the end, the entire FDF was imaged effec-

tively for 100 min in the two NIR filters. Due to the overlap of the individual subsets a narrow region was observed effectively for 200 min and the central region (including the QSO) effectively for 400 min. An overview of the optical and NIR observing runs and the filters used is given in Table 2.2.

2.4 Optical data reduction³

Since in the FDF we wanted to analyze galaxies to fainter limiting magnitudes than other ground-based studies, a dedicated data reduction procedures had to be developed. On the other hand, the first spectroscopic follow-up observations of FDF galaxies were to start a few months after the last photometric observations of the FDF. In order to get suitable candidate galaxies at intermediate and high redshift for the spectroscopic follow-up, a preliminary reduction (hereafter PR) of the photometric data taken in visitor mode was made and an I-band selected catalog with photometric redshifts was created. The content of this preliminary catalog has been described in Heidt *et al.* (2001), whereas a description of the photometric redshifts can be found in Bender *et al.* (2001). In a second step, all data (including the photometric data taken in service mode) were reduced as described below. The final photometric catalog described in the present paper is based on this data-set.

2.4.1 Basic reduction

Because of the time variations of the CCD characteristics and of the telescope mirror (dust accumulation) each individual run was reduced separately. However, in order to have a homogeneous data set, the data reduction strategy was identical for all 5 runs.

First, the images had to be corrected for the bias. Since the observations were done in 4-port readout mode, each port had to be processed individually. For that purpose a masterbias was

³Modified section

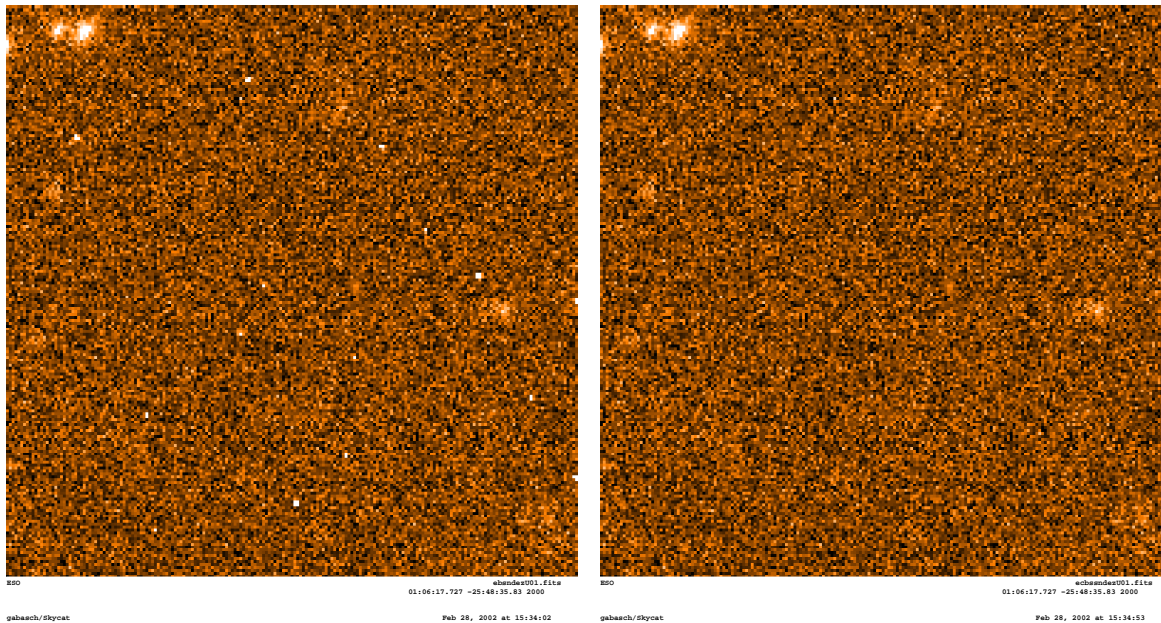


Figure 2.2: Left panel: Part of a single U-band image before cosmic ray rejection. Right panel: The same image as shown in the left panel after cosmic ray rejection.

produced for each port by combining (scaled median average) typically 20 bias frames taken during each run. The masterbias was subsequently subtracted from the images after scaling the bias level with the overscan.

In the next step the images were corrected for the pixel-to-pixel variations and large-scale sensitivity gradients. Since the twilight flatfields did not properly correct the large-scale gradients, a combination of the twilight flatfields and the science frames themselves was used. The twilight flatfields taken in the morning and evening generally differed considerably, and the twilight flatfields were not able to eliminate all large-scale gradients properly on the reduced science frames (probably as a result of stray-light effects in the telescope and the strong gradient of the sky background at the beginning and the end of the night). Therefore, for each science frame, a sequence of flatfields was determined, which minimized the large-scale gradient. These sequences were normalized, median filtered and used for a 1st order correction of the pixel-to-pixel variations. Typ-

ically 2-3 flatfields per filter per run had to be created this way, leaving residuals of the order of 2-8% (peak-to-peak) depending on the filter. To remove these residuals, the twilight-flatfielded science frames were grouped according to similar large-scale residuals, normalized and stacked, using a 1.8σ clipped median. Afterwards, a correction frame was created by a 2-dimensional 2nd order polynomial fit to each median frame. This was done on a rectangular grid of 50×50 pixels, where the level of each grid point was taken as the median of a box with a width of 40 pixels. In this way it was guaranteed that residuals from stars did not affect the fit and a noise free correction frame was achieved. Finally, each science frame was corrected for the pixel-to-pixel variations by a combination of the corresponding twilight flatfield and the noise free correction frame. The left-over peak-to-peak residuals on the final reduced science frames were typically 0.2% or less.

As no clipping or median algorithm is used for image stacking (see below), cosmic ray events have to be detected and rejected based on a sin-

gle image. Therefore cosmic ray events were detected by fitting a two-dimensional Gaussian to each local maximum in the frame. All signals with a FWHM smaller than 1.5 pixels and an amplitude larger than 8 times the background noise were classified as a cosmic ray event. Afterwards these pixels were removed and replaced by the mean value of the surrounding pixels. This provides a very reliable identification and cleaning of cosmic ray events (for details see Gössl & Riffeser, 2002). To illustrate the efficiency of the method, Fig. 2.2 shows a small part of a U-band frame before (left panel) and after (right panel) cosmic ray rejection. All cosmic rays of the left panel were detected and replaced by the surrounding pixels. The resulting frame can be seen in the right panel.

In order to ensure that non linear regions on the CCD are not taken into account during the stacking process, a bad pixel mask was created for every single image. The positions of bad pixels on the CCD were determined for each filter individually (as the non linear regions change slightly from band to band) using normalized flat-fields. All pixels whose flatfield correction would exceeded 20% were flagged and excluded in the stacking process. The necessity of this approach can be seen in Fig. 2.3. The figure shows part of an I-band difference image of the PR and the final reduction. The image of the PR was stacked without masking non linear regions on the CCD properly. In the final reduction those non linear regions have been masked out in every single frame by the procedure described above. The visible pattern stems from the PR and is due to a single bad region on the CCD. As images have to be aligned (shifted) before stacking, the bad region is visible 16 times in the stacked image. As we are interested in detecting very faint sources and deriving precise magnitudes in the FDF it is crucial to eliminate these systematics in the final stacked images. Each science frame was also inspected for other disturbed regions (satellite trails, border effects) and their positions included in the corresponding bad pixel mask.

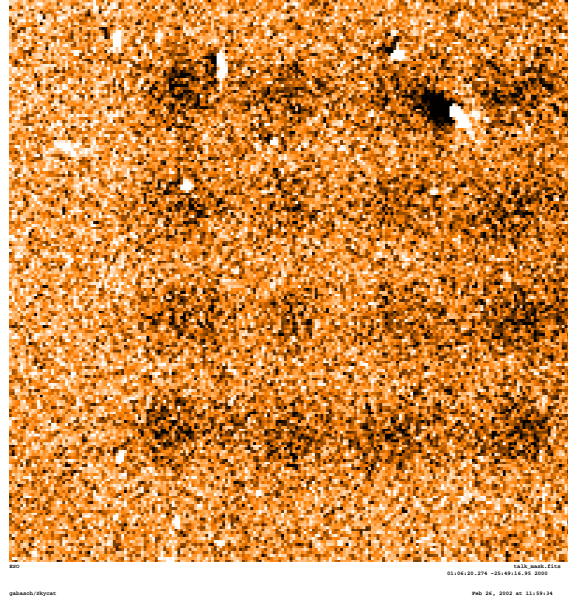


Figure 2.3: Part of an I-band difference image of the PR and the final reduction. The image of the PR was stacked without masking non linear regions on the CCD properly. In the final reduction those non linear regions has been masked out in every single frame by the procedure described in the text. The visible pattern stems from the PR and is due to a single bad region on the CCD. As images have to be aligned (shifted) before stacking, the bad region is visible 16 times in the final stacked image.

The alignment of the individual images and the correction for the field distortion was done simultaneously. This minimizes image smoothing and S/N reduction due to sub-pixel shifts and interpolations. As a reference frame, an I-filter image of the FDF taken under the best seeing conditions in October 1999 was used. Depending on the filter, the positions of 15-25 reference stars were measured via a PSF fit on each frame. A linear coordinate transformation was then calculated to project the images with respect to the reference image. The transformation included a rotation, a translation and a global scale variation. Finally, the correction for the field distortion was applied. Following the ESO FORS Manual, Version 2.4,

we derive the FORS1 distortion corrected coordinates (x', y') in pixel units as a function of the distorted coordinates (x, y) :

$$x' = x - f(r)(x - x_0), \quad (2.1)$$

$$y' = y - f(r)(y - y_0), \quad (2.2)$$

where (x_0, y_0) are the coordinates of the reference pixel, $r = \sqrt{(x - x_0)^2 + (y - y_0)^2}$ and

$$f(r) = 3.602 \cdot 10^{-4} - 1.228 \cdot 10^{-4} r + 2.091 \cdot 10^{-9} r^2. \quad (2.3)$$

The flux interpolation for non-integer coordinate shifts was calculated from a 16-parameter, 3rd-order polynomial interpolation using 16 pixel base points (for details see Riffeser *et al.*, 2001). The same shifting procedure was applied to the corresponding bad pixel masks, flagging as 'bad' every pixel affected by bad pixels in the interpolation.

2.4.2 Image stacking

As the single exposures were not all taken under the same observing conditions the sky levels, the seeings and the zeropoints differ slightly. On the other hand this gives us the possibility to stack the single images with weighting factors in order to achieve a final combined frame with optimal Signal to Noise (S/N).

Thus we calculated the weight α to be applied to an individual image following the general *Ansatz* for two images (denoted by index 1 and index 2):

$$\begin{aligned} S_{tot} &= S_1 + \alpha_2 S_2 \\ N_{tot} &= \sqrt{N_1^2 + (\alpha_2 N_2)^2} \end{aligned} \quad (2.4)$$

where S_{tot} and N_{tot} is the signal and the noise of the combined image. This transforms to:

$$\frac{S_{tot}}{N_{tot}} = \frac{f_1 + \alpha_2 f_2}{\sqrt{(f_1 + h_1 \sigma_1^2 \pi) + \alpha_2^2 (f_2 + h_2 \sigma_2^2 \pi)}} \quad (2.5)$$

where f_1 and f_2 are the fluxes of an object without sky (signal), h_1 and h_2 are the sky-values and σ_1 and σ_2 correspond to the seeing in the two frames. α_2 is the weighting factor to be applied to frame 2. It is than straight forward to compute the value of α_2 for which S_{tot}/N_{tot} is maximized:

$$\frac{\partial \frac{S_{tot}}{N_{tot}}}{\partial \alpha_2} \stackrel{!}{=} 0 \Rightarrow \alpha_2 = \frac{f_2 (f_1 + h_1 \sigma_1^2 \pi)}{f_1 (f_2 + h_2 \sigma_2^2 \pi)} \quad (2.6)$$

For bright objects which are not dominated by the sky noise ($f \gg h$) Eq. (2.6) transforms into

$$\alpha_2 = 1, \quad (2.7)$$

whereas for faint, sky-dominated objects ($f \ll h$) Eq. (2.6) transforms into

$$\alpha_2 = \frac{f_2 \cdot (h_1 \sigma_1^2)}{f_1 \cdot (h_2 \sigma_2^2)} \quad (2.8)$$

As the overwhelming majority of the objects in the FDF are very faint point sources and therefore dominated by the sky-noise, Eq. (2.8) is used to derive the weighting-parameter α .

To reduce errors when determine the weighting-parameter α , the fluxes $f_{1/2}$ are derived from a bright star, the sky levels $h_{1/2}$ correspond to the mode⁴ of the image and the seeings $\sigma_{1/2}$ have been calculated from the median seeing of more than 10 stars. The weighting factor (α_1) for the 1st frame (randomly chosen) was set to unity. The factors for all other ($N - 1$) images were then derived following Eq. (2.8) relative to this image. The final stacked frame I_{sum} can then be calculated according to:

$$I_{sum} = \sum_{i=1}^N \alpha_i B_i \tilde{I}_i \cdot \frac{\sum_{i=1}^N \alpha_i f_i}{\sum_{i=1}^N \alpha_i f_i B_i} \quad (2.9)$$

where the index i denotes a single image. α_i is the weighting factor according to Eq. (2.8); \tilde{I}_i is the sky-subtracted single image; B_i is the bad pixel mask⁵ and f_i is the flux derived from the bright star (used to derive α_i ; see also Eq. 2.5).

⁴most frequent value in the pixel histogram of the image

⁵zero for a bad pixel, unity otherwise

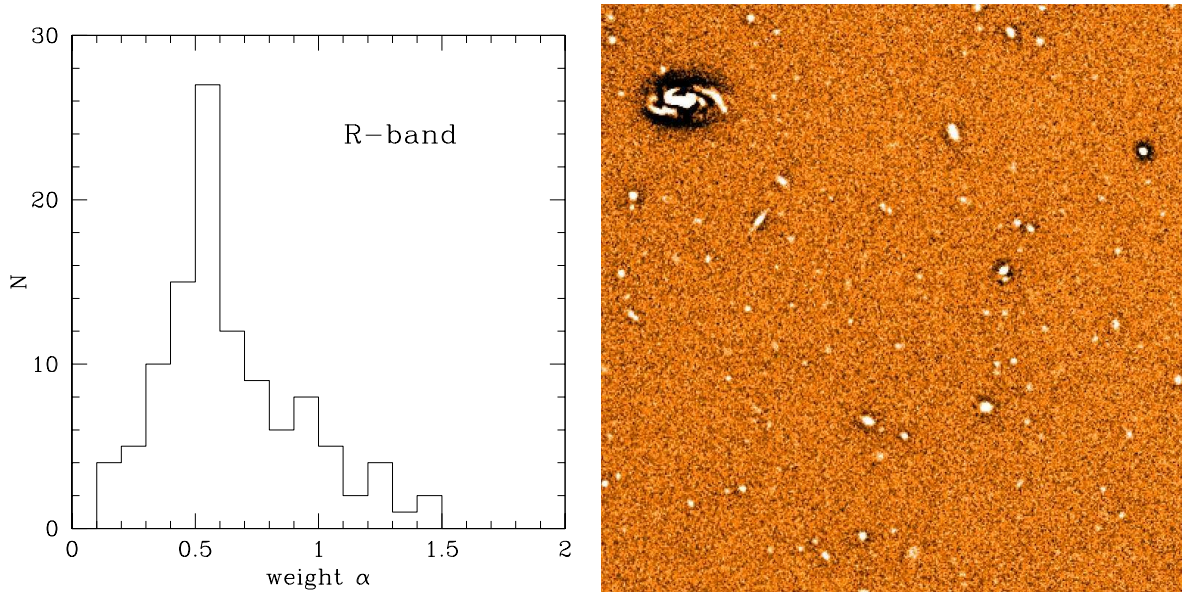


Figure 2.4: Left panel: histogram of the weighting factors α as derived for the R-band. Right panel: $80'' \times 80''$ difference image of the FDF R-band. The stacked image derived without weighting has been subtracted from the image derived according to Eq. (2.8) (see also text)

In Fig. 2.4 the efficiency of stacking the images with and without weighting factors is illustrated. Fig. 2.4 (left panel) shows a histogram of the weighting factors α as derived for the R-band. The right panel of the figure shows a difference image where the final image derived without weighting has been subtracted from the image derived according to Eq. (2.8). Both images were calibrated to the same zeropoint before subtraction. The faint visible sources were pushed above the background noise due to the weighting procedure and can therefore be better detected by a source detection program.

After stacking the images, the weighted sum was normalized to an exposure time of 1 sec. Since a different number of dithered frames contributed to each pixel in the co-added images (producing a position-dependent noise pattern) a combined weight map for each frame was constructed. The latter was used during source detection (see section 2.7) and photometry procedure to properly account for the position-dependent noise level.

2.4.3 Calibration

The photometric calibration of our co-added frames was done via ‘reference’ standard stars in the FDF. We first determined the zero points for two photometric nights (Oct. 10/11 and 11/12, 1999) during which the FDF was imaged in all 5 optical filters. The color correction and extinction coefficients on the ESO Web-page were used to derive the zero points for our FORS filter set in the Vega system. As no calibration images were available in the g -band, transformation from V to g was performed following Jorgensen (1994). We then convolved all the FDF images from the two photometric nights to the same seeing as the co-added frames and determined the magnitudes of 2 (U) - 10 (I) stars. Based on a curve of growth for these stars, a fixed aperture with a diameter of $8''$ was used. Using these reference stars, we finally determined the zero points of the co-added frames. The difference of the magnitudes between the reference stars on the individual frames on the two photometric nights and on the co-added frames is 0.01mag or less. We verified our

zero points by repeating the procedure described above using observations from two photometric nights during our November 1999 run.

2.5 NIR data reduction

About $\sim 10 - 20\%$ of the observed NIR frames were found to contain an electronic pattern caused by the fast motion of the telescope near the zenith. These frames were excluded from the analysis. The remaining data were reduced using standard image processing algorithms implemented within IRAF⁶. After dark-subtraction, for each frame a sky frame was constructed typically from the 10 subsequent frames which were scaled to have the same median counts. These frames were then median-combined using clipping (to suppress fainter sources and otherwise deviant pixels) to produce a sky frame. The sky frame was scaled to the median counts of each image before subtraction to account for variations of sky brightness on short time-scales. The sky-subtracted images were cleaned of bad-pixel defects and flat-fielded using dome flats to remove detector pixel-to-pixel variations. The frames were then registered to high accuracy, using the brightest ~ 10 objects following the same procedure as described in section 2.4, and finally co-added, after being scaled to airmass zero and an exposure time of 1 second.

The additionally observed photometric standard stars were used to measure the photometric zero point. The typical formal uncertainties in the zero-points were 0.02 mag in J and 0.01 mag in Ks.

2.6 Basic properties of the co-added images

A summary of the properties of the individual co-added images is presented in Table 2.3. The total

⁶IRAF is distributed by the National Optical Astronomy Observatories, which are operated by the Association of Universities for Research in Astronomy, Inc., under cooperative agreement with the National Science Foundation.

integration time for the co-added images is given as well as the number of frames used, the average FWHM measured on 10 stars across the field, the area with 80% weight for each individual image and the 50% completeness limits for a point source as described in section 2.7.

The integration times are in total almost a factor of 2 higher than originally planned (except for the U-filter). This is due to our strict seeing limits during the first observing runs. It compensates, at least in part, the loss of resolution/depth of the images due to the less than optimal seeing. Still, the completeness limits are somewhat lower than expected for the integration times since the efficiencies of the telescope (reflectivity of the main mirror) and the CCD were below expected at the time of the observations. In general, the zero points remained relatively constant during the observations carried out in 1999, whereas they differed considerably between the observations taken in 1999 and 2000. This resulted in a loss of approx. 0.3 mag (see the ESO-Web page, Paranal zero points).

The area with 80% weight is very similar for all optical bands and 30% larger for the NIR bands. The latter is due to the 4 subsets taken during the NIR observations. The common area with 80% weight in *all* filters is 39.8 arcmin².

As an example, the co-added I-band image of the FDF is displayed in Fig. 2.5 and a color version can be seen on the thesis-cover. The common area of the input images for a $6' \times 6'$ region is shown here. It contains ~ 6100 galaxies. In general, the galaxies are distributed evenly across the field. There is a poor galaxy cluster (at $z \sim 0.3$) in the southwestern corner of the FDF. The QSO Q 0103-260 is south of the center of the frame and is marked with an arrow. The brightest object in the field is an elliptical galaxy with $m_1 = 16.5$ at $z \sim 0.2$ in the southeastern part of the FDF.

Table 2.3: Overview of the photometric observations.

Band	Exposure Time [s]	Frames	FWHM ["]	80% weight [$'^2$]	50% compl. limit [mag]
U	44400	37	0.97	40.7	25.64
B	22660	44	0.60	40.5	27.69
g	22145	43	0.87	41.1	26.86
R	26400	110	0.75	40.8	26.68
I	24900	83	0.53	40.9	26.37
J	4800*	80*	1.20	4.2/53.8	23.60/22.85
Ks	4800*	80*	1.24	4.4/53.7	21.57/20.73

*Minimum exposure time and number of frames for each subset. Due to the overlap of the subsets for some (small) regions of the FDF the total time was twice or even four times this value. The 80% weight and 50% completeness levels in J and Ks are given for the 320 (central field) and 80-minutes co-added data, respectively.

2.7 Source detection and photometry

We used SExtractor (Bertin & Arnouts, 1996) with the WEIGHT-IMAGE-option and WEIGHT-TYPE = MAP-WEIGHT for the source detection and extraction on the images. The weight-maps described above were used to account for the spatial dependent noise pattern in the co-added images, and in particular to pass the local noise level of the data to the SExtractor program.

To use SExtractor, three parameters have to be set: i) The detection threshold t , which is the minimum signal-to-noise ratio of a pixel to be regarded as a detection, ii) the number n of contiguous pixels exceeding this threshold, iii) the filtering of the data prior to detection (e.g. with a top-hat or a Gaussian filter). We used a Gaussian filter with a width θ_F , for the θ_F values see below.

We varied these parameters to maximize the number of source detections, while minimizing

false detections. The following procedure, described here for the I-band data, was used for all filters. We first considered only those pixels in the field where the exposure time equaled the total exposure time (the weight-map took care of the correct scaling of RMS for the full field later on) and called this part of data the ‘central field’.

If there were no objects in the field and if the data reduction resulted in a perfectly flat sky we would expect the histogram of the pixel-values to be a Gaussian, with a width reflecting the photon-noise and the correlated noise of the data reduction and coaddition procedure. The actual histogram of pixel-values of the central-field is shown in Fig. 2.6 (upper panel, thin line). Even ignoring the wings, the histogram is asymmetric around its center at zero. This stems from the non-uniformities of the sky background, that amount to about 1% (see Sect. 2.4). Therefore, we determined the sky-curvature on large scales and subtracted a 2-dimensional fit to this surface from the

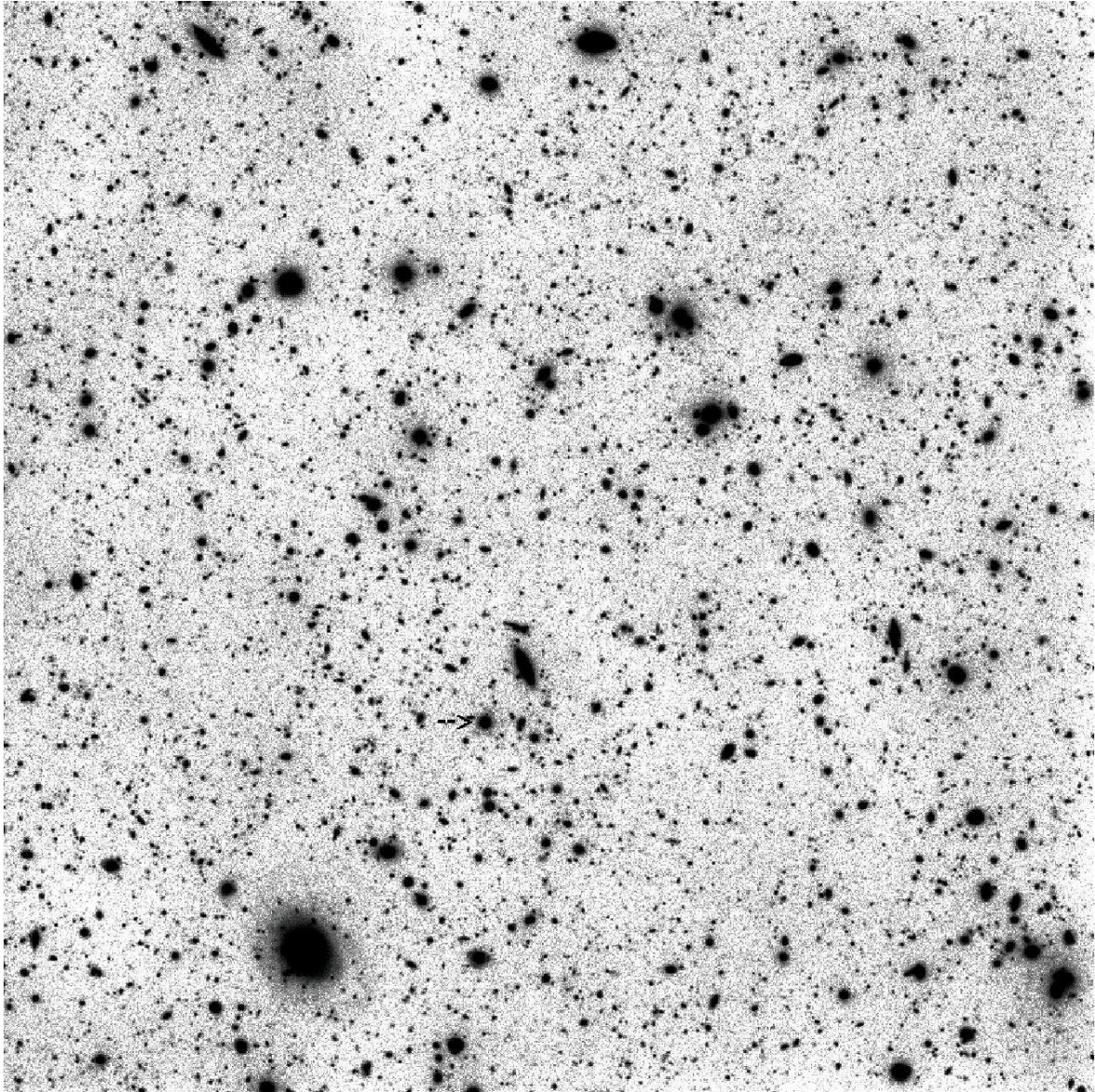


Figure 2.5: The FDF in I-band from FORS observations. The common area of all input frames for a field of view of $6' \times 6'$ is shown here. North is up, east to the left. The total integration time was 6.9 h, mean FWHM $\sim 0''.53$. The QSO Q 0103-260 is south of the center of the frame and marked with an arrow. This area contains ~ 6100 galaxies. Note the even distribution of galaxies across the frame, except for the small galaxy concentration in the southwestern corner. The brightest object in the field is the large elliptical galaxy in the southeastern part of the FDF at $z \sim 0.2$ with $m_1 = 16.5$.

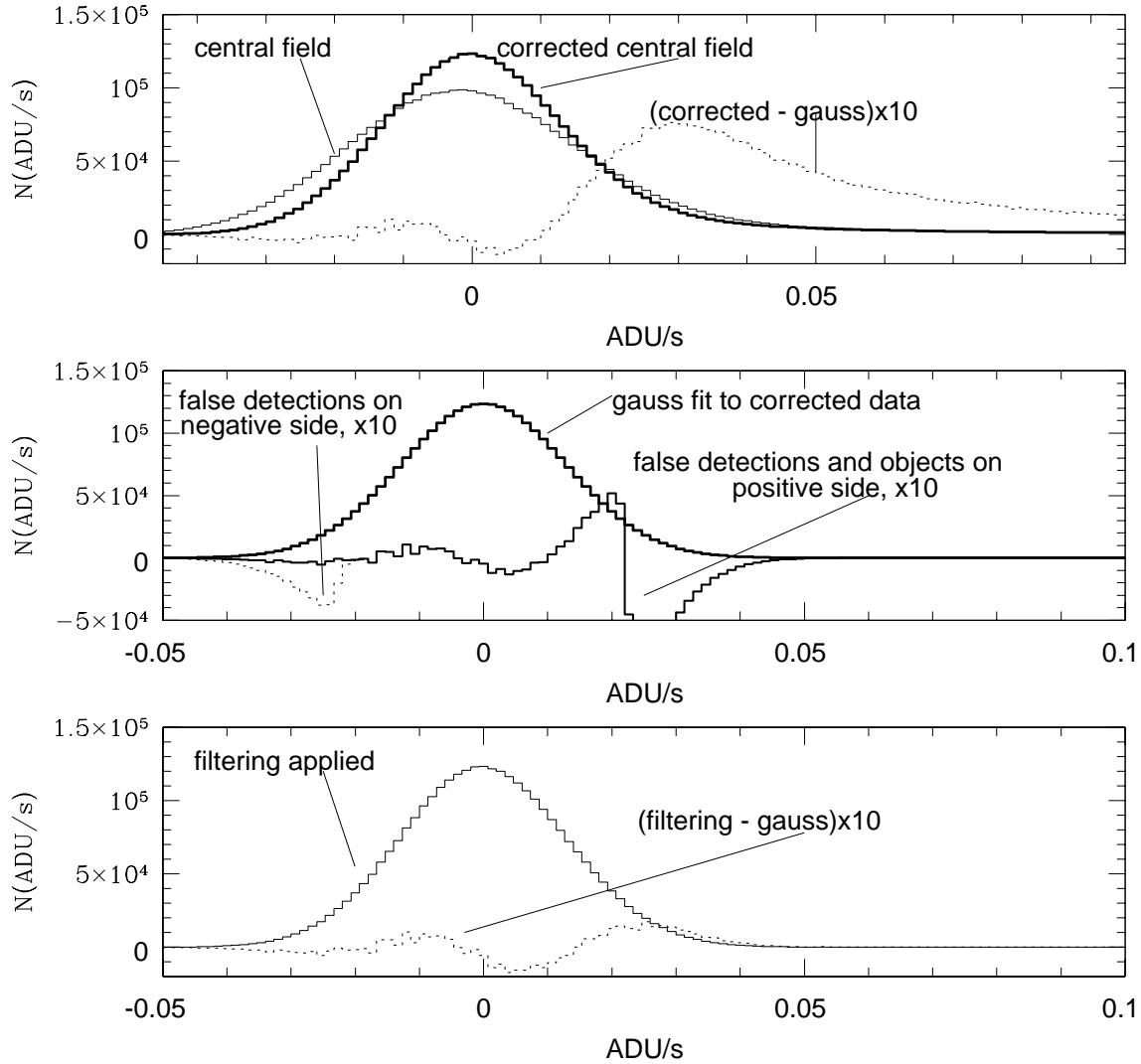


Figure 2.6: Pixel-value histograms (in ADU per second) for the (central field) I image at various analysis stages. *Upper panel:* Histogram of the original data (thin line) and after subtracting the low frequency spatial variations due to the non-uniform sky background (thick line). Also included is the difference of the corrected histogram and a Gaussian (shown as thick line in the *middle panel*) fitted to its negative ($\text{ADU/s} < 0$) wing. This negative wing should not be affected by real objects and therefore should represent the true noise in the image. For clarity the difference has been scaled up by a factor of 10 and the curve has been labeled accordingly. The real objects show up as a positive excess of the pixel values in the corrected data distribution and in the difference function at positive ADU/s . *Middle panel:* The thick line shows the Gaussian derived by fitting the negative wing of the corrected data distribution as described above. Its difference to the pixel-value distribution derived for those pixels where SExtractor (with optimal parameters but without filtering) finds no objects (or object contributions) is shown as a solid line. The corresponding difference distribution of the inverted image is shown dotted for the negative ADU/s only. The negative excess shows the false detections due to the correlated error. The difference curves are again scaled up by a factor of 10. *Lower panel:* The thin line shows the histogram of the pixel values of pixels not belonging to objects when SExtractor is run after filtering the corrected data with a (2 pixel FWHM) Gaussian. The dotted line shows the difference between this histogram and the Gaussian fit shown in the middle panel. The number of significant false detections has now dropped to nearly zero.

original data. The corrected histogram of pixel-values (Fig. 2.6, upper panel, thick curve) is now symmetric around its center at zero and the left-hand part is well described by a Gaussian (with a width of 0.01295 ADU/s). The right hand part shows an excess above ≈ 0.015 ADU/s, which is due to the objects in the field (see difference curve in Fig. 2.6, scaled up by a factor 10). We have checked that it does not make any difference for the detection and the photometry of reliable objects whether the procedure is applied to the original or to the corrected data: for each object, the difference between the magnitude estimates of these two cases is smaller than the assigned magnitude RMS-error. This implies that we can carry out the adjustment of optimum SExtractor parameters in the corrected version of the data.

To optimize the pre-detection filtering procedure we made the following numerical experiment. We generated a "negative version" of an image by multiplying it by -1 and a "randomized version" by randomly assigning measured pixel values to new positions (the weights of the weight-map are re-localized the same way). With no filtering ($\theta_F = 0$) and using $t = 1.7$ and $n = 3$ SExtractor finds about 9000 objects in the original image, 5600 in the negative one and 1100 in the randomized one. The fact that many more objects are detected in the negative image than in the randomized one indicates that correlated noise is present in both the negative and the positive images. Therefore filtering must be used to specifically suppress the small-scale noise. It is possible that large-scale noise is still present, but there is no way to remove such a component. By varying the width θ_F of a Gaussian filter we found that $\theta_F = 2$ is an optimal choice. With $n = 3$ and $t = 1.7$ the number of objects detected on the negative image dropped to the expected random number, nearly zero. Of course, once θ_F is fixed, one is still left with the freedom of trading n for t by increasing the number of pixels above the threshold and decreasing the threshold value at the same time. We decided to keep n small, in order to obtain an unbiased detection of faint point sources.

This choice allows us to exploit the excellent seeing of the I-band data, where the FWHM is only 2.5 pixels.

Now we illustrate our procedure more quantitatively: we ran SExtractor (for each choice of θ_F , n and t) on the positive, the negative and the randomized images. We registered all pixels which were covered by objects, removed them from the pixel-value statistics and normalized the corresponding pixel-value histogram to the total number of pixels in the central field, and we call that the 'background-histogram'. We expect that for good source extraction parameters, the background histograms will look like a Gaussian, more precisely like that Gaussian derived by fitting the negative wing of the corrected data distribution, which we call the 'optimum-background-histogram' below. The difference (magnified by a factor of 10) to that optimum background histogram is shown in the middle panel of Fig. 2.6 for $n = 3$, $t = 1.7$, $\theta_F = 0$ for detection on the positive (solid) and negative (dotted, for negative ADU/s only) image. The negative excess of these histograms below zero are false detections due to correlated noise. Increasing θ_F these false detections drop dramatically when $\theta_F = 2$ pixels is reached. Then, $n = 3$ and $t = 1.7$ were fixed by requiring no false detections on the negative image, i.e. no detections due to correlated noise. We finally run SExtractor with this set of parameters on the positive image, obtain the background histogram and show the difference to the optimum background histogram in the lower panel of Fig. 2.6 (dotted histogram, magnified by a factor of 10). The difference is indeed very small.

Using the above parameters ($\theta_F = 2$ with a Gaussian convolution, $n = 3$ and $t = 1.7$), obtained from the optimum pre-detection filtering and the requirement of no-detection on the negative image, we find that the extended wing in the ADU-histogram due to the presence of objects disappears and that the histogram becomes symmetrical and Gaussian (see Fig. 2.6, bottom panel). This demonstrates that with this choice of parameters we are optimally extracting all objects

above the noise level, without getting significant false detections. The adopted parameters give a (total) photometric accuracy better than 5σ .

The optimum parameters were finally used to run SExtractor on the (positive and negative) images of the total FDF. We found about 6900 objects on the positive and less than a handful of objects on the negative side of the entire I image. All these spurious detections occurred near discontinuities of the S/N level outside the central field and were caused by the non perfectly flat sky, which makes some of the discontinuities more pronounced than they should be according to the photon-noise and the corresponding weight-map.

The same analysis described for the I-band image was carried out for the other filters. We emphasize here that our extraction procedure was optimized to maximize the number of real detections for a reliable photometry and hence reliable photometric redshifts rather than to study galaxy number counts at the faintest limits. For the optical bands, we used the same extraction parameters. For the NIR-data we opted for $\theta_F = 3$ pixels to match the pixel size of the original NIR-data, which is roughly 1.5 the pixel size of FORS, and $t = 2.0$ and $n = 5$ for the J-band, and $t = 1.9$ and $n = 5$ for the Ks-band, to take into account the poorer seeing and the different noise level. To illustrate the reliability of our detection procedure we display a detection file returned from SExtractor for a $1' \times 1'$ region of the northern part of the FDF in Fig. 2.7.

The photometric errors presented in the final catalog are those derived by the SExtractor routine. To make sure that the error calculation was not influenced by correlated noise in the sky background, the results of the SExtractor were verified with aperture photometry with different apertures in areas not covered by objects and by estimating the expected photometric errors from the background variations. In general we found good agreement with the SExtractor derived errors. In particular the SExtractor errors were found to be quite accurate for point sources and for small objects. Only in the case of large extended objects

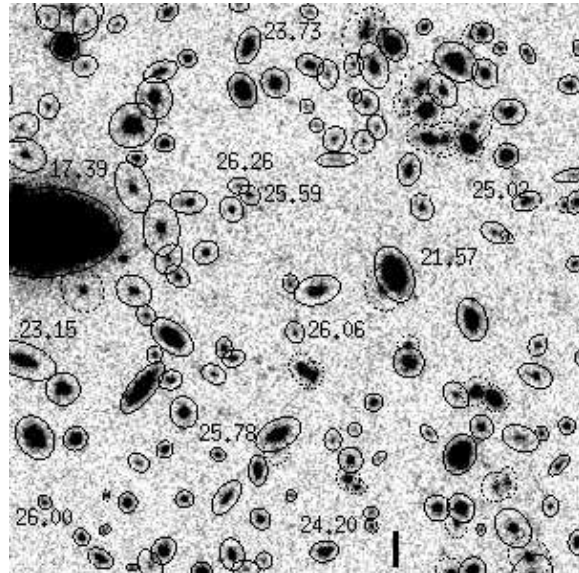


Figure 2.7: Detection file returned from SExtractor for a $1' \times 1'$ region of the northern part of the FDF. It illustrates the reliability of our detection and photometry procedure. The I-band image shown here contains ~ 160 objects. For some objects the integrated magnitudes are displayed. The detection file shows the elliptical aperture limits used to derive `mag_auto`. Dashed ellipses denote blended objects.

non-stochastic background variations may result in an underestimate of the photometric errors. But the few objects possibly affected are normally bright and have small errors, which should still be correct within the numbers given in the catalog.

Finally, we calculated the 50% completeness levels in each filter band using our extraction parameters and the formula given in (Snigula *et al.*, 2002). This approach estimates the completeness limit by calculating the brightness at which the area of pixels brighter than the applied flux limit falls below the size threshold of the detection algorithm (for a given FWHM of a point source). To allow a comparison with other deep fields, the data were corrected for galactic extinction as described in section 2.8. The results are summarized in Table 2.3.

2.8 Photometric catalog

2.8.1 Compilation of the photometric catalog

To create the final photometric catalog we merged the individual catalogs of the objects detected in the co-added B-filter image and in the co-added I-filter image. We decided to use these two catalogs as a basis, since the images in these two filters correspond to the best seeing conditions and since most types of objects are expected to be detected in at least one of these two bands.

The merging of the I and B catalogs was carried out as follows: We first matched the positions of the detected objects and their corresponding images in the two filters. This was done by visual inspection of the entries of the objects on both frames. This procedure gave us a clear view of the success of our automatic detection procedure and allowed us to reject obviously false identifications. In order to avoid mis-matches in the final catalog, each entry in the B catalog was first assigned a corresponding entry in the I catalog and vice versa. A cross-match of the B versus I and I versus B entries allowed us to identify false matches, which were checked again until a perfect cross-match was derived.

The initial catalogs in B and I contained 7206 and 6900 entries, respectively. After the visual cross-matching, we deleted 15 objects from the B catalog and 8 objects from the I catalog. These were mostly objects close to the edges of the field. In a few cases, 2 objects separated by a few pixels (e.g. a merging pair of galaxies) were detected in the B-band, whereas in the I-band only one object in between the two B-band objects was found (essentially at the center of the common envelope of both galaxies). In such cases the entry in the I-band was deleted. This left us with 7191 entries in the B catalog and 6892 entries in the I catalog. Now we merged both catalogs to form the final photometric catalog. This catalog contains 8753 objects. 5327 out of the 8753 objects were detected in both filters (61%), whereas 1864

(21%) were detected in B only and 1562 (18%) were detected in I only. We emphasize here that a non-detection does not necessarily mean that the object is not present on the frame, it rather means that the object was not detected by SExtractor with the parameters set here.

Since SExtractor may use a different number of pixels to derive the total magnitudes in B and I, the colors of very extended objects computed from the total magnitudes are not reliable. Therefore the catalog also contains aperture magnitudes in UBGRIJKs. An aperture of $2''$ was chosen in order to minimize the errors due to blending and since the faint objects usually have diameters of $\leq 2''$. The aperture magnitudes were derived by first convolving all frames to the same seeing ($1''$ FWHM) and then performing aperture photometry on the positions of the objects detected in B and I in the convolved frames. For objects detected in B only, we used the aperture photometry based on the positions in the B catalog, whereas the aperture photometry based on the positions in the I catalog were used for the remaining objects (detection on both frames or I-only detections). Thus for many objects, which were initially not detected in either filter, useful photometric data could be given.

Finally, the galactic absorption towards the FORS Deep Field was estimated. We used the formulae 2 and 3 in Cardelli *et al.* (1989) and adopted $E(B - V) = 0.018$ (Burstein & Heiles, 1982) and $A_V = 3.1 \times E(B - V)$ to calculate the extinction correction for each filter. The central wavelengths for each filter were taken from the ESO Web-page. We derived $A_U/A_V = 1.555$, $A_B/A_V = 1.365$, $A_g/A_V = 1.105$, $A_R/A_V = 0.790$, $A_I/A_V = 0.631$, $A_J/A_V = 0.283$ and $A_{K_S}/A_V = 0.117$ resulting in $A_U = 0.087$ mag, $A_B = 0.076$ mag, $A_g = 0.062$ mag, $A_R = 0.041$ mag, $A_I = 0.035$ mag, $A_J = 0.016$ mag and $A_{K_S} = 0.007$ mag, respectively. The values for the extinction agree to ≤ 0.01 mag with those listed in the NED. The photometric catalog described below is not corrected for galactic extinction. However, the completeness limits as well as the number counts

shown in section 2.9 were derived with a galactic extinction correction.

2.8.2 Contents of the photometric catalog

The full catalog containing 8753 objects is available in electronic form at CDS via anonymous ftp to cdsarc.u-strasbg.fr (130.79.128.5) or via [http://cdsweb.u-strasbg.fr/cgi-bin/qcat?J/A+A/\(vol\)/\(page\)](http://cdsweb.u-strasbg.fr/cgi-bin/qcat?J/A+A/(vol)/(page)).

As an illustration of its content we list in Table 2.4 the entries 2630 – 2639.

For each object we report the following parameters:

ID: The identification number. The objects have been sorted first by right ascension (2000), followed by declination (2000). The identification numbers provide a cross-reference to the spectroscopic and other observations of the FDF (e.g. Noll *et al.* 2004).

RA, Dec: The positions of the objects in the FDF for J2000.0. Their accuracy has been examined by comparing the positions of 31 well-isolated, evenly distributed objects on the I frame of the FDF, to those listed in the USNO catalog (Monet, 1998). The mean difference in right ascension is $0''.21 \pm 0''.38$ and the mean difference in declination is $0''.14 \pm 0''.40$. Given a typical accuracy of $0''.25$ for objects in the USNO catalog our positions have an accuracy of $\sim 0''.5$.

m_{BT} , σ_{BT} , m_{IT} , σ_{IT} : The total magnitudes (Vega-system) and associated mean errors of the detected sources in the B and I band images, respectively, as measured using the SExtractor routine `mag_auto` on the co-added and unconvolved frames. `Mag_auto` is an automatic aperture routine based on Kron's (Kron, 1980) 'first moment' algorithm, which determines the sum of counts in an elliptical aperture. The semimajor axis of this aperture is defined by 2.5 times the first moments of the flux distribution within an ellipse roughly twice the isophotal radius, within a minimum semimajor axis of 3.5 pixels. This routine is intended to give the most precise estimate of

'total magnitudes', at least for galaxies, and takes into account the blending of nearby objects.

$m_{UBgRIJKs[2'']}$, $\sigma_{UBgRIJKs}$: UBgRIJKs magnitudes (Vega-System) and associated errors within an aperture of $2''$. They (and their errors) were measured on the co-added and convolved frames using SExtractor. The positions listed in the catalog were used for this procedure. An aperture of $2''$ was chosen in order to minimize the errors due to blending. Moreover, the faint objects in the FDF usually have diameters of $\leq 2''$. Choosing a larger aperture would result in larger photometric errors due to the sky background. For extended objects, the mean errors of the aperture magnitudes are generally smaller than for the total magnitudes, as the aperture photometry selected the regions of high surface brightness. The magnitudes were not corrected for blending. Blended objects can be identified from the column `Flag1` (see below).

The next four columns (FWHM, elongation, position angle, star-galaxy classification parameter) describe the morphology of the objects. Since the FWHM, elongation and position angle may have high errors and are sometimes unreliable for faint objects, this information is provided for objects brighter than our 50% completeness limit (27.69 in B, 26.37 in I) only. Moreover, we do not list these values for objects where SExtractor derived a $FWHM < 0.4$ (FWHM is $0''.53$ in co-added I-band frame and $0''.6$ in co-added B-band frame). The information should also be treated with caution for brighter objects having a star-galaxy classification parameter > 0.9 .

FWHM: Full width at half maximum of the objects in arcsec as determined by SExtractor by a Gaussian fit to the core.

Elong: Elongation of the images. The elongation is defined as A/B , where A and B are given by the 2nd order moment of the light distribution along the major and minor axis, respectively.

PA: The position angle of the major axis, measured from North to East, with $N-S = 0$.

Cstar: Star-galaxy classification parameter returned by SExtractor based on the morphology of

Table 2.4: Excerpt from the FDF object catalog. The entries with the IDs 2630 – 2639 are displayed as examples.

ID	RA (2000)	Dec (2000)	m_{BT}	σ_{BT}	m_{IT}	σ_{IT}	$m_U [2'']$	σ_U	$m_B [2'']$	σ_B	$m_g [2'']$	σ_g	$m_R [2'']$	σ_R	$m_I [2'']$	σ_I
2630	1 5 57.28	-25 48 02.3	27.75	0.19	25.30	0.10	26.99	0.27	27.61	0.05	27.72	0.10	26.10	0.03	25.34	0.02
2631	1 5 57.29	-25 45 00.1			24.42	0.03					30.73	1.65	26.57	0.04	24.49	0.01
2632	1 5 57.29	-25 48 46.9	26.13	0.05	24.98	0.07	25.96	0.10	26.20	0.01	25.92	0.02	25.42	0.02	25.05	0.02
2633	1 5 57.30	-25 44 56.6	24.47	0.01	22.75	0.01	24.60	0.03	24.60	0.01	23.74	0.01	23.26	0.01	22.87	0.01
2634	1 5 57.30	-25 48 14.2	27.69	0.16					27.77	0.06	28.23	0.17	26.84	0.06	26.78	0.09
2635	1 5 57.31	-25 43 52.3			25.02	0.09	26.22	0.13	26.42	0.02	26.11	0.02	25.66	0.02	25.33	0.02
2636	1 5 57.31	-25 44 02.2	24.85	0.04	23.43	0.04	25.53	0.07	25.53	0.01	25.12	0.01	24.56	0.01	24.12	0.01
2637	1 5 57.31	-25 44 15.2	26.60	0.09	26.19	0.17	26.76	0.22	26.83	0.02	26.72	0.04	26.46	0.04	26.16	0.05
2638	1 5 57.31	-25 46 23.5	27.36	0.16	25.65	0.09	27.58	0.46	27.43	0.04	27.45	0.08	26.72	0.05	25.67	0.03
2639	1 5 57.31	-25 47 51.1	26.17	0.08	25.11	0.10	26.42	0.16	26.85	0.02	26.74	0.04	26.22	0.03	25.60	0.03

ID	$m_J [2'']$	σ_J	$m_{Ks} [2'']$	σ_{Ks}	FWHM ["]	Elong	PA [°]	Cstar	Flag1	Flag2	Flag3	weight_B	weight_I
2630			21.97	0.20	0.74	1.17	17.9	0.40	0			1.000	1.000
2631	21.36	0.01	20.35	0.03	0.52	1.02	111.7	0.98	0	Ionly	L star	1.000	1.000
2632	26.58	2.38	22.37	0.29	0.78	1.12	82.1	0.26	0			1.000	1.000
2633	22.09	0.03	20.91	0.06	0.53	1.04	36.2	0.98	0		QSO	1.000	1.000
2634					1.01	1.25	00.6	0.61	0	Bonly		1.000	
2635	23.70	0.18			1.13	1.19	129.3	0.00	3	Ionly			0.984
2636	22.71	0.07	20.75	0.07	0.73	1.34	90.2	0.09	3			0.984	1.000
2637					1.07	1.87	76.9	0.40	0			1.000	1.000
2638					0.80	1.49	19.1	0.43	0			1.000	1.000
2639	24.02	0.23	22.96	0.50	1.34	1.16	21.6	0.01	2			1.000	1.000

the objects on the image. A classification near 1.0 describes point like sources whereas a classification close to 0.0 describes extended sources.

Flag1: Flags returned by SExtractor with the following notation:

1: Object has neighbors bright and close enough to bias significantly mag_auto; 2: The object was originally blended with another one; 3: Sum of 1 + 2; 4: At least one pixel of the object is saturated (or very close to saturation); 7: Sum of 1 + 2 + 4; 8: The object is truncated (e.g. too close to the image boundary); 16: Object aperture data are incomplete or corrupted; 17: Sum of 1 + 16; 18: Sum of 2 + 16; 19: Sum of 1 + 2 + 16; 24: Sum of 8 + 16.

Flag2: Here we report if an object was detected on the B frame only ('Bonly'), on the I frame only ('Ionly'). If there is no entry, the object is detected by SExtractor on both frames.

Flag3: A preliminary classification of 35 point-like objects (QSOs, stars) from our spectroscopic survey (Noll *et al.*, 2004).

weight_B, weight_I: Averaged weights of all pixels used to determine m_{BT} and m_{IT} , respectively. They were derived from the combined weight maps which are described in section 2.4. A weight of 1 means that all pixels used to derive the magnitude are fully exposed and not affected by bad areas. Most of the detections with low weights are close to the edges of the FDF where the total integration times are lower.

2.9 Galaxy number counts

The number counts can be used for a quick check of the approximate photometric calibration and for the depth of the data. We did not put much effort in star-galaxy separation at the faint end, where the galaxies dominate the counts anyway. At the bright end, where SExtractor is able to disentangle a stellar and a galaxy profile, we derived limits by investigating the class-FWHM diagram for the objects. In the following figures, the counts for all objects are shown as dashed his-

tograms, while for the solid line histograms obvious stellar objects have been omitted. The magnitudes are given in the Vega-system. The number counts are given only for the area with maximum integration-times (weight-map ≈ 1) for the optical data and for weight - map $\gtrsim 0.25$ for the NIR-data (i.e. we exclude the edges of the fields). They are not corrected for incompleteness. Also indicated is the 50% completeness limit for the detection of point sources. For each filter we also included for comparison number-magnitude-relations obtained in earlier observations which are compiled and transformed to standard filter systems in Metcalfe *et al.* (2001) for the optical filters. In all cases we plot raw number counts only, i.e. we do not correct for incompleteness at the faint end.

In the U-band the FDF is 50% complete to $U = 25.64$ mag for a point source. The slope agrees with earlier measurements (roughly 0.4 - 0.5) for $U < 23$ and it becomes shallower (0.35 at $U = 23 - 25$), in agreement with the slopes of the HDF-S, WHDF and Hogg *et al.* (1997) (see Metcalfe *et al.* 2001). In Fig. 2.8 (left panel) we have transformed the HDF number counts as proposed by Metcalfe *et al.* using $F_{300,Vega} = U - 0.4$ and Table 5 in their paper. We further assume $U_{WHDF} \approx U$ to include the WHDF U-band-raw counts (Table 4 of Metcalfe *et al.* (2001) -in fact the central wavelengths and the transmission curves of the U-filters used for the FDF and WHDF observations are similar. The values of Hogg *et al.* (1997) have been obtained from their Fig. 3 and been transformed as proposed by Metcalfe, $U \approx U_{Hogg} + 0.08$. The HDFN/S and WHDF number counts are not corrected for reddening (Metcalfe, private comm., $E(B - V)_{WHDF} \approx 0.02$ which is similar to the FDF and thus would shift the number counts by ≈ -0.1).

Our B-band number counts as shown in Fig. 2.8 (right panel) are 50%-complete at 27.69 mag. Within the field-to-field variations they agree well with the HDFN/S (we follow Metcalfe *et al.* (2001) and use the transformation

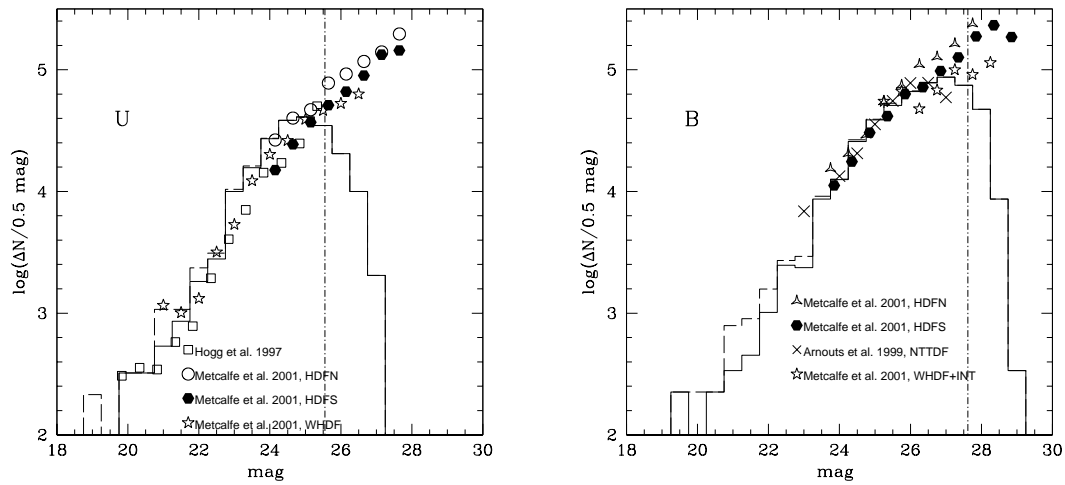


Figure 2.8: Left panel: Galaxy number counts of the FDF in the U-band (not corrected for incompleteness) as compared to other deep surveys. The vertical dash-dotted line indicates the 50% completeness limits. Right panel: Galaxy number counts of the FDF in B-band (not corrected for incompleteness) as compared to other deep surveys. The vertical dash-dotted line indicates the 50% completeness limits.

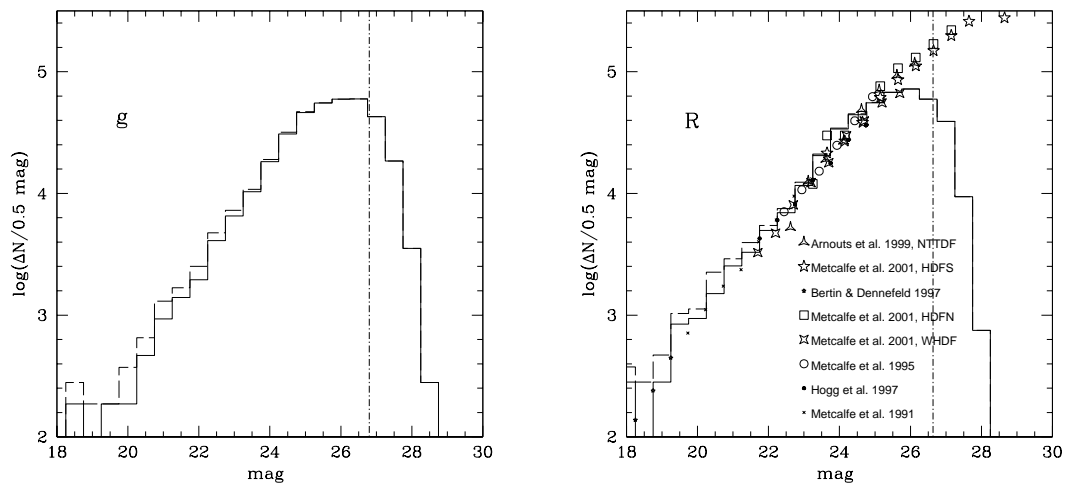


Figure 2.9: Left panel: Galaxy number counts of the FDF in g-band (not corrected for incompleteness). The vertical dash-dotted line indicates the 50% completeness limits. Right panel: Galaxy number counts of the FDF in R-band (not corrected for incompleteness) as compared to other deep surveys. The vertical dash-dotted line indicates the 50% completeness limits.

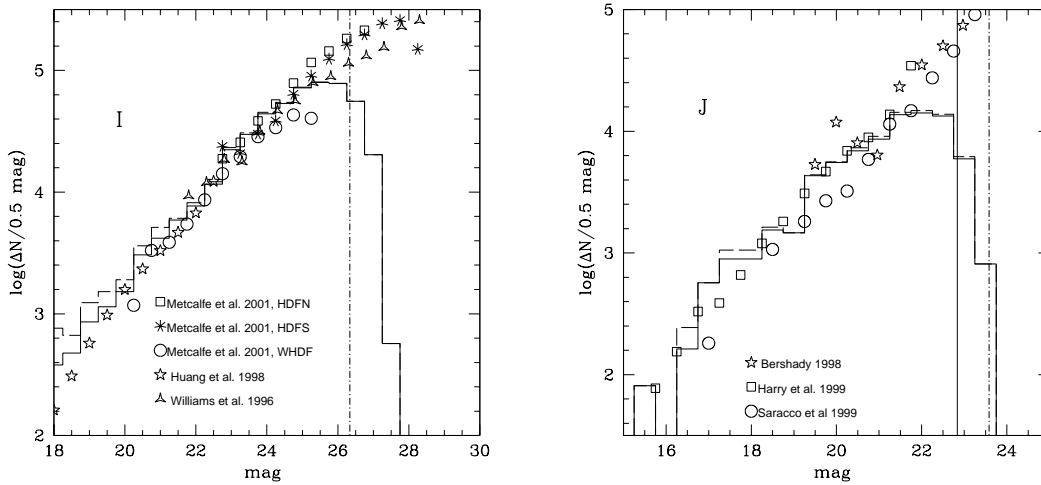


Figure 2.10: Left panel: Galaxy number counts of the FDF in I-band (not corrected for incompleteness) as compared to other deep surveys. The vertical dash-dotted line indicates the 50% completeness limits. Right panel: Galaxy number counts of the FDF in J-band (not corrected for incompleteness) as compared to other deep surveys. The vertical solid line indicates the 50% completeness for the shallower exposed part of the field, whereas the vertical dash-dotted line indicates the 50% completeness for the deeply exposed part of the field.

$F_{450,Vega} \approx B - 0.1$) and the raw-counts in the NTT deep field (Arnouts *et al.*, 1999b). We also included the raw counts in the Herschel deep field, assuming $B_{FDF} \approx B_{WHDF}$.

For the g-band, we just show our results in Fig. 2.9 (left panel) without comparison, since no adequate number counts have been presented in the literature for this passband. Our estimated 50% completeness limit is 26.86 mag in this filter.

Our R-band and I-band data are 50%-complete at 26.68 mag and 26.37 mag, respectively. Amplitude and slope agree well with previously published fields. For the transformation of the HDF-counts we followed Metcalfe *et al.* (2001) and used $R \approx R_{606,Vega} - 0.1$ and $I \approx I_{814,Vega}$; we also assumed that $R \approx R_{WHDF}$. The counts are shown in Fig. 2.9 (right panel) and 2.10 (left panel).

Our number counts in the J-band (Fig. 2.10, right panel) agree with those derived by Saracco *et al.* (1999), and precisely match those of Teplitz

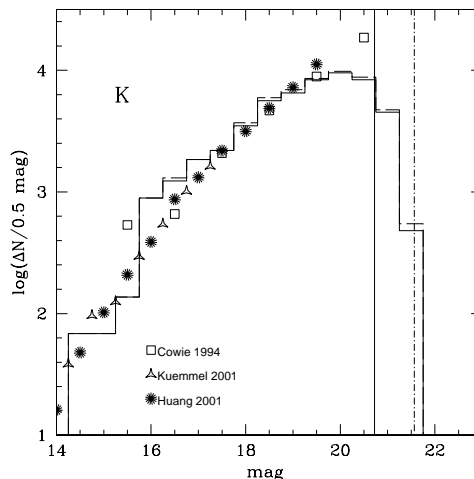


Figure 2.11: Galaxy number counts of the FDF in Ks-band (not corrected for incompleteness) as compared to other deep surveys. The vertical solid line indicates the 50% completeness for the shallower exposed part of the field, whereas the vertical dash-dotted line indicates the 50% completeness for the deeply exposed part of the field.

et al. (1999). The completeness is 22.85 mag and 23.60 mag for the shallower and deeply exposed (factor of four in integration time) part of the field, respectively. Our number counts in the K-band (Fig. 2.11) agree well with those of Kümmel & Wagner (2001) and Huang *et al.* (1998). The completeness limits are 20.73 mag and 21.57 mag for the shallow and deep exposed part of the field. For fairly shallow J and K pointings ($J \lesssim 22$ and $K \lesssim 20$) the field-to-field variations are expected to be significant for our field size, since the distribution of massive, old systems dominating the NIR frames varies considerably on small scales. This has been demonstrated e.g. in the different pointings of the MUNICS survey by Drory *et al.* (2001). The agreement with other surveys is good and the quoted detection limit correspond to the 50% completeness limit of our sample.

2.10 z- and 835nm-band⁷

The reduction of the images in the z-band and in the special filter centered at 834 nm follows the same recipe as the optical filters. Since the z-band showed considerable fringing we had to add a further step in our reduction pipeline in order to properly deal with the fringe pattern (see Fig. 2.12). The major causes for fringing are the night sky emission lines (mainly OH transition) in the upper atmosphere. If monochromatic lines are reflected within the CCD they interfere producing a fringe-pattern (variable over night). To correct for the latter a fringe image was created from the science exposures in two steps. In the first step we eliminated in every frame pixels belonging to an object using SExtractor. In the second step we use a $\kappa - \sigma$ clipping algorithm with $\kappa = 3$ to combine the source-depleted single images. The resulting fringe-image was then appropriately scaled and subtracted from the science frames.

For illustration we show in Fig. 2.12 a part of the fringe-pattern ($80'' \times 80''$) as extracted from the z-band images. There are no residual sources

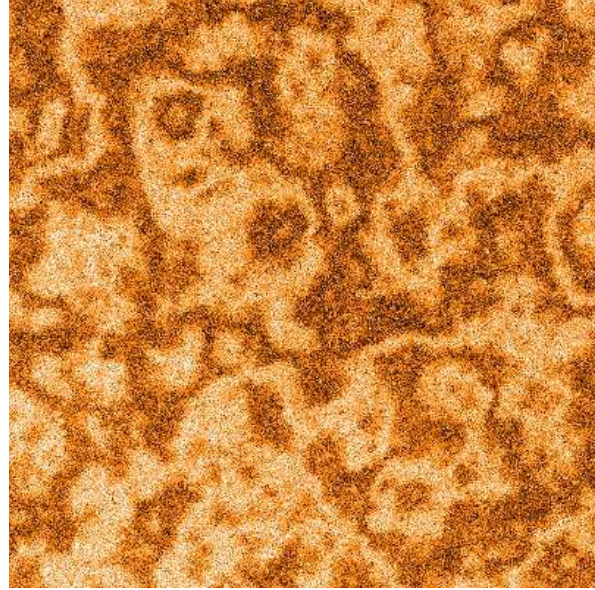


Figure 2.12: Fringe-pattern extracted from the z-band image ($80'' \times 80''$).

visible in the image beside the fringes and thus subtracting the image from the science images does not alter their photometry.

We summarize the properties of the co-added images in Table 2.5. The total integration time as well as the number of frames, the average FWHM (from 10 stars across the field), the area with 80% weight for each individual image and the 50% completeness limit are listed in the Table.

Table 2.5: Photometric properties of the z- and 834nm-band.

Band	z	834nm
Exposure	18000 s	10800 s
Frames	10	6
FWHM	0.48''	0.72''
80% weight	40.84 ¹²	40.17 ¹²
50% compl. limit	~ 25.3 mag	~ 25.0 mag

⁷Added section

Chapter 3

The evolution of the luminosity functions in the FORS Deep Field from low to high redshift: I. The blue bands¹

Abstract. We use the very deep and homogeneous I-band selected dataset of the FORS Deep Field (FDF) to trace the evolution of the luminosity function over the redshift range $0.5 < z < 5.0$. We show that the FDF I-band selection down to $I_{AB} = 26.8$ misses of the order of 10 % of the galaxies that would be detected in a K-band selected survey with magnitude limit $K_{AB} = 26.3$ (like FIRES). Photometric redshifts for 5558 galaxies are estimated based on the photometry in 9 filters (U, B, Gunn g, R, I, SDSS z, J, K and a special filter centered at 834 nm). A comparison with 362 spectroscopic redshifts shows that the achieved accuracy of the photometric redshifts is $\Delta z / (z_{spec} + 1) \leq 0.03$ with only $\sim 1\%$ outliers. This allows us to derive luminosity functions with a reliability similar to spectroscopic surveys. In addition, the luminosity functions can be traced to objects of lower luminosity which generally are not accessible to spectroscopy. We investigate the evolution of the luminosity functions evaluated in the restframe UV (1500 Å and 2800 Å), u', B, and g' bands. Comparison with results from the literature shows the reliability of the derived luminosity functions. Out to redshifts of $z \sim 2.5$ the data are consistent with a slope of the luminosity function approximately constant with redshift, at a value of -1.07 ± 0.04 in the UV (1500 Å, 2800 Å) as well as u', and -1.25 ± 0.03 in the blue (g', B). We do not see evidence for a very steep slope ($\alpha \leq -1.6$) in the UV at $\langle z \rangle \sim 3.0$ and $\langle z \rangle \sim 4.0$ favoured by other authors. There may be a tendency for the faint-end slope to become shallower with increasing redshift but the effect is marginal. We find a brightening of M^* and a decrease of ϕ^* with redshift for all analyzed wavelengths. The effect is systematic and much stronger than what can be expected to be caused by cosmic variance seen in the FDF. The evolution of M^* and ϕ^* from $z = 0$ to $z = 5$ is well described by the simple approximations $M^*(z) = M_0^* + a \ln(1+z)$ and $\phi^*(z) = \phi_0^*(1+z)^b$ for M^* and ϕ^* . The evolution is very pronounced at shorter wavelengths ($a = -2.19$, and $b = -1.76$ for 1500 Å rest wavelength) and decreases systematically with increasing wavelength, but is also clearly visible at the longest wavelength investigated here ($a = -1.08$, and $b = -1.29$ for g'). Finally we show a comparison with semi-analytical galaxy formation models.

¹This chapter is a slightly modified and updated version of the article Gabasch *et al.* (2004b). Modified sections are highlighted by footnotes.

3.1 Introduction

Observational constraints on galaxy formation have improved significantly over the last years and it has become possible to study the evolution of global galaxy properties up to very high redshifts. A crucial step to probe the properties of galaxies up to the highest redshifts was the work of Steidel & Hamilton (1993) and Steidel *et al.* (1996) who used color selection to discriminate between low redshift and high redshift galaxies. Although the Lyman-break technique is very efficient in selecting high redshift galaxies (see Blaizot *et al.* 2004 for a detailed discussion) with a minimum of photometric data, it has the disadvantage that it does not sample galaxies homogeneously in redshift space and may select against certain types of objects. With the advent of deep multi-band photometric surveys (Hubble Deep Field North (HDFN; Williams *et al.* 1996), NTT SUSI deep Field (NDF; Arnouts *et al.* 1999b), Hubble Deep Field South (HDFS; Williams *et al.* 2000; Casertano *et al.* 2000), Chandra Deep Field South (CDFs; Arnouts *et al.* 2001), William Herschel Deep Field (WHDF; McCracken *et al.* 2000; Metcalfe *et al.* 2001), Subaru Deep Field/Survey (SDF; Maihara *et al.* 2001; Ouchi *et al.* 2003), The Great Observatories Origins Deep Survey (GOODS; Giavalisco *et al.* 2004b)) the photometric redshift technique (essentially a generalization of the drop-out technique) has increasingly been used to identify high-redshift galaxies. Several methods have been described in the literature to derive photometric redshifts (Baum, 1962; Koo, 1985; Brunner *et al.*, 1999; Fernández-Soto *et al.*, 1999; Benítez, 2000; Le Borgne & Rocca-Volmerange, 2002; Firth *et al.*, 2003).

Based on either spectroscopic redshifts, drop-out techniques, or photometric redshifts, it has been possible to derive luminosity functions at different redshifts in the ultraviolet (UV) (Treyer *et al.*, 1998; Steidel *et al.*, 1999; Cowie *et al.*, 1999; Adelberger & Steidel, 2000; Cohen *et al.*, 2000; Sullivan *et al.*, 2000; Ouchi *et al.*, 2001;

Poli *et al.*, 2001; Wilson *et al.*, 2002; Wolf *et al.*, 2003; Rowan-Robinson, 2003; Kashikawa *et al.*, 2003; Ouchi *et al.*, 2003; Iwata *et al.*, 2003) and in the blue bands (Lilly *et al.*, 1995b; Heyl *et al.*, 1997; Lin *et al.*, 1997; Sawicki *et al.*, 1997; Small *et al.*, 1997; Zucca *et al.*, 1997; Loveday *et al.*, 1999; Marinoni *et al.*, 1999; Fried *et al.*, 2001; Cross & Driver, 2002; Im *et al.*, 2002; Marinoni *et al.*, 2002; Norberg *et al.*, 2002; Bell *et al.*, 2004; de Lapparent *et al.*, 2003; Liske *et al.*, 2003; Poli *et al.*, 2003; Pérez-González *et al.*, 2003a). Within the uncertainties given by IMF and dust content, the flux in the UV makes it possible to trace the star formation rate (SFR; Madau *et al.* 1998) in the galaxies, while the optical luminosities provide constraints on more evolved stellar populations (Hunter *et al.*, 1982; Franx *et al.*, 2003).

Locally, the 2dF Galaxy Redshift Survey (2dFGRS; Colless *et al.* 2001), the Sloan Digital Sky Survey (SDSS; Stoughton *et al.* 2002) and the 2MASS survey (Jarrett *et al.*, 2000) have provided superb reference points for galaxy luminosity functions over a large wavelength range (see Norberg *et al.* 2002 for 2dFGRS, Blanton *et al.* 2001, 2003 for the SDSS, and Kochanek *et al.* 2001; Cole *et al.* 2001 for 2MASS).

In parallel to the observational effort, theoretical models have been developed within the framework of the cold dark matter cosmology. Most notably, semi-analytic models (SAMs) (Kauffmann *et al.*, 1993; Cole *et al.*, 1994; Somerville & Primack, 1999; Kauffmann *et al.*, 1999; Poli *et al.*, 1999; Wu *et al.*, 2000; Cole *et al.*, 2000; Menci *et al.*, 2002, 2004) and simulations based on smoothed-particle hydrodynamics (SPH) (Davé *et al.*, 1999; Weinberg *et al.*, 2002; Nagamine, 2002; Nagamine *et al.*, 2004) have made testable predictions. Starting with the mass function of dark matter halos and their merging history, SAMs use simplified recipes to describe the baryonic physics (gas cooling, photoionization, star formation, feedback processes, etc., see Benson *et al.* 2003) to derive stellar mass and luminosity functions.

Ideally, a comparison between observations and models should be done with deep multiwavelength datasets that also cover a large area. The dataset has to be sufficiently deep in order to be able to derive the faint-end slope of the luminosity function. On the other hand, one also needs as large an area as possible to overcome cosmic variance and to quantify the density of rare bright galaxies, which define the cut-off of the luminosity function.

The FORS Deep Field (Heidt *et al.*, 2003) has a depth close to the HDFs but an area of 8–10 times the area of the HDFN. This depth allows us to detect galaxies at $z > 2$ which would be missed by Lyman-break studies which usually reach only $R_{AB} < 25.5$ (see also Franx *et al.* 2003 and van Dokkum *et al.* 2003).

Very reliable photometric redshifts are crucial for the analysis of the evolution of the luminosity functions in the FDF. Photometric redshifts have been determined with a template matching algorithm described in Bender *et al.* (2001) that applies Bayesian statistics and uses semi-empirical template spectra matched to broad band photometry. We achieved an accuracy of $\Delta z / (z_{spec} + 1) \leq 0.03$ with only $\sim 1\%$ extreme outliers (numbers based on a comparison with 362 spectroscopic redshifts). Redshifts of galaxies that are several magnitudes fainter than typical spectroscopic limits could be determined reliably and thus allowed better constraints on the faint-end slope of the luminosity functions.

In this paper we present the redshift evolution of the luminosity function evaluated in the rest-frame UV-range (1500 Å, 2800 Å), u' (SDSS), B, and g' (SDSS) bands in the redshift range $0.5 < z < 5.0$. Luminosity functions at longer wavelengths as well as the evolution of the luminosity density and the star formation rate will be presented in future papers (Gabasch *et al.*, in preparation).² We provide a short description of the FDF in Sect. 3.2 where we also present the selection criteria of our galaxies. In Sect. 3.3 we

investigate possible selection effects due to our purely I-band selected catalog. In Sect. 3.4 we discuss the accuracy of the photometric redshifts as well as the redshift distribution of the selected galaxies. In Sect. 3.5 and in Sect. 3.10 we show luminosity functions at different wavelengths and redshifts. In Sect. 3.6, a parameterization of the redshift evolution of the Schechter (1976) parameters M^* and ϕ^* is given. We compare our results with previous observational results in Sect. 3.7, and with model predictions in Sect. 3.8, before we summarize this work in Sect. 3.9.

We use AB magnitudes and adopt a Λ cosmology throughout the paper with $\Omega_M = 0.3$, $\Omega_\Lambda = 0.7$, and $H_0 = 70 \text{ km s}^{-1} \text{ Mpc}^{-1}$.

3.2 The FORS Deep Field

The FORS Deep Field (Appenzeller *et al.*, 2000) is a multi-color photometric and spectroscopic survey of a $7' \times 7'$ region near the south galactic pole including the QSO Q 0103-260 at redshift $z = 3.36$. The data have been taken with FORS1 and FORS2 at the ESO VLT and SofI at the NTT.

The data in the U, B, g, R, I, J and Ks filters were reduced and calibrated (including the correction for galactic extinction) as described in Heidt *et al.* (2003) (see also Chap. 2). The reduction of the images in the z-band and in a special filter centered at 834 nm follows the same recipe, except for additional de-fringing in the z-band (see Sect. 2.10).

The images were stacked with weights to get optimal signal to noise for point-like faint objects. The formal 50% completeness limits for point sources are 26.5, 27.6, 26.9, 26.9, 26.8, ~ 25.5 , ~ 25.8 , 23.8, 22.6 in U, B, g, R, I, 834 nm, z, J and Ks, respectively. The seeing varied from 0.5 arcsec in the I and z band to 1.0 arcsec in the U-band. Because the depth of the images decreases towards the borders, we limited our analysis to the inner 39.81 arcmin^2 of our field. The signal-to-noise ratio (S/N) in this ‘deep’ region is at least 90 % of the best S/N in every filter. This prevents

²see Chap. 4 as well as Chap. 6 in this thesis.

a possible bias of the photometric redshifts (see Sect. 3.4) due to a not completely homogeneous dataset.

Object detection was done in the I-band image using SExtractor (Bertin & Arnouts, 1996), and the catalog for this ‘deep’ part of the FDF includes 5636 objects. To avoid contamination from stars, we rely on three sources of information: The star-galaxy classifier of the detection software SExtractor, the goodness of fit for galaxy objects of the photometric redshift code and, if available, on the spectroscopic information. We first exclude all bright ($I < 22^m$) starlike objects (SExtractor star galaxy classifier > 0.95). Then we exclude all objects whose best fitting stellar spectral energy distribution (SED) – according to the photometric redshift code – gives a better match to the flux in the different wavebands than any galaxy template ($2\chi_{star}^2 < \chi_{galaxy}^2$). These objects are subsequently flagged as star and removed from our catalog. Further inspection of the images confirms that none of these flagged objects are extended. Finally, we reject all objects spectroscopically classified as stars. We checked the influence of misidentified or missed stars on the luminosity functions. If stars are fitted by galaxy templates their redshifts are mostly very small ($z < 0.15$, especially if they are G and K stars) and, therefore, did not enter the analysis. M stars interpreted as galaxies tend to be distributed more evenly in redshift space but they do not contribute significantly to the number density in any redshift interval. Even if all stars were included as galaxies in the sample, they would not affect the derived luminosity functions at a noticeable level.

In total 78 objects were classified as stars and removed from our sample. Our final I-band selected catalog comprises therefore 5558 objects.

3.3 I selection versus K selection

We use the ultradeep near-infrared ISAAC observations of the Hubble Deep Field South (Labbé *et al.*, 2003) for a more quantitative analysis of

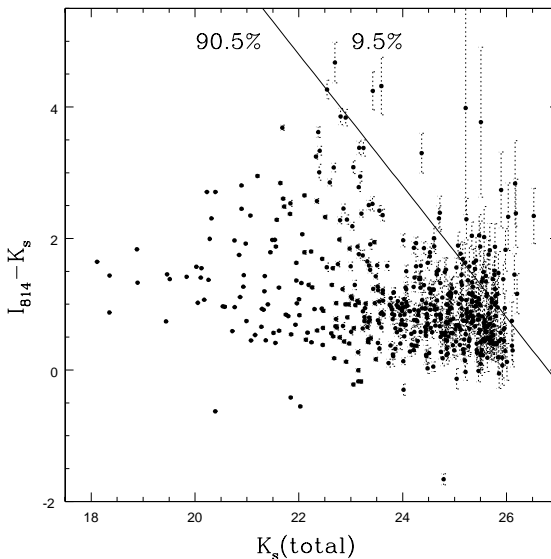


Figure 3.1: $I_{814} - K_s$ versus K_s color-magnitude relation for K_s -selected objects of the HDF-S as given by Labbé *et al.* (2003). Following Labbé *et al.* (2003) only sources with a minimum of 20% of the total exposure time in all bands are included and shown as filled symbols. Colors are plotted with 1σ error bars. The solid line corresponds to the limiting magnitude of the FDF ($I=26.8$). Only the objects to the right of the solid line are beyond our I-band limit.

possible selection effects between K and I band selected samples.

In Fig. 3.1 we show the $I_{814} - K_s$ versus K_s color-magnitude relation for K_s -selected objects of the HDF-S as given by Labbé *et al.* (2003) (data were taken from: <http://www.strw.leidenuniv.nl/~fires/>). Following Labbé *et al.* (2003), only sources with a minimum of 20% of the total exposure time in all bands are included and shown as filled symbols. Colors are plotted with 1σ error bars. The solid line corresponds to the 50% completeness limiting magnitude of the FDF in the I-band ($I \sim 26.8$). The figure clearly shows that, although we selected in I, we miss only about 10% of the objects that would have been

detected in deep K-band images (with a 50 % completeness limiting magnitude of $K_{AB} \sim 26.3$). All objects on the left of the solid line would have been detected in the I-selected FDF catalog as well. Therefore we conclude that only a small fraction (~ 10 %) of galaxies is missed in deep I-band selected samples relative to deep K-band selected samples, provided the I-band images are about 0.5 AB-magnitudes deeper than the K-band images. Of course, this holds only for galaxies at redshift below 6. At higher redshifts no signal is detectable in the I-band, due to the Lyman break and intervening intergalactic absorption.

Another indication that we are unlikely to miss a large population of high redshift red galaxies comes from Fig. 3.4 (left panel). Out to redshifts of about 1.5, red galaxies define the bright end of the luminosity function. Beyond $z \sim 1.5$ bluer star-forming galaxies take over. Red galaxies could still be detected at $z > 1.5$ but seem to be largely absent. In any case, even if we missed a few objects, the evolution of luminosity functions that we discuss below will not be affected.

As a side remark we note that also a B-band selected FDF catalog delivers similar conclusions on the evolution of the luminosity functions out to redshift ~ 3 (see also Chap. 6). Again, above this redshift no signal is detectable in the B-band due to the Lyman break and intervening intergalactic absorption.

3.4 Photometric redshifts

A brief summary of the photometric redshift technique used to derive the distances to the galaxies in the FDF can be found in Bender *et al.* (2001), a more detailed description will be published in a future paper (Bender *et al.* 2004). Well determined colors of the objects which implies very precise zeropoints in all filters are crucial to derive accurate photometric redshifts. Therefore we checked and fine-tuned the calibration of our zeropoints by means of color-color plots of stars. We compared the colors of FDF stars with the col-

Table 3.1: Galaxy distribution in the FDF for the redshift intervals used for computing the luminosity function. Note that we derive the luminosity function in all redshift bins, but exclude the lowest ($z < 0.45$) and highest redshift bin ($z > 5.01$) from our analysis of the luminosity function evolution, since the lowest redshift bin corresponds to a too small volume while the $z > 5.01$ bin suffers from incompleteness.

redshift interval	number of galaxies	fraction of galaxies
0.00 - 0.45	808	14.54 %
0.45 - 0.81	998	17.96 %
0.81 - 1.11	885	15.92 %
1.11 - 1.61	898	16.16 %
1.61 - 2.15	504	9.07 %
2.15 - 2.91	746	13.42 %
2.91 - 4.01	549	9.88 %
4.01 - 5.01	150	2.70 %
> 5.01	18	0.32 %
unknown	2	0.04 %

ors of stellar templates from the library of Pickles (1998) converted to the FORS filter system. In general, corrections to the photometric zeropoints of only a few hundredth of a magnitude were needed to obtain an optimal match to the stars and best results for the photometric redshifts. In order to avoid contamination from close-by objects, we derived object fluxes for a fixed aperture of $1.5''$ ($1.5 \times$ seeing) from images which had been convolved to the same point spread function. A redshift probability function $P(z)$ was then determined for each object by matching the object's fluxes to a set of 30 template spectra redshifted between $z = 0$ and $z = 10$ and covering a wide range of ages and star formation histories. As templates we used (a) local galaxy templates from Mannucci *et al.* (2001), and Kinney *et al.* (1996) and (b) semi-empirical templates more appropriate for modest to high redshift galaxies. The semi-empirical templates were constructed by fitting

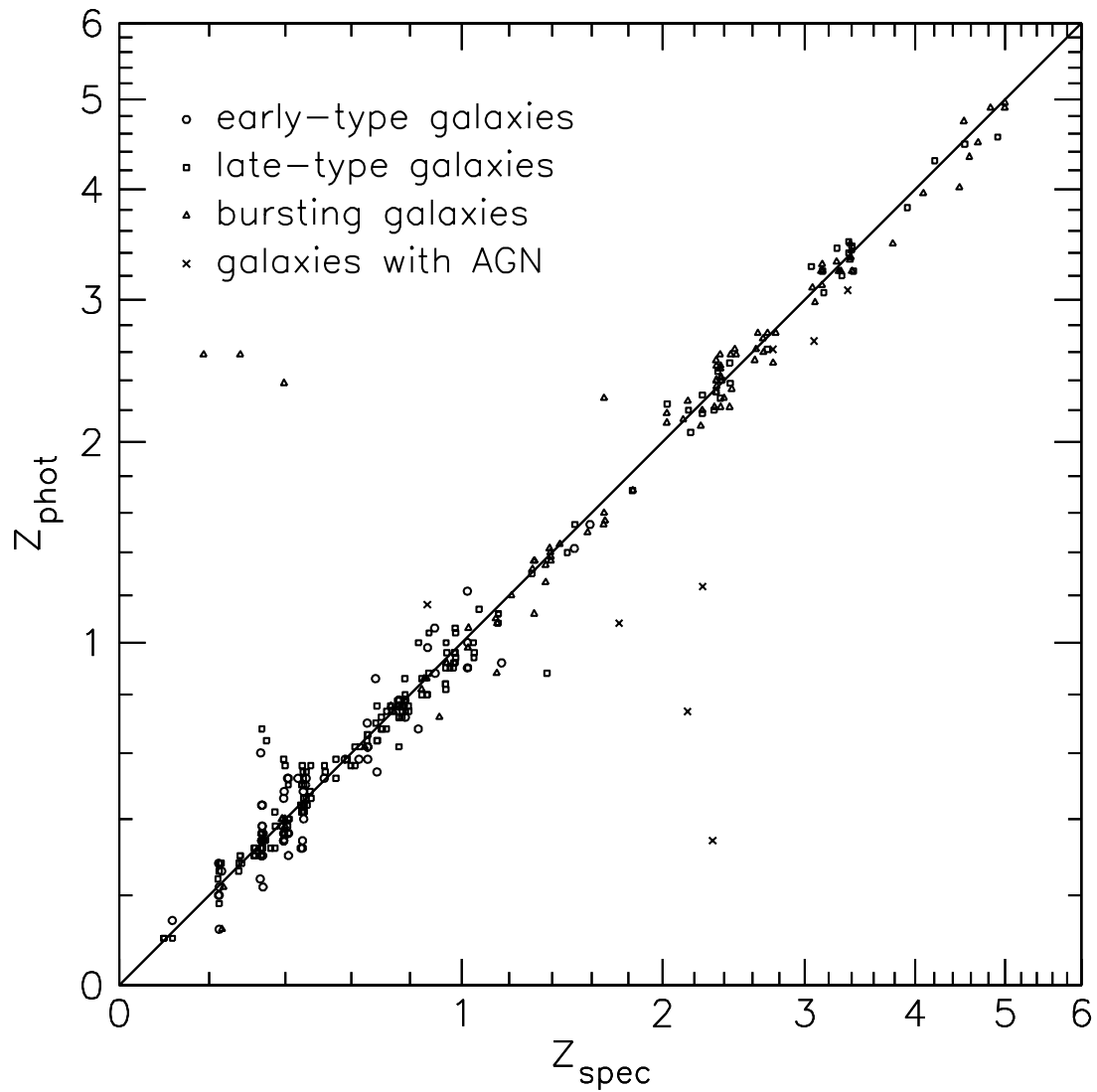


Figure 3.2: Comparison of spectroscopic (Noll *et al.*, 2004; Böhm *et al.*, 2004) and photometric redshifts for different galaxy types and quasars in the FDF (362 objects).

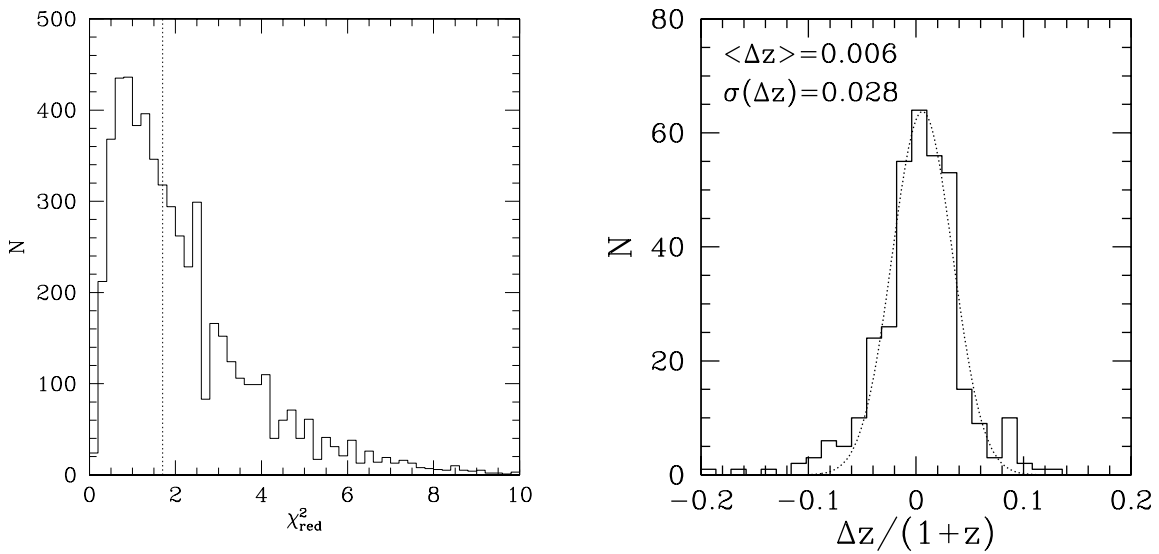


Figure 3.3: Left panel: Histogram of the reduced χ^2 for all galaxies in the FDF as obtained for the best fitting template and redshift. The dotted vertical line indicates the median reduced χ^2 . Right panel: Histogram of the photometric redshift errors. The error distribution can be approximated by a Gaussian centered at 0.006 with an rms of 0.028 (dotted line).

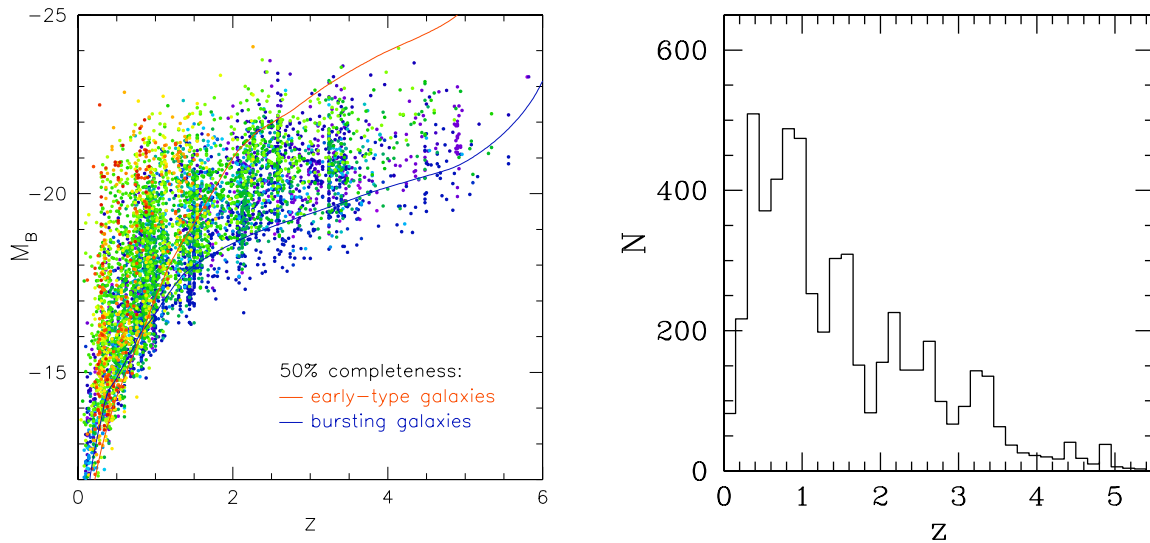


Figure 3.4: Left panel: Absolute B magnitudes of galaxies in the FDF against redshift. Colors indicate spectral types (red to blue: old to young). The two lines indicate the 50% completeness limit for a red and a blue spectral energy distribution corresponding to an I-band limiting magnitude of 26.8. Right panel: Redshift number distribution of all galaxies in the FDF sample. The clustering observed in photometric redshift space (both panels) is probably mostly real, as we see clustered *spectroscopic* redshifts at $z = 0.22$, $z = 0.33$, $z = 0.39$, $z = 0.45$, $z = 0.77$, $z = 2.35$ and possibly at $z = 0.95$, $z = 3.15$, and $z = 3.4$.

combinations of theoretical spectral energy distributions of different ages from Maraston (1998) and Bruzual & Charlot (1993) with variable reddening (Kinney *et al.*, 1994) to the observed broad band colors of about 100 galaxies in the Hubble Deep Field and about 180 galaxies from the FDF with spectroscopic redshifts. The remaining 180 galaxies in the FDF with spectroscopic redshift were used as an independent control sample. Lyman forest absorption was parameterized following Madau (1995) and references therein.

In Fig. 3.2 we compare the photometric and spectroscopic redshifts of 362 galaxies and QSOs in the FDF (see Noll *et al.* 2004; Böhm *et al.* 2004 for the spectroscopic redshifts). The agreement is very good and we have only 6 outliers with a redshift error larger than $\Delta z > 1$ among 362 objects. Three of the outliers are quasars or galaxies with a strong power-law AGN component (crosses). The others are very blue objects with an almost featureless continuum (triangles). Fig. 3.3 (left panel) presents the χ^2 distribution for the best fitting template and photometric redshifts. Note that to calculate the χ^2 we have used the observational photometric errors and, in addition, have assumed that the templates have an intrinsic uncertainty of typically 5% in the optical bands and 20% in the infrared bands. The larger errors for the near-IR take into account the slightly lower quality of the infrared data if compared to the optical. Allowing for this intrinsic uncertainty turns a discrete set of templates into a template-continuum. Observational errors and intrinsic ‘errors’ were added in quadrature. The median value of the reduced χ^2 is below 1.7 and demonstrates that the galaxy templates describe the vast majority of galaxies in the FDF very well. The right panel of Fig. 3.3 shows the distribution of the redshift errors. It is nearly Gaussian and scatters around zero with an rms error of $\Delta z / (z_{spec} + 1) \approx 0.03$. In Fig. 3.4 (left panel), we plot the absolute B-band magnitudes against the photometric redshifts of the objects. Colors from red to blue indicate increasingly bluer spectral energy distributions. The two lines indicate the 50% completeness limit for a

red and a blue spectral energy distribution corresponding to an I-band limiting magnitude of 26.8. The redshift histogram of all objects in the FDF is shown in the right panel of Fig. 3.4 (see also Table 3.1). Most if not all peaks in the distribution are due to real clustering in redshift space. From the 362 spectroscopic redshifts, we have identified clusters, groups or filaments of galaxies with more than 10 identical or almost identical redshifts at $z = 0.22$, $z = 0.33$, $z = 0.39$, $z = 0.45$, $z = 0.77$, $z = 2.35$. Other structures (with only a few identical spectroscopic redshifts) are possibly present at $z = 0.95$, $z = 3.15$, and $z = 3.4$.

3.5 Luminosity functions

3.5.1 The method

We compute the absolute magnitudes of our galaxies using the I-band selected catalog as described in Sect. 3.2 and the photometric redshifts described in Sect. 3.4. To derive the absolute magnitude for a given band we use the best fitting SED as determined by the photometric redshift code and convolve it with the appropriate filter function. As the SED fits all 9 observed-frame wavebands simultaneously, possible systematic errors which could be introduced by using K-corrections applied to a single observed magnitude are reduced. Since the photometric redshift code works with 1.5” aperture fluxes, we only need to correct to total luminosities by applying an object dependent scale factor. For this scale factor we used the ratio of the I-band aperture flux to the total flux as provided by SExtractor (MAG_APER and MAG_AUTO). We have chosen the I-band because (a) our I-band data are very deep, (b) all objects were detected and selected in the I-band, and (c) high redshift galaxies have only poorly determined or no flux at shorter wavelengths. This procedure may introduce a slight bias, as galaxies are more compact or knotty in the rest-frame UV bands (tracing HII regions) than at longer wavelengths. However, scaling factors derived in the deep B-band turned out to be similar

(for low enough redshifts).

In a given redshift interval, the luminosity function is computed by dividing the number of galaxies in each magnitude bin by the volume V_{bin} of the redshift interval. To account for the fact that some fainter galaxies are not visible in the whole survey volume we perform a V/V_{max} (Schmidt, 1968) correction. Using the best fitting SED we calculate the maximum redshift z_{max} at which the object could have been observed given the magnitude limit of our field. We weight each object by $V_{\text{bin}}/V_{\text{max}}$ where V_{bin} is the volume of our redshift bin enclosed by z_{low} and z_{high} and V_{max} is the volume enclosed between $[z_{\text{low}}, \min(z_{\text{high}}, z_{\text{max}})]$.

To derive reliable Schechter parameters we limit our analysis of the luminosity function to the bin where the V/V_{max} begins to contribute by at most a factor of 3 (we also show the uncorrected luminosity function in the various plots as open circles). The redshift binning was chosen such that we have good statistics in every redshift bin and that the influence of redshift clustering was minimized. The redshift binning and the number of galaxies in every bin is shown in Table 3.1.

The errors of the luminosity functions are calculated by means of Monte-Carlo simulations as follows. The photometric redshift code provides redshift probability distributions $P(z)$ for each single galaxy. In each Monte-Carlo realization, we randomly pick a new redshift for each object from a sample of redshifts distributed like $P(z)$ and calculate the corresponding luminosity. This we repeat 250 times which allows us to derive the dispersion of the galaxy number density $\phi(M, z)$ for each magnitude and redshift bin due to the finite width of $P(z)$ for each galaxy. The total error in ϕ is finally obtained by adding in quadrature the error from the Monte-Carlo simulations and the Poissonian error derived from the number of objects in the bin.

Photometric redshift errors may, in principle, affect the shape of the luminosity function at the bright end: By scattering objects to higher redshifts they let the steep fall-off at high luminosities appear shallower (Drory *et al.*, 2003). How-

ever, in the case of the FDF the redshift errors are so small that the influence on the shape of the luminosity function is negligible.

3.5.2 The slope of the luminosity function

We first investigate the redshift evolution of the faint-end slope of the luminosity function by fitting all three parameters of the Schechter function (M^* , ϕ^* , and α). The best fitting α and the corresponding 1σ errors for all wavebands and redshifts are listed in Table 3.2.

Despite the depth of the FDF, Table 3.2 shows that it is only possible to obtain reasonably tight constraints on the slope α for $z < 1.5$. In addition, strong parameter coupling is observed between M^* and α (see Fig. 3.25 in Sect. 3.10.3). We find only marginal evidence for a change of α with redshift for all wavebands. The lowest redshift bin ($0.15 < z < 0.45$), which we excluded from the fit because of poor number statistics in bright objects, generally shows the steepest faint-end slope. Beyond redshift 0.5, all data are consistent with a constant and shallow faint-end slope.

We obtain as best error-weighted values for all redshifts between 0.45 and 5.0 the numbers given in Table 3.3 (upper part), assuming that α does not depend on redshift. The slopes in the 1500 Å, 2800 Å, and u' band are very similar. The same applies for the slope in the g' and B band. Therefore, we combined the data for the 1500 Å, 2800 Å, and u' band as well as for the g' and B band and derived combined slopes with an error-weighted fit to the data of Table 3.2. The results are also listed in Table 3.3 (lower part).

Almost all of the slopes listed in Table 3.2 are compatible within 2σ with the slopes in Table 3.3. Therefore, we fixed the slope to these values for further analysis. This simplification is also justified by the fact that for all subsequent fits with fixed slope the reduced χ^2 was generally close to 1.

As a last test, we investigated the influence of the redshift binning on the slope α . We enlarged our first two redshift bins to $0.41 < z \leq 0.91$ (1433

Table 3.2: Slope of the luminosity function for all wavelengths and all redshifts as derived from 3-parameter Schechter fits.

z	α (1500 Å)	α (2800 Å)	α (u')	α (g')	α (B)
[0.45, 0.81]	-1.14 (+0.08 -0.07)	-1.23 (+0.08 -0.07)	-1.27 (+0.06 -0.05)	-1.34 (+0.05 -0.03)	-1.30 (+0.05 -0.03)
[0.81, 1.11]	-0.96 (+0.13 -0.10)	-0.99 (+0.10 -0.08)	-0.93 (+0.09 -0.07)	-1.16 (+0.07 -0.04)	-1.21 (+0.07 -0.04)
[1.11, 1.61]	-1.05 (+0.18 -0.16)	-1.03 (+0.13 -0.11)	-0.95 (+0.10 -0.09)	-1.13 (+0.11 -0.09)	-1.12 (+0.09 -0.07)
[1.61, 2.15]	-0.81 (+0.48 -0.45)	-0.97 (+0.32 -0.28)	-0.80 (+0.31 -0.27)	-1.29 (+0.24 -0.21)	-1.33 (+0.27 -0.20)
[2.15, 2.91]	-0.38 (+0.21 -0.15)	-0.67 (+0.18 -0.15)	-0.70 (+0.16 -0.16)	-0.89 (+0.22 -0.15)	-0.70 (+0.24 -0.21)
[2.91, 4.01]	-0.98 (+0.28 -0.24)	-0.95 (+0.19 -0.17)	-1.25 (+0.19 -0.14)	-1.24 (+0.23 -0.20)	-1.30 (+0.27 -0.20)
[4.01, 5.01]	-0.77 (+0.38 -0.26)	-1.03 (+0.46 -0.35)	-1.09 (+0.54 -0.27)	-1.18 (+0.37 -0.21)	-0.77 (+0.49 -0.39)

Table 3.3: Slope α of the luminosity functions for the different wavebands as determined from an error-weighted fit to the data in Table 3.2 under the assumption that $\alpha(z) = \text{const.}$ (upper part). In the lower part of the table we show the best values of α after combining the UV bands and the blue optical bands.

filter	$\alpha(z) = \text{const}$
1500 Å	-1.01 ± 0.08
2800 Å	-1.06 ± 0.07
u'	-1.10 ± 0.08
g'	-1.26 ± 0.04
B	-1.24 ± 0.04
1500 Å & 2800 Å & u'	-1.07 ± 0.04
g' & B	-1.25 ± 0.03

galaxies) and $0.91 < z \leq 1.61$ (1438 galaxies) which allowed us to determine luminosity functions with lower errors in all wavebands. The slopes derived in these two larger bins were compatible with our previously derived fixed slope in every waveband.

3.5.3 The restframe luminosity functions

In this section we analyze the luminosity function in the UV (1500 Å, 2800 Å), u', g', and B band by means of a Schechter function fit with fixed slope (see Sect. 3.5.2).

In the UV, we evaluate the luminosity function in two rectangular filters centered at 1500 ± 100 Å and 2800 ± 100 Å. There are three reasons to analyze both wavelengths. First, for our lowest redshift bin ($\langle z \rangle \sim 0.6$) the restframe magnitude derived at 2800 Å is more robust than the one at 1500 Å because the restframe wavelength of 2800 Å corresponds to the observed U and does not need extrapolation to shorter wavelength. Second, we also include the 1500 Å luminosity function as it corresponds to a frequently used reference wavelength and is very well determined beyond redshifts of 2.5. Third, we want to show that the galaxy luminosity functions at the two wavelengths are very similar and show the same redshift evolution.

In the optical bands, we calculated the evolution of the luminosity functions in the u' and g' bands (g' of SDSS, see Fukugita *et al.* 1996, not to be confused with Gunn g which was part of the filter set with which we observed the FDF). Because many authors have already published luminosity functions in the Johnson B-band, we include also this filter in our analysis.

In Figs. 3.5 and 3.6 we present the luminosity functions at 2800 Å and in the g' band, while

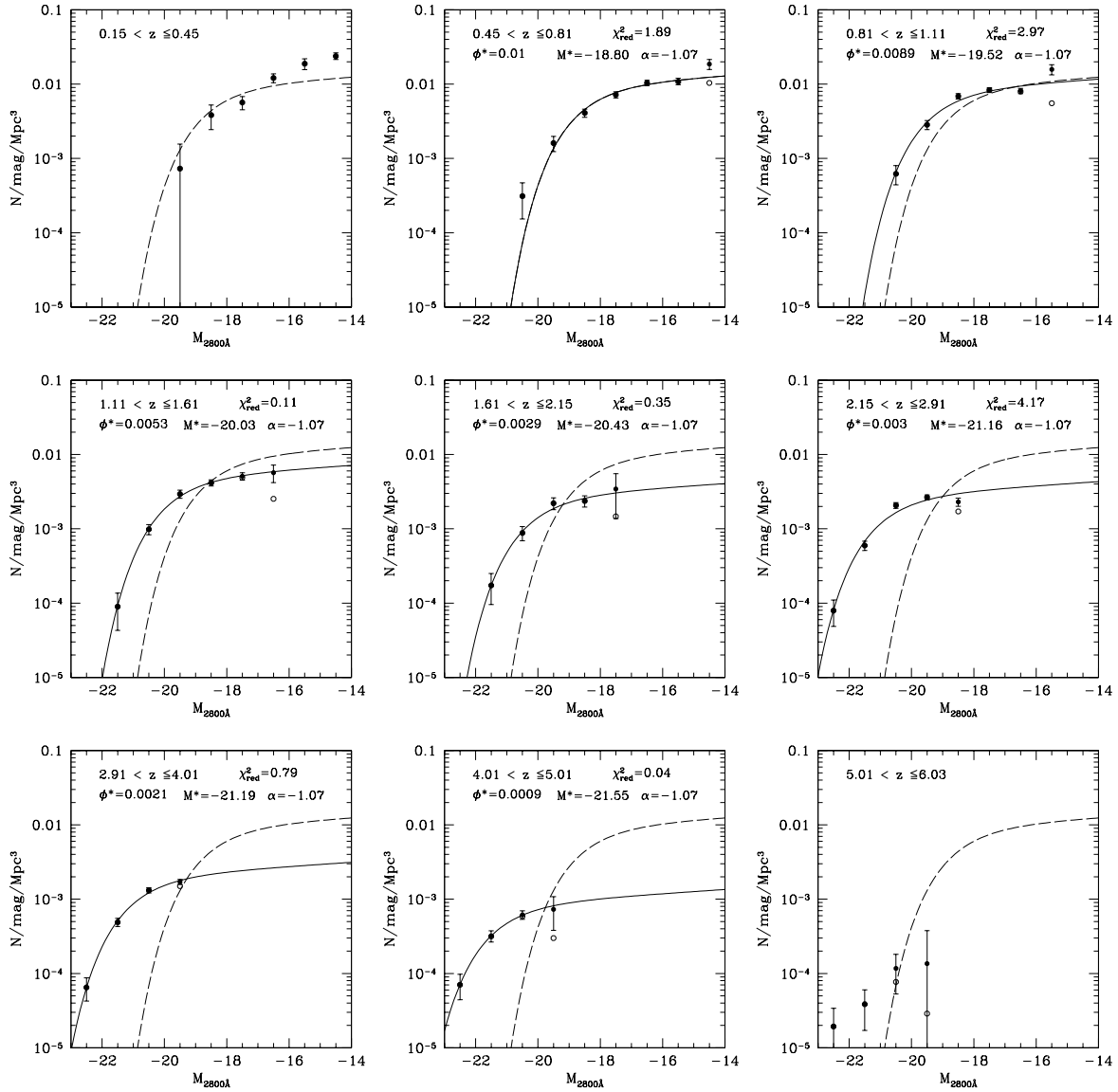


Figure 3.5: Luminosity functions at 2800 \AA from low redshift ($\langle z \rangle = 0.3$, upper left panel) to high redshift ($\langle z \rangle = 5.5$, lower right panel). The filled (open) symbols show the luminosity function corrected (uncorrected) for V/V_{max} . The fitted Schechter functions for a fixed slope α are shown as solid lines. Note that we only fit the luminosity functions from $\langle z \rangle = 0.6$ to $\langle z \rangle = 4.5$. The parameters of the Schechter functions are given in Table 3.6. The Schechter fit for redshift $\langle z \rangle = 0.6$ is indicated as a dashed line in all panels.

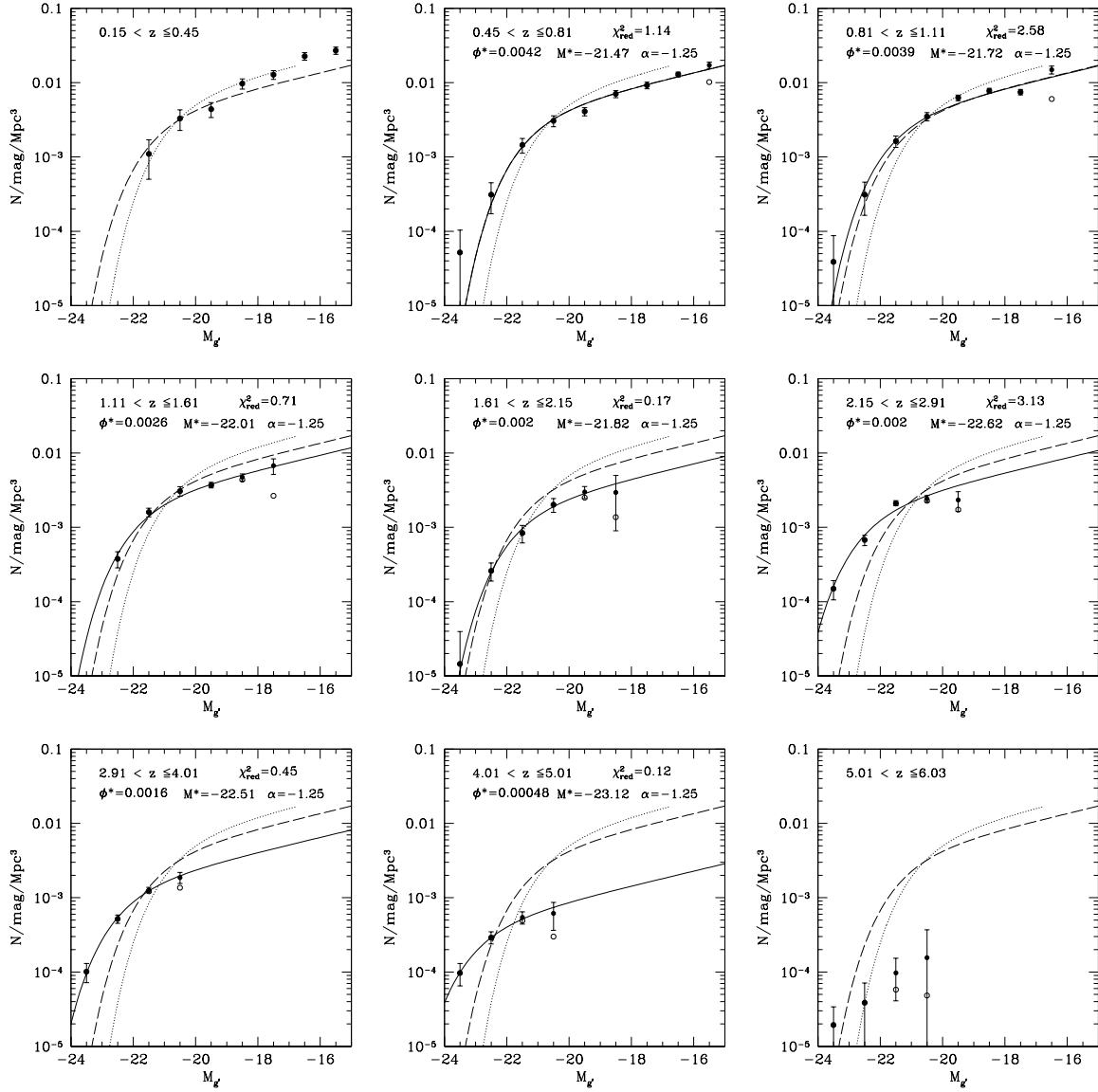


Figure 3.6: Luminosity functions in the g' -band from low redshift ($\langle z \rangle = 0.3$, upper left panel) to high redshift ($\langle z \rangle = 5.5$, lower right panel). The filled (open) symbols show the luminosity function corrected (uncorrected) for V/V_{max} . The fitted Schechter functions for a fixed slope α are shown as solid lines. Note that we only fit the luminosity functions from $\langle z \rangle = 0.6$ to $\langle z \rangle = 4.5$. The parameters of the Schechter functions α can be found in Table 3.8. The dotted line represents the local g' -band luminosity function derived from the SDSS (Blanton *et al.*, 2001). The Schechter fit for redshift $\langle z \rangle = 0.6$ is indicated as a dashed line in all panels.

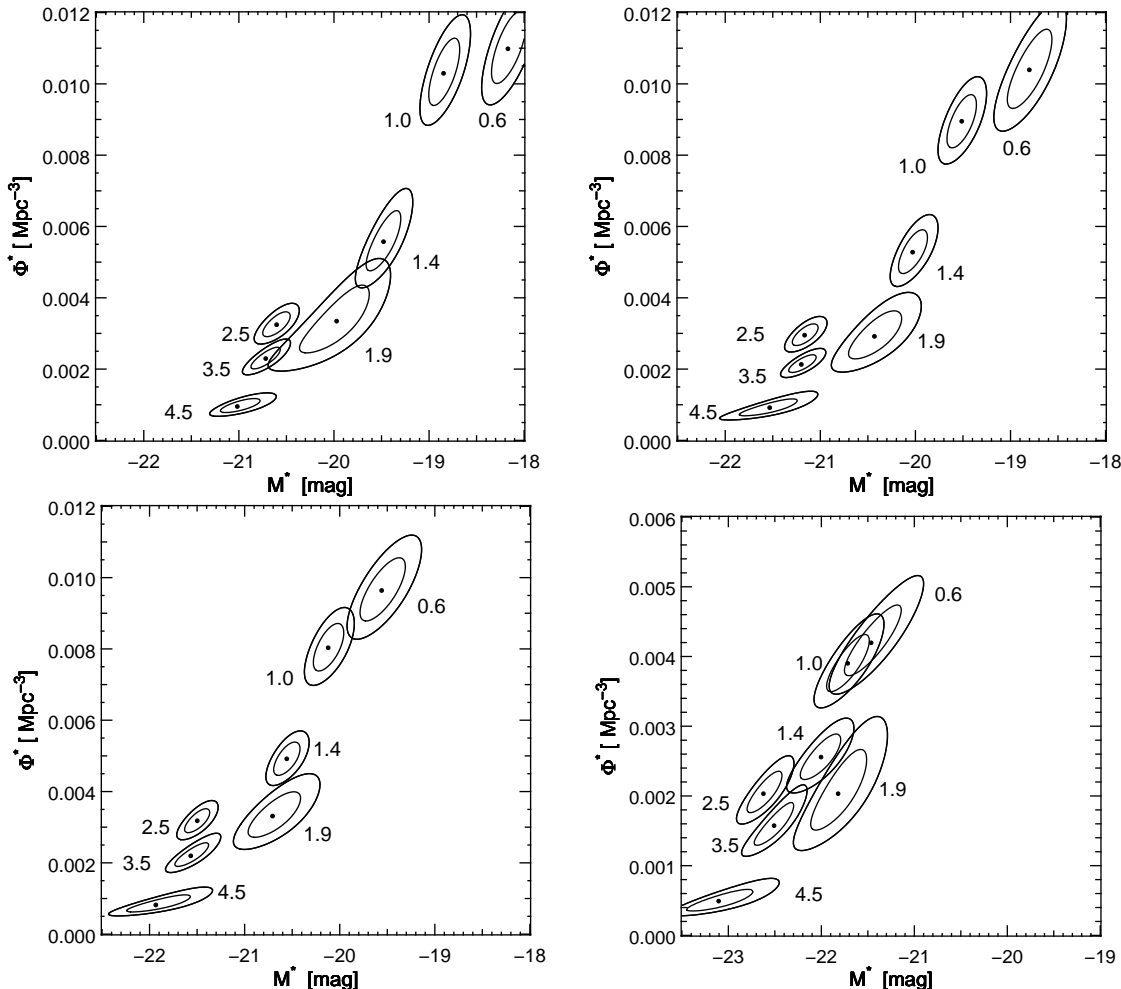


Figure 3.7: 1σ and 2σ confidence levels in Schechter parameter space for the different redshift bins, labeled by their mean redshift. A Schechter function with a fixed slope (see Table 3.3) has been fitted to the luminosity function at 1500 \AA (*upper left panel*), 2800 \AA (*upper right panel*), in the u' -band (*lower left panel*) and in the g' -band (*lower right panel*). The parameters of the Schechter function can be found in Table 3.5, Table 3.6 Table 3.7 and Table 3.8.

the results at 1500 \AA as well as for the u' and B bands can be found in Figs. 3.14, 3.15 and 3.16 in Sect. 3.10.1. The filled (open) symbols denote the luminosity function with (without) completeness correction.

Even without fitting Schechter functions to the data, it is obvious that there is strong evolution in characteristic luminosity and number density between redshifts 0.6 and 4.5.

The solid lines show the Schechter function

fitted to the luminosity function. The best fitting Schechter parameter, the redshift binning as well as the reduced χ^2 are also listed. The reduced χ^2 are quite good for all but one redshift bin ($2.15 < z \leq 2.91$). The slope we adopted is not suitable for that bin and increases the χ^2 . The depth of the FDF allows us to trace the luminosity function over a relatively large magnitude range. Even in our highest redshift bin ($4.01 < z \leq 5.01$) the luminosity function spans an interval of 4

magnitudes.

In Fig. 3.7 we show the 1σ and 2σ confidence contours of M^* and ϕ^* for the different redshift bins, illustrating the correlation of the two Schechter parameters. The contours correspond to $\Delta\chi^2 = 2.30$ and $\Delta\chi^2 = 6.17$ above the minimum χ^2 . The best fitting Schechter parameters and their 1σ errors are summarized in Tables 3.5, 3.6, 3.7, 3.8 and 3.9 for the 1500 Å, 2800 Å, u', g' and B bands, respectively. The 1σ errorbars of the single parameters are derived from the projections of the two-dimensional contours using $\Delta\chi^2 = 1$.

We find a systematic brightening of M^* and a systematic decrease of ϕ^* from low to high redshift. The evolution is very strong at 1500 Å (upper left panel), 2800 Å (upper right panel) and in the u'-band (lower left panel) and moderately strong in the g'-band (lower right panel). We do not show the B-band results as they behave almost identical as those of the g'-band. Although the variation of M^* and ϕ^* between adjacent redshift bins is in part influenced by large scale structure, the overall trend in the evolution of M^* and ϕ^* is very robust.

Since the integral of the luminosity function in the UV is strongly related to the star-formation rate (SFR) (Madau *et al.*, 1998), we can derive the star-formation history from the evolution of the luminosity function. The brightening of M^* and decrease of ϕ^* in the UV leads to an increase of the SFR between $0.5 < z < 1.5$, whereas it remains approximately constant between $1.5 < z < 4.0$. A detailed analysis of the star-formation history will be presented in a future paper (Gabasch *et al.* 2004c; see also Chap. 6). Preliminary results are published in Gabasch *et al.* (2004a).

3.6 Parameterizing the evolution of the luminosity function

In order to quantify the redshift evolution of M^* and ϕ^* we assume the simple relations of the form:

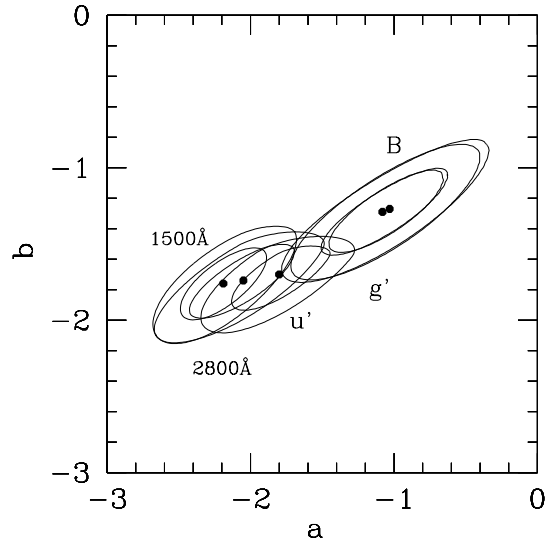


Figure 3.8: 1σ and 2σ confidence levels of the parameters a and b in different bands (1500 Å, 2800 Å, u', g' and B) for the evolutionary model described in the text. The values for a and b can be found in Table 3.4.

$$\begin{aligned} M^*(z) &= M_0^* + a \ln(1+z), \\ \phi^*(z) &= \phi_0^* (1+z)^b, \text{ and} \\ \alpha(z) &= \alpha_0 \equiv \text{const.} \end{aligned} \quad (3.1)$$

Parameterizing $M^*(z) = M_0^* + a \ln(1+z)$ is equivalent to assuming a dependence of $L^*(z) = L_0^* (1+z)^\xi$ with $\xi = -0.4 \ln(10) a \approx -0.921 a$.

The best fitting values for a , b , M_0^* , and ϕ_0^* are derived by minimizing

$$\begin{aligned} \chi^2 &= \chi^2(a, b, M_0^*, \phi_0^*) \\ &= \sum_{j=1}^{N_j} \sum_{i=1}^{N_i} \frac{[\phi(M_{ij}) - \Psi(M_{ij}, z_j, a, b, M_0^*, \phi_0^*)]^2}{\sigma_{ij}^2}, \end{aligned} \quad (3.2)$$

for the galaxy number densities in all magnitude and redshift bins *simultaneously*. $\phi(M_{ij})$ is the number density of galaxies in magnitude

Table 3.4: Evolution parameters according to Eq. (3.1)

filter	a	b	M_0^* (mag)	ϕ_0^* (10^{-2}Mpc^{-3})
1500 Å	$-2.19^{+0.19}_{-0.19}$	$-1.76^{+0.15}_{-0.15}$	$-17.40^{+0.25}_{-0.22}$	$2.71^{+0.47}_{-0.38}$
2800 Å	$-2.05^{+0.23}_{-0.24}$	$-1.74^{+0.15}_{-0.16}$	$-18.16^{+0.27}_{-0.26}$	$2.46^{+0.39}_{-0.37}$
u'	$-1.80^{+0.24}_{-0.21}$	$-1.70^{+0.14}_{-0.15}$	$-18.95^{+0.24}_{-0.26}$	$2.19^{+0.37}_{-0.28}$
g'	$-1.08^{+0.30}_{-0.28}$	$-1.29^{+0.18}_{-0.18}$	$-21.00^{+0.32}_{-0.31}$	$0.83^{+0.15}_{-0.12}$
B	$-1.03^{+0.23}_{-0.28}$	$-1.27^{+0.16}_{-0.19}$	$-20.92^{+0.32}_{-0.25}$	$0.82^{+0.14}_{-0.12}$

bin i at redshift z_j ; $\Psi(M_{ij}, z_j, a, b, M_0^*, \phi_0^*)$ is the Schechter function evolved to the redshift z_j according to the evolution model defined in Eq. (3.1), and σ_{ij} is the rms error of the luminosity function value. The resulting values for a , b , M_0^* , and ϕ_0^* can be found in Table 3.4.

The 1σ and 2σ confidence levels of the evolution parameters a and b are shown for the different filters in Fig. 3.8. These contours were derived by projecting the four-dimensional χ^2 distribution to the a - b plane, i.e. for given a and b we use the value of M_0^* and ϕ_0^* which minimizes the $\chi^2(a, b)$.

In Fig. 3.9 we show the relative redshift evolution of M^* (left panel) and ϕ^* (right panel) in the chosen filters. The Schechter parameters are the ones given in the tables in Sect. 3.10.1. The solid lines show the relative change according to our evolutionary model with the parameters from Table 3.4.

Note that a , b , M_0^* , and ϕ_0^* were derived by minimizing Eq. (3.2) and not the differences between the (best fitting) lines and the data points in Fig. 3.9.

Fig. 3.9 shows that the simple parameterization we have chosen with Eq. (3.1) describes the evolution of the galaxy luminosity functions very well. Still, the reduced χ^2_{ν} values are somewhat larger than unity (~ 4), because our approximations for evolution and faint-end slope may not be adequate for every redshift bin and because of the influence of large scale structure. Neverthe-

less, as there are no stringent theoretical predictions for the evolution of M^* and ϕ^* we do not want to increase the number of free parameters, but increase the errors of a , b , M_0^* , and ϕ_0^* instead. We do this by an appropriate scaling of the errors σ_{ij} of Eq. (3.2) to obtain a χ^2_{ν} of unity.

For comparison, we also show in Fig. 3.9 the local values from the SDSS (Blanton *et al.*, 2001). There is good agreement in the u'-band for both M^* and ϕ^* between our extrapolated values and the SDSS values. In the g'-band the value of M^* is lower than the predicted one, but still within the 1σ error of the M_0^* .

3.7 Comparison with literature

In this section we compare the luminosity functions derived in the FDF with the luminosity functions of other surveys. As the cosmology and the wavebands in which the luminosity functions were determined are different from ours for most of the surveys we chose the following approach. *First* we convert results from the literature to our cosmology ($\Omega_M = 0.3$, $\Omega_\Lambda = 0.7$ and $H_0 = 70 \text{km s}^{-1} \text{Mpc}^{-1}$). Note that this conversion may not be perfect, because we can only transform number densities and magnitudes but lack the knowledge of the individual magnitudes and redshifts of the galaxies. Nevertheless, the errors introduced in this way are not large and

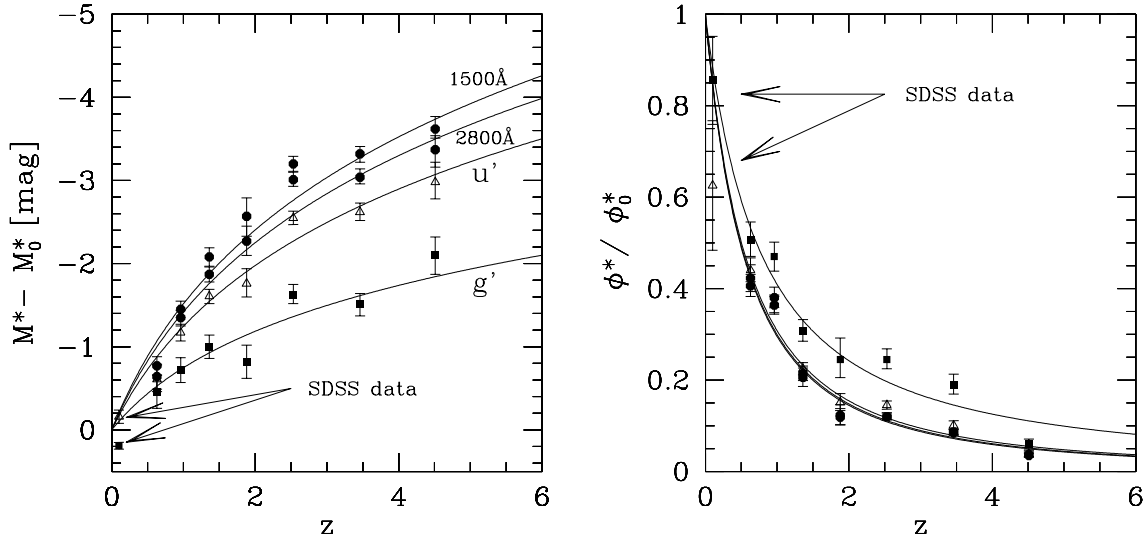


Figure 3.9: Redshift evolution of M^* (left panel) and ϕ^* (right panel) for the filters g' (filled squares), u' (open triangles) and the two UV bands at 2800 Å and 1500 Å (filled circles). The arrows mark the values for M^* and ϕ^* as derived in the SDSS (Blanton *et al.*, 2001).

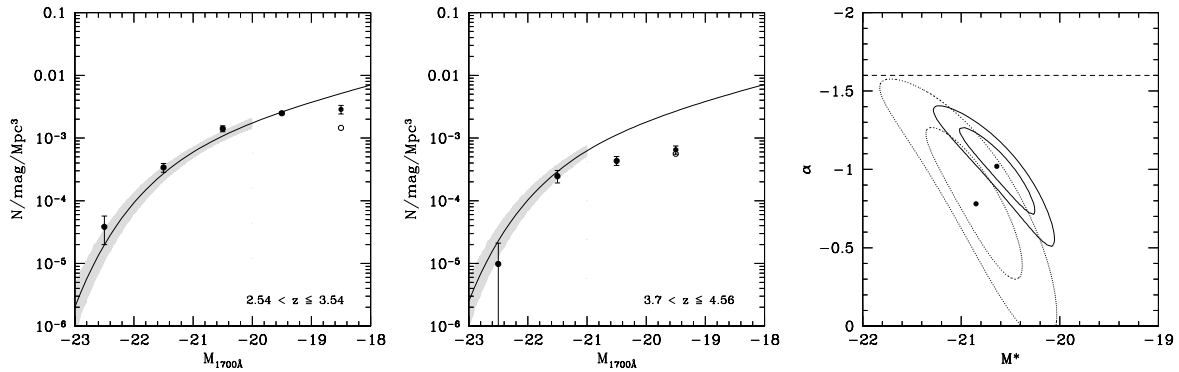


Figure 3.10: Comparison of the luminosity function at 1700 Å of the FDF with the Schechter function derived in Steidel *et al.* (1999): $\langle z \rangle \sim 3.04$ (left panel) and $\langle z \rangle \sim 4.13$ (middle panel). The filled (open) symbols show the luminosity function corrected (uncorrected) for V/V_{max} . The shaded region in all plots is based only on ΔM^* , and $\Delta \alpha$ (a detailed discussion concerning the errors ΔM^* , and $\Delta \alpha$ can be found in Sect. 3.7), where the cut-off at low luminosity indicates the limiting magnitude of the sample. In the right panel the 1σ and 2σ confidence levels for M^* and α for a 3 parameter Schechter fit as derived in the FDF in the redshift interval $2.54 < z \leq 3.54$ (solid contours) and $3.70 < z \leq 4.56$ (dotted contours) are shown. The horizontal dashed line marks the slope $\alpha = -1.6$ as derived in Steidel *et al.* (1999).

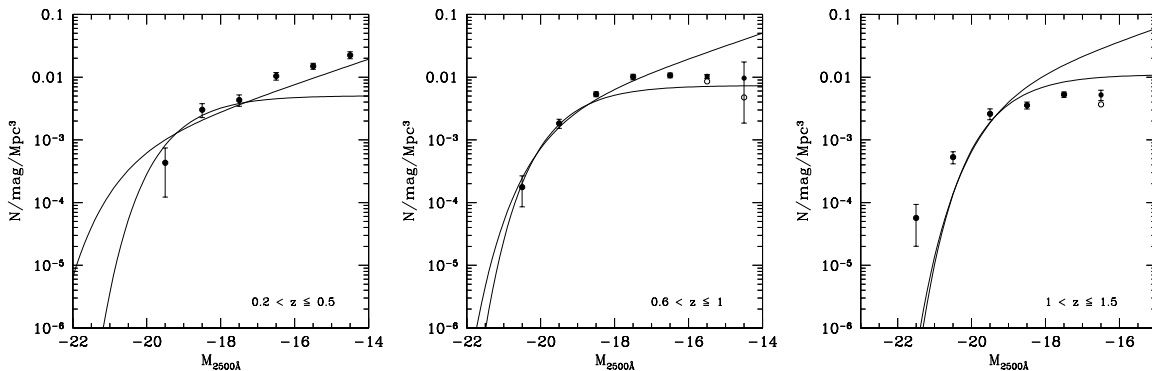


Figure 3.11: Comparison of the luminosity function at 2500 Å of the FDF with the Schechter function derived in *Wilson et al. (2002)*: $0.2 < z \leq 0.5$ (left panel), $0.6 < z \leq 1.0$ (middle panel), and $1.0 < z \leq 1.5$ (right panel). *Wilson et al. (2002)* fixed the slope to $\alpha = -1.0$ (thick line) and $\alpha = -1.5$ (thin line) and used only M^* and ϕ^* as free parameters to determine the Schechter functions.

the method is suitable for our purpose. *Second*, in order to avoid uncertainties due to conversion between different filter bands, we always use the same band as the survey we want to compare with. *Third*, we also try to use the same redshift binning if possible. In addition, if the number of galaxies in the FDF is too small to derive a well sampled luminosity function we increase the binning.

To visualize the errors of the literature luminosity functions we perform Monte-Carlo simulations using the ΔM^* , $\Delta \phi^*$, and $\Delta \alpha$ given in the papers. In cases where not all of these values could be found in the paper, this is mentioned in the figure caption. We do not take into account any correlation between the Schechter parameters and assume a Gaussian distribution of the errors ΔM^* , $\Delta \phi^*$, and $\Delta \alpha$. From 1000 simulated Schechter functions we derive the region where 68.8 % of the realizations lie. The resulting region, roughly corresponding to 1σ errors, is shaded in the figures. The luminosity functions derived in the FDF are also shown as filled and open circles. The filled circles are completeness corrected whereas the open circles are not corrected. The redshift binning used to derive the luminosity function in the FDF is given in the lower right part of every figure. Moreover, the limiting magnitude of the respective survey is indicated by

the low-luminosity cut-off of the shaded region in all figures. If the limiting magnitude was not explicitly given it was estimated from the figures in the literature.

We first compare our luminosity functions in the UV to the results of *Steidel et al. (1999)* and the spectroscopic studies of *Wilson et al. (2002)*.

Fig. 3.10 shows a comparison of the 1700 Å luminosity function derived by *Steidel et al. (1999)* at redshift $\langle z \rangle \sim 3.04$ (left panel) and $\langle z \rangle \sim 4.13$ (middle panel) with the luminosity function in the FDF. The galaxy sample of *Steidel et al. (1999)* is based on a R-band ($\langle z \rangle \sim 3.04$) and an I-band ($\langle z \rangle \sim 4.13$) selected catalog and therefore similar to our I-band selected sample. Candidate galaxies were identified with the Lyman-break technique and most of them spectroscopically confirmed (564 galaxies of the $\langle z \rangle \sim 3.04$ and 46 of the $\langle z \rangle \sim 4.13$ sample, respectively).

To derive the associated errors (shaded region) of the Schechter functions derived by *Steidel et al. (1999)* we use the errors of M^* and α of the $\langle z \rangle \sim 3.04$ sample as given in Fig. 8 of their paper. As there are no errors reported for the $\langle z \rangle \sim 4.13$ sample we assume the same errors as for the $\langle z \rangle \sim 3.04$ sample. Therefore, the shaded region in Fig. 3.10 (middle panel) is probably a lower limit. For the luminosity function

in the FDF we use a redshift binning of $2.54 < z \leq 3.54$ (789 galaxies), and $3.70 < z \leq 4.56$ (144 galaxies) with the mean redshift of $\langle z \rangle \sim 3.04$ and $\langle z \rangle \sim 4.13$ to be as close as possible to Steidel *et al.* (1999)'s mean redshifts.

Fig. 3.10 (left and middle panel) shows that there is very good agreement between the results derived in the FDF and the luminosity function of Steidel *et al.* (1999) if we focus only on the luminosity function brighter than the limiting magnitudes (shaded regions). On the other hand, because of the depth of the FDF we can trace the luminosity function 2 magnitudes deeper and therefore give better constraints on the slope of the Schechter function. We show in Fig. 3.10 (right panel) the 1σ and 2σ confidence levels for M^* and α for a 3 parameter Schechter fit as derived from the FDF in the redshift interval $2.54 < z \leq 3.54$ (solid line) and $3.70 < z \leq 4.56$ (dotted line). The steep slope $\alpha = -1.6$ derived by Steidel *et al.* (1999) as marked by the horizontal dashed line can be excluded on a 2σ level.

Wilson *et al.* (2002) used galaxies selected in the restframe UV with spectroscopic redshifts to derive the luminosity function at 2500 \AA in 3 redshift bins: $0.2 < z \leq 0.5$ (U'-selected; 403 galaxies), $0.6 < z \leq 1.0$ (B-selected; 414 galaxies) and $1.0 < z \leq 1.5$ (V-selected; 518 galaxies). As the sample is not deep enough to constrain the slope of the Schechter function Wilson *et al.* (2002) used two fixed slopes of $\alpha = -1.0$ and $\alpha = -1.5$ to derive the best-fitting Schechter parameters. Since the errors of those parameters are not reported in the paper we can only make qualitative statements about the consistency of their and our luminosity functions: Fig. 3.11 shows that in the low and intermediate redshift bin there is reasonable agreement with our data, while in contrast to our result, the Schechter functions of Wilson *et al.* (2002) do not show a significant brightening of M^* in their highest redshift bin.

Comparison of the FDF luminosity function

with the Schechter functions derived in Sullivan *et al.* (2000), Wolf *et al.* (2003), Kashikawa *et al.* (2003), Poli *et al.* (2001), Iwata *et al.* (2003), Ouchi *et al.* (2004a), Blanton *et al.* (2001), Blanton *et al.* (2003), and Poli *et al.* (2003) are presented in Sect. 3.10.2. In general, we find good agreement at the bright end, where literature datasets are complete. Differences in the faint-end slope in some cases can be attributed to the shallower limiting magnitudes of most of the other surveys.

3.8 Comparison with model predictions

As discussed in Sect. 3.1, key physical processes are involved in shaping the bright and the faint-end of the galaxy luminosity function. Therefore, it is interesting to compare luminosity functions predicted by models with observational results to better constrain those processes. In this section we compare the B-band luminosity function in different redshift bins with model predictions of Kauffmann *et al.* (1999) and Menci *et al.* (2002).

Kauffmann et al. (1999):

In Fig. 3.12 we show the B-band luminosity function of the FDF together with the semi-analytic model predictions by Kauffmann *et al.* (1999)³ for the following redshifts: $\langle z \rangle \sim 0.20$, $\langle z \rangle \sim 0.62$, $\langle z \rangle \sim 1.05$, $\langle z \rangle \sim 1.46$, $\langle z \rangle \sim 2.12$, and $\langle z \rangle \sim 2.97$.

There seems to be reasonably good agreement between the models (solid lines) and the luminosity functions derived in the FDF up to redshift $\langle z \rangle \sim 2.12$. Of course at $z \approx 0$ the model is tuned to reproduce the data. At $z \sim 3$, the discrepancy increases as the model does not contain enough bright galaxies. Unfortunately, the models only predict luminosities for massive galaxies and, therefore, they do not predict galaxy number densities below M^* .

³The models were taken from:

http://www.mpa-garching.mpg.de/Virgo/data_download.html

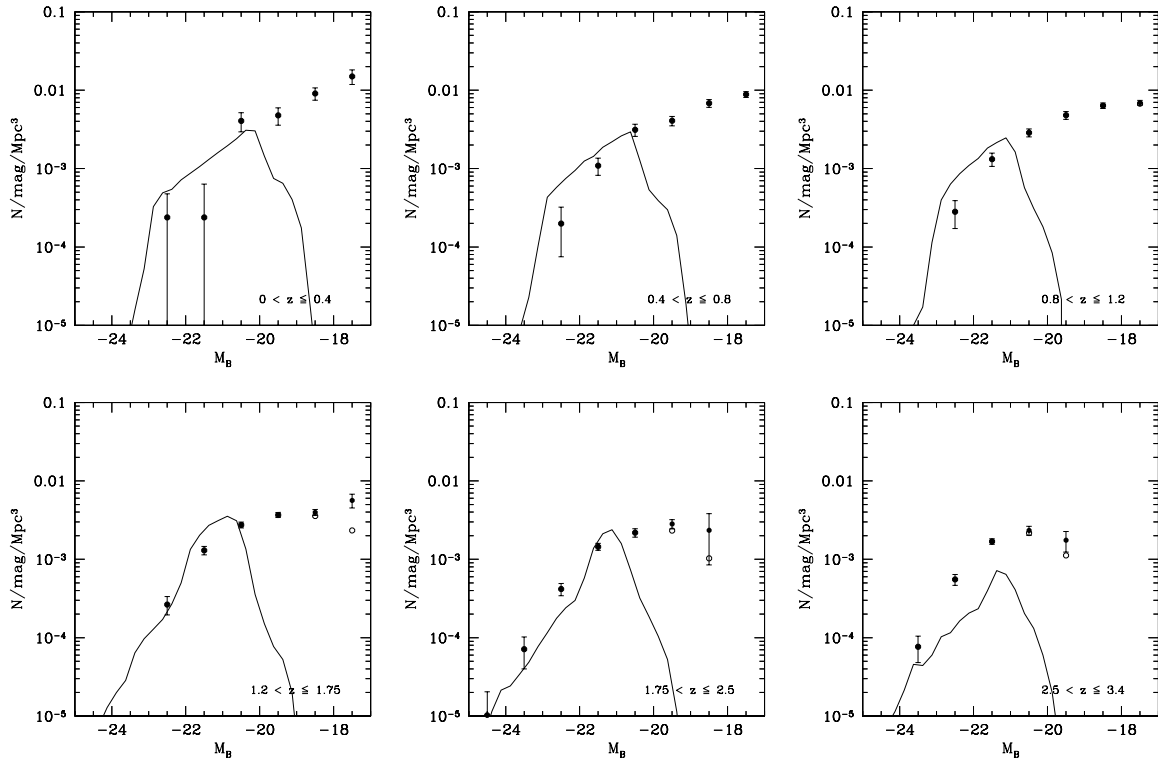


Figure 3.12: Comparison of the B-band luminosity function of the FDF with predictions based on *Kauffmann et al. (1999)* (solid line): $\langle z \rangle \sim 0.20$, $\langle z \rangle \sim 0.62$, $\langle z \rangle \sim 1.05$, $\langle z \rangle \sim 1.46$, $\langle z \rangle \sim 2.12$, and $\langle z \rangle \sim 2.97$ (from upper left to lower right panel). The filled (open) symbols show the luminosity function corrected (uncorrected) for V/V_{max} . The drops of the theoretical curves towards the faint end is caused by the limited mass resolution of the models, see *Kauffmann et al. (1999)* for details.

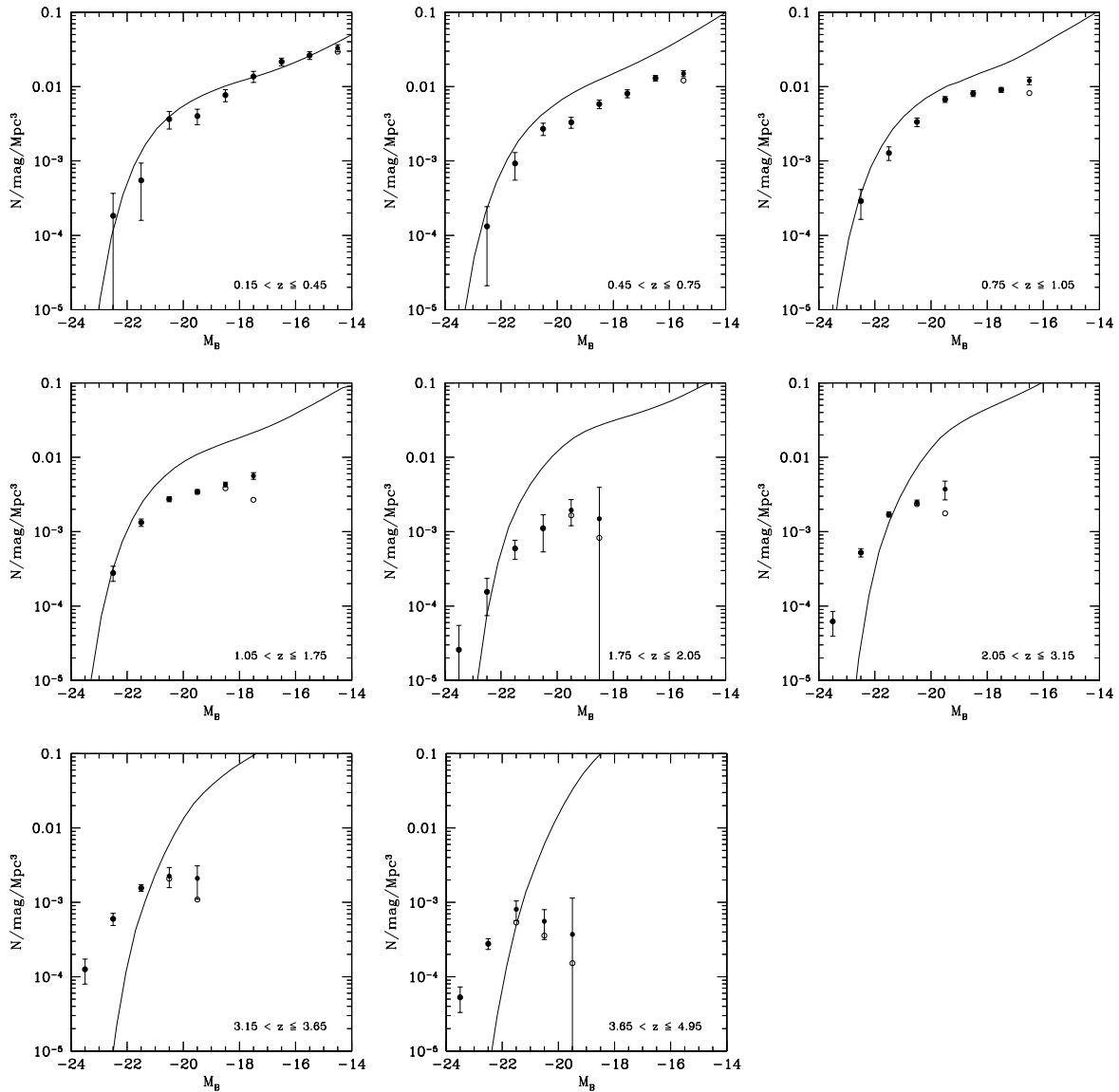


Figure 3.13: Comparison of the B-band luminosity function of the FDF with predictions based on the CDM model of *Menci et al. (2002)* (private communication; solid line): $\langle z \rangle \sim 0.3$, $\langle z \rangle \sim 0.6$, $\langle z \rangle \sim 0.9$, $\langle z \rangle \sim 1.4$, $\langle z \rangle \sim 1.9$, $\langle z \rangle \sim 2.6$, $\langle z \rangle \sim 3.4$, and $\langle z \rangle \sim 4.3$ (from upper left to lower right panel). The filled (open) symbols show the luminosity function corrected (uncorrected) for V/V_{max} .

Menci et al. (2002):

In Fig. 3.13 we compare the B-band luminosity functions of the FDF with the semi-analytic model by Menci *et al.* (2002) for the following redshifts: $\langle z \rangle \sim 0.3$, $\langle z \rangle \sim 0.6$, $\langle z \rangle \sim 0.9$, $\langle z \rangle \sim 1.4$, $\langle z \rangle \sim 1.9$, $\langle z \rangle \sim 2.6$, $\langle z \rangle \sim 3.4$, and $\langle z \rangle \sim 4.3$.

The agreement between the FDF data and the model in the lowest redshift bin $\langle z \rangle \sim 0.3$ is very good, but this is again expected (see comment above). Moreover, if in the comparison one focuses only on the higher luminosity bins considered by Kauffmann *et al.* (1999), similar acceptable agreement with the data is observed. However, at lower luminosities and higher redshifts, the galaxy density of the simulation is much higher than the observed one.

3.9 Summary and conclusions

We analyzed a sample of about 5600 I-band selected galaxies in the FORS Deep Field down to a limiting magnitude of $I = 26.8$ mag.

A comparison with the very deep K-selected catalog of Labbé *et al.* (2003) shows that more than 90 % of their objects are brighter than our limiting I-band magnitude. Therefore our scientific conclusions are not affected by this color bias.

Based on 9 filters we derived accurate photometric redshifts with $\Delta z / (z_{spec} + 1) \approx 0.03$ if compared with the spectroscopic sample (Noll *et al.*, 2004; Böhm *et al.*, 2004) of 362 objects. We calculated and presented the luminosity functions in the UV (1500 Å and 2800 Å), u', B, and g' bands in the redshift range $0.5 < z < 5.0$. The error budget of the luminosity functions includes the photometric redshift error as well as the Poissonian error.

The faint-end slope of the luminosity function does not show a large redshift evolution and is compatible within 2σ with a constant slope in

most of the redshift bins and wavelengths considered here. Furthermore, the slopes in the 1500 Å, 2800 Å, and u' bands are very similar but differ from the slopes in the g' and B bands. We derive a best fitting slope of $\alpha = -1.07 \pm 0.04$ for the combined 1500 Å, 2800 Å and u' bands and $\alpha = -1.25 \pm 0.03$ for the combined g' and B bands. We find no evidence for a very steep slope ($\alpha \leq -1.6$) at $z \sim 3$ and 1700 Å rest wavelength as reported by other authors (e.g., Steidel *et al.* 1999, Ouchi *et al.* 2004a). From our data we can exclude a slope of $\alpha \leq -1.6$ at redshift $\langle z \rangle \sim 3.0$ and $\langle z \rangle \sim 4.0$ at the 2σ level.

We investigate the evolution of M^* and ϕ^* by means of a redshift parameterization of the form $M^*(z) = M_0^* + a \ln(1+z)$ and $\phi^*(z) = \phi_0^*(1+z)^b$. We find a substantial brightening of M^* and a decrease of ϕ^* with redshift in all analyzed wavelengths. If we follow the evolution of the characteristic luminosity from $\langle z \rangle \sim 0.5$ to $\langle z \rangle \sim 5$, we find an increase of ~ 3.1 magnitudes in the UV, of ~ 2.6 magnitudes in the u' and of ~ 1.6 magnitudes in the g' and B band. Simultaneously the characteristic density decreases by about 80 % – 90 % in all analyzed wavebands.

Moreover, we compare the luminosity function derived in the FDF with previous observational datasets, mostly based on photometric results, and discuss discrepancies. In general, we find good agreement at the bright end, where their samples are complete. Differences in the faint-end slope in some cases can be attributed to the shallower limiting magnitudes of most of the other surveys. The only observations which reach the same limiting magnitudes as the FDF observations are those of Poli *et al.* (2001, 2003) and the K-selected sample of Kashikawa *et al.* (2003). The FDF results for the faint-end slope are in excellent agreement with those of Kashikawa *et al.* (2003) but the slope of the Schechter function favored by Poli *et al.* (2001, 2003) is steeper than we would expect from the FDF.

The semi-analytical models predict luminosity functions which describe (by construction) the data at low redshift quite well, but show growing

disagreement with increasing redshifts.

Acknowledgements:

We thank the referee, Dr. A. J. Bunker, for his careful reading of the manuscript and several constructive comments which helped us to improve the presentation of the results. Moreover, we thank Dr. N. Menci for providing an electronic version of his unpublished model calculation and for interesting remarks. AG thanks Dr. C. Maraston, J. Fliri and J. Thomas for stimulating discussions as well as A. Riffeser and C. A. Gössl for help dealing with their image reduction software. We acknowledge the support of the ESO Paranal staff during several observing runs. This work was supported by the *Deutsche Forschungsgemeinschaft*, *DFG*, SFB 375 (Astroteilchenphysik), SFB 439 (Galaxies in the young Universe) and Volkswagen Foundation (I/76 520).

3.10 Appendix of Chapter 3

3.10.1 Schechter parameters

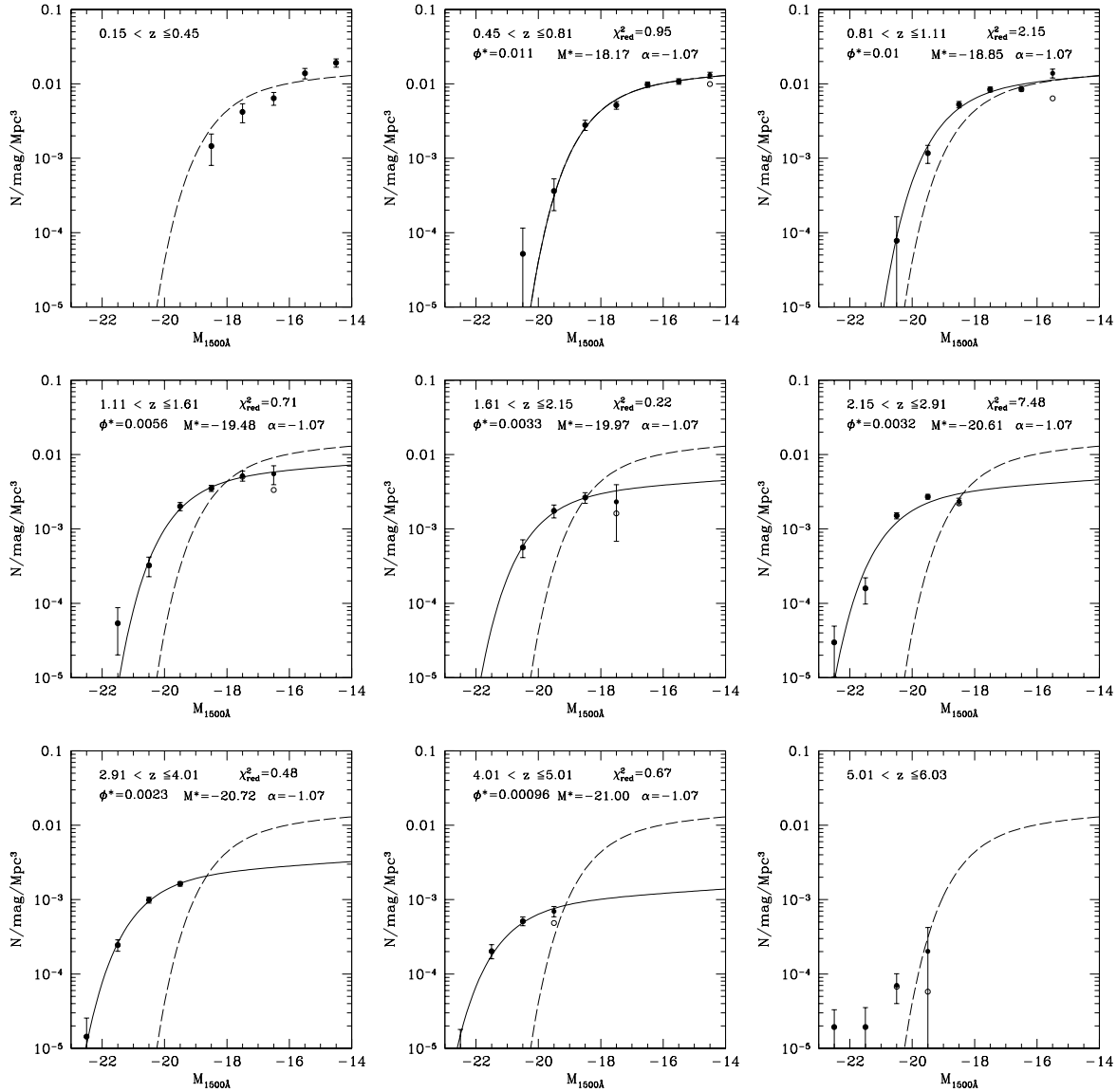


Figure 3.14: Luminosity functions at 1500 \AA from low redshift ($\langle z \rangle = 0.3$, upper left panel) to high redshift ($\langle z \rangle = 5.5$, lower right panel). The filled (open) symbols show the luminosity function corrected (uncorrected) for V/V_{max} . The fitted Schechter functions for a fixed slope α are shown as solid lines. Note that we only fit the luminosity functions from $\langle z \rangle = 0.6$ to $\langle z \rangle = 4.5$. The parameters of the Schechter functions can be found in Table 3.5. The Schechter fit for redshift $\langle z \rangle = 0.6$ is indicated as a dashed line in all panels.

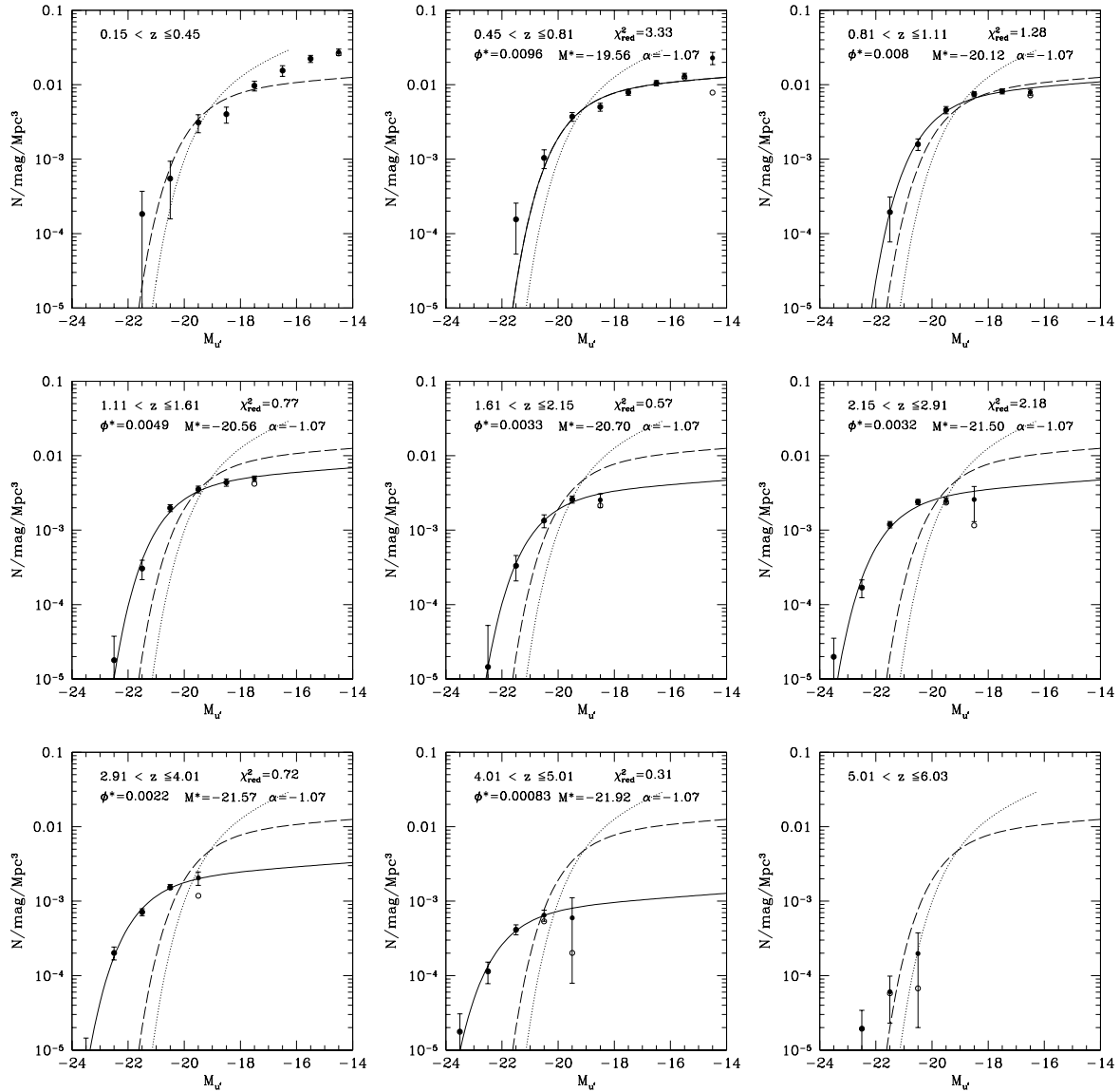


Figure 3.15: Luminosity functions in the u' -band from low redshift ($\langle z \rangle = 0.3$, upper left panel) to high redshift ($\langle z \rangle = 5.5$, lower right panel). The filled (open) symbols show the luminosity function corrected (uncorrected) for V/V_{max} . The fitted Schechter functions for a fixed slope α are shown as solid lines. Note that we only fit the luminosity functions from $\langle z \rangle = 0.6$ to $\langle z \rangle = 4.5$. The parameters of the Schechter functions can be found in Table 3.7. The dotted line represents the local u' -band luminosity function derived from the SDSS (Blanton *et al.*, 2001). The Schechter fit for redshift $\langle z \rangle = 0.6$ is indicated as a dashed line in all panels.

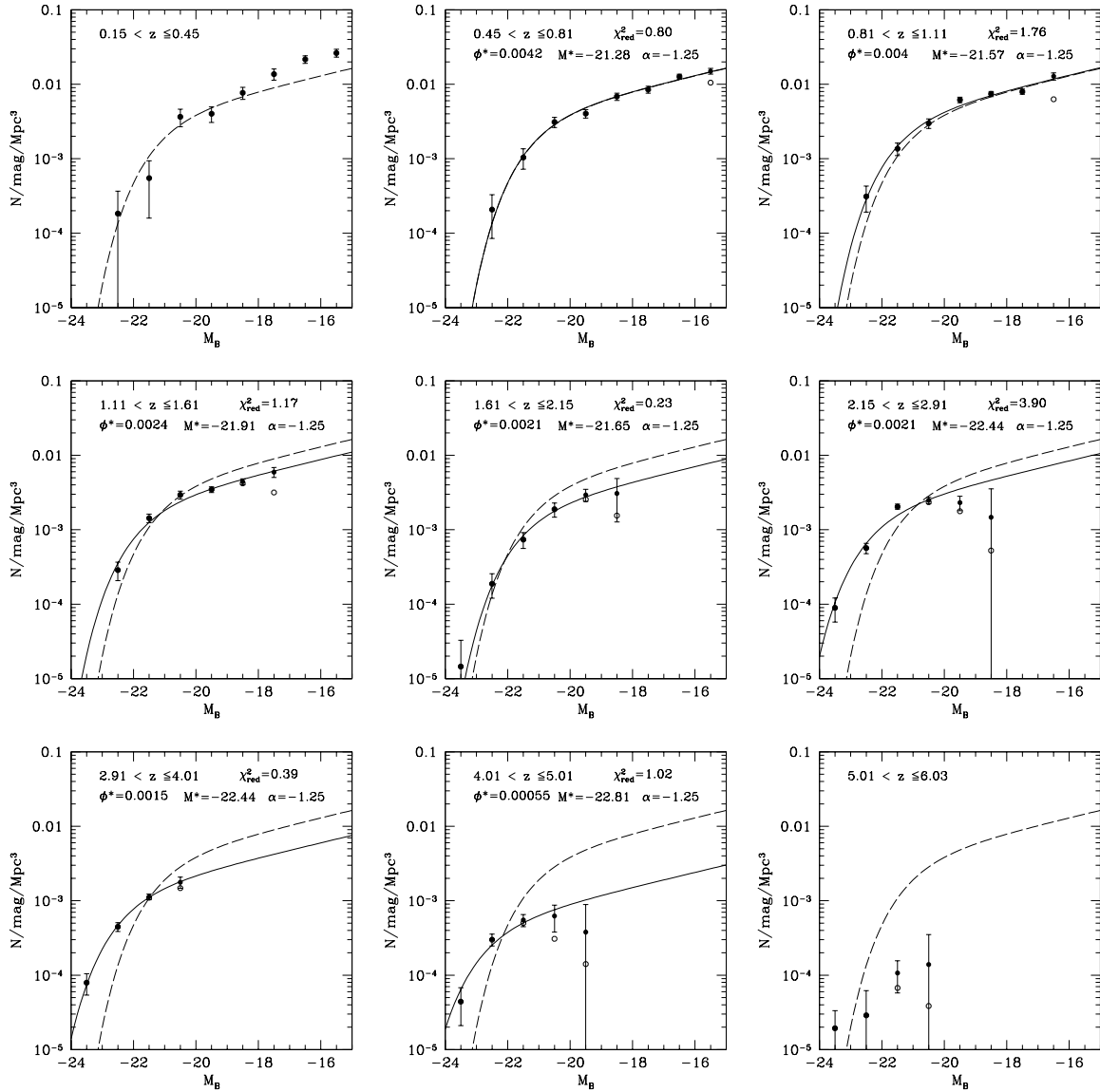


Figure 3.16: Luminosity functions in the B -band from low redshift ($\langle z \rangle = 0.3$, upper left panel) to high redshift ($\langle z \rangle = 5.5$, lower right panel). The filled (open) symbols show the luminosity function corrected (uncorrected) for V/V_{max} . The fitted Schechter functions for a fixed slope α are shown as solid lines. Note that we only fit the luminosity functions from $\langle z \rangle = 0.6$ to $\langle z \rangle = 4.5$. The parameters of the Schechter functions can be found in Table 3.9. The Schechter fit for redshift $\langle z \rangle = 0.6$ is indicated as a dashed line in all panels.

Table 3.5: Schechter function fit at 1500 Å

redshift interval	M^* (mag)	ϕ^* (Mpc^{-3})	α (fixed)
0.45 – 0.81	-18.17 +0.11 -0.11	0.0110 +0.0007 -0.0006	-1.07
0.81 – 1.11	-18.85 +0.10 -0.10	0.0103 +0.0006 -0.0006	-1.07
1.11 – 1.61	-19.48 +0.11 -0.11	0.0056 +0.0006 -0.0005	-1.07
1.61 – 2.15	-19.97 +0.22 -0.24	0.0033 +0.0006 -0.0006	-1.07
2.15 – 2.91	-20.61 +0.09 -0.09	0.0032 +0.0002 -0.0002	-1.07
2.91 – 4.01	-20.72 +0.09 -0.10	0.0023 +0.0002 -0.0002	-1.07
4.01 – 5.01	-21.00 +0.15 -0.11	0.0010 +0.0001 -0.0001	-1.07

Table 3.6: Schechter function fit at 2800 Å

redshift interval	M^* (mag)	ϕ^* (Mpc^{-3})	α (fixed)
0.45 – 0.81	-18.80 +0.15 -0.15	0.0104 +0.0007 -0.0007	-1.07
0.81 – 1.11	-19.52 +0.09 -0.10	0.0089 +0.0005 -0.0005	-1.07
1.11 – 1.61	-20.03 +0.09 -0.09	0.0053 +0.0004 -0.0004	-1.07
1.61 – 2.15	-20.43 +0.18 -0.17	0.0029 +0.0005 -0.0004	-1.07
2.15 – 2.91	-21.16 +0.09 -0.08	0.0030 +0.0002 -0.0002	-1.07
2.91 – 4.01	-21.19 +0.10 -0.08	0.0021 +0.0002 -0.0001	-1.07
4.01 – 5.01	-21.55 +0.17 -0.21	0.0009 +0.0001 -0.0001	-1.07

Table 3.7: Schechter function fit in the u'-band

redshift interval	M^* (mag)	ϕ^* (Mpc^{-3})	α (fixed)
0.45 – 0.81	-19.56 +0.16 -0.15	0.0096 +0.0006 -0.0006	-1.07
0.81 – 1.11	-20.12 +0.10 -0.10	0.0080 +0.0004 -0.0004	-1.07
1.11 – 1.61	-20.56 +0.08 -0.09	0.0049 +0.0003 -0.0003	-1.07
1.61 – 2.15	-20.70 +0.18 -0.16	0.0033 +0.0004 -0.0004	-1.07
2.15 – 2.91	-21.50 +0.08 -0.08	0.0032 +0.0002 -0.0002	-1.07
2.91 – 4.01	-21.57 +0.11 -0.10	0.0022 +0.0002 -0.0002	-1.07
4.01 – 5.01	-21.92 +0.24 -0.20	0.0008 +0.0002 -0.0001	-1.07

Table 3.8: Schechter function fit in the g'-band

redshift interval	M^* (mag)	ϕ^* (Mpc^{-3})	α (fixed)
0.45 – 0.81	-21.47 +0.20 -0.20	0.0042 +0.0003 -0.0003	-1.25
0.81 – 1.11	-21.72 +0.15 -0.15	0.0039 +0.0003 -0.0003	-1.25
1.11 – 1.61	-22.01 +0.14 -0.14	0.0026 +0.0002 -0.0002	-1.25
1.61 – 2.15	-21.82 +0.20 -0.20	0.0020 +0.0004 -0.0003	-1.25
2.15 – 2.91	-22.62 +0.13 -0.10	0.0020 +0.0002 -0.0002	-1.25
2.91 – 4.01	-22.51 +0.13 -0.14	0.0016 +0.0002 -0.0002	-1.25
4.01 – 5.01	-23.12 +0.22 -0.23	0.0005 +0.0001 -0.0001	-1.25

Table 3.9: Schechter function fit in the B-band

redshift interval	M^* (mag)	ϕ^* (Mpc^{-3})	α (fixed)
0.45 – 0.81	-21.28 +0.21 -0.18	0.0042 +0.0004 -0.0003	-1.25
0.81 – 1.11	-21.57 +0.15 -0.13	0.0040 +0.0003 -0.0002	-1.25
1.11 – 1.61	-21.91 +0.13 -0.13	0.0024 +0.0002 -0.0002	-1.25
1.61 – 2.15	-21.65 +0.22 -0.22	0.0021 +0.0004 -0.0004	-1.25
2.15 – 2.91	-22.44 +0.11 -0.09	0.0021 +0.0002 -0.0002	-1.25
2.91 – 4.01	-22.44 +0.15 -0.14	0.0015 +0.0002 -0.0002	-1.25
4.01 – 5.01	-22.81 +0.21 -0.25	0.0005 +0.0001 -0.0001	-1.25

3.10.2 Comparison with literature

In this appendix we compare the luminosity functions derived in the FDF with the results of further publications as introduced in Sect. 3.7. The filled (open) circles show the completeness-corrected (uncorrected) luminosity function as derived in the FDF in the redshift bin listed in the lower right corner. The solid lines represent the Schechter function given in the different papers transformed to our cosmology. To visualize the errors associated to this Schechter function we perform a Monte-Carlo simulation using the errors of the Schechter parameters reported in the specific paper (see Sect. 3.7 for more details). As the errors for all three Schechter parameters (ΔM^* , $\Delta \phi^*$, and $\Delta \alpha$) are not always given in the paper, we denote in the caption the errors used to perform the simulation. The regions wherein 68.8 % of the realizations lie are shown as shaded regions in the plots and correspond roughly to the 1σ error due to the Schechter errors reported in the figure captions. Moreover the cut-off of the shaded region marks the limiting magnitude of the survey we compare with.

UV bands

Sullivan et al. (2000):

Although the volume of the FDF at low redshift is rather small, and therefore is not well suited to properly sample the bright end of the Schechter function, we compare for completeness in Fig. 3.17 our luminosity function also with the luminosity function derived in Sullivan *et al.* (2000). Their sample contains 433 UV-selected sources within an area of 2.2 deg^2 . 273 of these objects are galaxies and cover the redshift range $z \simeq 0 - 0.4$. The solid line in Fig. 3.17 represents the luminosity function at 2000 \AA from Sullivan *et al.* (2000) whereas the filled circles show our V/V_{max} corrected luminosity function derived at $0.15 < z \leq 0.4$. Despite the small volume, the I-selected catalog and the extrapolated 2000 \AA luminosity function (see above) there is a general agreement with only

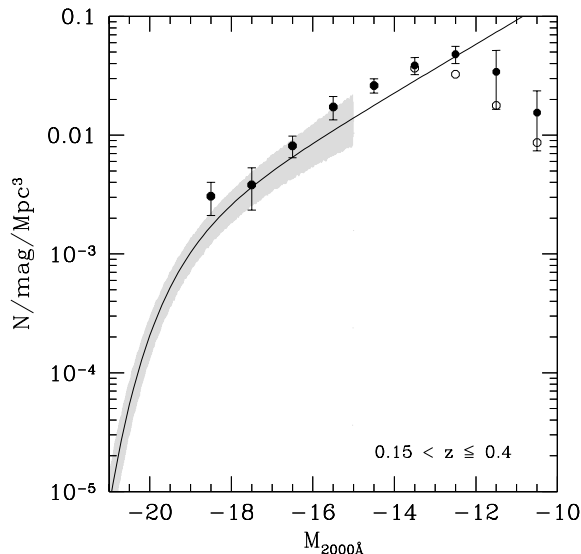


Figure 3.17: Comparison of the luminosity function at 2000 \AA of the FDF with the Schechter function derived in Sullivan *et al.* (2000) ($z \simeq 0 - 0.4$). The shaded region is based on ΔM^* , $\Delta \phi^*$, and $\Delta \alpha$, where the cut-off at low luminosity indicates the limiting magnitude of the sample.

small systematic offsets (probably also due to a known cluster at $z \sim 0.33$ (Noll *et al.*, 2004)). This is an additional confirmation of the validity of our technique to derive the luminosity function as described in Sect. 3.5.1.

Wolf et al. (2003):

In Fig. 3.18 we compare the luminosity function at 2800 \AA of the FDF with the R-band selected luminosity function derived in the COMBO-17 survey (Wolf *et al.*, 2003) for different redshift bins: $0.2 - 0.6$, $0.6 - 0.8$, $0.8 - 1.0$, $1.0 - 1.2$. Because of the limited sample size of the FDF at low redshift we could not use the same local redshift binning as Wolf *et al.* (2003). We compare therefore in Fig. 3.18 (upper left panel) the COMBO17 Schechter function at $\langle z \rangle \sim 0.3$ (light gray) and $\langle z \rangle \sim 0.5$ (dark gray) with the

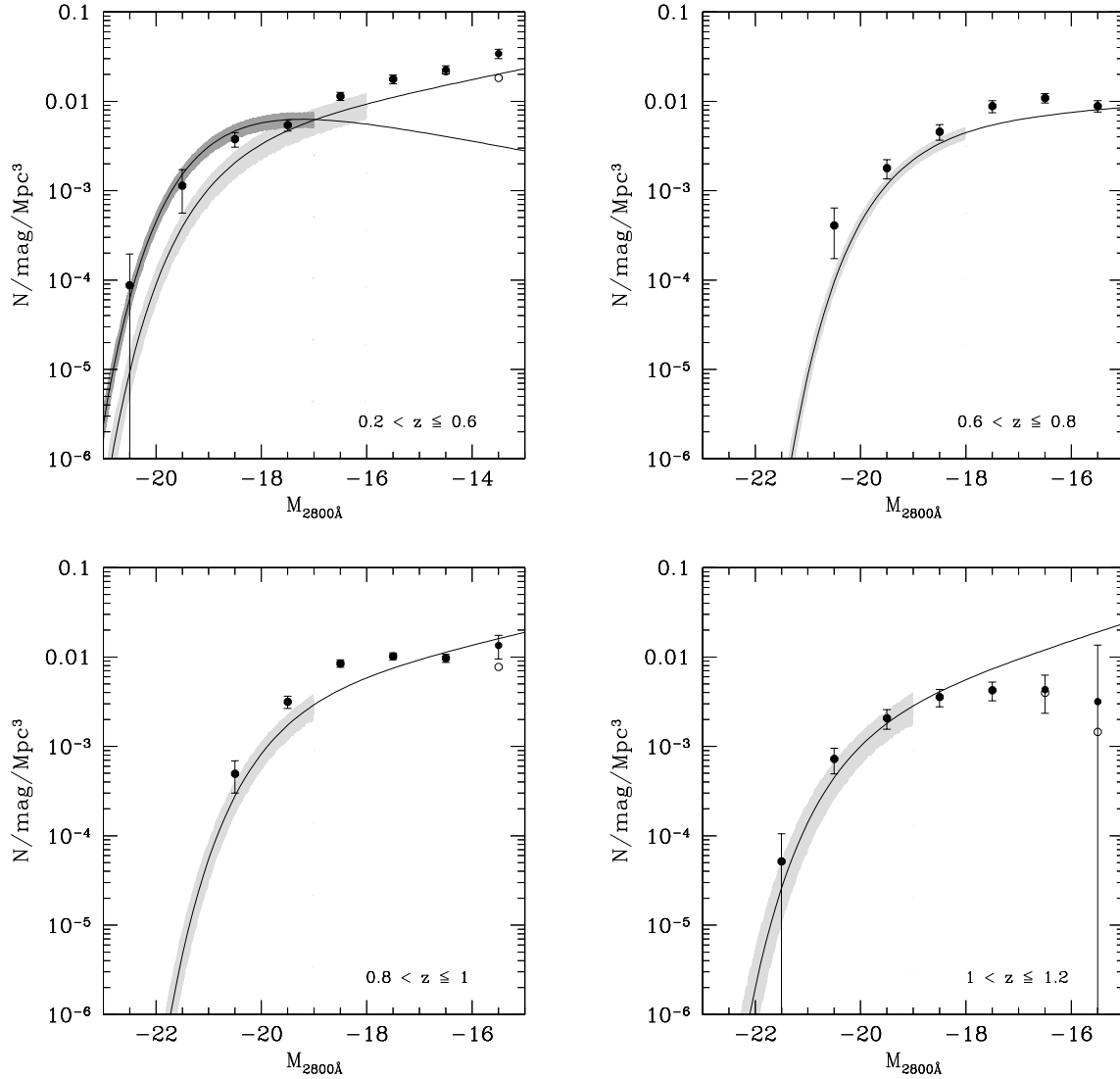


Figure 3.18: Comparison of the luminosity function at 2800 \AA of the FDF with the Schechter function derived in *Wolf et al. (2003)*: $0.2 < z \leq 0.4$ (upper left panel, light gray), $0.4 < z \leq 0.6$ (upper left panel, dark grey), $0.6 < z \leq 0.8$ (upper right panel), $0.8 < z \leq 1.0$ (lower left panel), $1.0 < z \leq 1.2$ (lower right panel). The shaded regions of all plots are based on ΔM^* , $\Delta \phi^*$, and $\Delta \alpha$, where the cut-off at low luminosity indicates the limiting magnitude of the sample.

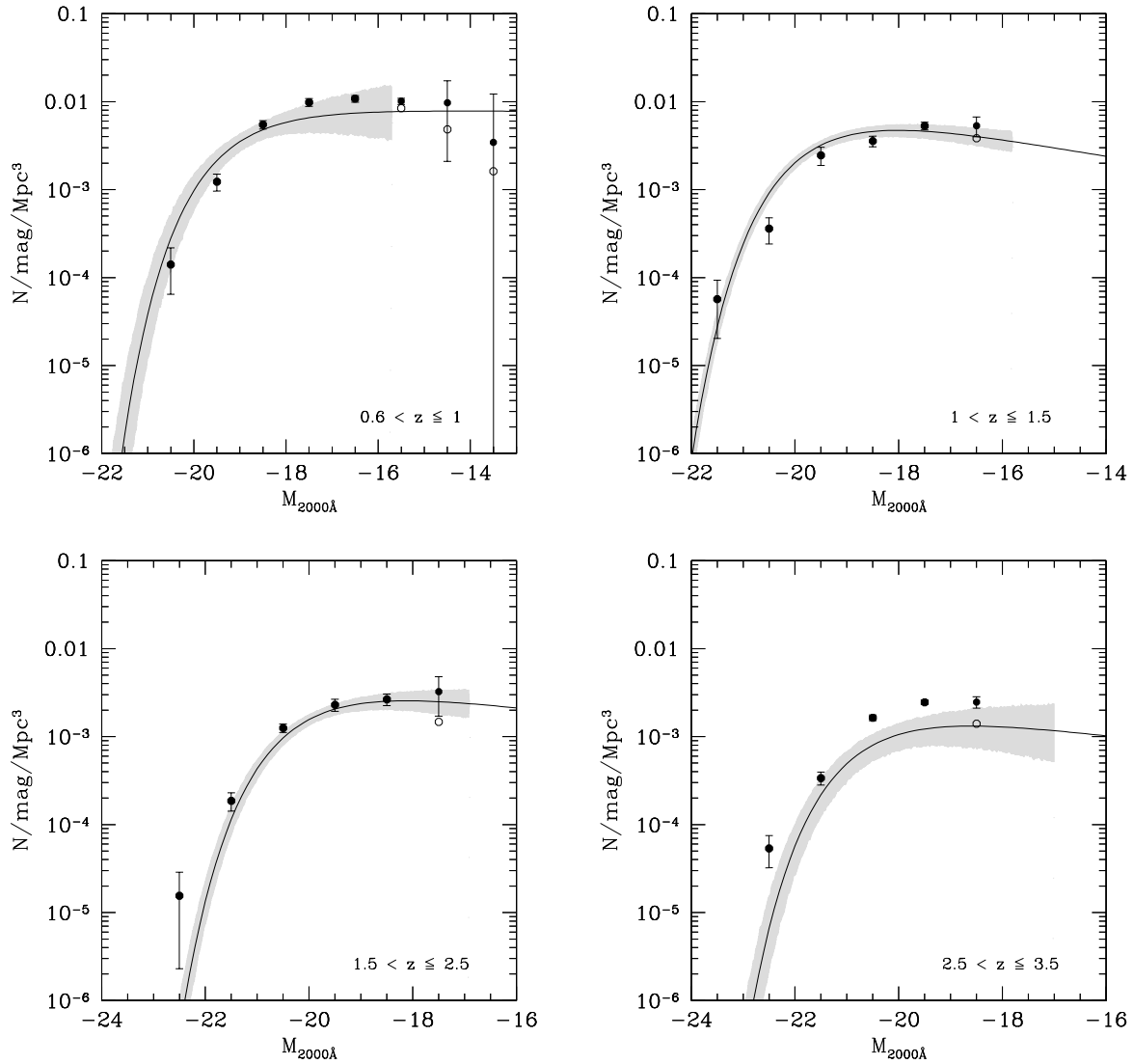


Figure 3.19: Comparison of the luminosity function at 2000 \AA of the FDF with the Schechter function derived in *Kashikawa et al. (2003)*: $0.6 < z \leq 1.0$ (upper left panel), $1.0 < z \leq 1.5$ (upper right panel), $1.5 < z \leq 2.5$ (lower left panel), $2.5 < z \leq 3.5$ (lower right panel). The shaded regions of all plots are based on ΔM^* , $\Delta \phi^*$, and $\Delta \alpha$, where the cut-off at low luminosity indicates the limiting magnitude of the sample.

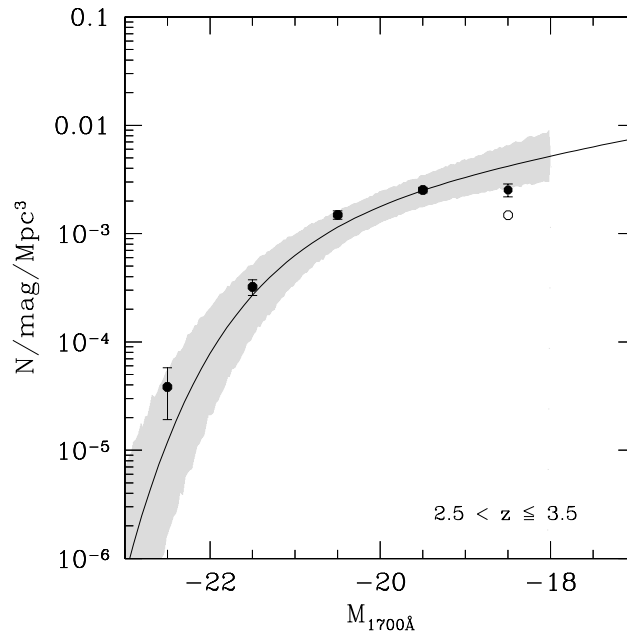


Figure 3.20: Comparison of the luminosity function at 1700 \AA of the FDF with the Schechter function derived in *Poli et al. (2001)* ($2.50 < z \leq 3.50$). The shaded region is based only on ΔM^* , and $\Delta \alpha$, where the cut-off at low luminosity indicates the limiting magnitude of the sample.

FDF luminosity function derived at $0.2 < z \leq 0.6$. There is an overall good agreement between the FDF data and the COMBO-17 survey at all redshifts under investigation if we compare only the magnitude range in common to both surveys (shaded region). Nevertheless the number density of the FDF seems to be slightly higher which most probably can be attributed to cosmic variance. The *Wolf et al. (2003)* team derived the faint-end slope from relatively shallow data which have only a limited sensitivity for the faint-end slope. Thus, the disagreement between the much deeper FDF data and the *Wolf et al. (2003)* results at $z \sim 0.5$ and for $z > 1$ does not come as a surprise.

Kashikawa et al. (2003):

In Fig. 3.19 we compare our luminosity function with the K-band selected 2000 \AA luminosity function of *Kashikawa et al. (2003)* derived in the Subaru Deep Survey. They used photometric

redshifts to determine the distance for 439 field galaxies. There is a good overall agreement of the luminosity functions in the redshift bins $0.6 < z \leq 1.0$, $1.0 < z \leq 1.5$, $1.5 < z \leq 2.5$. Only in the highest redshift bin ($2.5 < z \leq 3.5$) is the number density derived in *Kashikawa et al. (2003)* lower by a factor of about 2 when compared with the FDF.

Poli et al. (2001):

Poli et al. (2001) combined three pencil beam surveys as the HDFN, the HDFS and the New Technology Telescope Deep Field (*Arnouts et al., 1999b*) reducing the influence of cosmic variance and derived the 1700 \AA luminosity function at $2.5 < z \leq 3.5$. In Fig. 3.20 we compare the result with the luminosity function in the FDF. There is very good agreement although the slope of the Schechter function ($\alpha = -1.37$) is slightly steeper than we would expect from the FDF.

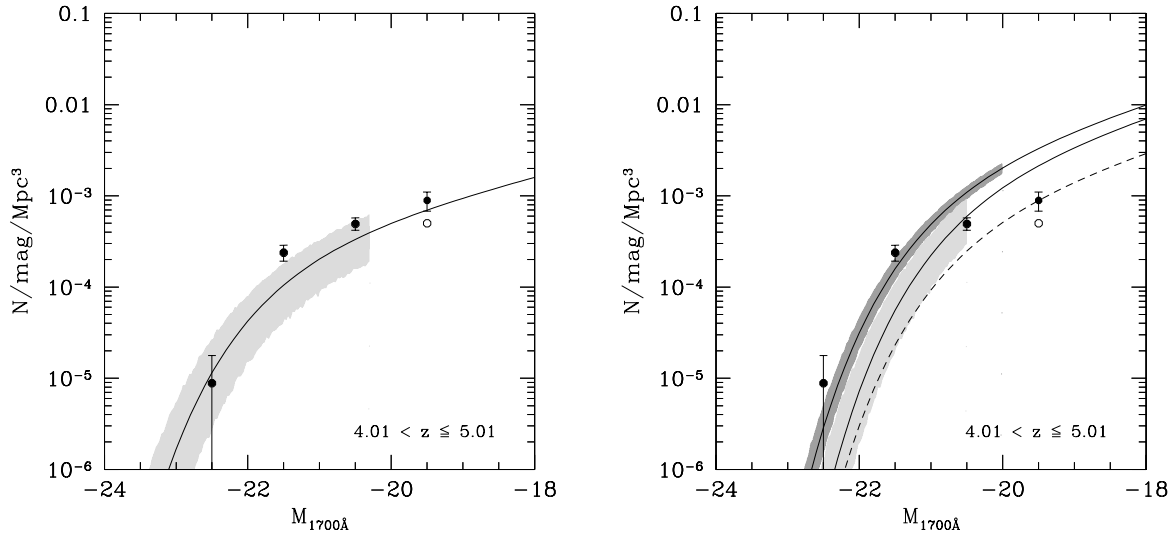


Figure 3.21: Left panel: Comparison of the luminosity function at 1700 \AA of the FDF with the Schechter function derived in *Iwata et al. (2003)* ($z \sim 5$). The shaded region is based only on ΔM^* , and $\Delta \phi^*$. Right panel: Comparison of the luminosity function at 1700 \AA of the FDF with the Schechter functions derived in *Ouchi et al. (2004a)*: $z = 4.0 \pm 0.5$ (dark shaded), $z = 4.7 \pm 0.5$ (light shaded), and $z = 4.9 \pm 0.3$ (not shaded; dashed line). Both shaded regions are based only on ΔM^* , and $\Delta \phi^*$, where the cut-off at low luminosity indicates the limiting magnitude of the sample.

Iwata et al. (2003):

Iwata et al. (2003) analyzed about 300 galaxies in a 575 square-arcmin field detected in the I and z band at redshift $z \sim 5$, selected by means of the Lyman-break technique. They derived the luminosity function at 1700 \AA statistically. We analyze Table 3 of *Iwata et al. (2003)* with the same method as described in Sect. 3.5.1 to get approximate errors for M^* and ϕ^* for a fixed slope of $\alpha = -1.5$ (as given in the paper). From these ΔM^* and $\Delta \phi^*$ we calculate the shaded region of Fig. 3.21 (left panel). Fig. 3.21 (left panel) compares the luminosity function of *Iwata et al. (2003)* with the luminosity function of the FDF derived at $4.01 < z \leq 5.01$. Although the number density of *Iwata et al. (2003)* at $z \sim 5$ seems to be slightly lower than the number density derived in the FDF at $\langle z \rangle \sim 4.5$ the overall agreement is rather good. On the other hand, part of this decrease in density may also be due to intrinsic evolution between redshift $\langle z \rangle \sim 4.5$ and

$\langle z \rangle \sim 5.0$. According to our evolution model as derived in Sect. 3.6 we would expect a decrease of ϕ^* of about 15 %.

SDSS bands (u' , g' , $^{0.1}u$, $^{0.1}g$)

In this section we want to compare the luminosity function in the FDF with the one from the SDSS.

In Fig. 3.22 (left panel) and Fig. 3.23 (left panel) we show the luminosity function derived in *Blanton et al. (2001)* for $z \sim 0.1$ in the u' and g' band, respectively, as light shaded regions. To make a more appropriate comparison between our ‘local’ results derived at $0.15 < z \leq 0.45$, we evolve the Schechter function of *Blanton et al. (2001)* to $\langle z \rangle \sim 0.3$ according to our evolutionary model described in Sect. 3.6. We use for the u' -band the parameter $a = -1.80$ and $b = -1.70$ whereas for the g' -band we use $a = -1.08$ and $b = -1.29$. The evolved Schechter function is

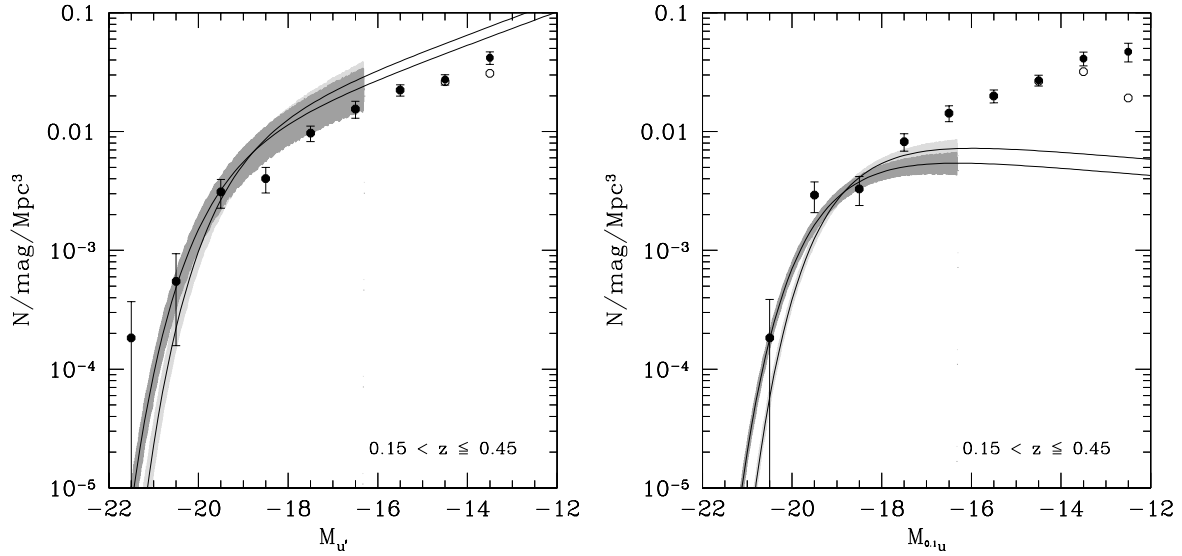


Figure 3.22: Left panel: Comparison of the u' -band luminosity function of the FDF with the Schechter function derived in *Blanton et al. (2001)* at $z \sim 0.1$ (light shaded). The dark shaded region shows the Schechter function of *Blanton et al. (2001)* evolved according to our evolutionary model described in Sect. 3.6 to redshift $z \sim 0.3$. The shaded regions are based on ΔM^* , $\Delta \phi^*$, and $\Delta \alpha$. Right panel: Comparison of the $^{0.1}u$ -band luminosity function of the FDF with the Schechter function derived in *Blanton et al. (2003)* at $z \sim 0.1$ (light shaded). The dark shaded region shows the Schechter function of *Blanton et al. (2003)* evolved according to our evolutionary model described in Sect. 3.6 to redshift $z \sim 0.3$. The shaded regions are based on ΔM^* , $\Delta \phi^*$, and $\Delta \alpha$, where the cut-off at low luminosity indicates the limiting magnitude of the sample.

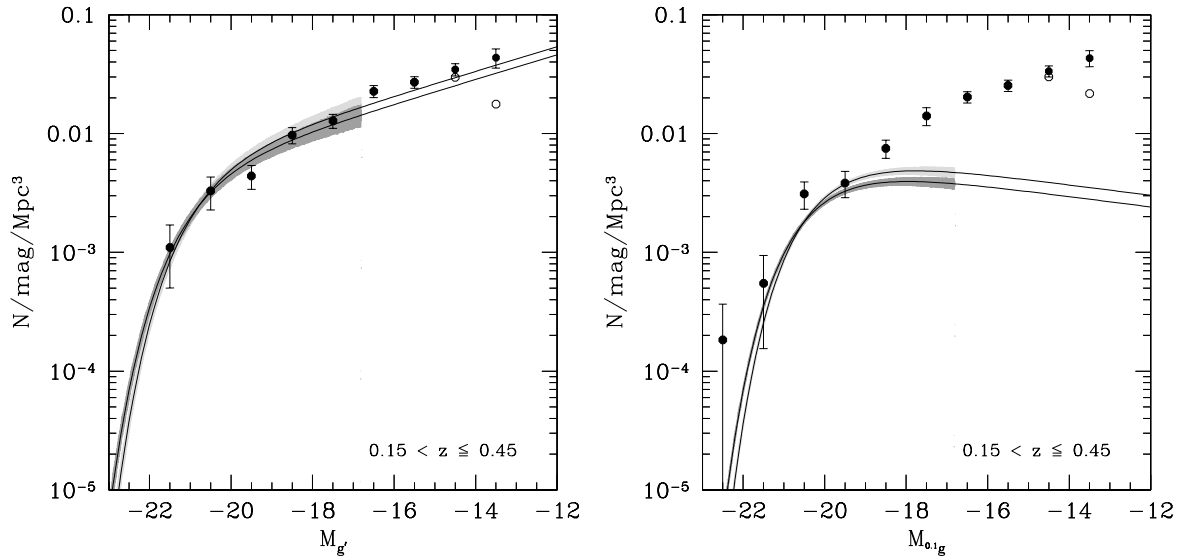


Figure 3.23: Left panel: Comparison of the g' -band luminosity function of the FDF with the Schechter function derived in *Blanton et al. (2001)* at $z \sim 0.1$ (light shaded). The dark shaded region shows the Schechter function of *Blanton et al. (2001)* evolved according to our evolutionary model described in Sect. 3.6 to redshift $z \sim 0.3$. The shaded regions are based on ΔM^* , $\Delta \phi^*$, and $\Delta \alpha$. Right panel: Comparison of the $^{0.1}g$ -band luminosity function of the FDF with the Schechter function derived in *Blanton et al. (2003)* at $z \sim 0.1$ (light shaded). The dark shaded region shows the Schechter function of *Blanton et al. (2003)* evolved according to our evolutionary model described in Sect. 3.6 to redshift $z \sim 0.3$. The shaded regions are based on ΔM^* , $\Delta \phi^*$, and $\Delta \alpha$, where the cut-off at low luminosity indicates the limiting magnitude of the sample.

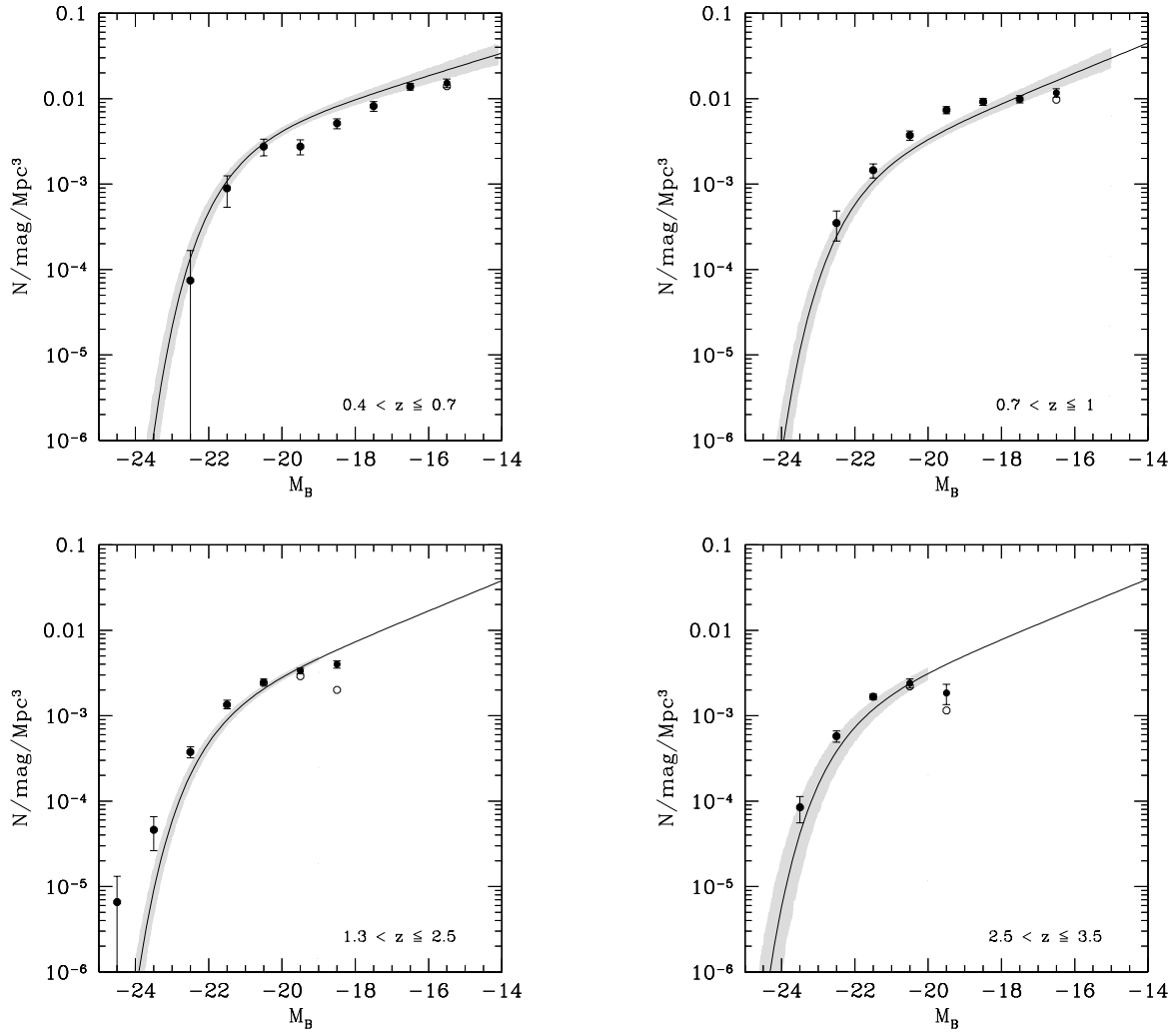


Figure 3.24: Comparison of the B-band luminosity function of the FDF with the Schechter function derived in *Poli et al. (2003)*: $0.4 < z \leq 0.7$ (upper left panel), $0.7 < z \leq 1.0$ (upper right panel), $1.3 < z \leq 2.5$ (lower left panel), and $2.5 < z \leq 3.5$ (lower right panel). The shaded region is based only on ΔM^* , and $\Delta \alpha$ for $0.4 < z \leq 0.7$, and $0.7 < z \leq 1.0$, whereas for the $1.3 < z \leq 2.5$, and $2.5 < z \leq 3.5$ the shaded region is based only on ΔM^* , where the cut-off at low luminosity indicates the limiting magnitude of the sample.

shown as dark shaded region in Fig. 3.22 (left panel) and Fig. 3.23 (left panel) for the u' and g' band, respectively. Despite the small volume of the FDF in the local redshift bin, the agreement is very good in both bands and especially in the g'-band. We therefore conclude that there is no hint of a possible systematic offset between the two datasets.

In Fig. 3.22 (right panel) and Fig. 3.23 (right panel) we also show the luminosity function derived in Blanton *et al.* (2003) for the blue-shifted filter $^{0.1}u$ and $^{0.1}g$. Again, the light shaded region represents the $\langle z \rangle \sim 0.1$ luminosity function whereas the dark shaded region shows the luminosity function evolved to $\langle z \rangle \sim 0.3$. We use the same evolution parameter as derived for u' and g'. The approach used by Blanton *et al.* (2003) differs from those used in all other studies, including ours and the previous SDSS (Blanton *et al.*, 2001) results. It is therefore beyond the scope of the paper to explain the discrepancies.

B-band

Poli et al. (2003):

Poli *et al.* (2003) analyzed 1541 I-selected and 138 K-selected galaxies to construct the B-band luminosity function up to redshift $\langle z \rangle \sim 3$. A comparison between the luminosity function of Poli *et al.* (2003) and the FDF is shown in Fig. 3.24 for the redshift bins $0.4 < z \leq 0.7$ (upper left panel), $0.7 < z \leq 1.0$ (upper right panel), $1.3 < z \leq 2.5$ (lower left panel) and $2.5 < z \leq 3.5$ (lower right panel).

In neither of the redshift bins an error for ϕ^* is reported in the paper and therefore could not be included in the simulation of the shaded region. For the two lower redshift bins ($0.4 < z \leq 0.7$ and $0.7 < z \leq 1.0$) the shaded region is based on ΔM^* and $\Delta \phi^*$ whereas in the high redshift bins ($1.3 < z \leq 2.5$ and $2.5 < z \leq 3.5$) the shown error of the Schechter function (shaded region) is based only on ΔM^* . If this is taken into account, the results of Poli *et al.* (2003) are in good agreement

with the FDF, but again, the slope of the Schechter function is too steep when compared with the FDF luminosity function. On the other hand the brightening of M^* with redshift is present in both samples.

3.10.3 Confidence levels for the slope

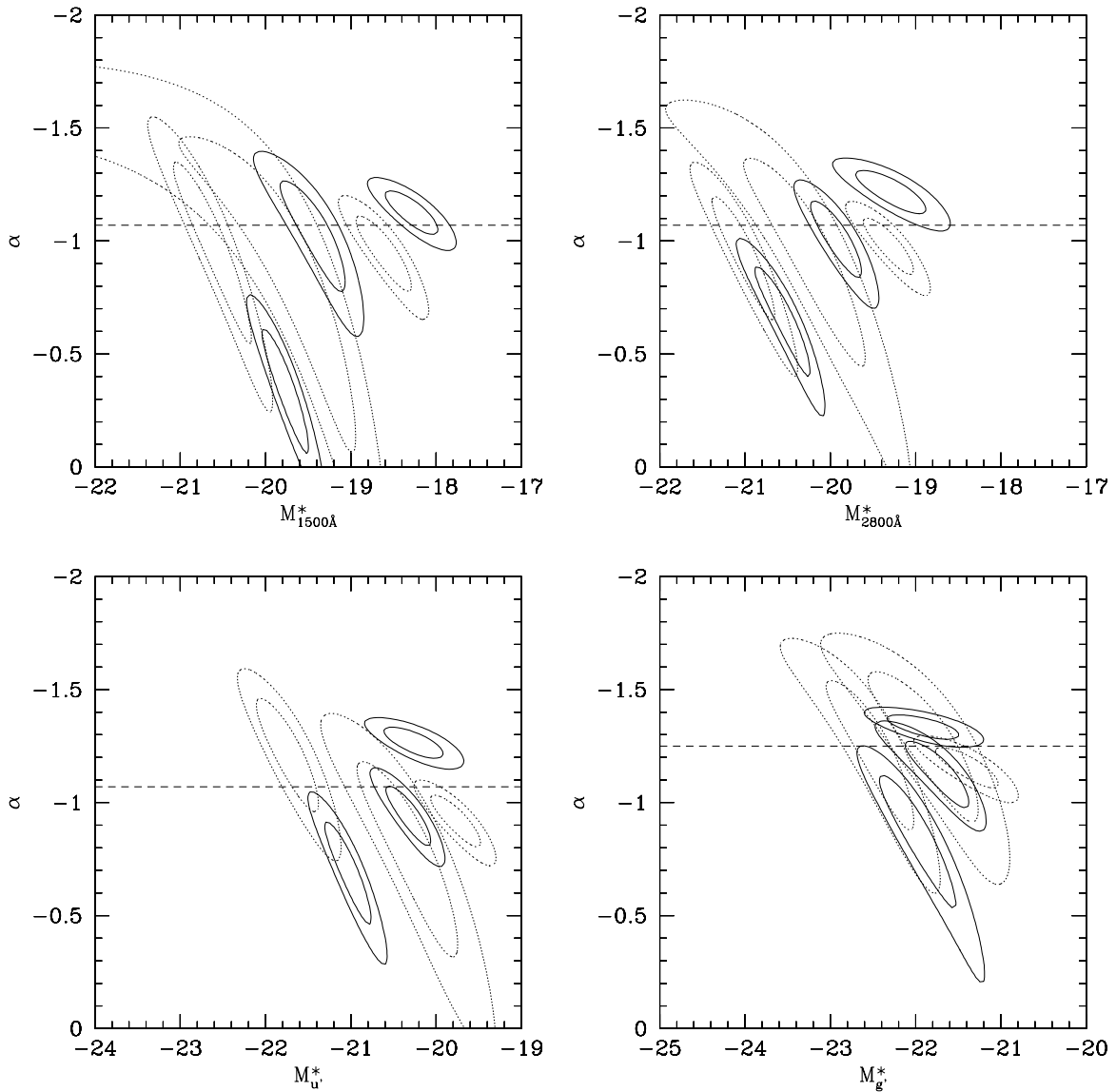


Figure 3.25: 1σ and 2σ confidence levels in Schechter parameter space. A Schechter function with three free parameters M^* , ϕ^* , and α has been fitted to the luminosity function at 1500 \AA (*upper left panel*), 2800 \AA (*upper right panel*), u' (*lower left panel*) and g' -band (*lower right panel*) and projected to the $M^* - \alpha$ plane. The various contours in each panel correspond to the different redshift bins, ranging from $\langle z \rangle = 0.6$ (low luminosity) to $\langle z \rangle = 3.5$ (high luminosity). We alternate continuous and dotted lines for clarity. The dashed line marks the fixed slope ($\alpha(z) = \text{const.}$) used to derive the luminosity functions in the different wavebands (see Table 3.3 lower part).

Chapter 4

The evolution of the luminosity functions in the FORS Deep Field from low to high redshift: II. The red bands

4.1 Introduction

While galaxy luminosities measured in the ultraviolet are sensitive to the energy output of hot, short-living O and B type stars and therefore to the instantaneous star formation rate (see Chap. 3 and Chap. 6), the optical luminosities provide constraints on more evolved stellar populations (Hunter *et al.*, 1982). To constrain the free parameters of theoretical models (e.g. SAMs or SPH models) it is very important to compare their theoretical predictions with observations. Moreover, this should be done simultaneously for all wavebands (UV, optical, NIR) and for different redshift slices as different stellar populations are involved in generating the flux in the different bands. The FDF therefore provides a unique testing ground for model predictions as it allows to derive precise measurements from the UV to the z' -band up to high redshift in a very homogeneous way.

In the following chapter we extend the measurements of the blue luminosity functions of Chap. 3 to the red r' , i' , and z' bands. In Sect. 4.2 we derive the LF for the red bands and show the best fitting Schechter parameters. In Sect. 4.3 we use the same parameterization already introduced in Sect. 3.6 to quantify the redshift evolution of the LFs. A comparison with the luminosity functions of other surveys as well as with model predictions is shown in Sect. 4.4 and in Sect. 4.5, respectively.

We use AB magnitudes and adopt a Λ cosmology throughout this chapter with $\Omega_M = 0.3$, $\Omega_\Lambda = 0.7$, and $H_0 = 70 \text{ km s}^{-1} \text{ Mpc}^{-1}$.

4.2 Luminosity functions in the r' , i' , and z' bands

The method to derive absolute magnitudes of the galaxies is the same as described in Chap. 3: We compute the absolute magnitudes of our galaxies using the I-band selected catalog as described in Sect. 3.2 and the photometric redshifts described in Sect. 3.4. To derive the absolute magnitude for a given band we use the best fitting SED as determined by the photometric redshift code, thus reducing possible systematic errors which could be introduced by using K-corrections applied to a single observed magnitude. To account for the fact that some fainter galaxies are not visible in the

Table 4.1: Galaxy distribution in the FDF for the redshift intervals used for computing the luminosity functions. Note that we derive the luminosity function in all redshift bins, but exclude the lowest ($z < 0.45$) and highest redshift bin ($z > 3.81$) from our analysis of the luminosity function evolution, since the lowest redshift bin corresponds to too small a volume while the $z > 3.81$ bin suffers from extrapolation errors.

redshift interval	number of galaxies	fraction of galaxies
0.00 - 0.45	808	14.54 %
0.45 - 0.85	1109	19.95 %
0.85 - 1.31	1029	18.51 %
1.31 - 1.91	880	15.83 %
1.91 - 2.61	816	14.68 %
2.61 - 3.81	718	12.92 %
> 3.81	196	3.53 %
unknown	2	0.04 %

whole survey volume we perform a V/V_{max} (Schmidt, 1968) correction. The errors of the luminosity functions are calculated by means of Monte-Carlo simulations and include the photometric redshift error of every single galaxy as well as the statistical error (Poissonian error).

To derive precise Schechter parameters we limit our analysis of the luminosity function to the bin where the V/V_{max} begins to contribute at most by a factor of 3 but we also show the uncorrected luminosity function in the various plots as open circles. The redshift binning was chosen such that we have good statistics in every redshift bin and that the influence of redshift clustering was minimized. In order to have good statistics also on the bright end of the luminosity function we had to slightly change some of the redshift bins when compared to the binning used in Chap. 3. The new redshift binning and the number of galaxies in every bin is shown in Table 4.1. As can be seen from Table 4.1 most of the results we are going to discuss below are based on 700 – 1000 galaxies per redshift bin.

4.2.1 The slope of the luminosity function

We first investigate the redshift evolution of the faint-end slope α of the luminosity function by fitting all three parameters of the Schechter function (M^* , ϕ^* , and α). The best fitting α and the corresponding 1σ errors for all wavebands and redshifts are listed in Table 4.2. Like for the blue bands, we find also in the red bands only marginal evidence for a change of α with redshift. Under the assumption that α does not depend on redshift we obtain as best error-weighted values for all redshifts between $\langle z \rangle \sim 0.65$ and $\langle z \rangle \sim 3.2$ the values given in Table 4.3 (upper part). Please note that for the highest redshift bin the restframe filters analyzed in this chapter are not any more bracketed by our observer frame J and K bands. On the other side, excluding the highest bin $\langle z \rangle \sim 3.2$ changes the fitting values for the slope α only marginally ($\Delta\alpha \approx 0.02$). As the slopes in all bands are very similar, we combine the data of Table 4.3 (upper part) and derive a combined slope of $\alpha_{r'&i'&z'} = -1.33 \pm 0.03$. The result is listed in Table 4.3 (lower part). Almost all of the single slopes listed in Table 4.2 are compatible within $1\sigma - 2\sigma$ with the combined slope $\alpha = -1.33 \pm 0.03$. Therefore, we fixed the slope to this value

Table 4.2: Slope of the luminosity function for all wavelengths and all redshifts as derived from 3-parameter Schechter fits.

z	α (r')	α (i')	α (z')
[0.45, 0.85]	-1.37 (+0.04 -0.04)	-1.37 (+0.04 -0.03)	-1.39 (+0.04 -0.04)
[0.85, 1.31]	-1.25 (+0.06 -0.04)	-1.27 (+0.06 -0.05)	-1.34 (+0.06 -0.04)
[1.31, 1.91]	-1.30 (+0.16 -0.09)	-1.50 (+0.13 -0.10)	-1.45 (+0.12 -0.09)
[1.91, 2.61]	-1.01 (+0.15 -0.14)	-1.03 (+0.17 -0.14)	-0.97 (+0.17 -0.12)
[2.61, 3.81]	-0.98 (+0.17 -0.17)	-1.03 (+0.15 -0.13)	-1.01 (+0.15 -0.13)

Table 4.3: Slope α of the luminosity functions for the different wavebands as determined from an error-weighted fit to the data in Table 4.2 under the assumption that $\alpha(z) = \text{const.}$ (upper part). In the lower part of the Table we show the best values of α after combining all bands.

filter	$\alpha(z) = \text{const}$
r'	-1.30 ± 0.05
i'	-1.33 ± 0.05
z'	-1.35 ± 0.05
r' & i' & z'	-1.33 ± 0.03

for the further analysis. Please note, that this slope is steeper than for the blue band ($\alpha_{UV\&u'} = -1.07$ and $\alpha_{g'\&B} = -1.25$), but it follows the trend observed in Chap. 3: With increasing wavelength the slope steepens, i.e. the ratio of faint to bright galaxies increases. A possible explanation is presented in Chap. 5.

4.2.2 The redshift evolution of the luminosity functions

In this section we analyze the luminosity function in the r', i', and z' bands by means of a Schechter function fit with fixed slope of $\alpha = -1.33$. The chosen filters allow us to use the SDSS luminosity functions (Blanton *et al.*, 2001) as a strong local constraint when parameterizing the luminosity function evolution in Sect. 4.3.

In Fig. 4.1 and 4.2 we present the luminosity functions in the r'-band and in the i'-band, while the results for the z'-band can be found in Fig. 4.3. The filled (open) symbols denote the luminosity function with (without) completeness correction. The solid lines show the Schechter function fitted to the luminosity function. The best fitting Schechter parameter, the redshift binning as well as the reduced χ^2 are also listed. The reduced χ^2 are very good for all redshift bins below $z \approx 2$. We do not analyze our lowest redshift bin ($\langle z \rangle \sim 0.3$) by means of a Schechter function fit, because the volume covered by the FDF is too small. Nevertheless there is a very good agreement with the local luminosity function derived from the SDSS (Blanton *et al.*, 2001, dotted line in Fig. 4.1, Fig. 4.2, and Fig. 4.3).

The best fitting Schechter parameters and their 1σ errors are summarized in Table 4.4, Table 4.5,

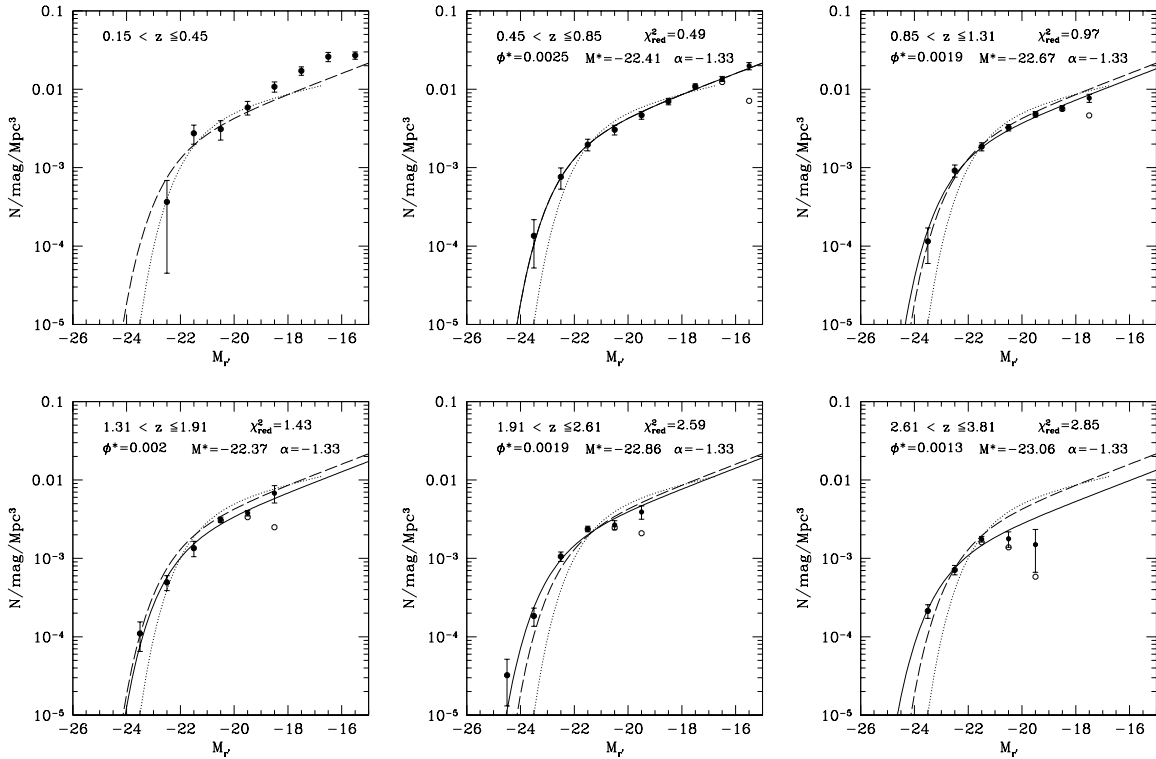


Figure 4.1: Luminosity functions in the r' -band from low redshift ($\langle z \rangle = 0.3$, upper left panel) to high redshift ($\langle z \rangle = 3.2$, lower right panel). The filled (open) symbols show the luminosity function corrected (uncorrected) for V/V_{max} . The fitted Schechter functions for a fixed slope α are shown as solid lines. Note that we only fit the luminosity functions from $\langle z \rangle = 0.6$ to $\langle z \rangle = 3.2$. The parameters of the Schechter functions can be found in Table 4.4. The dotted line represents the local r' -band luminosity function derived from the SDSS (Blanton *et al.*, 2001). The Schechter fit for redshift $\langle z \rangle = 0.6$ is indicated as dashed line in all panels.

Table 4.4: Schechter function fit in the r' -band

redshift interval	M^* (mag)	ϕ^* (Mpc^{-3})	α (fixed)
0.45 – 0.85	$-22.41^{+0.23}_{-0.18}$	$0.0025^{+0.0002}_{-0.0002}$	-1.33
0.85 – 1.31	$-22.67^{+0.14}_{-0.13}$	$0.0019^{+0.0001}_{-0.0001}$	-1.33
1.31 – 1.91	$-22.37^{+0.16}_{-0.16}$	$0.0020^{+0.0002}_{-0.0002}$	-1.33
1.91 – 2.61	$-22.86^{+0.13}_{-0.11}$	$0.0019^{+0.0002}_{-0.0002}$	-1.33
2.61 – 3.81	$-23.06^{+0.15}_{-0.15}$	$0.0013^{+0.0002}_{-0.0001}$	-1.33

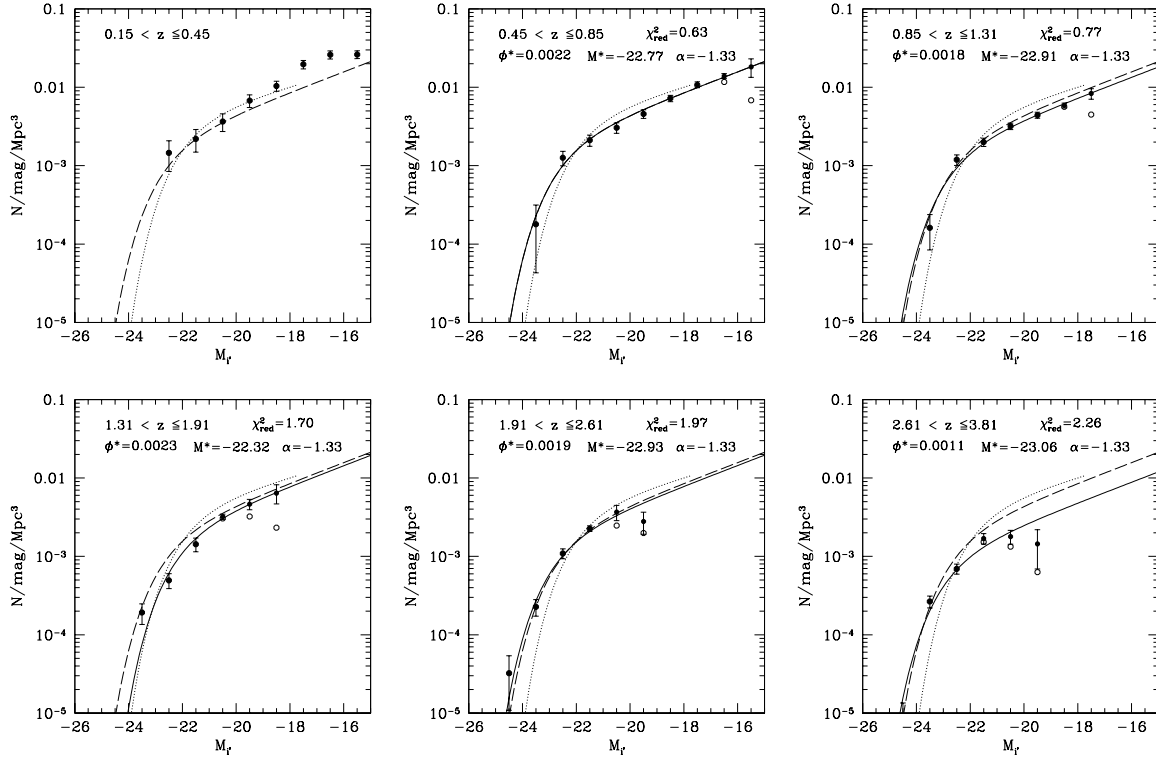


Figure 4.2: Luminosity functions in the i' -band from low redshift ($\langle z \rangle = 0.3$, upper left panel) to high redshift ($\langle z \rangle = 3.2$, lower right panel). The filled (open) symbols show the luminosity function corrected (uncorrected) for V/V_{max} . The fitted Schechter functions for a fixed slope α are shown as solid lines. Note that we only fit the luminosity functions from $\langle z \rangle = 0.6$ to $\langle z \rangle = 3.2$. The parameters of the Schechter functions can be found in Table 4.5. The dotted line represents the local i' -band luminosity function derived from the SDSS (Blanton *et al.*, 2001). The Schechter fit for redshift $\langle z \rangle = 0.6$ is indicated as dashed line in all panels.

Table 4.5: Schechter function fit in the i' -band

redshift interval	M^* (mag)	ϕ^* (Mpc^{-3})	α (fixed)
0.45 – 0.85	$-22.77^{+0.23}_{-0.24}$	$0.0022^{+0.0002}_{-0.0002}$	-1.33
0.85 – 1.31	$-22.91^{+0.16}_{-0.15}$	$0.0018^{+0.0001}_{-0.0001}$	-1.33
1.31 – 1.91	$-22.32^{+0.21}_{-0.18}$	$0.0023^{+0.0003}_{-0.0003}$	-1.33
1.91 – 2.61	$-22.93^{+0.14}_{-0.13}$	$0.0019^{+0.0002}_{-0.0002}$	-1.33
2.61 – 3.81	$-23.06^{+0.10}_{-0.09}$	$0.0011^{+0.0001}_{-0.0001}$	-1.33

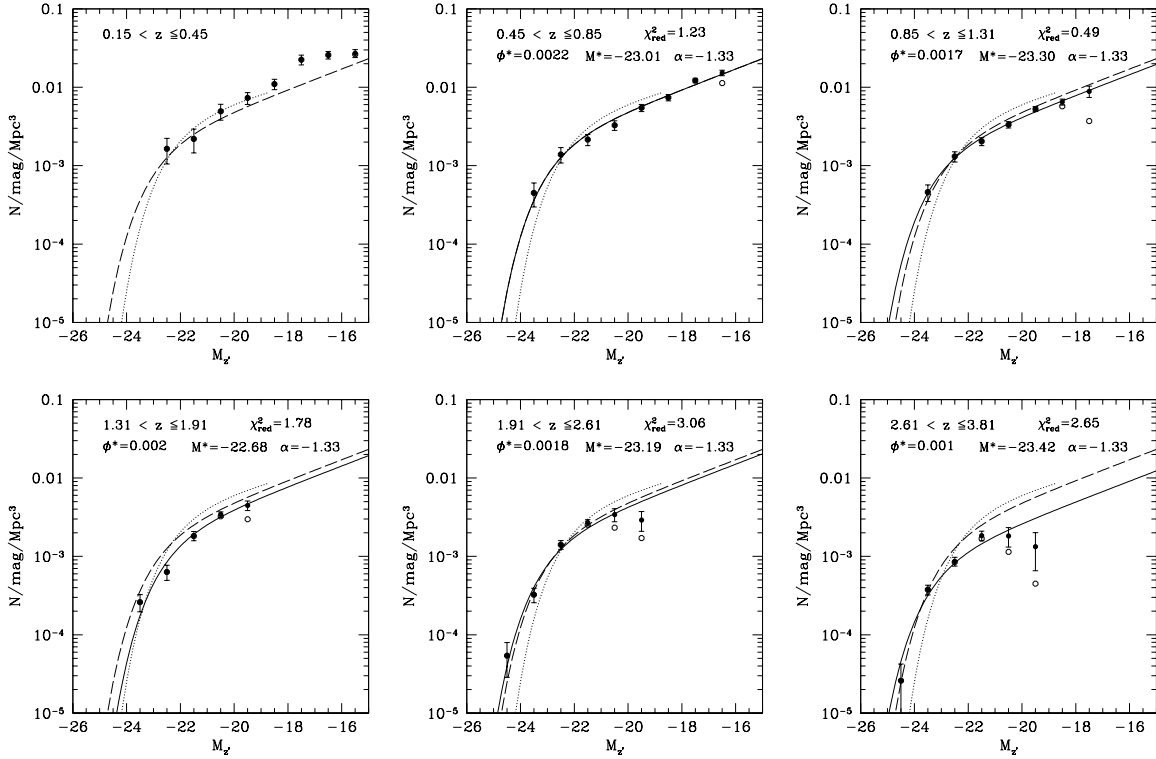


Figure 4.3: Luminosity functions in the z' -band from low redshift ($\langle z \rangle = 0.3$, upper left panel) to high redshift ($\langle z \rangle = 3.2$, lower right panel). The filled (open) symbols show the luminosity function corrected (uncorrected) for V/V_{max} . The fitted Schechter functions for a fixed slope α are shown as solid lines. Note that we only fit the luminosity functions from $\langle z \rangle = 0.6$ to $\langle z \rangle = 3.2$. The parameters of the Schechter functions can be found in Table 4.6. The dotted line represents the local z' -band luminosity function derived from the SDSS (Blanton *et al.*, 2001). The Schechter fit for redshift $\langle z \rangle = 0.6$ is indicated as dashed line in all panels.

Table 4.6: Schechter function fit in the z' -band

redshift interval	M^* (mag)	ϕ^* (Mpc^{-3})	α (fixed)
0.45 – 0.85	$-23.01 \pm 0.25 \pm 0.21$	$0.0022 \pm 0.0002 \pm 0.0002$	-1.33
0.85 – 1.31	$-23.30 \pm 0.20 \pm 0.21$	$0.0017 \pm 0.0002 \pm 0.0001$	-1.33
1.31 – 1.91	$-22.68 \pm 0.18 \pm 0.17$	$0.0020 \pm 0.0003 \pm 0.0002$	-1.33
1.91 – 2.61	$-23.19 \pm 0.13 \pm 0.13$	$0.0018 \pm 0.0002 \pm 0.0002$	-1.33
2.61 – 3.81	$-23.42 \pm 0.10 \pm 0.13$	$0.0010 \pm 0.0001 \pm 0.0001$	-1.33

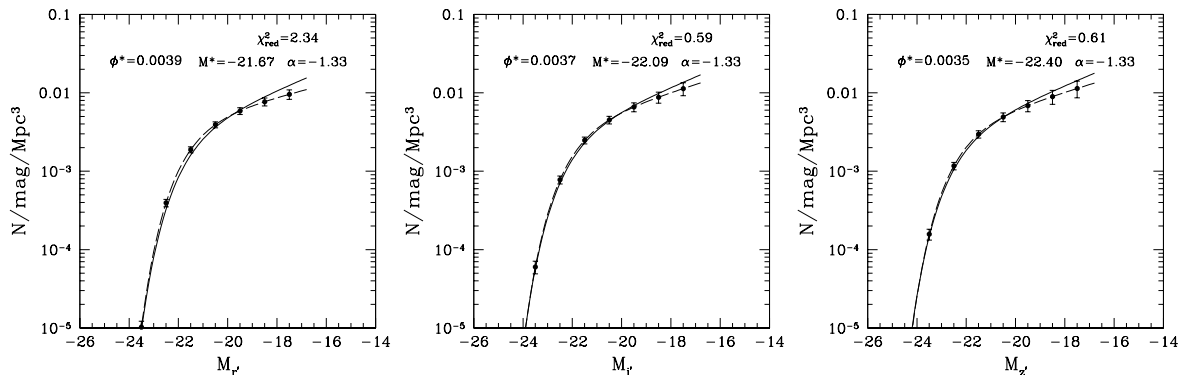


Figure 4.4: The local luminosity functions as given by Blanton *et al.* (2001) for the r' (left panel), i' (middle panel), and z' (left panel) bands. The dashed lines in all plots represent the best fitting Schechter function of Blanton *et al.* (2001). The solid points and the associated errorbars are derived by the Schechter values and corresponding errors of the latter (see text). For completeness we fit a Schechter function (solid line) with a fixed slope of -1.33 as derived from the FDF data do the luminosity function (solid dots). The corresponding M^* , ϕ^* , as well as the reduced χ^2 of the fit is also given in the figures.

and Table 4.6 for the r' , i' and z' bands, respectively. Even without fitting Schechter functions to the data, it is obvious that the evolution in characteristic luminosity and number density between redshifts $\langle z \rangle = 0.6$ and $\langle z \rangle = 3.2$ is very moderate if compared to the evolution in the blue bands (see Sect. 3.5.3).

4.3 Parameterizing the evolution of the luminosity function

In this section we analyze the redshift evolution of the Schechter parameters in a more quantitative way. We parameterize the redshift evolution of M^* and ϕ^* assuming the simple relations of Eq. (3.1). We derive the best fitting values for the free parameters a , b , M_0^* , and ϕ_0^* by minimizing the χ^2 of Eq. (3.2) for the galaxy number densities in all magnitude and redshift bins *simultaneously*. This is required because, as already described in Sect. 3.5.2, strong parameter coupling is observed between the Schechter parameters. The free parameters of the evolutionary model were constrained for three different cases:

- *Case 1*: Only FDF luminosity functions between redshift $\langle z \rangle \sim 0.65$ and $\langle z \rangle \sim 2.26$ are used.
- *Case 2*: Only FDF luminosity functions between redshift $\langle z \rangle \sim 0.65$ and $\langle z \rangle \sim 3.21$ are used.
- *Case 3*: FDF luminosity functions between redshift $\langle z \rangle \sim 0.65$ and $\langle z \rangle \sim 2.26$ as well as the local luminosity function of Blanton *et al.* (2001) are used.

In *Case 1* and *Case 2* we analyze the FDF data without further constraints from other datasets. Since in our highest redshift bin with $\langle z \rangle \sim 3.2$ all the luminosity functions are extrapolations (at redshift $\langle z \rangle \sim 2.5$ restframe r' roughly corresponds to the observerframe K-band) we calculate the evolution excluding (*Case 1*) and including (*Case 2*) this highest redshift bin. Further, we include

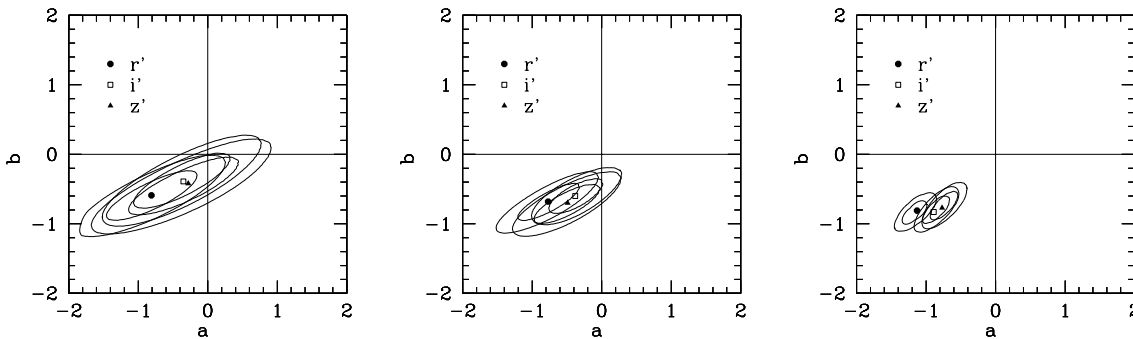


Figure 4.5: 1σ and 2σ confidence levels of the parameters a and b in different bands (r' , i' and z') for the evolutionary model described in the text. Left panel: Only FDF luminosity functions between redshift $\langle z \rangle \sim 0.65$ and $\langle z \rangle \sim 2.26$ are used (*Case 1*). The values for a and b can be found in Table 4.7. Middle panel: Only FDF luminosity functions between redshift $\langle z \rangle \sim 0.65$ and $\langle z \rangle \sim 3.21$ are used (*Case 2*). The values for a and b can be found in Table 4.8. Right panel: FDF luminosity functions between redshift $\langle z \rangle \sim 0.65$ and $\langle z \rangle \sim 2.26$ as well as the local luminosity function of Blanton *et al.* (2001) are used (*Case 3*). The values for a and b can be found in Table 4.9.

also the local luminosity functions as derived by Blanton *et al.* (2001) (*Case 3*). As the Schechter parameters are coupled, and M^* and ϕ^* of Blanton *et al.* (2001) are derived for a slightly different slope α , we decide not to use M^* and ϕ^* itself, but to reconstruct a magnitude binned luminosity function out of the Schechter values M^* , ϕ^* , and α given in Blanton *et al.* (2001). Following the method described in Sect. 3.7 to visualize the errors of the literature luminosity functions (shaded regions in the plots) we derive the 1-magnitude-binned luminosity function as shown in Fig. 4.4 as solid points. Fig. 4.4 clearly shows that a Schechter function with a slope of $\alpha = -1.33$ as derived from the FDF data is compatible with the results of Blanton *et al.* (2001) in the i' and z' bands ($\chi_{red}^2 \lesssim 1$). Only in the r' -band the slope derived in Blanton *et al.* (2001) is less steep resulting in a reduced $\chi_{red}^2 \sim 2.3$. The discrepancy in the r' -band diminishes if we limit the analysis to a limiting magnitude of -18 ($\chi_{red}^2 \lesssim 1.5$).

At this point a note of remark: Blanton and collaborators rederived the luminosity functions in the SDSS using a larger galaxy sample in Blanton *et al.* (2003). This time they used another approach explicitly allowing for density and luminosity evolution within the covered redshift range. The new luminosity functions are not as steep as those derived in Blanton *et al.* (2001). On the other hand the slope is strongly dependent on the depth of the survey. The flux limit in the r -band selected SDSS survey is about $m_r < 17.79$. A very rough estimate of the absolute limiting magnitude at the mean redshift of the survey ($\langle z \rangle = 0.1$) is therefore $M_r \approx -20$. This means that the faint end of the luminosity function as shown in Fig. 4.4 depends on the applied completeness correction, although the completeness correction is more precise for an spectroscopic survey as for an survey based on photometric redshift (see also the discussion in Andreon, 2004).

We then use the 1-magnitude-binned local luminosity functions shown in Fig. 4.4 ($\langle z \rangle \sim 0.1$) together with the FDF luminosity functions in the higher redshift bins to constrain the free parameters a , b , M_0^* , and ϕ_0^* of Eq. (3.1) by minimizing Eq. (3.2).

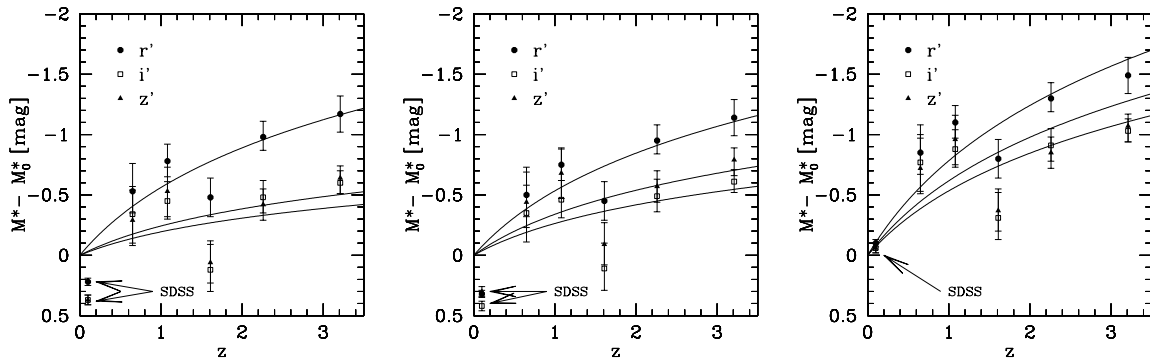


Figure 4.6: Relative evolution of M^* with redshift. The solid line represent the best fit of the evolutionary model according to Eq. (3.1). Left panel: Only FDF luminosity functions between redshift $\langle z \rangle \sim 0.65$ and $\langle z \rangle \sim 2.26$ are used to constrain the evolutionary model (*Case 1*). Middle panel: Only FDF luminosity functions between redshift $\langle z \rangle \sim 0.65$ and $\langle z \rangle \sim 3.21$ are used to constrain the evolutionary model (*Case 2*). Right panel: FDF luminosity functions between redshift $\langle z \rangle \sim 0.65$ and $\langle z \rangle \sim 2.26$ as well as the local luminosity function of Blanton *et al.* (2001) are used to constrain the evolutionary model (*Case 3*) (see also text).

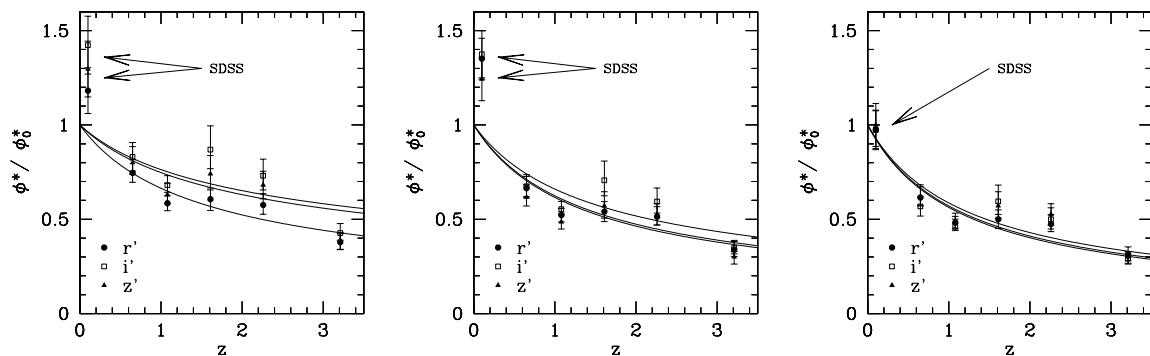


Figure 4.7: Relative evolution of ϕ^* with redshift. The solid line represent the best fit of the evolutionary model according to Eq. (3.1). Left panel: Only FDF luminosity functions between redshift $\langle z \rangle \sim 0.65$ and $\langle z \rangle \sim 2.26$ are used to constrain the evolutionary model (*Case 1*). Middle panel: Only FDF luminosity functions between redshift $\langle z \rangle \sim 0.65$ and $\langle z \rangle \sim 3.21$ are used to constrain the evolutionary model (*Case 2*). Right panel: FDF luminosity functions between redshift $\langle z \rangle \sim 0.65$ and $\langle z \rangle \sim 2.26$ as well as the local luminosity function of Blanton *et al.* (2001) are used to constrain the evolutionary model (*Case 3*) (see also text).

Table 4.7: Evolution parameters according to Eq. (3.1). Only FDF luminosity functions between redshift $\langle z \rangle \sim 0.65$ and $\langle z \rangle \sim 2.26$ are used to constrain the parameters (*Case 1*).

filter	a	b	M_0^* (mag)	ϕ_0^* (10^{-2}Mpc^{-3})
r'	$-0.81^{+0.43}_{-0.41}$	$-0.59^{+0.23}_{-0.23}$	$-21.89^{+0.39}_{-0.42}$	$0.0033^{+0.0007}_{-0.0005}$
i'	$-0.35^{+0.43}_{-0.48}$	$-0.39^{+0.27}_{-0.24}$	$-22.46^{+0.44}_{-0.41}$	$0.0026^{+0.0006}_{-0.0004}$
z'	$-0.28^{+0.46}_{-0.58}$	$-0.42^{+0.24}_{-0.30}$	$-22.77^{+0.56}_{-0.45}$	$0.0027^{+0.0008}_{-0.0004}$

Table 4.8: Evolution parameters according to Eq. (3.1). Only FDF luminosity functions between redshift $\langle z \rangle \sim 0.65$ and $\langle z \rangle \sim 3.21$ are used to constrain the parameters (*Case 2*).

filter	a	b	M_0^* (mag)	ϕ_0^* (10^{-2}Mpc^{-3})
r'	$-0.77^{+0.30}_{-0.28}$	$-0.68^{+0.17}_{-0.17}$	$-21.92^{+0.30}_{-0.30}$	$0.0037^{+0.0005}_{-0.0005}$
i'	$-0.38^{+0.26}_{-0.25}$	$-0.60^{+0.15}_{-0.16}$	$-22.45^{+0.30}_{-0.30}$	$0.0032^{+0.0004}_{-0.0004}$
z'	$-0.49^{+0.29}_{-0.31}$	$-0.70^{+0.17}_{-0.19}$	$-22.62^{+0.38}_{-0.32}$	$0.0035^{+0.0006}_{-0.0006}$

The 1σ and 2σ confidence levels of the evolution parameters a and b are shown for the different filters and different cases in Fig. 4.5. These contours were derived by projecting the four-dimensional χ^2 distribution to the a - b plane, i.e. for given a and b we use the value of M_0^* and ϕ_0^* which minimizes the $\chi^2(a, b)$. For *Case 1* (left panel) the errorbars of a and b are rather large and although the best fitting values suggest a redshift evolution we are also compatible (within 2σ) with no evolution of M^* and ϕ^* . The error ellipses for *Case 2* (middle panel) are smaller as in *Case 1* and for the r'-band luminosity function we see a luminosity and a density evolution on a 2σ level. For the i'-band and z'-band luminosity functions we see only a density evolution (on a 2σ level). Including also the local luminosity function of Blanton *et al.* (2001) in the evolution analysis as in *Case 3* (left panel) we are able to derive a and b with high precision. The luminosity and density evolution is clearly visible on more than 2σ level. Please note that combining different datasets like the FDF and the SDSS can introduce possible systematic errors. On the other hand we compare in Fig. 4.1, Fig. 4.2 and Fig. 4.3 (upper left panel) our luminosity function at $\langle z \rangle = 0.3$ with the SDSS Schechter function at $\langle z \rangle = 0.1$ and see a remarkable agreement. Furthermore, a detailed comparison of the UV luminosity functions of the FDF with the LF derived in large surveys e.g. Wolf *et al.* (2003, based on COMBO-17), Steidel *et al.* (1999, based on LBG analysis), Iwata *et al.* (2003); Ouchi *et al.* (2004a, based on Subaru Deep Field/Survey) or pencil beam surveys e.g. Poli *et al.* (2001, based on both HDFs) was presented in Chap. 3 and shows good agreement in the overlapping magnitude range at all redshifts. This disfavors larger systematic errors mainly due to the influence of large scale structure in the FDF.

The resulting values for the free parameters a , b , M_0^* , and ϕ_0^* as well as the associated errors can be found in Table 4.7 for *Case 1*, in Table 4.8 for *Case 2*, and Table 4.9 for *Case 3*. It is quite remarkable

Table 4.9: Evolution parameters according to Eq. (3.1). FDF luminosity functions between redshift $\langle z \rangle \sim 0.65$ and $\langle z \rangle \sim 2.26$ as well as the local luminosity function of Blanton *et al.* (2001) are used to constrain the parameters (*Case 3*).

filter	a	b	M_0^* (mag)	ϕ_0^* (10^{-2}Mpc^{-3})
r'	$-1.13^{+0.09}_{-0.15}$	$-0.81^{+0.09}_{-0.13}$	$-21.57^{+0.03}_{-0.02}$	$0.0040^{+0.0003}_{-0.0001}$
i'	$-0.89^{+0.16}_{-0.09}$	$-0.83^{+0.17}_{-0.10}$	$-22.03^{+0.04}_{-0.03}$	$0.0038^{+0.0001}_{-0.0003}$
z'	$-0.77^{+0.15}_{-0.10}$	$-0.77^{+0.16}_{-0.10}$	$-22.34^{+0.04}_{-0.05}$	$0.0035^{+0.0003}_{-0.0002}$

that the evolution parameters a , b , M_0^* , and ϕ_0^* derived in *Case 1*, *Case 2*, and *Case 3* agree *all* within 2σ . Most of the values differ only by 1σ or less.

In Fig. 4.6 we illustrate the relative redshift evolution of M^* for the different filters and different cases, whereas the relative redshift evolution of ϕ^* is shown in Fig. 4.7. Note that a , b , M_0^* , and ϕ_0^* were derived by minimizing Eq. (3.2) and not the differences between the (best fitting) lines and the data points in Fig. 4.6 and Fig. 4.7. As for the blue bands (see Chap. 3) the simple parameterization we have chosen with Eq. (3.1) describes the evolution of the galaxy luminosity functions very well also in the red bands.

If we compare the evolutionary parameters a and b of the red bands with those derived in the blue bands (Chap. 3), the following trend can be seen: with increasing waveband ($UV \rightarrow u' \rightarrow g' \rightarrow r' \rightarrow i' \rightarrow z'$) the redshift evolution of M^* and ϕ^* decreases. On the other hand, if we include in our analysis also the results obtained in the SDSS the brightening of M^* and the decrease in ϕ^* for increasing redshift is still seen also in the red bands (at more than 3σ).

4.4 Comparison with literature

In this section we compare the luminosity functions derived in the FDF with the luminosity functions of other surveys following the procedure describe in Sect.3.7:

First we convert results from the literature to our cosmology ($\Omega_M = 0.3$, $\Omega_\Lambda = 0.7$ and $H_0 = 70 \text{km s}^{-1} \text{Mpc}^{-1}$). Note that this conversion may not be perfect, because we can only transform number densities and magnitudes but lack the knowledge of the individual magnitudes and redshifts of the galaxies. Nevertheless, the errors introduced in this way are not large and the method is suitable for our purpose. *Second*, in order to avoid uncertainties due to conversion between different filter bands, we always use the same band as the survey we want to compare with. *Third*, we also try to use the same redshift binning if possible. In addition, if the number of galaxies in the FDF is too small to derive a well sampled luminosity function we increase the binning.

To visualize the errors of the literature luminosity functions we perform Monte-Carlo simulations using the ΔM^* , $\Delta \phi^*$, and $\Delta \alpha$ given in the papers. In cases where not all of these values could be found in the paper, this is mentioned in the figure caption. We do not take into account any correlation between the Schechter parameters and assume a Gaussian distribution of the errors ΔM^* , $\Delta \phi^*$, and $\Delta \alpha$. From 1000 simulated Schechter functions we derive the region where 68.8 % of the

realizations lie. The resulting region, roughly corresponding to 1σ errors, is shaded in the figures. The luminosity functions derived in the FDF are also shown as filled and open circles. The filled circles are completeness corrected whereas the open circles are not corrected. The redshift binning used to derive the luminosity function in the FDF is given in the lower right part of every figure. Moreover, the limiting magnitude of the respective survey is indicated by the low-luminosity cut-off of the shaded region in all figures. If the limiting magnitude was not explicitly given it was estimated from the figures in the literature.

Blanton et al. (2001):

In the upper left panel of Fig. 4.1, Fig. 4.2 and Fig. 4.3 we compare the LF of the (r' selected) SDSS ($\langle z \rangle = 0.1$) with the LF derived in the FDF ($\langle z \rangle = 0.3$) in the r' , i' , and z' , respectively. Despite the small volume of the FDF in the local redshift bin, the agreement is very good in the i' and z' bands. In the r' -band there is a disagreement in the faint part of the LF, but a good agreement at the intermediate and bright part.

Lin et al. (1996):

Although the volume of the FDF at low redshift is rather small, and therefore is not well suited to properly sample the bright end of the Schechter function, we compare in Fig. 4.8 (left panel) our luminosity function also with the luminosity function derived by Lin *et al.* (1996) in the Las Campanas Redshift Survey (LCRS). Their sample contains 18678 sources selected from CCD photometry in a “hybrid” red Kron-Cousins R-band with a mean redshift of $\langle z \rangle \sim 0.1$

The solid line in Fig. 4.8 (left panel) represents the luminosity function in the R-band from Lin *et al.* (1996) whereas the filled circles show our V/V_{max} corrected luminosity function derived at $0.15 < z \leq 0.45$. There is a rather large disagreement between the LF in the FDF and in the LCRS, which is mainly due to the different slope ($\alpha = -0.7$ for the LCRS) but also the FDF galaxy number density at the bright end seems to be slightly higher than in the LCRS.

Lin et al. (1997):

Based on 389 field galaxies from the Observational Cosmology cluster redshift survey (CNOC1) selected in the Gunn-r-band Lin *et al.* (1997) derived the LF in the restframe Gunn-r-band. In Fig. 4.8 (right panel) we compare our luminosity function with the luminosity function derived by Lin *et al.* (1997) in the redshift range $z = 0.2-0.6$. There is a very good agreement between the FDF data and the CNOC1 survey concerning the LF, if we compare only the magnitude range in common to both surveys (shaded region). Also the slope derived in Lin *et al.* (1997) ($\alpha = -1.25 \pm 0.19$, Table 2 of the paper) is compatible with the slope in the FDF.

Brown et al. (2001):

Brown *et al.* (2001) use 64 deg^2 of V and R images to measure the local V- and R-band LF. They analyzed about 1250 V & R selected galaxies from the Century Survey (Geller *et al.*, 1997) with a mean spectroscopic redshift of $\langle z \rangle \sim 0.06$.

A comparison between the luminosity function of Brown *et al.* (2001) and the FDF is shown in Fig. 4.9 for the V-band (left panel) and the R-band (right panel). Although the agreement is quite good for the bright end, the number-density of the faint end is substantially higher in the FDF (while the slope of the LF derived in the FDF is $\alpha = -1.25$, the slope derived by Brown *et al.* (2001) is $\alpha = -1.09$ in the V-band as well as in the R-band).

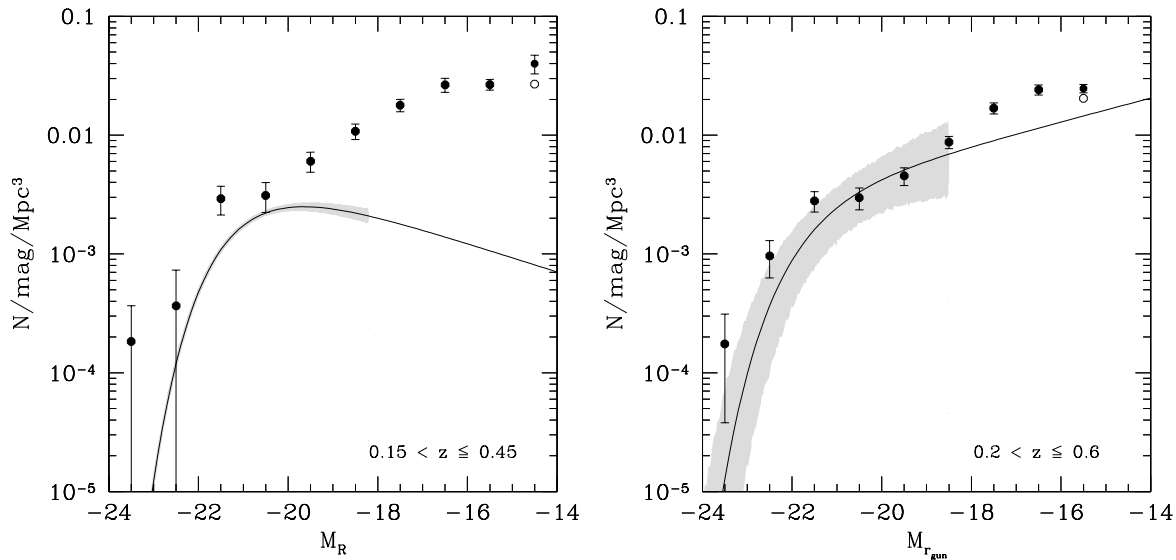


Figure 4.8: Left panel: Comparison of the R-band luminosity function of the FDF ($\langle z \rangle \sim 0.3$) with the Schechter function derived in Lin *et al.* (1996) ($\langle z \rangle \sim 0.1$). The shaded region is based on ΔM^* , $\Delta \phi^*$, and $\Delta \alpha$. Right panel: Comparison of the Gunn-r-band luminosity function of the FDF with the Schechter function derived in Lin *et al.* (1997) ($z = 0.2\text{--}0.6$). The shaded region is based on ΔM^* , $\Delta \phi^*$, and $\Delta \alpha$.

Wolf et al. (2003):

In Fig. 4.10 we compare the r' -band luminosity function of the FDF with the R-band selected luminosity function derived in the COMBO-17 survey (Wolf *et al.*, 2003) for different redshift bins: 0.2 – 0.6, 0.6 – 0.8, 0.8 – 1.0, 1.0 – 1.2. Because of the limited sample size of the FDF at low redshift we could not use the same local redshift binning as Wolf *et al.* (2003). We compare therefore in Fig. 4.10 (upper left panel) the COMBO17 Schechter function at $\langle z \rangle \sim 0.3$ (light gray) and $\langle z \rangle \sim 0.5$ (dark gray) with the FDF luminosity function derived at $0.2 < z \leq 0.6$. There is a very good agreement between the FDF data and the COMBO-17 survey at all redshifts under investigations if we compare only the magnitude range in common to both surveys (shaded region). Although the number density of the FDF seems to be slightly higher for the UV (see Fig. 3.18), this is not the case if we compare the luminosity function in the R-band. Wolf *et al.* (2003) derived the faint-end slope from relatively shallow data which have only a limited sensitivity for the latter. This may explain the disagreement between the extrapolated faint-end slope of Wolf *et al.* (2003) and the FDF result.

Chen et al. (2003):

The galaxy sample analyzed by Chen *et al.* (2003) contains ~ 6700 H-band selected galaxies (within 847 arcmin^2) in the HDFs region with complementary optical U, B, V, R, and I colors, and ~ 7400 H-band selected galaxies (within 561 arcmin^2) in the Chandra deep field South region with complementary optical V, R, I, and z' colors. The galaxy sample is part of the Las Campanas Infrared Survey (LCIR Marzke *et al.*, 1999; McCarthy *et al.*, 2001) and based on photometric redshifts.

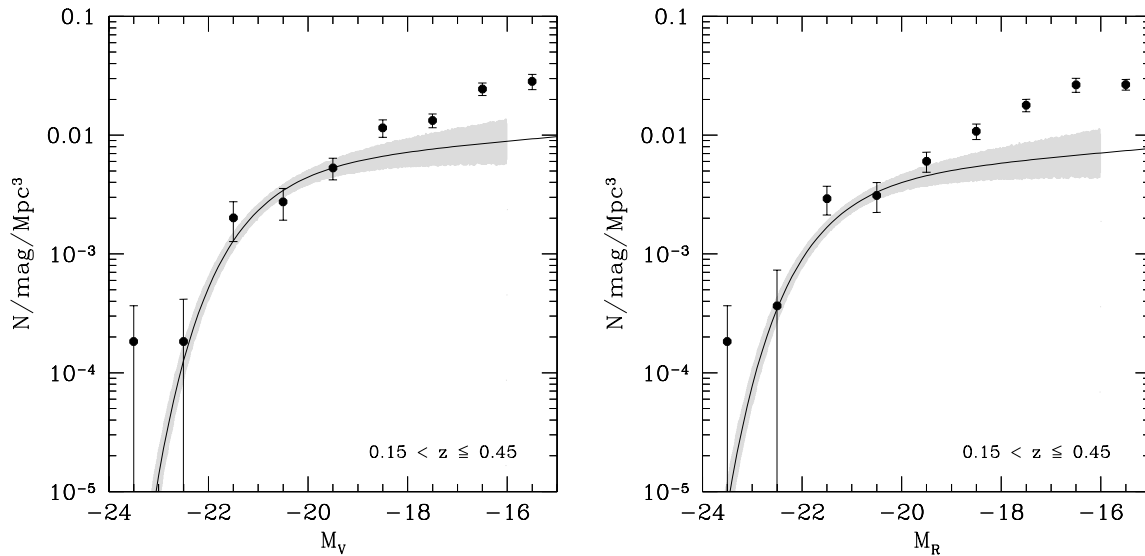


Figure 4.9: Comparison of the V-band (left panel) and R-band (right panel) luminosity function of the FDF with the local ($\langle z \rangle \sim 0.06$) Schechter function derived in *Brown et al. (2001)*. The shaded region is based on ΔM^* , $\Delta \phi^*$, and $\Delta \alpha$.

Fig. 4.11 shows a comparison of the R-band luminosity function derived by *Chen et al. (2003)* with the luminosity function in the FDF for three different redshift bins: 0.50–0.75 (left panel), 0.75–1.00 (middle panel), and 1.00–1.50 (right panel). There is a good agreement between the FDF LF and the Schechter function derived by *Chen et al. (2003)* in the lowest redshift bin ($z = 0.50$ –0.75) if we compare only the magnitude range in common to both surveys (shaded region). At intermediate redshift ($z = 0.75$ –1.00) the number-density of the bright end of the FDF luminosity function is slightly higher as in *Chen et al. (2003)*. On the other hand, for the highest redshift bin ($z = 1.00$ –1.50) the number-density of the bright end derived by *Chen et al. (2003)* roughly agrees with the results obtained in the FDF.

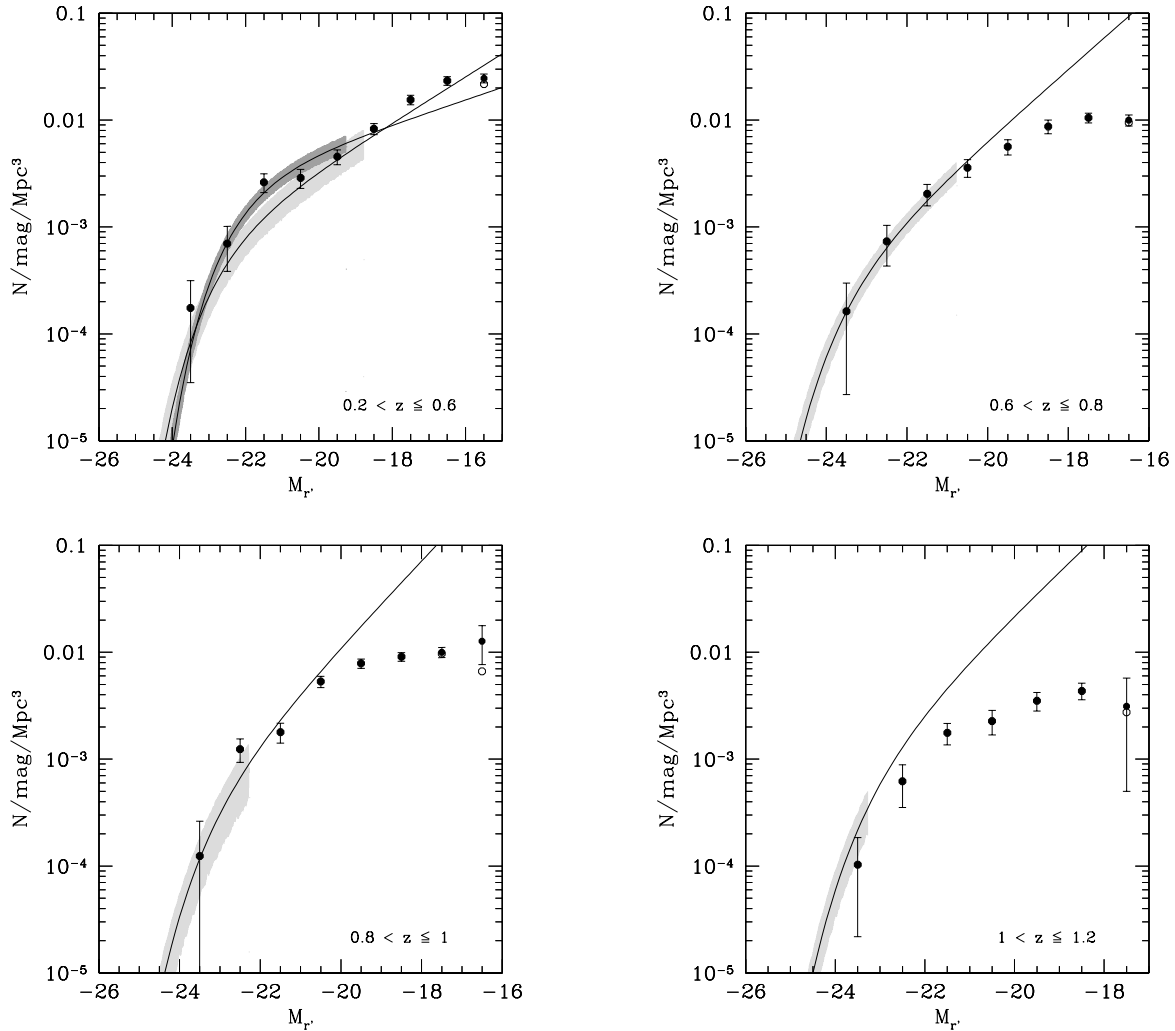


Figure 4.10: Comparison of the luminosity function in the r' -band of the FDF with the Schechter function derived in *Wolf et al. (2003)*: $0.2 < z \leq 0.4$ (upper left panel, light gray), $0.4 < z \leq 0.6$ (upper left panel, dark grey), $0.6 < z \leq 0.8$ (upper right panel), $0.8 < z \leq 1.0$ (lower left panel), $1.0 < z \leq 1.2$ (lower right panel). The shaded regions of nearly all plots are based on ΔM^* , $\Delta \phi^*$, and $\Delta \alpha$. Only in the highest redshift bin (lower right panel) the shaded region is based only on ΔM^* and $\Delta \phi^*$. The cut-off at low luminosity indicates the limiting magnitude of the sample.

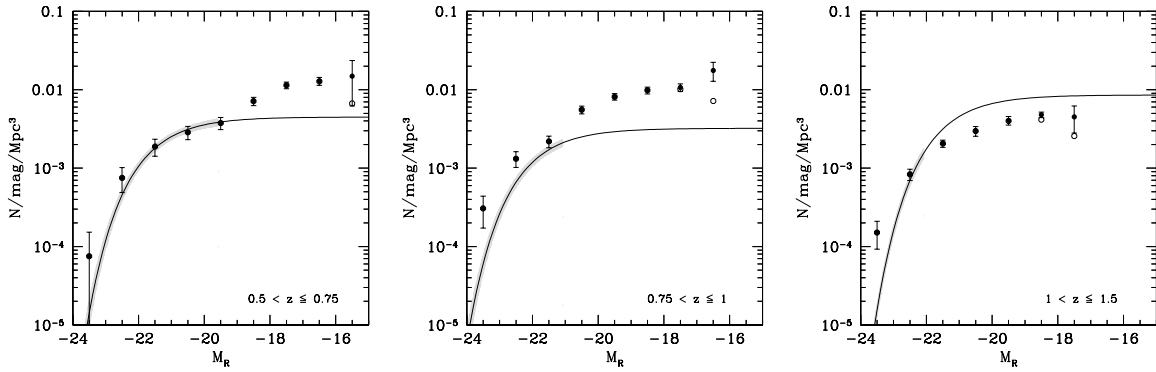


Figure 4.11: Comparison of the luminosity function in the R-band of the FDF with the Schechter function derived in *Chen et al. (2003)*: $0.50 < z \leq 0.75$ (left panel), $0.75 < z \leq 1.00$ (middle panel), and $1.00 < z \leq 1.50$ (right panel). The shaded region is based on ΔM^* , $\Delta \phi^*$ and $\Delta \alpha$ for $0.50 < z \leq 0.75$ (left panel). For $0.75 < z \leq 1.00$ (middle panel) and $1.00 < z \leq 1.50$ (right panel) the shaded region is based only on ΔM^* and $\Delta \phi^*$. The cut-off at low luminosity indicates the limiting magnitude of the sample.

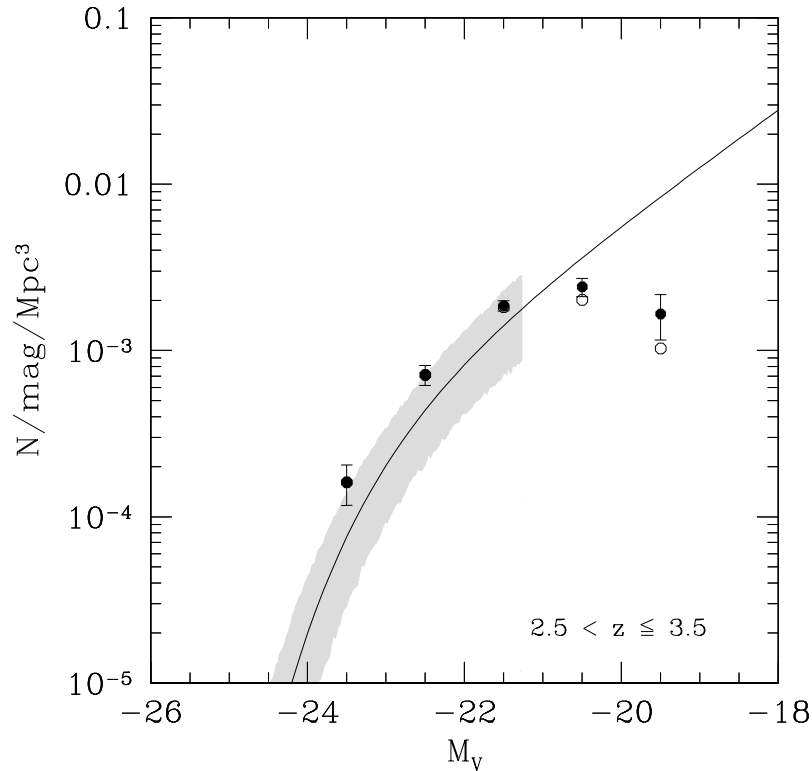


Figure 4.12: Comparison of the V-band luminosity function of the FDF with the Schechter function derived in *Shapley et al. (2001)* at $\langle z \rangle \sim 3.0$. The shaded region is based on ΔM^* , $\Delta \phi^*$, and $\Delta \alpha$, where the cut-off at low luminosity indicates the limiting magnitude of the sample.

Shapley et al. (2001):

Shapley *et al.* (2001) analyzed 118 photometrically selected LBGs with Ks-band measurements covering an area of 30 arcmin². 63 galaxies have also J-band measurements and 81 galaxies are spectroscopically confirmed. Using this sample Shapley *et al.* (2001) derived the luminosity function in the restframe V-band at redshift of $\langle z \rangle \sim 3.0$. Fig. 4.12 shows a comparison of the V-band luminosity function derived by Shapley *et al.* (2001) with the luminosity function in the FDF at $\langle z \rangle \sim 3.0$. The agreement is very good if we again concentrate on the shaded region (the magnitude range in common to both surveys). On the other hand, because of the depth of the FDF we can trace the luminosity function 2 magnitudes deeper and therefore give better constraints on the slope of the Schechter function. Comparing the faint end of the FDF luminosity function with the extrapolated Schechter function of Shapley *et al.* (2001) clearly shows, that the steep slope of $\alpha = -1.85$ as obtained by Shapley *et al.* (2001) is not seen in the FDF dataset.

The comparison of the luminosity functions derived in the FDF with previous observational datasets shows in general good agreement at the bright end, where their samples are complete. Differences in the faint-end slope in some cases can be attributed to the shallower limiting magnitudes of most of the other surveys.

4.5 Comparison with model predictions

As discussed in Sect. 3.1, key physical processes are involved in shaping the bright and the faint-end of the galaxy luminosity function (Benson *et al.*, 2003). Therefore, it is interesting to compare luminosity functions predicted by models with observational results to better constrain those processes. In this section we compare the R-band and I-band luminosity functions in different redshift bins with model predictions of Kauffmann *et al.* (1999).

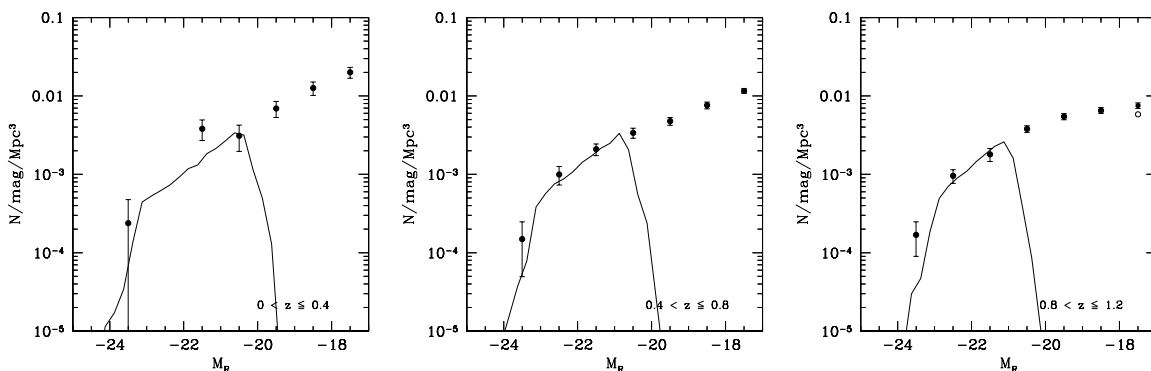


Figure 4.13: Comparison of the R-band luminosity function of the FDF with predictions based on Kauffmann *et al.* (1999) (solid line): $\langle z \rangle \sim 0.20$, $\langle z \rangle \sim 0.62$, and $\langle z \rangle \sim 1.05$, (from left to right panel). The filled (open) symbols show the luminosity function corrected (uncorrected) for V/V_{max} . The drops of the theoretical curves towards the faint end is caused by the limited mass resolution of the models, see Kauffmann *et al.* (1999) for details.

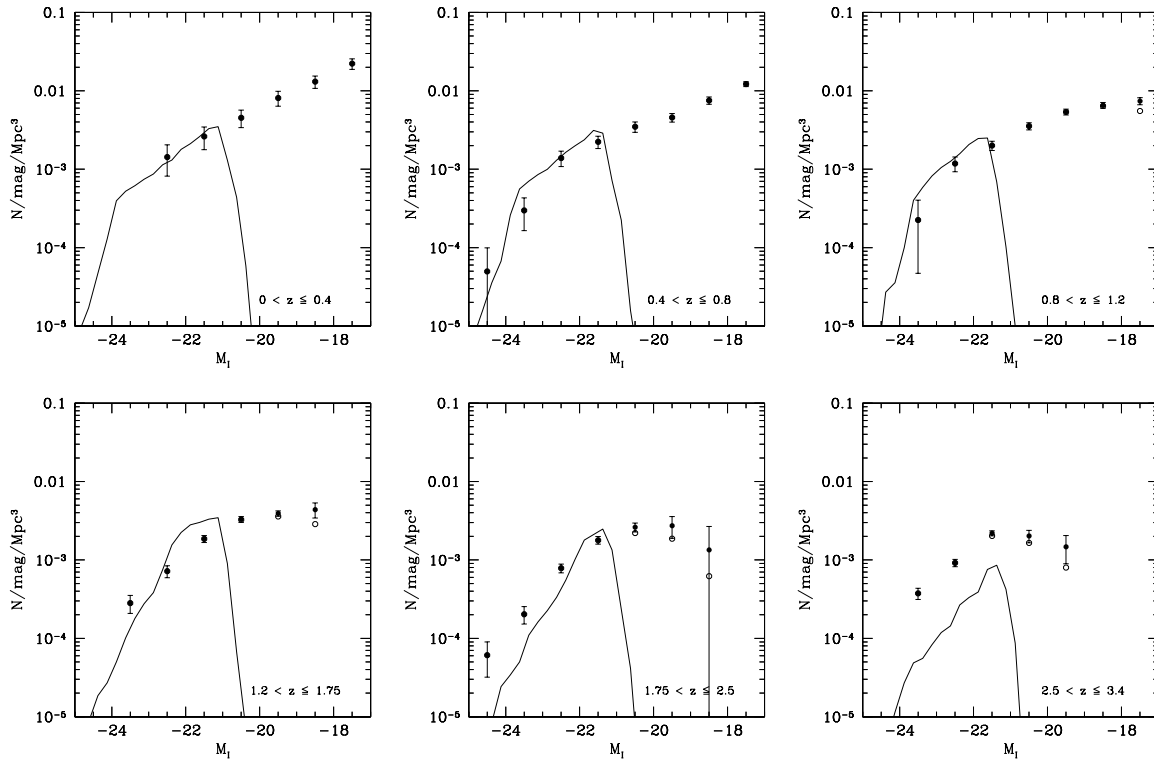


Figure 4.14: Comparison of the I-band luminosity function of the FDF with predictions based on *Kauffmann et al. (1999)* (solid line): $\langle z \rangle \sim 0.20$, $\langle z \rangle \sim 0.62$, $\langle z \rangle \sim 1.05$, $\langle z \rangle \sim 1.46$, $\langle z \rangle \sim 2.12$, and $\langle z \rangle \sim 2.97$ (from upper left to lower right panel). The filled (open) symbols show the luminosity function corrected (uncorrected) for V/V_{max} . The drops of the theoretical curves towards the faint end is caused by the limited mass resolution of the models, see *Kauffmann et al. (1999)* for details.

In Fig. 4.13 we show the R-band luminosity function of the FDF together with the semi-analytic model predictions by *Kauffmann et al. (1999)*¹ for the following redshifts: $\langle z \rangle \sim 0.20$, $\langle z \rangle \sim 0.62$, $\langle z \rangle \sim 1.05$, whereas in Fig. 4.14 we show the I-band luminosity function in the redshift bins: $\langle z \rangle \sim 0.20$, $\langle z \rangle \sim 0.62$, $\langle z \rangle \sim 1.05$, $\langle z \rangle \sim 1.46$, $\langle z \rangle \sim 2.12$, and $\langle z \rangle \sim 2.97$. For the R-band no semi-analytic model predictions are available for redshifts larger than $\langle z \rangle \sim 1.05$.

We see a similar behavior as in the B-band (see Fig. 3.12 in Chap. 3): there is a good agreement between the models (solid lines) and the luminosity functions derived in the FDF in the R-band. Also for the I-band there is a good agreement between the models and the luminosity functions derived in the FDF up to redshift $\langle z \rangle \sim 1.46$ (of course at $z \approx 0$ the model is tuned to reproduce the data). At $\langle z \rangle > 1.46$ the discrepancy increases as the model does not contain enough bright galaxies. Unfortunately, the models only predict luminosities for massive galaxies and, therefore, they do not predict galaxy number densities below M^* .

¹The models were taken from:
http://www.mpa-garching.mpg.de/Virgo/data_download.html

Chapter 5

LF redshift evolution as a function of SED type

5.1 Introduction

A comparison of the results of Chap. 3 and Chap. 4 clearly shows that the LF redshift evolution in the blue band is much stronger than in the red bands. This holds not only for the luminosity evolution, but also for the evolution in number density. However, we only analyzed the galaxy population as a whole and therefore mixing together all different galaxy types. In this chapter we subdivide our galaxy sample into 4 different SED types and analyze the type-dependent LF evolution. This allows us to determine the contribution of a typical SED type to the total LF (as derived in Chap. 3 and Chap. 4). Furthermore, it also allows us to build up the shape of the total LF and give a reasonable explanation for the different slopes α seen in the different wavebands.

We use AB magnitudes and adopt a Λ cosmology throughout this chapter with $\Omega_M = 0.3$, $\Omega_\Lambda = 0.7$, and $H_0 = 70 \text{ km s}^{-1} \text{ Mpc}^{-1}$.

5.2 Galaxy classification

The photometric redshift technique as described in Sect. 3.4 derives not only the most probable redshift of a galaxy but also the best fitting SED. As a consequence the evolution of the luminosity function can be investigated in sub-samples split by restframe spectral types. As there is no unique definition of SED types along a spectral parameter axis (since galaxies cover a continuum of parameter values) we decided to group the SED models in 4 main SED types. The SEDs in the 4 main spectral types are shown color coded in Fig. 5.1:

- SED type 1: red
- SED type 2: green
- SED type 3: cyan
- SED type 4: blue

The SEDs are mainly grouped according to the UV-K color: for increasing type (SED type 1 \rightarrow SED type 4) the SEDs become bluer, i.e. the UV flux (and thus the recent star formation rate) increases if compared to the K-band flux.

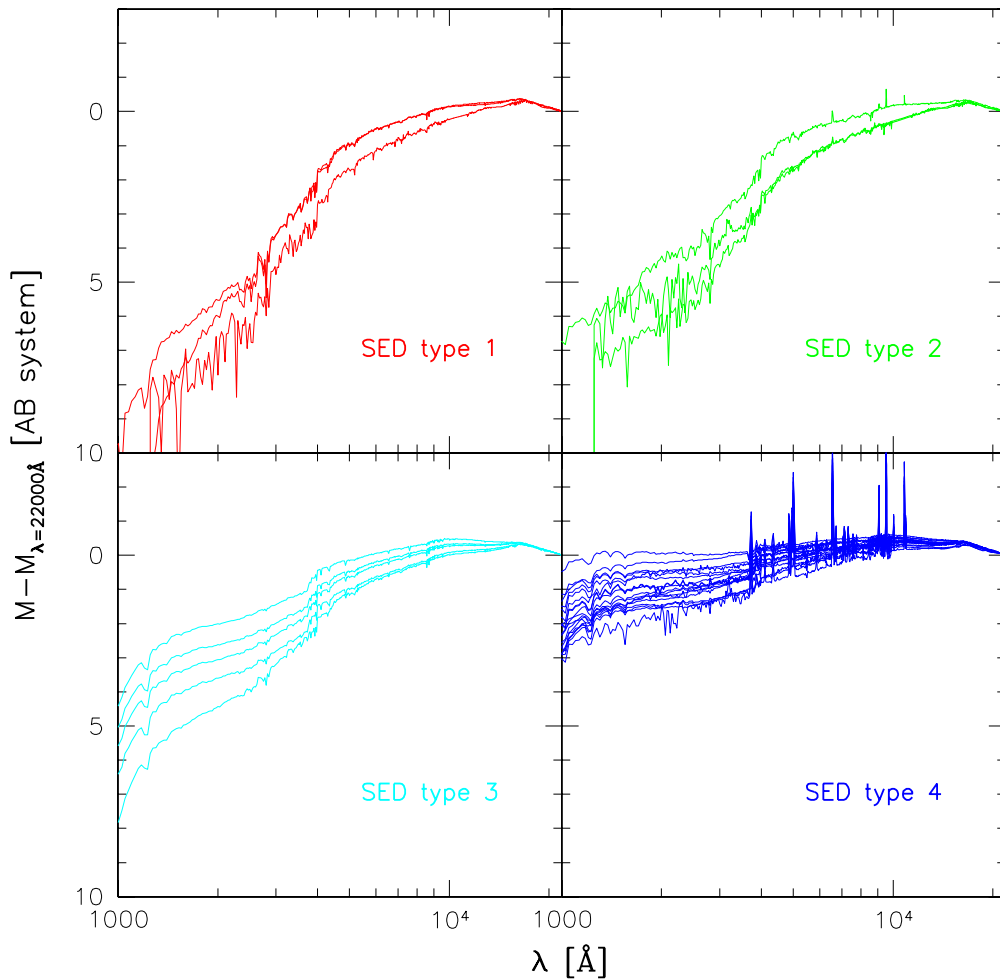


Figure 5.1: SEDs grouped according to their spectral type: Upper left panel: SED type 1; Upper right panel: SED type 2; Lower left panel: SED type 3; Lower right panel: SED type 4.

Moreover, Pannella *et al.* (2004) also analyzed the morphology of about 1400 galaxies in the FDF down to $I \sim 25$ mag on space based HST (ACS) data. The superb HST images allow a much better spatial resolution of the substructure and light profiles of galaxies when compared to ground based images. Basic galaxy properties such as color, luminosity and rotational velocity vary according to the morphology. As different morphological types have distinct surface brightness profiles, an analysis of the latter can be used to derive the morphological type of an object. Usually, the radial dependence of the surface brightness profiles of galaxies can be well approximated by the following relation:

$$I(r) \propto \exp \left[- \left(\frac{r}{r_0} \right)^{\frac{1}{n}} \right], \quad (5.1)$$

where n is known as the Sérsic index (Sérsic, 1968), such that $n = 1$ for a purely exponential disk, and

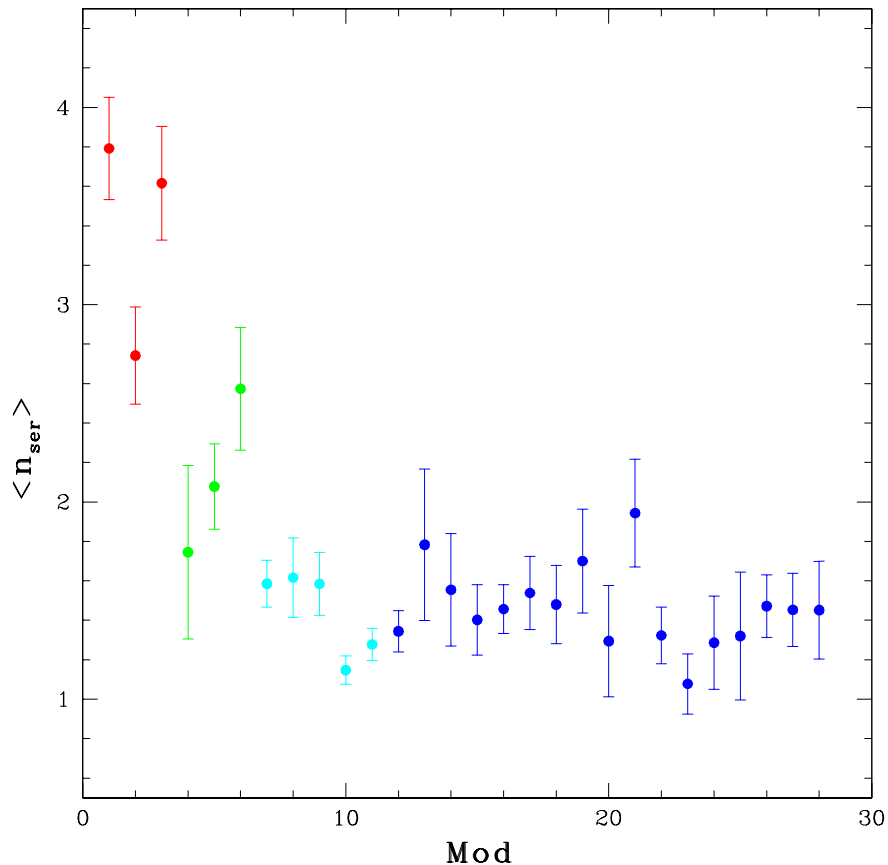


Figure 5.2: Sérsic index as a function of SED type (Mod) for the FDF as derived by Pannella *et al.* (2004): SED type 1 (red dots), type 2 (green dots), type 3 (cyan dots), and type 4 (blue dots).

$n = 4$ for a de Vaucouleurs profile (de Vaucouleurs, 1948). The parameter r_0 is known as the effective radius such that half of the total flux is within r_0 . Galaxies with nearly exponential profiles (Sérsic index $n \sim 1$) tend to be considered “late-type”, while galaxies with nearly de Vaucouleurs profiles (Sérsic index $n \sim 4$) tend to be considered “early-type”.

Fig. 5.2 shows the Sérsic index as a function of the SED models (with the same color coding as in Fig. 5.1). There is a good correlation between our 4 main SED types and the Sérsic index, i.e. the 4 SED types of the galaxies in the FDF are also related to the morphology of the galaxies (at least up to redshift $z \sim 1.5$; see Pannella *et al.* 2004 for details).

5.3 Type-dependent luminosity function

In Sect. 5.4 we show the luminosity functions in different redshift bins and filters subdivided into the 4 different SED types described in Sect. 5.2. We chose the redshift binning as described in Tab. 4.1 in order to get good statistics for all analyzed bands: $0.45 < z \leq 0.85$, $0.85 < z \leq 1.31$, $1.31 < z \leq 1.91$,

$1.91 < z \leq 2.61$, and $2.61 < z \leq 3.81$. Furthermore we add a high redshift bin of $3.81 < z \leq 4.51$. We follow the same recipe as described in Sect. 3.5.1 to derive the LF for the different types, i.e. we account not only for the statistical errors, but include also the photometric redshift errors. Furthermore we limit our analysis of every luminosity function to the limiting magnitude where the V/V_{max} begins to contribute by at most a factor of 1.5.

As it is very instructive to follow the type dependent LF evolution not only as a function of redshift, but also as a function of waveband, we show both groupings: In Fig. 5.3, Fig. 5.4, Fig. 5.5, Fig. 5.6, Fig. 5.7, Fig. 5.8, and Fig. 5.9 the luminosity functions are grouped according to the filter for the different redshift bins. In Fig. 5.10, Fig. 5.11, Fig. 5.12, Fig. 5.13, Fig. 5.14, and Fig. 5.15 we group the LF according to redshift for the UV (1500Å, 2800Å), u', g', r', and i' bands (we do not show the z'-band, as it behaves like the i'-band). In all plots we show the LF for SED type 1 (red dots), type 2 (green dots), type 3 (cyan dots), and type 4 (blue dots). For clarity we connect the dots. The total LF is shown by open black circles. Furthermore, we mark in every plot the best fitting Schechter function of the total number density for our low redshift bin ($0.45 < z \leq 0.85$) by a dashed line. The redshift binning used to derive the LFs and the filter is given in the upper right and the upper left corner of every figure, respectively.

First of all we can see from the figures in Sect. 5.4 that independent of the waveband the SED type 1 and type 2 do not contribute at all to the LF for redshifts larger than $z \sim 1.9$. As the depth of the FDF allows us to detect early-type galaxies down to $M_B \lesssim -20.5$ at $z \sim 1.9$ (see Fig. 3.4), the absence of those galaxy is probably real and not due to a selection effect (provided their dust extinction is not exceedingly large). Another argument against a large biasing due to a selection effect is given by Fig. 3.1. There we show that the I-band FDF catalog might be missing only about 10 % of the galaxies that would be detected in a deep K-band selected survey with magnitude limit $K_{AB} \approx 26$ (like in Labbé *et al.*, 2003).

If we focus on the first two redshift bins (Fig. 5.10 and Fig. 5.11) the errors of the LFs are small for all types and we can see that the number densities of SED type 1 and type 2 galaxies are about the same for all filters. There seems to be no strong correlation with the absolute magnitude, i.e. in the optical bands we see the same number density for bright and faint SED type 1 and type 2 galaxies. If we assume that there is no magnitude dependence of the number-density for SED type 1 galaxies (and exclude the brightest bin in every band), we can derive a mean value of ≈ 0.00034 galaxies per mag per Mpc^3 with a typical error of 20% in every waveband for the redshift bin $0.45 < z \leq 0.85$. This assumption is justified since the reduced χ_{red}^2 of the fit is about unity ($0.8 < \chi_{red}^2 \lesssim 1.8$ for all wavebands).

On the other hand, the contribution of SED type 1 and type 2 to the total luminosity function (black open circles) increases from the UV to the z'-band: In the UV the bright end of the LF is purely dominated by SED type 3 and type 4, whereas SED type 1 and type 2 dominate the bright end of the LF in the r'- and z'-band. Moreover, the faint end of the total LFs in Fig. 5.10 and Fig. 5.11 is dominated by SED type 3 and type 4 galaxies in *all* bands.

The relative contribution of type 1/2 and type 3/4 SEDs to the total LF may also explain the steeper slope in the red bands (Table 4.3) if compared to the blue bands (Table 3.3). We see in Fig. 5.10 and Fig. 5.11 that for the UV bands the bright end of the LF is dominated by the SED of type 3 and type 4. If we look at the LF for increasing wavebands ($u' \rightarrow g' \rightarrow r' \rightarrow i'$), the bright end is more and more dominated by SED of type 1 and type 2. On the other hand bright galaxies of SED type 4 decrease in number density very fast for increasing wavebands ($u' \rightarrow i'$). This decrease can hardly be compensated by the other SED types. Ergo, the slope of the total luminosity function steepens for

increasing wavebands ($u' \rightarrow g' \rightarrow r', i', z'$). For $1.31 < z \leq 1.91$ (Fig. 5.12) the contribution of SED type 1/2 to the bright end in the red filters is still non negligible supporting the interpretation of the steeper slope in the red bands (see Table 4.2 for the 3-parameter Schechter fits).

For $1.91 < z \leq 2.61$ (Fig. 5.13) and higher redshift the LF is entirely dominated by galaxies of SED type 3 and type 4. The slope as derived by the single 3-parameter Schechter fits (Table 4.2) seems to decrease for the red bands, which also supports the interpretation given before. Please note that since in our high redshift bins with $\langle z \rangle \sim 3.2$ or higher all the luminosity functions are extrapolations for the red bands (at redshift $\langle z \rangle \sim 2.5$ restframe r' roughly corresponds to the observerframe K-band) we have to make a note of caution at this point. One would need deep data at wavelength larger than $2.2\mu\text{m}$ (K-band) to address this issue in a more quantitative way. This point will be addressed very soon by the Spitzer (alias SIRTf) satellite (Fanson *et al.*, 1998). Spitzer will obtain images and spectra by detecting the infrared energy, or heat, radiated by objects in space between wavelengths of $3\mu\text{m}$ and $180\mu\text{m}$.

5.4 Appendix of Chapter 5

In this appendix we show the V/V_{max} corrected luminosity functions in the different redshift bins and filters subdivided into the 4 different SED types (see Sect. 5.2). In all plots we show the LF for SED type 1 (red dots), type 2 (green dots), type 3 (cyan dots), and type 4 (blue dots). For clarity we connect the dots. The best fitting Schechter function of the total number density (black circles) for our low redshift bin ($0.45 < z \leq 0.85$) is marked in every plot by a dashed line. The redshift binning used to derive the LFs and the filter is given in the upper right and the upper left part of every figure, respectively. We show only points with $V/V_{max} < 1.5$.

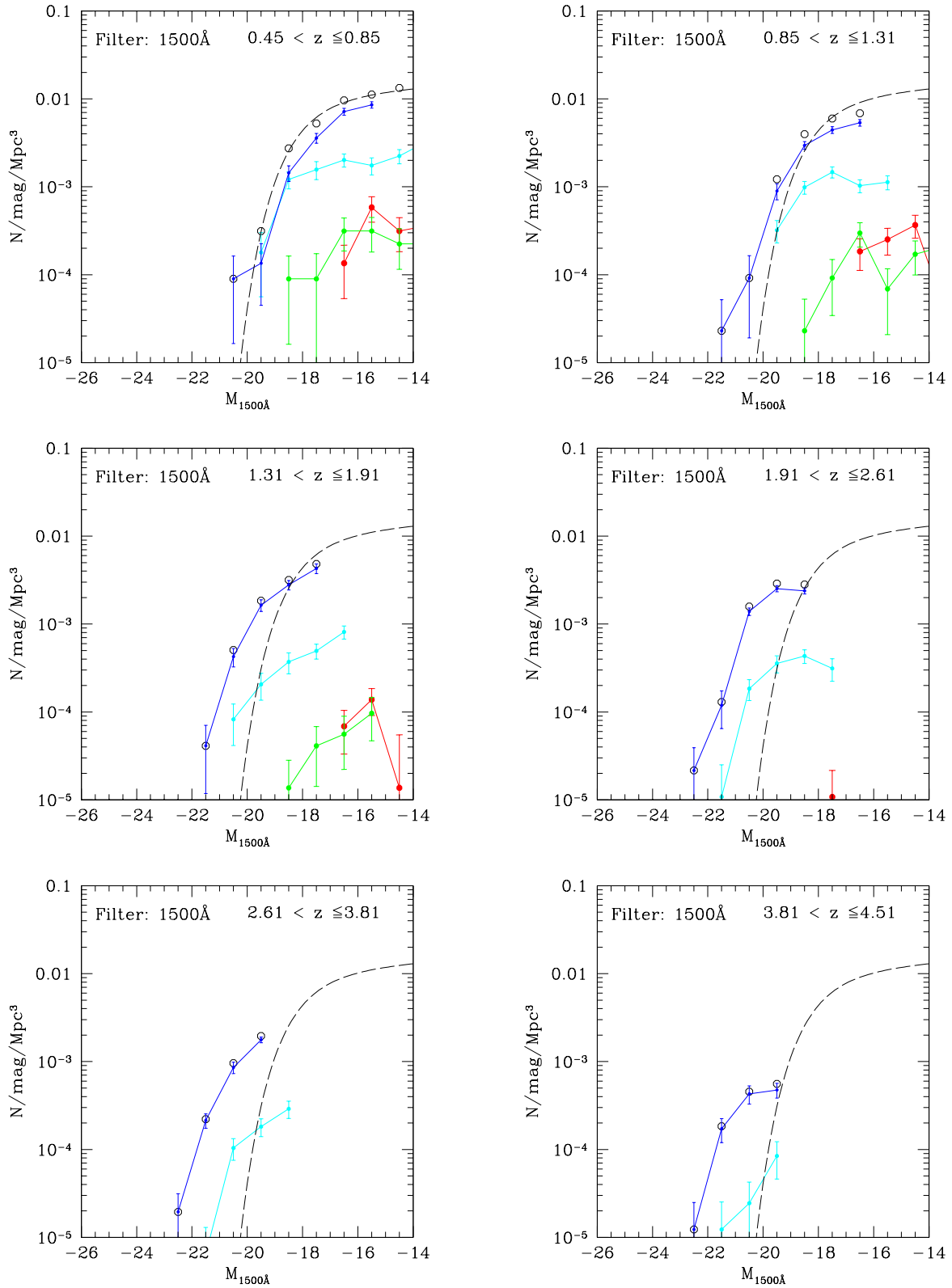


Figure 5.3: Luminosity function per SED type grouped by the 1500 \AA filter. See text in Sect. 5.4

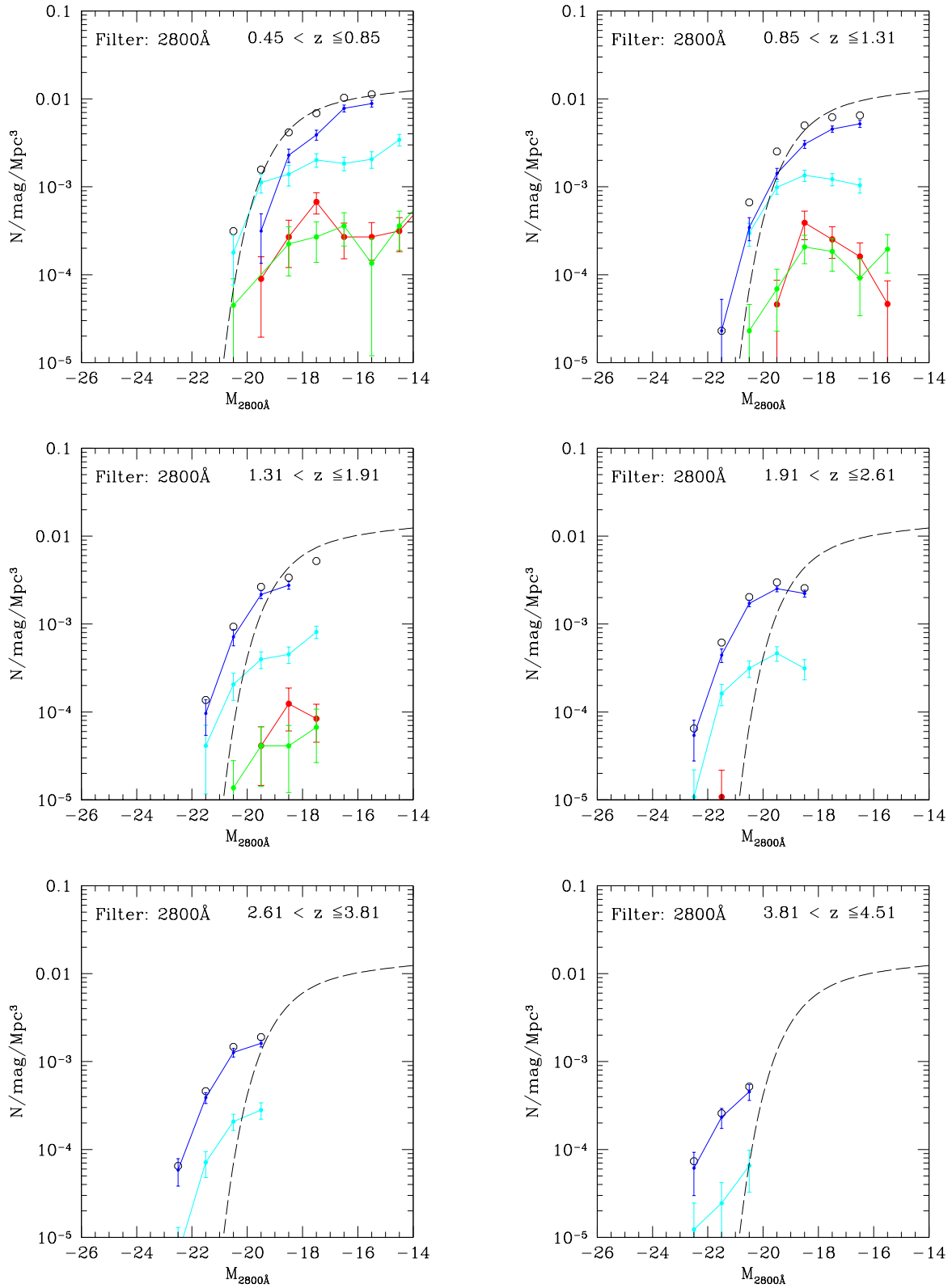


Figure 5.4: Luminosity function per SED type grouped by the 2800 \AA filter . See text in Sect. 5.4

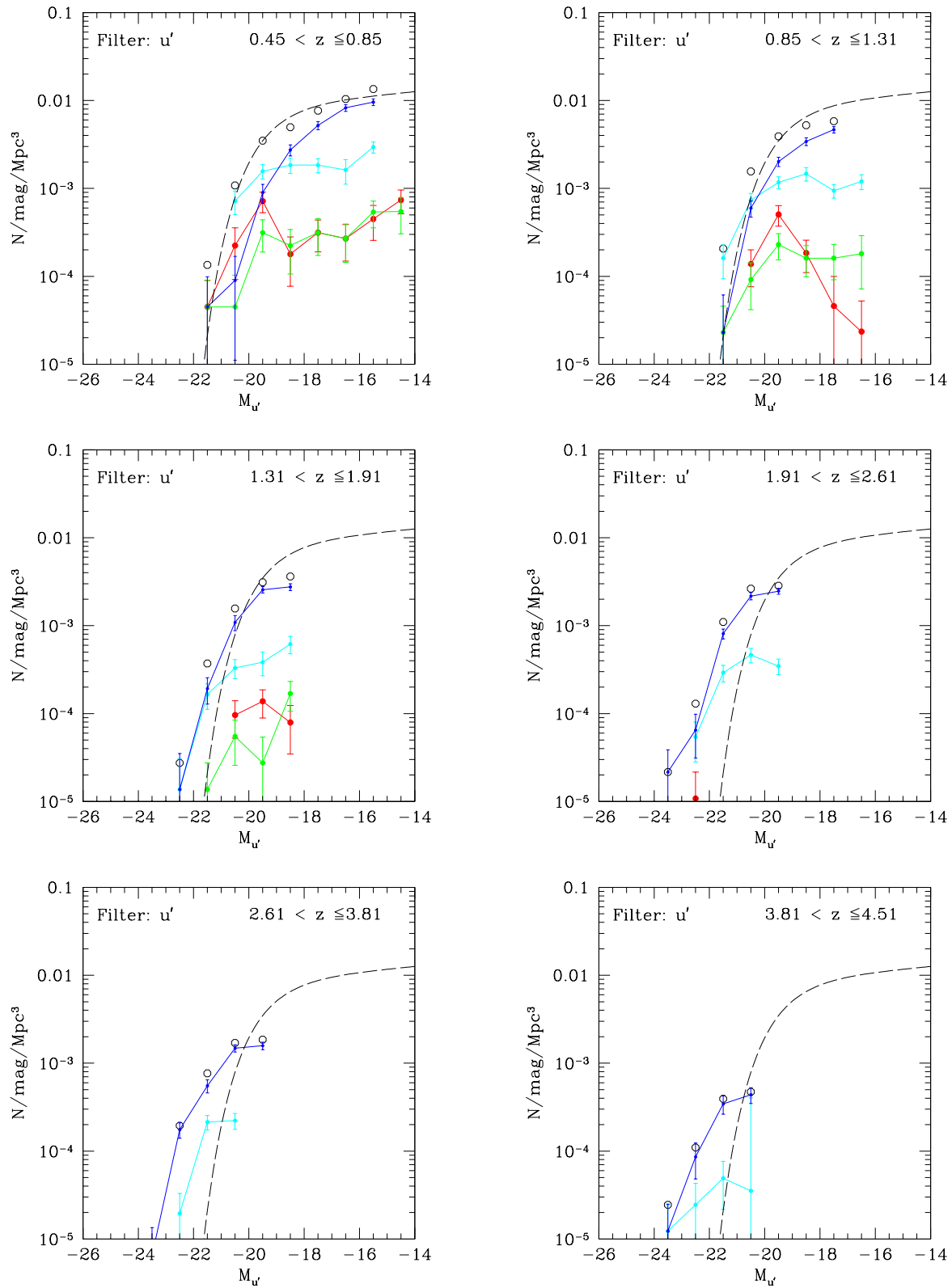


Figure 5.5: Luminosity function per SED type grouped by the u' -band. See text in Sect. 5.4

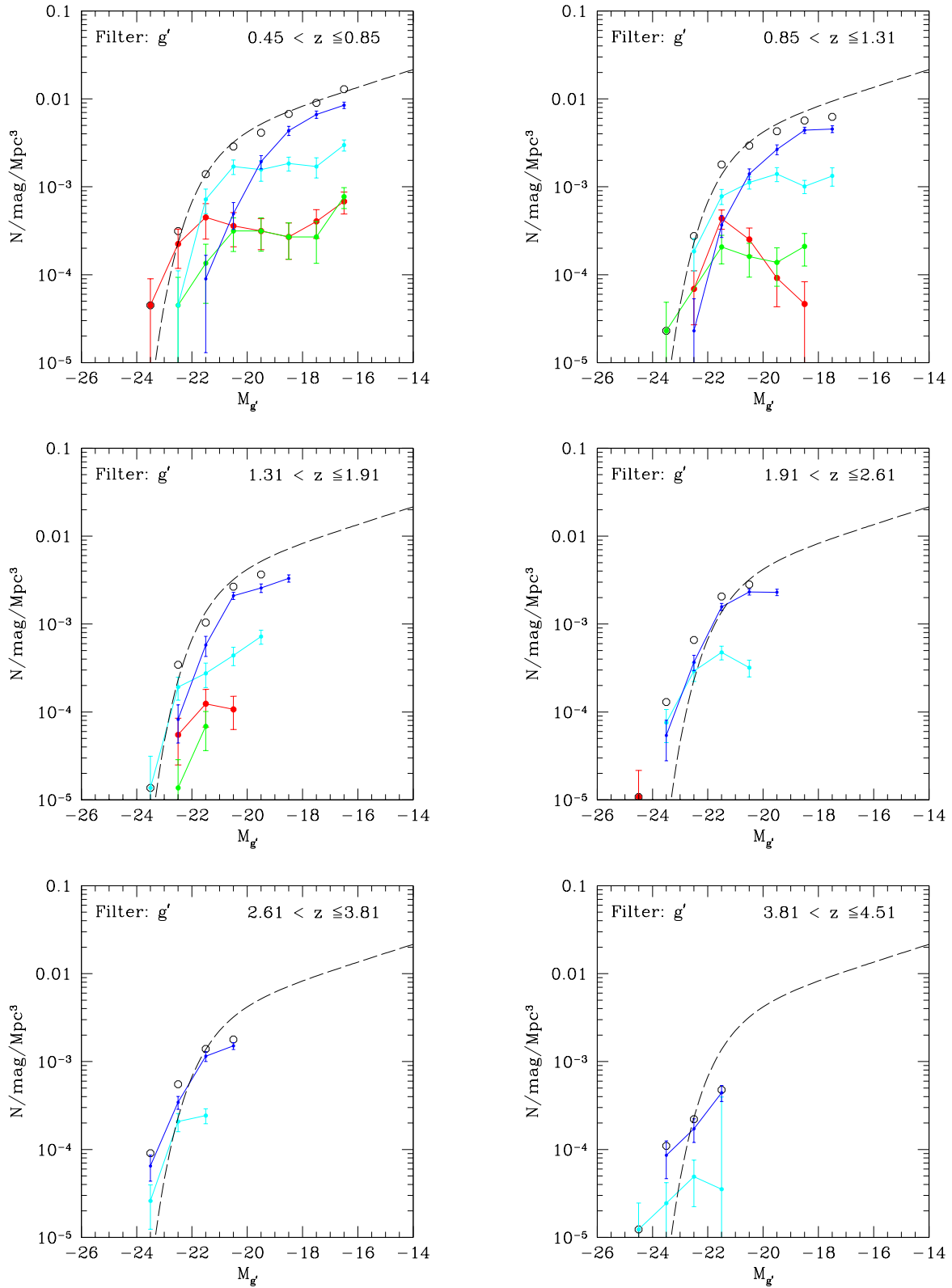


Figure 5.6: Luminosity function per SED type grouped by the g' -band. See text in Sect. 5.4

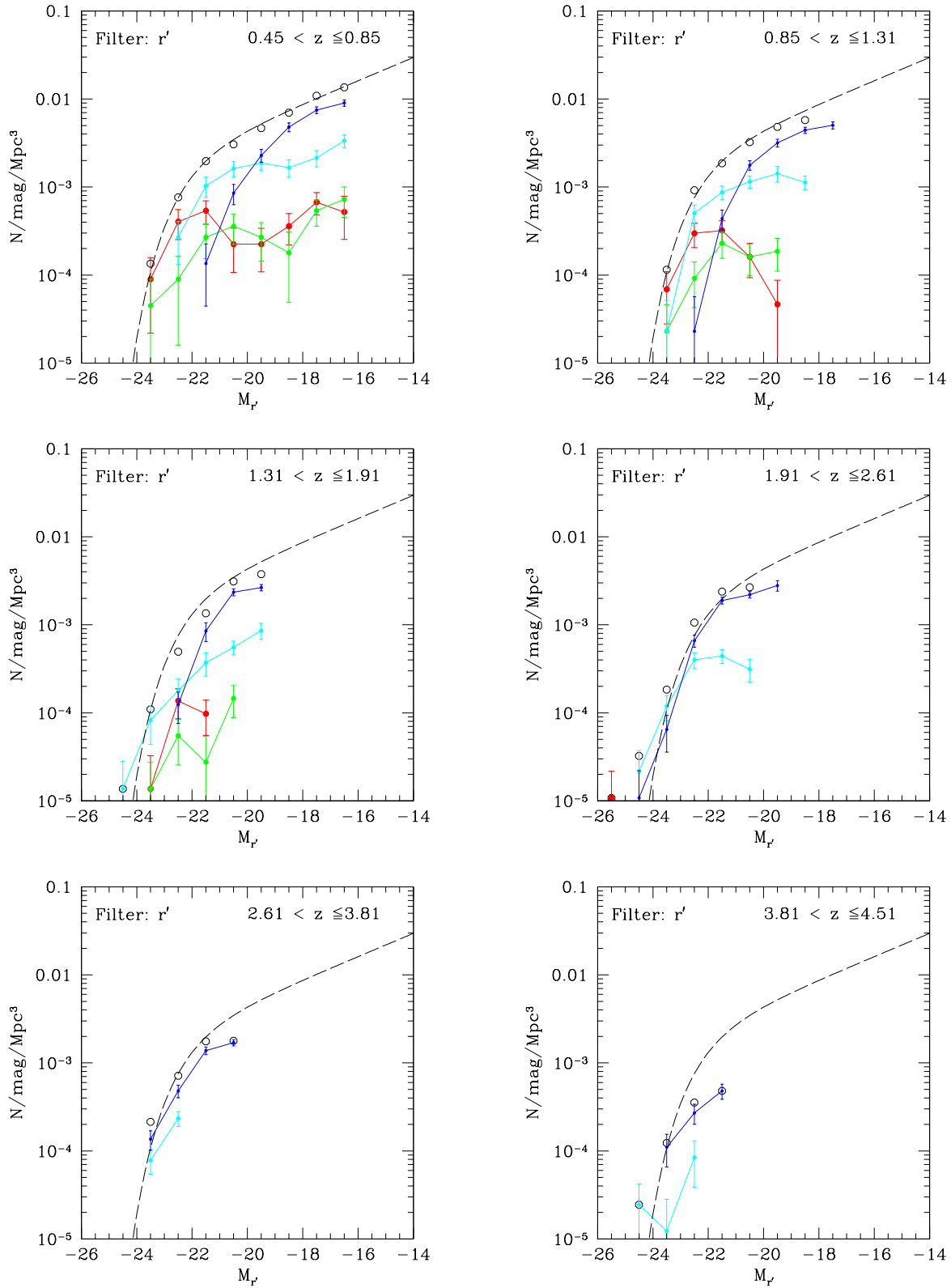


Figure 5.7: Luminosity function per SED type grouped by the r' -band. See text in Sect. 5.4

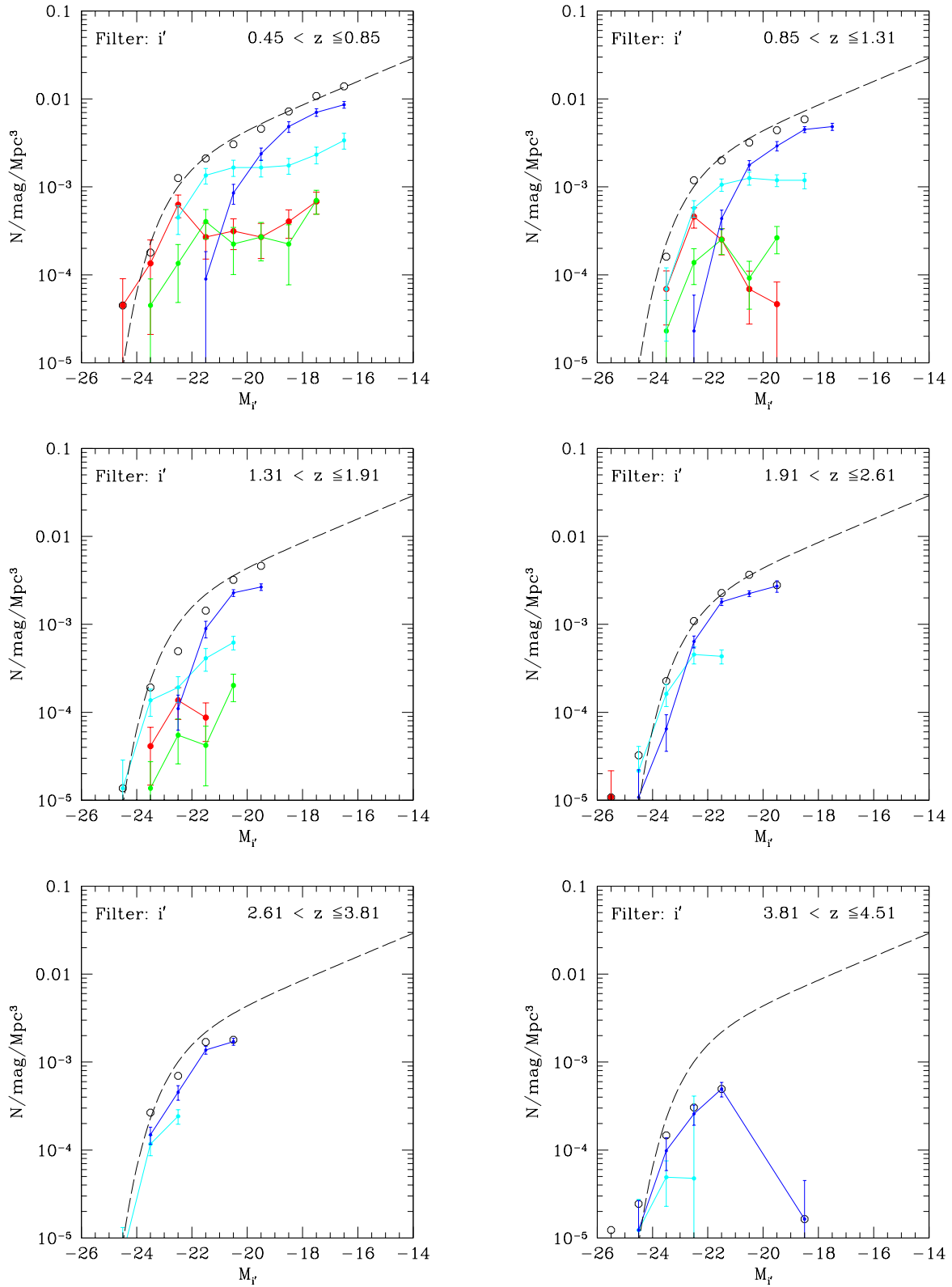


Figure 5.8: Luminosity function per SED type grouped by the i' -band. See text in Sect. 5.4

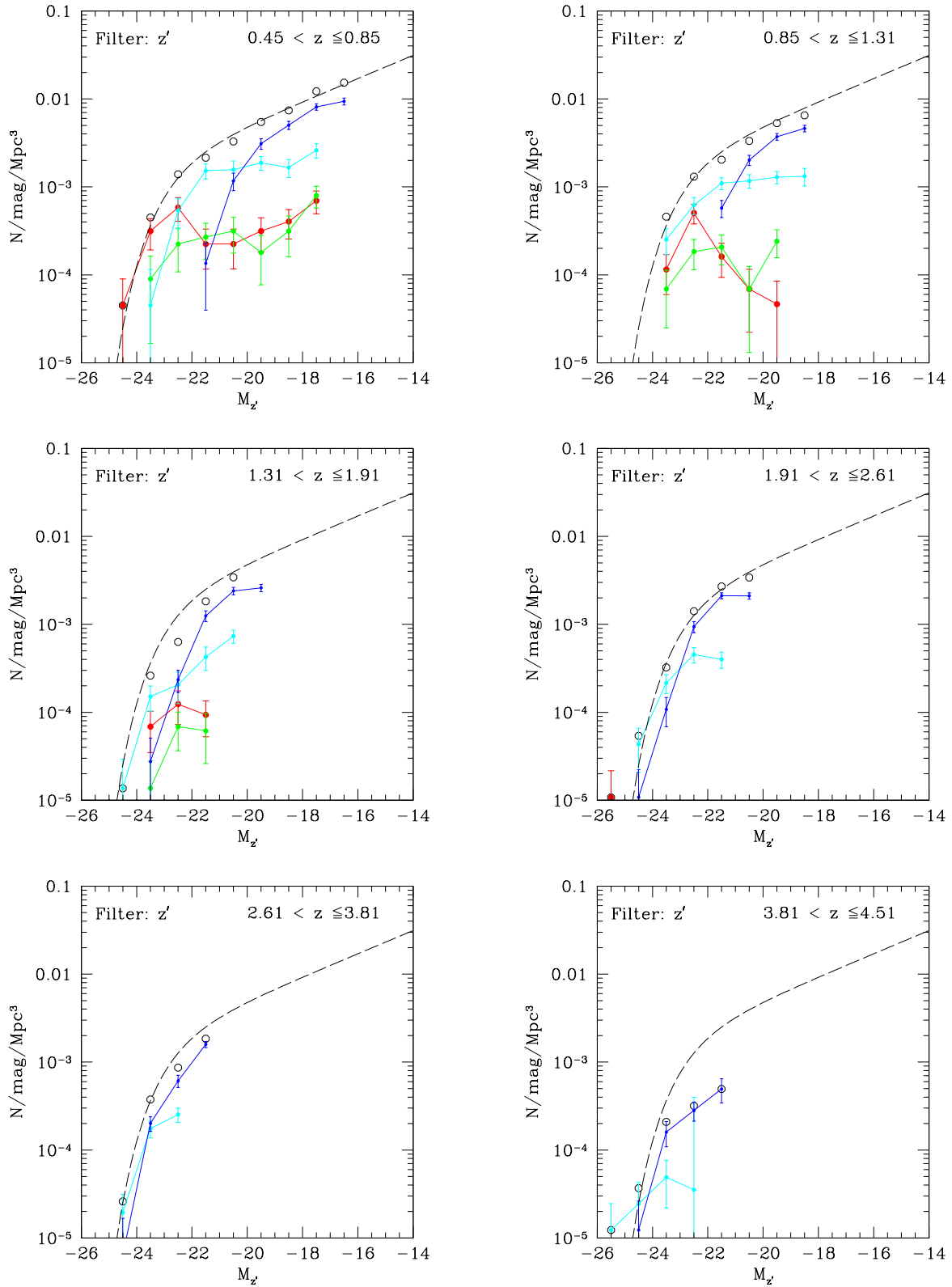


Figure 5.9: Luminosity function per SED type grouped by the z' -band. See text in Sect. 5.4

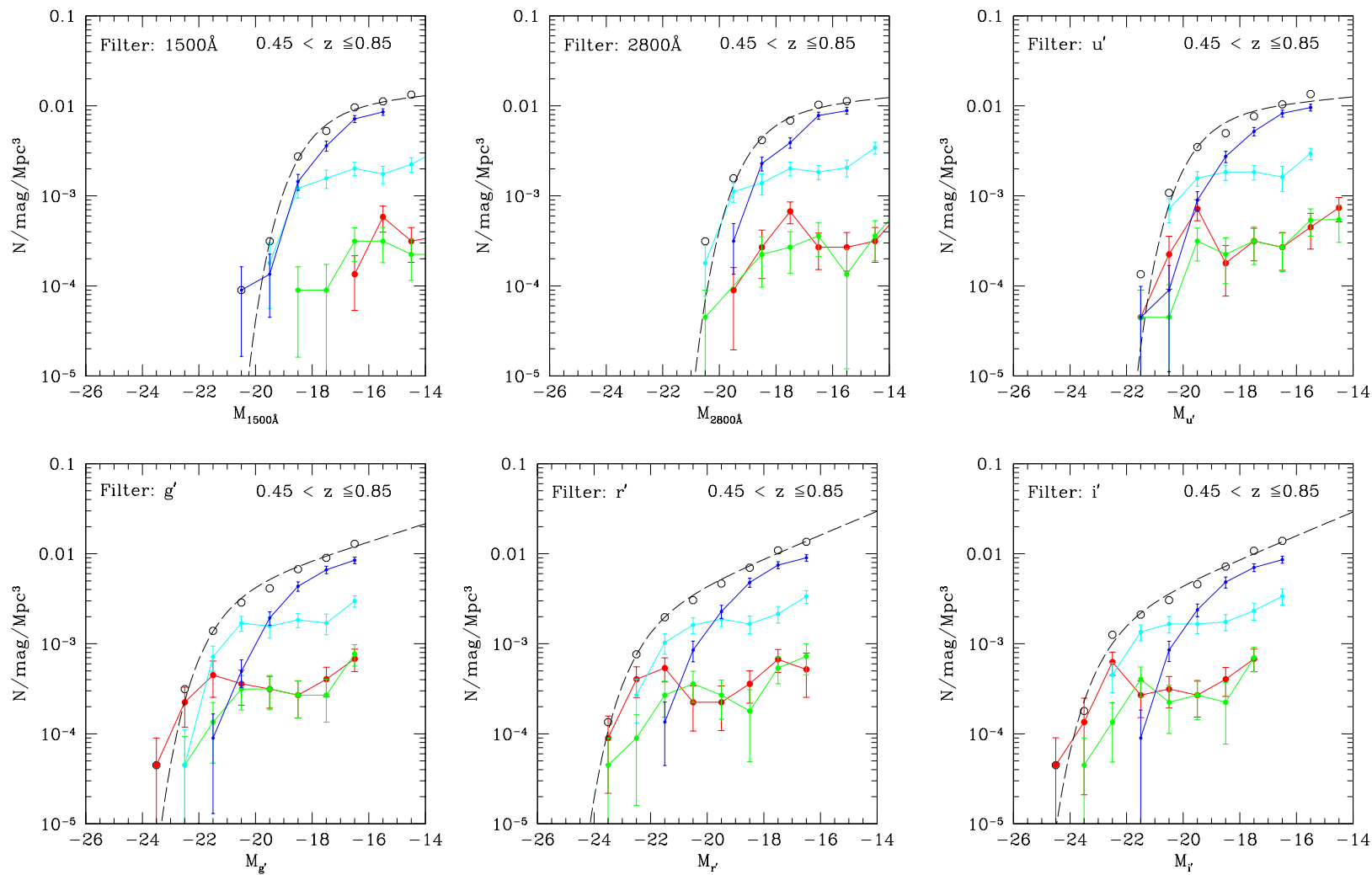


Figure 5.10: Luminosity function per SED type grouped by *redshift*: $0.45 < z \leq 0.85$. See text in Sect. 5.4

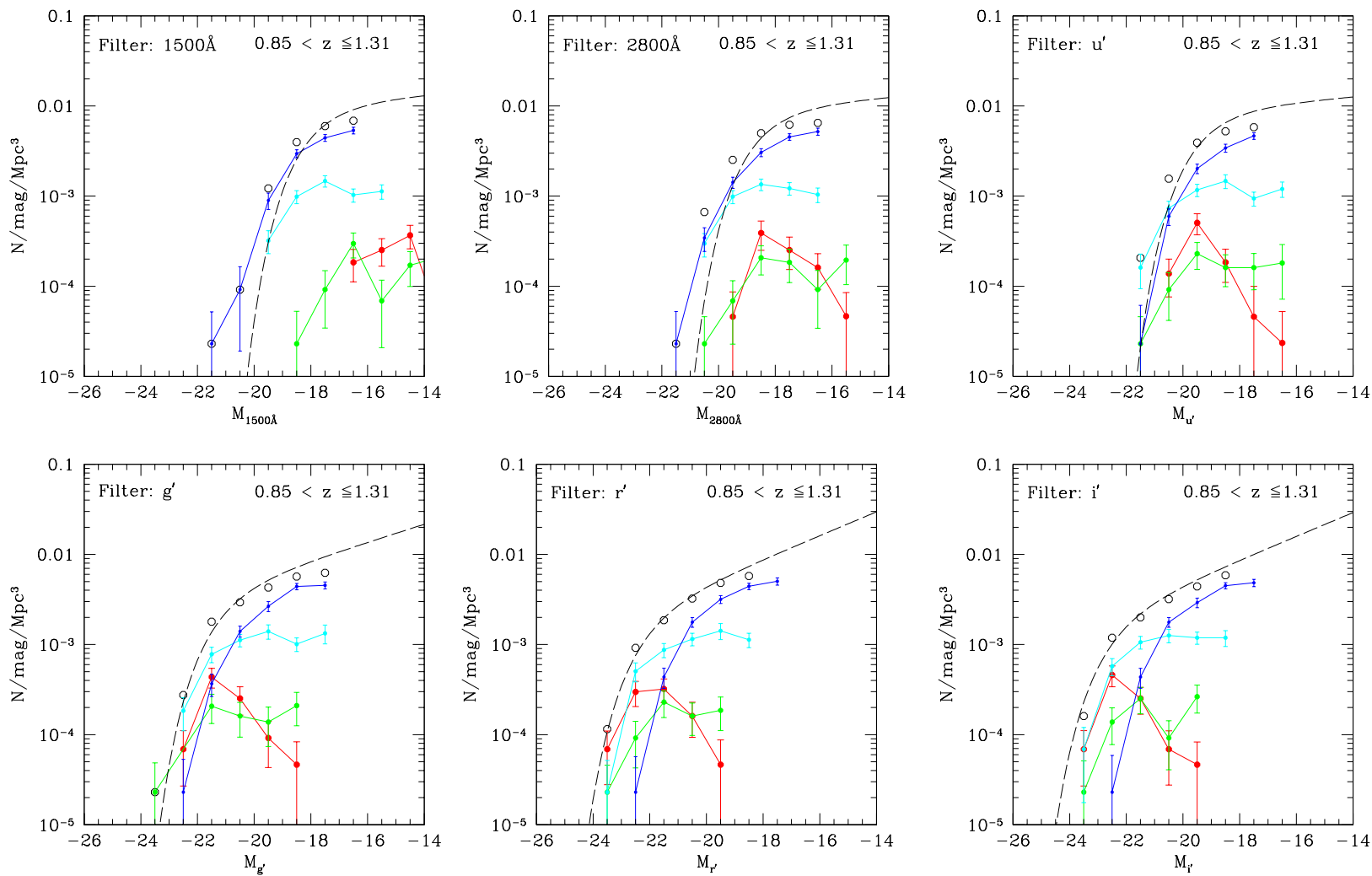


Figure 5.11: Luminosity function per SED type grouped by *redshift*: $0.85 < z \leq 1.31$. See text in Sect. 5.4

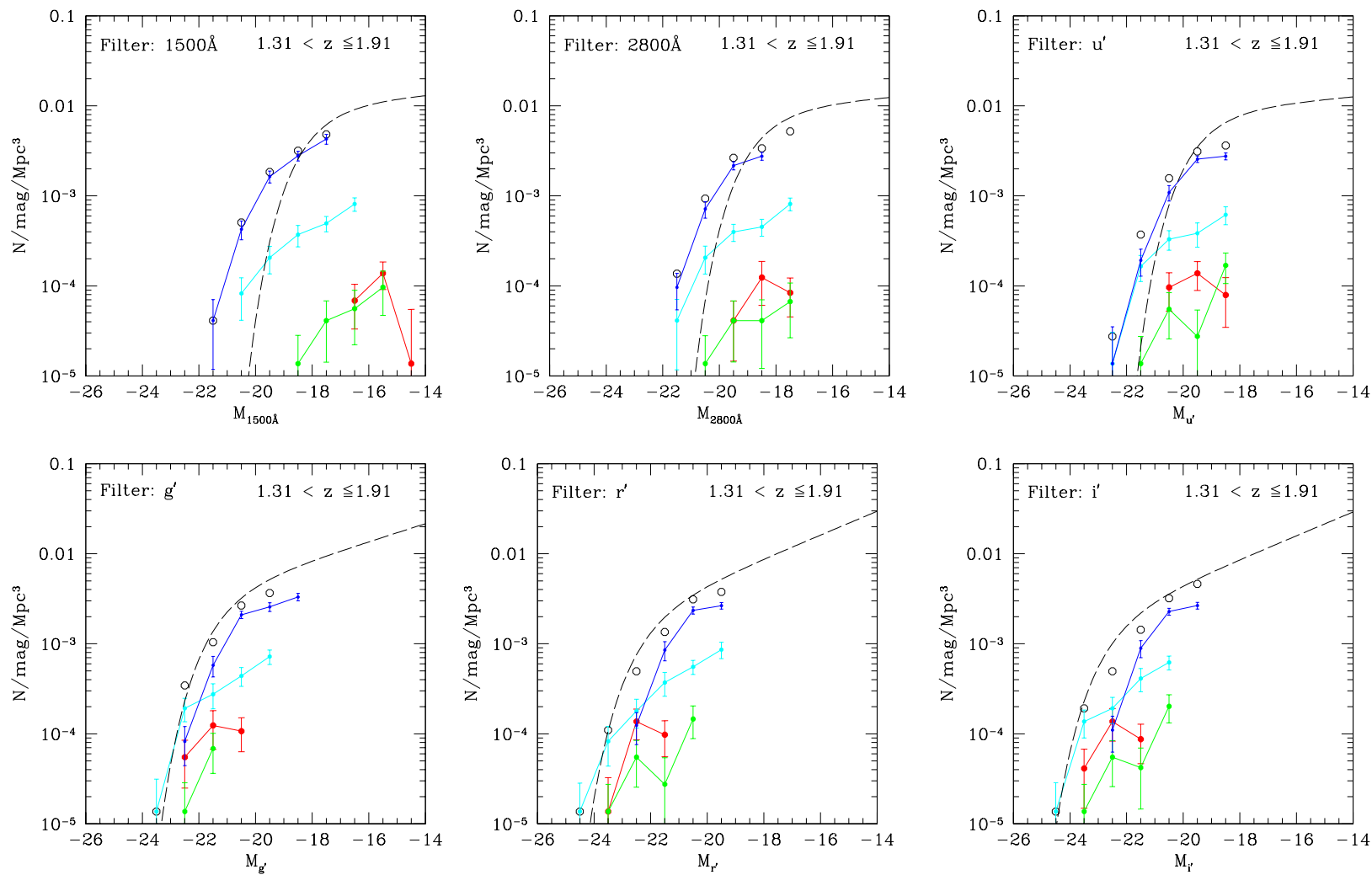


Figure 5.12: Luminosity function per SED type grouped by *redshift*: $1.31 < z \leq 1.91$. See text in Sect. 5.4

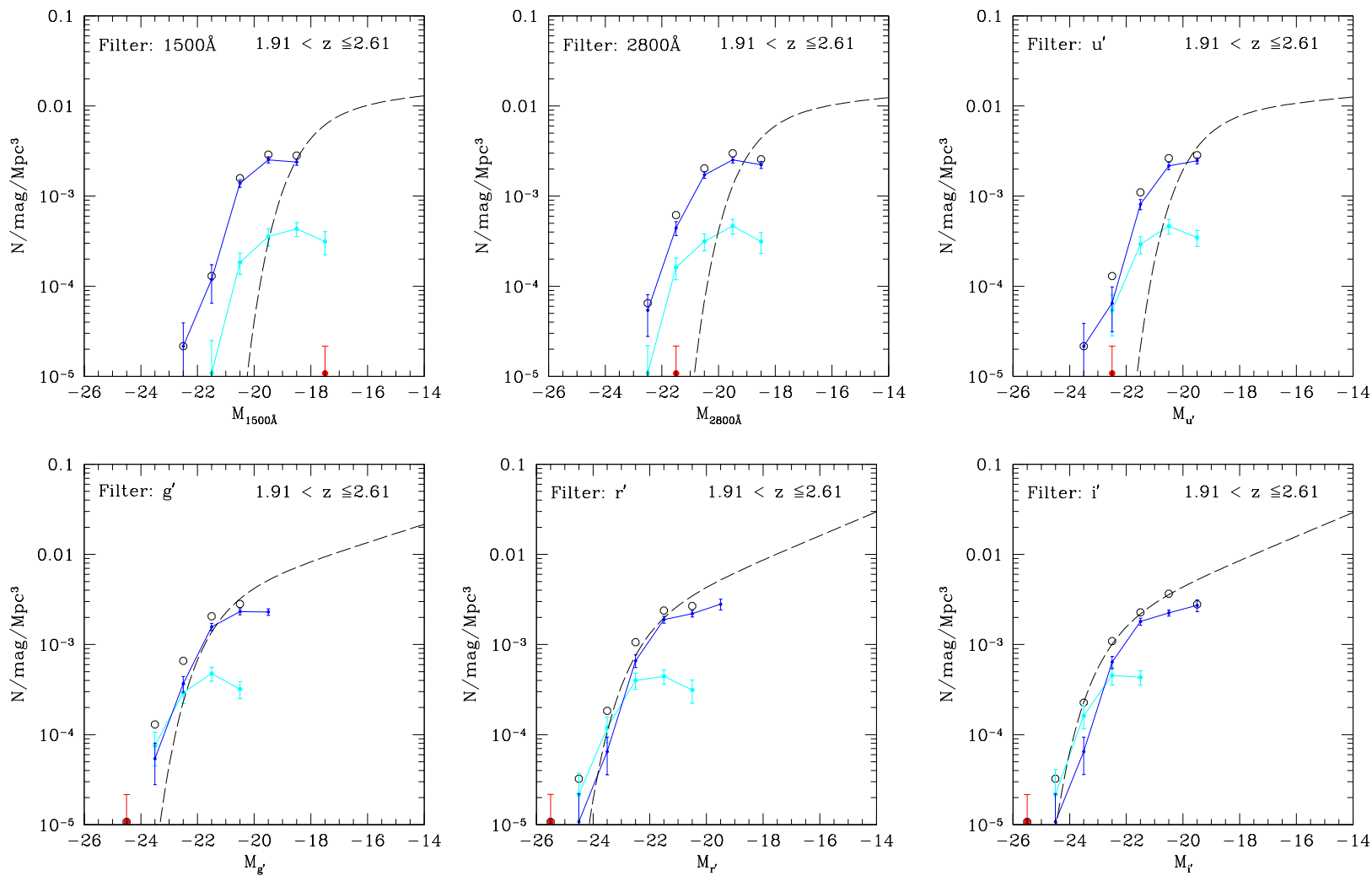


Figure 5.13: Luminosity function per SED type grouped by *redshift*: $1.91 < z \leq 2.61$. See text in Sect. 5.4

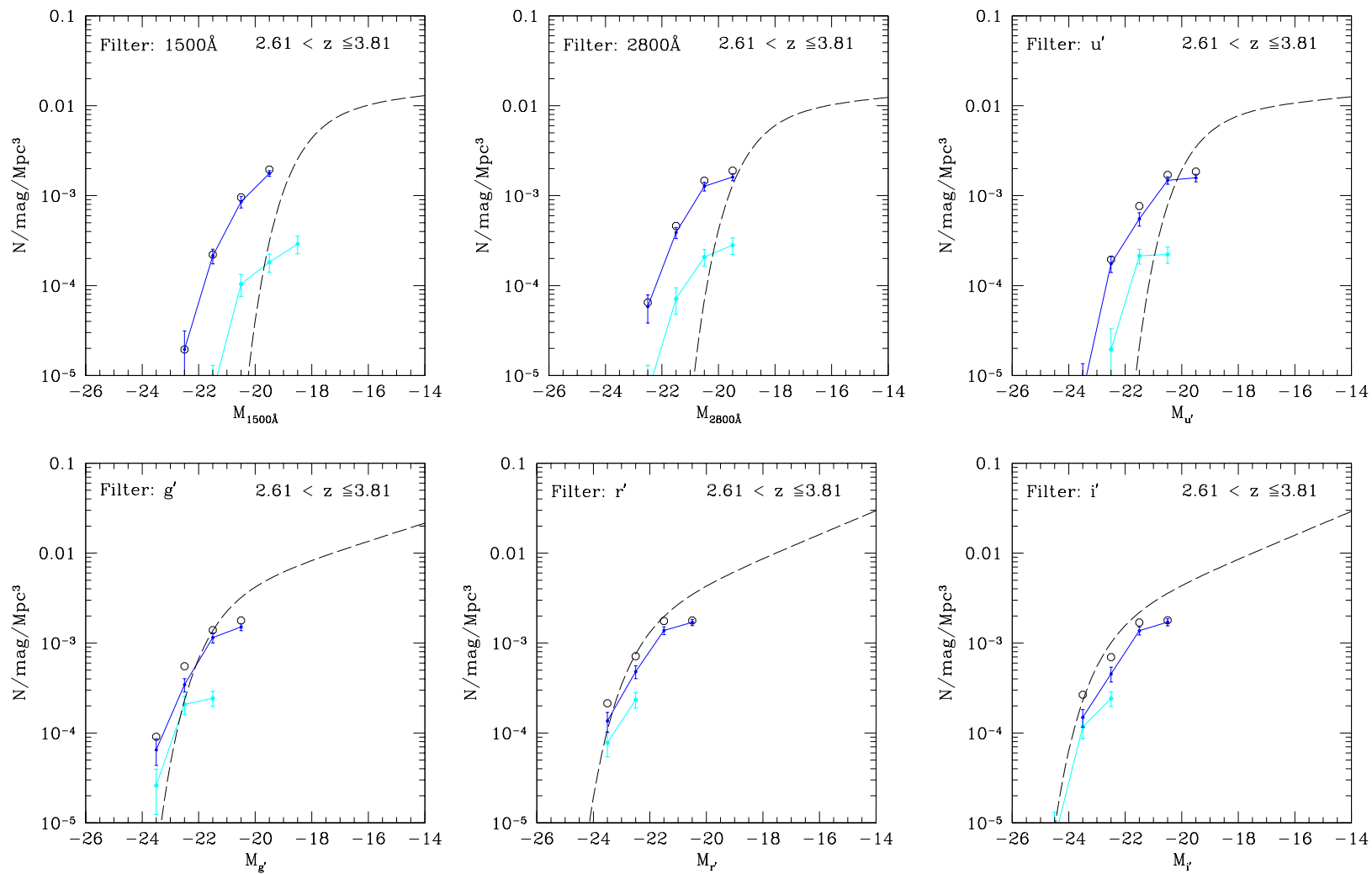


Figure 5.14: Luminosity function per SED type grouped by *redshift*: $2.61 < z \leq 3.81$. See text in Sect. 5.4

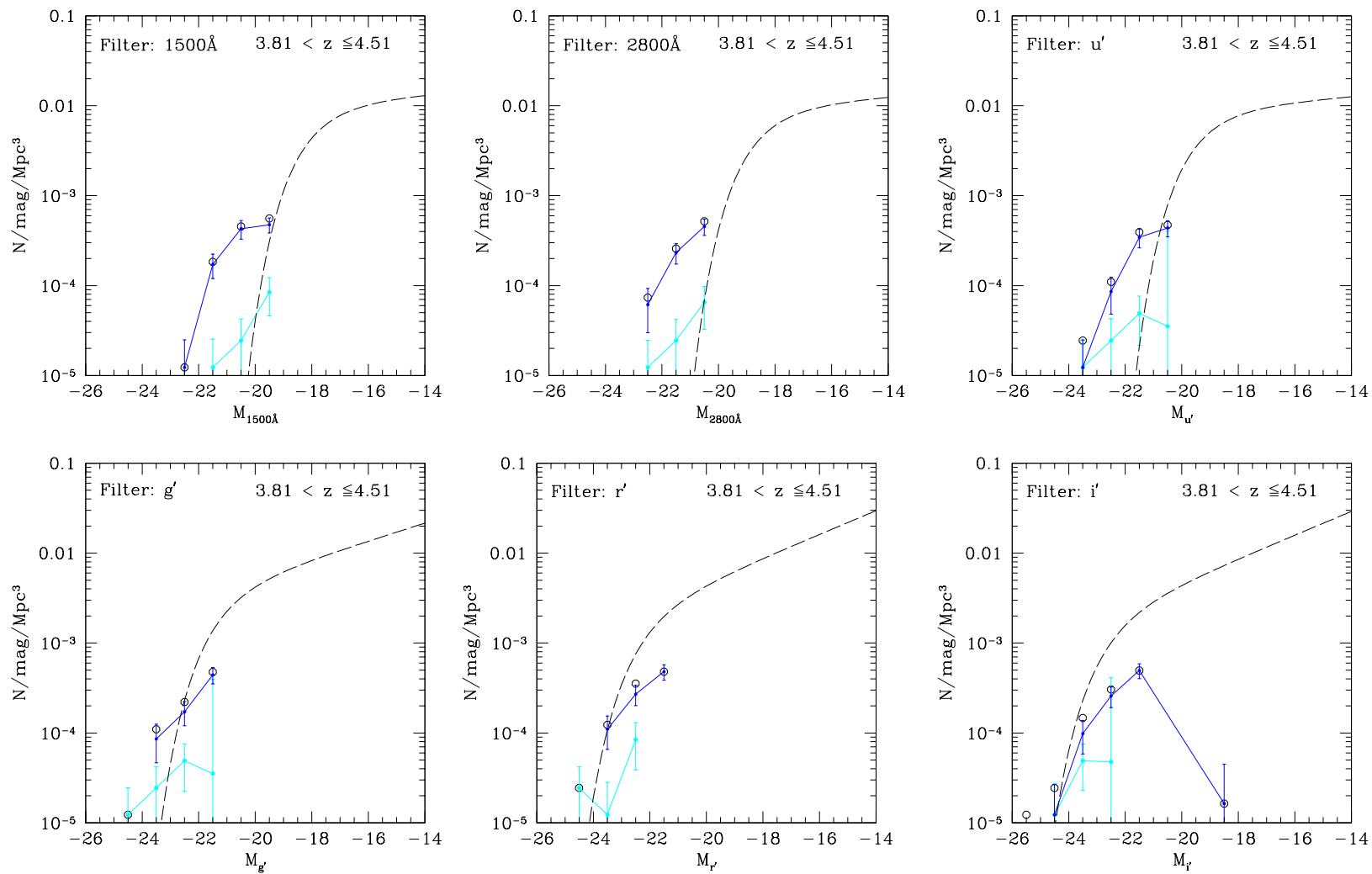


Figure 5.15: Luminosity function per SED type grouped by *redshift*: $3.81 < z \leq 4.51$. See text in Sect. 5.4

Chapter 6

The star formation rate history in the FORS Deep and GOODS South Fields¹

Abstract. We measure the star formation rate (SFR) as a function of redshift z out to $z \approx 4.5$, based on B, I and (I+B) selected galaxy catalogs from the FORS Deep Field (FDF) and the K-selected catalog from the GOODS-South field. Distances are computed from spectroscopically calibrated photometric redshifts accurate to $\Delta z_i / (z_{spec} + 1) \leq 0.03$ for the FDF and ≤ 0.056 for the GOODS-South field. The SFRs are derived from the luminosities at 1500 \AA . We find that the total SFR estimates derived from B, I and I+B catalogs agree very well ($\lesssim 0.1$ dex) while the SFR from the K catalog is lower by ≈ 0.2 dex. We show that the latter is solely due to the lower star-forming activity of K-selected intermediate and low luminosity ($L < L_*$) galaxies. The SFR of bright ($L > L_*$) galaxies is independent of the selection band, *i.e.* the same for B, I, (I+B), and K-selected galaxy samples. At all redshifts, luminous galaxies ($L > L_*$) contribute only $\sim \frac{1}{3}$ to the total SFR. There is no evidence for significant cosmic variance between the SFRs in the FDF and GOODS-South field, $\lesssim 0.1$ dex, consistent with theoretical expectations. The SFRs derived here are in excellent agreement with previous measurements provided we assume the same faint-end slope of the luminosity function as previous works ($\alpha \sim -1.6$). However, our deep FDF data indicate a shallower slope of $\alpha = -1.07$, implying a SFR lower by ≈ 0.3 dex. We find the SFR to be roughly constant out to $z \approx 4$ and then to decline slowly beyond, if dust extinctions are assumed to be constant with redshift.

¹This chapter is a slightly modified and updated version of the article Gabasch *et al.* (2004c). Modified sections are highlighted by footnotes

6.1 Introduction

The determination of the star formation rate (SFR) history of the universe is one of the most interesting results extracted from the deep photometric and spectroscopic surveys of the last decade. A large number of measurements have been collected, at low (the Canada-France redshift survey at $z < 1$, Lilly *et al.*, 1996), and high redshift from the Hubble Deep Field North (Madau *et al.*, 1996), the large samples of U and B drop-out galaxies (Steidel *et al.*, 1999), up to the most recent determinations based on I-dropouts at redshift ≈ 6 from the GOODS, UDF and UDF-Parallel ACS fields (Giavalisco *et al.*, 2004a; Bunker *et al.*, 2004; Bouwens *et al.*, 2004). These studies show that the SFR (uncorrected for dust) increases from $z = 0$ to $z = 1$, stays approximately constant in the redshift range 1 – 4, and starts to decline at larger redshifts. In all the cases quoted above the determination is based on the estimate of the total UV galaxy luminosity density, that for a given IMF is proportional to the instantaneous SFR (Madau *et al.*, 1996, 1998). As discussed by many authors (e.g. Hopkins *et al.* 2001) this approach is affected by the uncertainties of dust correction, but roughly agrees with other estimators at low to intermediate redshifts ($z \leq 1$). Theoretical models of galaxy formation and evolution can be tested against the measured SFR history (Somerville *et al.*, 2001; Hernquist & Springel, 2003).

So far, all determinations of the SFR history have suffered from some major limitations. High redshift samples have been small in number due to the limited field of view of deep pencil-beam surveys, resulting in large Poissonian fluctuations and large field-to-field variations (cosmic variance). The faint-end of the luminosity function (LF) is thusfar only poorly constrained at high redshifts, implying large completeness correction factors. Finally, the technique used to generate the high-redshift galaxy catalogs (drop-out selection, optical magnitude limited survey) might have introduced biases by selecting only specific types of

galaxies and possibly missing relevant fractions of UV light (Ilbert *et al.*, 2004).

Here we try to minimize these uncertainties and determine the SFR history of the universe with improved accuracy out to $z \approx 4.5$. Our sample of high redshift galaxies is based on two deep fields, the (I and B selected) FORS Deep Field (FDF, Heidt *et al.*, 2003), and the (K-selected) GOODS-South field (Giavalisco *et al.*, 2004b). Both cover a relatively large sky area, reducing the problem of cosmic variance. Both are deep enough to allow the detection of several $\times 10^3$ galaxies, thus minimizing the effect of shot noise.

Accurate photometric redshifts ($\Delta z / (z_{spec} + 1) \leq 0.03$ for the FDF and ≤ 0.056 for the GOODS-South field) with only $\approx 1\%$ catastrophic failures allow us to measure the UV luminosity function down to fainter limits than spectroscopic samples. A detailed comparison of the UV luminosity functions of the FDF with the LF derived in large surveys was presented in Gabasch *et al.* (2004b) and shows good agreement in the overlapping magnitude range at all redshifts. Finally and most importantly, the two fields provide us with B-band, I-band and K-band selected catalogs, making it possible to assess the dependence of the SFR on the detection band and galaxy colors and the associated selection biases.

The Letter is organized as follows. In §6.2 we discuss the photometry and the photometric redshifts of the two fields, in §6.3 we present our results on the SFR history, and in §6.4 we draw our conclusions. Throughout the paper we use AB magnitudes and adopt a concordance cosmology with $\Omega_M = 0.3$, $\Omega_\Lambda = 0.7$, and $H_0 = 70 \text{ km s}^{-1} \text{ Mpc}^{-1}$.

6.2 Data sets

The present results are based on photometric catalogs derived for the FDF (Heidt *et al.*, 2003; Gabasch *et al.*, 2004b, UBgRI,834 nm,zJKs bands) and the GOODS-South fields (Salvato *et al.*, 2004, UBVRIJKs bands). The two

fields cover approximately the same area (39.81 arcmin² for FDF and 50 arcmin² for GOODS); the FDF reaches effective absolute magnitude limits ≈ 1 mag deeper than GOODS-South (see below). We use the I-band and B-band selected FDF catalogs as derived in Heidt *et al.* (2003) and Gabasch *et al.* (2004b). The B and I selected catalogs list 5488 and 5557 bona-fide galaxies (having excluded the one known bright quasar in the field) down to $B_{lim} = 27.6$ and $I_{lim} = 26.8$, respectively. The I+B catalog obtained by merging these two contains 6756 entries. Photometric redshifts for the FDF galaxies have an accuracy of $\Delta z / (z_{spec} + 1) \leq 0.03$ with only $\sim 1\%$ catastrophic outliers (Gabasch *et al.*, 2004b).

Our K-band selected catalog for the GOODS-South field is based on the $8 \times 2.5 \times 2.5$ arcmin² J, H, Ks VLT-ISAAC images publically available, taken with seeing in the range $0.4'' - 0.5''$. The U and I images are from GOODS/EIS public survey, while B V R are taken from the Garching-Bonn Deep Survey. Data reduction is described in Arnouts *et al.* (1999a) and Schirmer *et al.* (2003), respectively. The data for the GOODS field were analyzed in a very similar way to the data of the FDF. The objects were detected in the K-band images closely following the procedure used for the FDF I and B band detection (Heidt *et al.*, 2003), using both SExtractor (Bertin & Arnouts, 1996) and the YODA package (Drory, 2003). A detailed description of the procedure can be found in Salvato *et al.* (2004). We detected 3367 objects in K-band for which we derived magnitudes (fixed aperture and total) in all bands. Number counts match the literature values down to $K \approx 25.4$, which is the completeness limit of the catalog, in agreement with the number obtained following Snigula *et al.* (2002). Note that much deeper ACS based catalogs are available (Giavalisco *et al.*, 2004b), but as we are focusing on the K-selection they are not relevant in this context. We computed photometric redshifts following Bender *et al.* (2001, 2004, in preparation) and using the same SED template spectra as for the FDF. The comparison with

the spectroscopic redshifts of the VIMOS team (Le Fevre *et al.*, 2004) and the FORS2 spectra released at <http://www.eso.org/science/goods/>, shows that the photometric redshifts have an accuracy $\Delta z / (z_{spec} + 1) \leq 0.056$. Similar results are obtained when comparing to the COMBO-17 (Wolf *et al.*, 2004) data. This is nearly a factor of 2 better than Mobasher *et al.* (2004) obtained using ground-based plus HST/ACS data. Stars are identified and excluded as in Gabasch *et al.* (2004b), as well as known AGN (Szokoly *et al.*, 2003), leaving 3297 bona-fide galaxies used in the further analysis.

Fig. 6.1 shows the distribution of galaxies (slightly smoothed with a Gaussian kernel) in the rest frame 1500Å absolute magnitude M_{1500} vs. redshift plane, computed by integrating the best fitting SED over the band definition (1500 ± 100 Å). The contours agree remarkably well at the bright-end showing that the number density of bright galaxies does not significantly depend on the wavelength at which they were selected (for the B-band, this is of course only true up to $z \approx 3$). For better comparability of the FDF and GOODS-South samples at the faint-end, we chose a consistent magnitude cut-off for all samples in Fig. 6.1. This magnitude cut-off corresponds to the completeness limit of the GOODS-South sample and is about one magnitude brighter than the completeness limits of the FDF B and I samples. For the redshift bins defined by the limits 0.45, 0.81, 1.21, 1.61, 2.43, 3.01, 4.01, 5.01, the cut-offs in M_{1500} are at -15, -16, -17, -18, -19, -20, -20.

The M_{1500} LFs and the related parameters M_* , Φ_* and α of the B, I, and (I+B) selected FDF samples are almost identical. We derived consistent values for α (-1.07 ± 0.04) for all three samples considered here, similar to that described in Gabasch *et al.* (2004b). Consistent faint-end slopes ($\alpha = -1.01 \pm 0.08$) were obtained using a brighter subset of the data set (i.e. 1 mag brighter than the 50% completeness limit). Objects that were detected in only one band and not in both are all faint and do not contribute significantly to SFR determined from the integral over the LF.

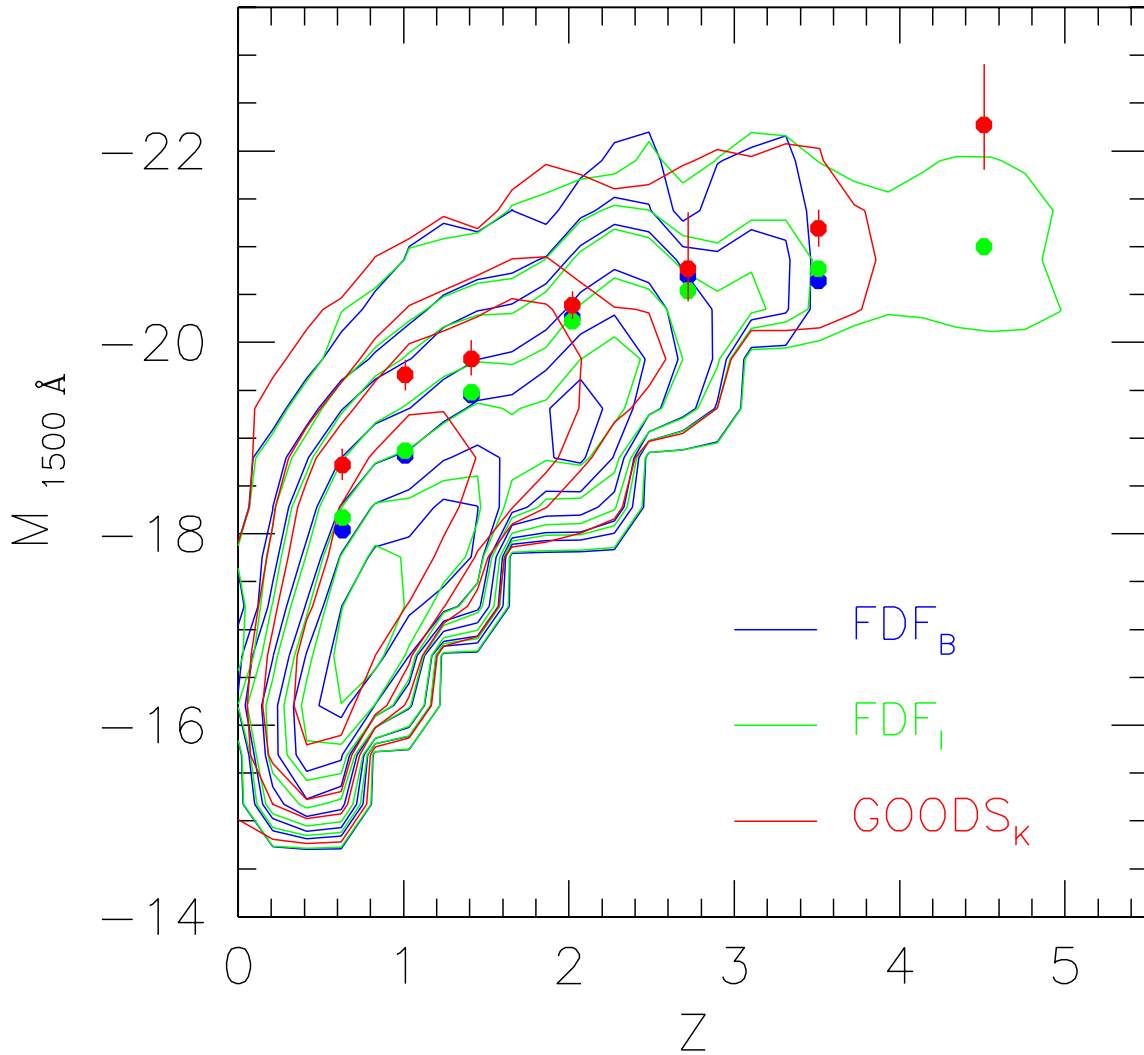


Figure 6.1: The distribution of galaxies in the rest-frame, 1500 \AA absolute magnitude vs. redshift space, slightly smoothed with a Gaussian kernel. The red colors refer to the K-selected galaxies of the GOODS-South field, the blue and the green colors to B and I selected galaxies of the FDF. The lowest contour corresponds to $0.75 \text{ galaxies/arcmin}^2/\text{mag}$ per unit redshift bin; the others give the 2.5, 3.75, 6.25, 8.75, 11.25 and $13.75 \text{ galaxies/arcmin}^2/\text{mag}$ per unit redshift bin density levels. For a better comparison of the FDF and GOODS-South samples at the faint-end, we chose the completeness limit of the GOODS-South as the magnitude cut-off for all samples. The solid circles show the best-fit values of M_* , with the errorbars of the K determinations (similar or smaller errors are derived in I and B).

Gabasch *et al.* (2004b) show that the steeper slope of other surveys is largely due to shallower limiting magnitudes. This is supported by an analysis of $z \sim 6$ dropouts from GOODS and the Hubble Ultra Deep Parallel Fields (Bouwens *et al.*, 2004) where an α of -1.15 was derived. Compared to LF parameters of the optically selected samples, the M_{1500} LF of the K-selected sample has slightly brighter values of M_* , significantly lower values in Φ_* and, within the large errors, a similar faint-end slope α . Since the slightly shallower K-selected sample does not allow us to constrain the faint-end slope to the same level as our FDF sample (but is consistent with the faint end slope $\alpha = -1.07$ determined for that field), we adopt this value for our K-selected sample.

We examine the consequences of these findings for the SFR in the next section.

6.3 The Star Formation Rate

We compute the SFR for all 4 catalogs from the total luminosity densities l_{1500} in the 1500 Å band. First, we derive l_{1500} at a given redshift by summing the completeness corrected (using a V/V_{max} correction, see Gabasch *et al.*, 2004b) LFs up to the 1500 Å absolute magnitude limits. Second, we apply a further correction (to zero galaxy luminosity) ZGL, to take into account the missing contribution to the luminosity density of the fainter galaxies. To this end we use the best-fitting Schechter function. For the FDF catalogs the ZGL corrections are only 2-20% in size. The small ZGL correction employed here owes itself to the faint magnitude limits probed by our deep FDF data set and the relatively flat slopes ($\alpha \approx -1.07$) of the Schechter function. Due to the brighter magnitude limit, the ZGL corrections for the GOODS catalog can be as high as 50%. Note that if we follow i.e. Steidel *et al.* (1999) who find $\alpha = -1.6$ (excluded at 2σ with our fits, see Gabasch *et al.*, 2004b), we would get much larger ZGL corrections for the same M_* , Φ_* (see the dotted line in Fig. 6.2 and the discussion be-

low).

Finally, following Madau *et al.* (1998) we derive the SFR by scaling the UV luminosity densities: $\text{SFR}_{1500} = 1.25 \times 10^{-28} \times l_{1500}$ in units of $M_{\odot} \text{yr}^{-1} \text{Mpc}^{-3}$, where the constant is computed for a Salpeter IMF. The resulting values of SFR_{1500} are shown in Fig. 6.2 as a function of redshift. Errors are computed from Monte Carlo simulations that take into account the probability distributions of photometric redshifts and the Poissonian error (Gabasch *et al.*, 2004b). Following Adelberger & Steidel (2000), we assume that dust extinction does not evolve with redshift and is about a factor of $\sim 5 - 9$ in the rest-frame UV. A more detailed discussion of the role of dust will be given in a future paper, like an analysis based on the SFR derived at 2800 Å. Thanks to the large area covered and the faint limiting magnitudes probed, our determination of the SFR is the most precise to date, with statistical errors less than 0.1 dex for the single redshift bins spanning the range $0.5 < z < 5$.

The considerations of §6.2 translate in the following conclusions about the SFR. Out to redshift $z \approx 3$ the SFRs derived from the I and B selected FDF, or the merged I+B catalog, are identical within the errors ($\lesssim 0.1$ dex; see plot at the bottom left of Fig. 6.2). At larger redshifts the B-selected SFRs underestimate the true values, since B dropouts are not taken into account. The strong evolution in both the M_* and ϕ_* parameters of the Schechter LF measured as a function of redshift by Gabasch *et al.* (2004b) results in a nearly constant SFR, because the strong brightening of M_* is compensated by the dramatic decrease of ϕ_* with z . Comparing the two lower panels of Fig. 6.2 shows that luminous galaxies ($L > L_*$) contribute only a third of the total SFR at all observed z , independent of the selection band.

The K-selected SFRs are similar in shape, but systematically lower by ≈ 0.2 dex at $z > 1$. This result holds independently of our completeness correction. If we consider only the contributions to the SFR down to the limiting magnitude set by the K-band, we find the same 0.2 dex difference

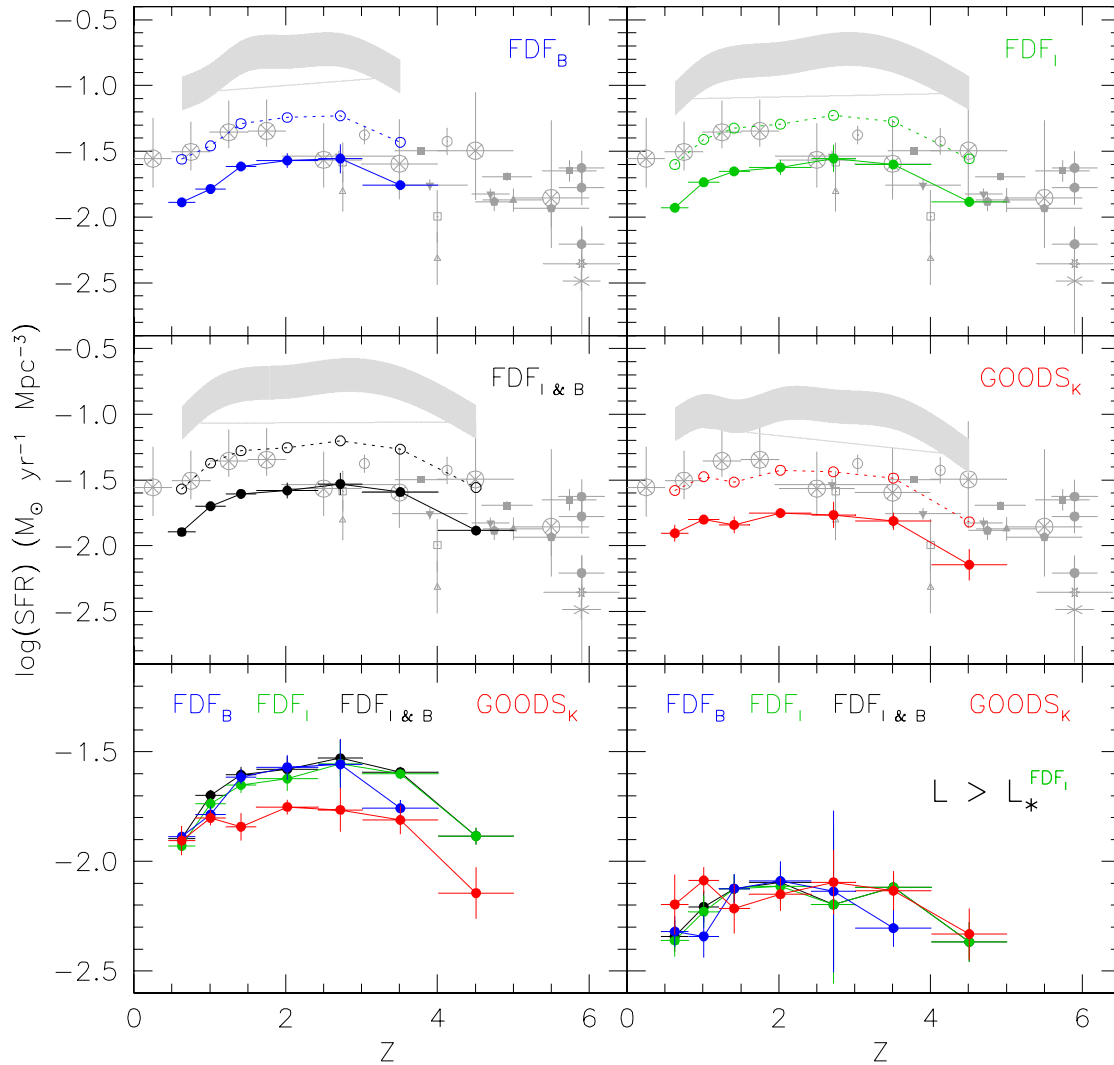


Figure 6.2: The four plots at the top show the SFR as a function of redshift derived from the 1500 \AA luminosity densities computed from the B-selected (blue), I (green) and I+B-selected (black) FDF, and K-selected (red) GOODS-South field. The points are connected by the thick lines for clarity. These SFRs are based on a faint-end slope of the LF of -1.07 as derived from the FDF and GOODS data. The dotted lines show the effect of assuming a slope of -1.6 . The grey-shaded region shows the effect of dust corrections with correction factors between 5 and 9, following Adelberger & Steidel (2000). The grey symbols show the results (taken from the table of Somerville *et al.*, 2001) of Pascarella *et al.* (1998, circled crosses), Steidel *et al.* (1999, open circles), Madau *et al.* (1996, open triangles), Madau *et al.* (1998, open squares), and (taken from Bunker *et al.*, 2004) Iwata *et al.* (2003, filled triangles), Giavalisco *et al.* (2004a, filled squares), Bouwens *et al.* (2003b, filled circles), Bouwens *et al.* (2004, hexagonal crosses), Fontana *et al.* (2003, filled pentagons), Bunker *et al.* (2004, open star), Bouwens *et al.* (2003a, inverted filled triangles). The plots at the bottom show the SFRs of the four catalogs together (left) and the SFRs derived considering the contributions of the galaxies brighter than L^* only (right).

for $1 < z \leq 3$, and 0.15 dex at $z > 3$. Fig. 6.1 shows that this result originates from the lower density of $M_{1500} > -19$ galaxies in the K-selected catalog, as intermediate and low luminosity blue galaxies contributing to the SFR budget are more easily detected in the bluer bands than in K. In fact, the contributions to the SFR coming from the galaxies brighter than L_*^I are identical within the errors for the I and K selected catalogs (see Fig. 6.2, bottom-right panel). Therefore, cosmic variance does not play a role, as we also verified by comparing the B-band number counts in the 2 fields. They agree within 0.1 dex, which is the expected variation derived by Somerville *et al.* (2004) scaled to the area of the GOODS-South field. On the other hand, Gabasch *et al.* (2004b) show that the I-band FDF catalog might be missing only about 10 % of the galaxies that would be detected in a deep K-band selected survey with magnitude limit $K_{AB} \approx 26$ (like in Labbé *et al.*, 2003). The missing galaxies would be faint and likely not contributing significantly to the SFR provided their dust extinction is not exceedingly large. Independent of the selection band the SFR declines beyond $z \sim 4.5$. Our results confirm the conjecture of Kashikawa *et al.* (2003) that the K-selected UV LFs match the optically selected LFs at high luminosities.

The comparison with the literature shows that our results are ~ 0.3 dex lower, independent of the selection band. This difference stems from the large completeness corrections applied by, e.g., Steidel *et al.* (1999), derived from the steep slopes fitted to the LF (see §6.2). Our results scale to the literature values if similar slopes are used for the same M_* and ϕ_* . This is shown by the dotted lines of Fig. 6.2, where we have assumed a slope of -1.6 for our data set while keeping M_* and ϕ_* the same as in our fit.

The overall agreement between the SFRs derived over a wide wavelength range (within 0.2 dex), from the optical B and I to the NIR K, sampling at $z \approx 4$ the rest-frame UV and B, shows that we are approaching (in the optical) the complete census of the galaxies contributing to the

stellar production of the universe up to this redshift. Therefore, we can expect possible biases induced by missing stellar energy distributions with redshift (Ilbert *et al.*, 2004) to be small, when deep enough optical or NIR catalogs are available. However, we might still not take into account the possible contribution to the SFR coming from faint, highly dust-absorbed red star-forming galaxies (Hughes *et al.*, 1998; Genzel *et al.*, 2001) which are likely missing from optically or near-infrared selected samples. Nevertheless, it is encouraging to find that recent Spitzer results (e.g. Egami *et al.* 2004) indicate that the majority of the star formation has already been accounted for using the dust-corrected SFR derived from optical studies.

6.4 Conclusions

We have measured the SFR of the universe out to $z \approx 4.5$ with unprecedented accuracy from the FORS Deep Field and the GOODS-South Field having a total area about 90 arcmin². Our main conclusions are:

- The cosmic variance in the SFR history between the FDF and GOODS-South field is negligibly small. The difference between these fields is $\lesssim 0.1$ dex, consistent with theoretical expectations.
- The SFR of galaxies brighter than L_*^I is the same ($\lesssim 0.1$ dex) in B, I, (I+B) and K selected catalogs. This indicates that present optical and NIR surveys have unlikely missed a substantial population of massive star forming objects, with the possible exception of heavily dust-enshrouded starbursts which may escape detection in both optical and NIR surveys.
- The total SFR integrated over all galaxy luminosities is the same in the B, I, and (I+B) selected catalogs and is lower in the K-selected catalog by 0.2 dex. This difference originates at luminosities lower than

L_* which implies that K-selected surveys miss a significant fraction of star-forming lower-luminosity galaxies.

- At all redshifts, luminous galaxies ($L > L_*$) contribute only $\sim \frac{1}{3}$ to the total SFR, i.e. the integrated SFR of $L < L_*$ galaxies is a factor of ~ 2 higher than the one of $L > L_*$ galaxies.
- Our fits to the FDF luminosity functions suggest a flat faint-end slope of $\alpha = -1.07 \pm 0.04$ in contrast to the assumed slope of $\alpha \sim -1.6$ in the literature. This implies that past determinations have overestimated the SFR by a factor 2.
- The SFR is approximately constant over the redshift range $1 \leq z \leq 4$ and drops by about 50% around $z = 4.5$, if dust corrections constant with redshift are assumed.

Acknowledgements:

We thank the anonymous referee for his helpful comments which improved the presentation of the paper considerably. This work was supported by SFB 375 of the DFG, by the German Ministry for Science and Education (BMBF) through DESY under the project 05AE2PDA/8, and by the Deutsche Forschungsgemeinschaft under the project SCHN 342/3-1 M. Schirmer und T. Erben thank C. Wolf for providing some of the optical images used here. Observations have been carried out using the Very Large Telescope at the ESO Paranal Observatory under Program ID(s): LP168.A-0485

Chapter 7

Evolution of the stellar mass density and dust correction

7.1 Introduction

The determination of the stellar mass content of the universe at different redshifts is one of the most challenging issues. Although dynamical mass measurements are very precise they derive not only the stellar mass but rather the total mass (stellar & dark matter & gas mass) of a galaxy within some radius set by observational limits. Moreover they are restricted to relatively bright galaxies. As an alternative one can convert measured light into stellar mass. The K-band galaxy luminosity is a good tracer for evolved stars and thus of the total stellar content (Cole *et al.*, 2000, and references therein). Therefore the near-infrared galaxy luminosity function (Loveday, 2000; Kochanek *et al.*, 2001; Cole *et al.*, 2001; Balogh *et al.*, 2001; Drory *et al.*, 2003; Huang *et al.*, 2003; Feulner *et al.*, 2003) is an important characteristic of the galaxy population. Furthermore the K-band is only negligibly affected by dust extinction. Unfortunately at higher redshift the observerframe K-band traces bluer restframe wavebands becoming more and more dominated by younger populations. Nevertheless, in the K-band the spread in the k-correction for different SED types is rather small up to redshift $z \sim 1$ (see e.g. Feulner *et al.*, 2003, and references therein).

Locally, Kauffmann *et al.* (2003) analyzed stellar masses of about 10^5 galaxies in the Sloan Digital Sky Survey. Cole *et al.* (2001) as well as Bell *et al.* (2003) derived mass functions and mass to light (M/L) ratios combining the 2dF Galaxy Redshift Survey and the 2MASS survey. At higher redshift Cohen (2002), Rudnick *et al.* (2003), Fontana *et al.* (2004) and Drory *et al.* (2004) derived stellar mass densities. A comparison of all these mass densities clearly shows a redshift evolution, i.e. the stellar mass density decreases with increasing redshift.

In this chapter we compare the stellar mass density as derived from measurements only negligibly affected by dust extinction with the mass density computed from the star formation rate. We derive the mass density in the redshift range $0.5 < z < 5$ from the FDF SFR in Sect. 7.2 and compare the result to values from the literature in Sect. 7.3. We will constrain the mean UV flux absorbed by dust in the galaxies, i.e. the amount of UV flux absorbed by dust and re-emitted in the FIR.

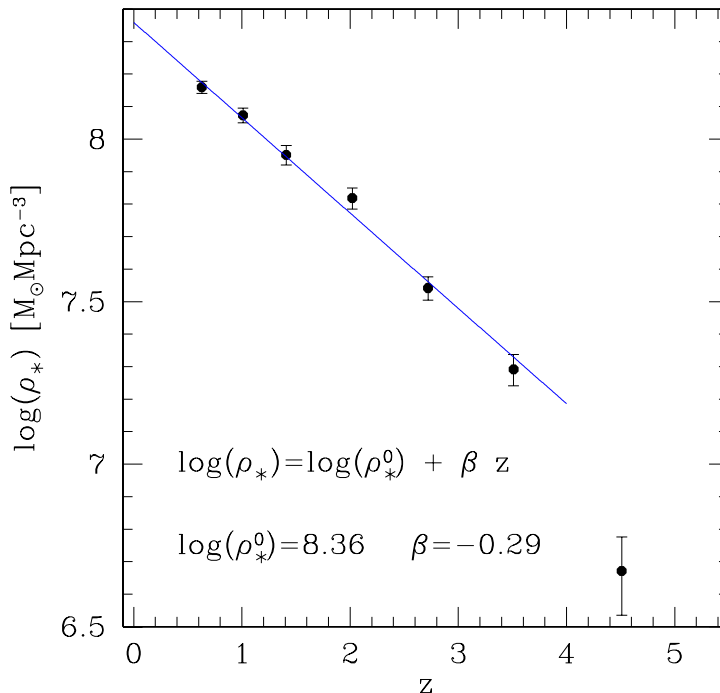


Figure 7.1: Redshift evolution of the total stellar mass fraction. Solid points show the mass density as derived from the completeness corrected SFR in the FDF (see Fig. 6.2). The FDF I-selected catalog has been used and no dust correction is applied. The solid blue line is the best fitting model with the parameterization $\log(\rho_*) = \log(\rho_*^0) + \beta z$ (see also text).

7.2 The stellar mass density from the SFR up to $z \sim 4.5$

In this section we calculate the stellar mass density from the SFR described in Sect. 6.3. In Chap. 6 we have shown that for redshifts $z \lesssim 3$ the SFR based on B, I and (I+B) selected FDF galaxy catalogs agree very well. We decided to use the I-selected FDF catalog since for redshifts $z \gtrsim 3$ B-dropouts do not affect the result. Furthermore we use a Salpeter IMF to transform the UV flux into a SFR.

Since the SFR is in units of $\mathcal{M}_\odot \text{yr}^{-1} \text{Mpc}^{-3}$, to derive the stellar mass density at a redshift z_0 we simply have to integrate the SFR over the age of the universe at z_0 (see e.g. Peacock, 1999). We neglect the stellar mass formed before $z \sim 5$ as the SFR seems to drop already at $z \sim 4.5$ (see Sect. 6.4) and the redshift interval $0 < z < 5$ already covers 90 % of the age of the universe. Please note that the age of the universe is highly non-linear in redshift, e.g. from $z = 1$ to $z = 0$ the universe has aged by 7.7 Gyr, while the age difference between $z = 5$ to $z = 1$ is 4.6 Gyr.

In Fig. 7.1 we show the mass density ρ_* as derived from the completeness corrected SFR as black solid points. Furthermore we parameterize the redshift evolution in the redshift range $0 \lesssim z \lesssim 4$ by the very simple assumption:

$$\log(\rho_*) = \log(\rho_*^0) + \beta z \quad (7.1)$$

where ρ_*^0 and β are two free parameters. As can be seen by the solid blue line of Fig. 7.1 this

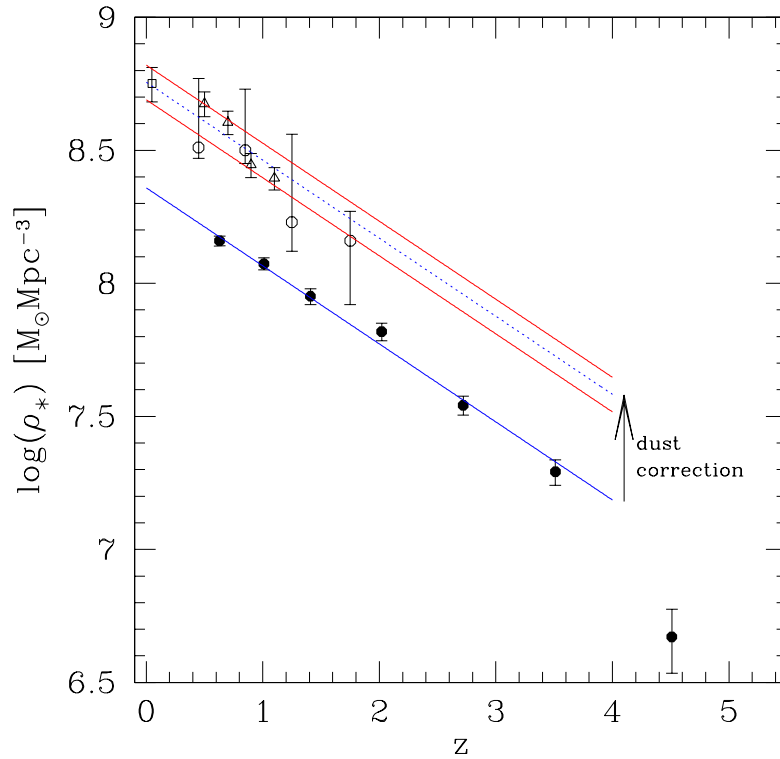


Figure 7.2: Redshift evolution of the total mass fraction in stars. As in Fig. 7.1 the solid points show the mass density as derived from the completeness corrected SFR in the FDF (see Fig. 6.2). The FDF I-selected catalog has been used and no dust correction is applied. The solid blue line is the best fitting model with the parameterization of Eq. (7.1). The mass density derived by Cole *et al.* (2001), Fontana *et al.* (2004), and Drory *et al.* (2004) is shown as open square, open circles and open triangles, respectively. The dotted blue line represents the mass density as derived from the FDF SFR after a mean dust correction of a factor of 2.50 (black arrow) has been applied. A dust correction by a factor of 2.5 best matches the literature mass densities (open symbols). The two red lines show maximal (2.89) and minimal (2.14) dust corrections (3σ) which can be applied to the solid blue line to fit the mass densities from the literature within 3σ . The best fitting values and the 1σ errors are listed in Table 7.1.

parameterization is able to describe the evolution of the mass density in the redshift range $0.5 < z < 4$ very well. The best fitting values are: $\log(\rho_*^0) = 8.36 \pm 0.02$ and $\beta = -0.29 \pm 0.02$ resulting in a reduced χ^2 of 1.08. In Sect. 7.3 we compare the stellar mass density with the stellar mass density as derived in the literature. These mass estimates are mostly based on K-band measurements and thus do not suffer from large dust corrections as for example the SFR does. Therefore a comparison of the mass densities derived from the SFR with the latter is able to put relatively tight constraints to the mean dust correction of the UV flux (\propto SFR, see Madau *et al.*, 1996).

Table 7.1: Evolution parameters for the mass density according to Eq. (7.1).

data used to derive the mass density	$\log(\rho_*^0)$ [$\mathcal{M}_\odot \text{Mpc}^{-3}$]	β	dust correction factor ³
FDF SFR ¹	8.36 ± 0.02	-0.29 ± 0.02	
literature ²	8.76 ± 0.03	-0.29 (fixed)	2.50 ± 0.2

¹fit to the mass density as derived from the FDF SFR without dust correction.

²fit to the mass density as derived by Cole *et al.* (2001), Fontana *et al.* (2004), and Drory *et al.* (2004).

³dust correction factor to apply to the mass density derived from the FDF SFR to fit the literature values.

7.3 Tight constraint to the mean dust correction

In this section we compare the FDF mass density as derived in Sect. 7.2 with results of Cole *et al.* (2001), Fontana *et al.* (2004), and Drory *et al.* (2004). We assume, that the difference in the stellar mass density is only due to dust correction which is not yet taken into account in the SFR. Therefore we fit Eq. (7.1) to the results derived by the three authors with ρ_*^0 as free parameter but keeping β fixed to the value derived in Sect. 7.2 i.e. $\beta = -0.29$. This is justified, as we are only interested in the mean dust correction in the redshift interval $0 < z < 5$. Please note that dust extinction is assumed to be constant with redshift. In principle it is also possible to derive a redshift dependent dust correction, but this would require precise mass measurements up to high redshift. This is very challenging, but measurements with e.g. the Spitzer satellite, which can trace the restframe K-band to high redshift, will give new insights in the near future.

In Fig. 7.2 we show the mass density ρ_* as derived from the completeness *and dust* corrected SFR. The solid black points as well as the solid blue line represent the uncorrected SFR mass density and the best fitting model as shown in Fig. 7.1. The mass density derived by Cole *et al.* (2001), Fontana *et al.* (2004), and Drory *et al.* (2004) is shown as open square, open circles and open triangles, respectively. The dotted blue line represents the mass density as derived from the FDF SFR after a mean dust correction of a factor of 2.50 (denoted by the black arrow) has been applied. A dust correction by a factor of 2.5 best matches the literature mass densities (open symbols) leading to a reduced χ^2 of 1.14. The two red lines show maximal (factor of 2.89) and minimal (factor of 2.14) dust corrections which can be applied to the solid blue line to fit the mass densities from the literature within 3σ . The best fitting values and the 1σ errors are listed in Table 7.1. Please note that fixing β to $\beta = -0.29$ very well describes the redshift evolution of the literature stellar mass density in the redshift range $0 \lesssim z \lesssim 2$ (Fig. 7.2).

This result confirms the conjecture of Cole *et al.* (2001) that the mass density measured e.g. from the K-band flux is consistent with that inferred from the cosmic star formation history only, if the dust correction assumed in the latter is modest. They favor a mean dust correction which is about 50 % smaller than the value preferred by Steidel and collaborators (Steidel *et al.*, 1999, \sim factor of 4 at 1700 \AA for LBGs at $z \sim 3$). This modest value roughly agrees with our result of 2.5.

Chapter 8

Summary and concluding synthesis

8.1 Summary

We have conducted a study of galaxy redshift evolution in the FORS Deep Field covering about 90 % of the age of the universe ($0 \lesssim z \lesssim 5$). The main goal of this study is to improve our understanding of the evolution of galaxies in the universe. The FORS Deep Field project is a multi-color, multi-object photometric and spectroscopic investigation of the sky. The relatively large field of view ($\sim 40 \text{ arcmin}^2$) reduces the problem of cosmic variance and allows the detection of nearly 10^4 galaxies. State of the art photometric redshifts ($\Delta z / (z_{spec} + 1) \leq 0.03$) make it possible to derive precise restframe absolute magnitudes, a key ingredient to follow the evolution of *intrinsic* properties of galaxy populations.

- In Chap. 2 the field selection, the photometric observations, and the data reduction are described. Since with the FDF we want to analyze galaxies to fainter limiting magnitudes when compared to other ground-based studies a dedicated data reduction procedure has been developed and its efficiency is illustrated. Furthermore the source detection and photometry of objects in the FORS Deep Field are discussed in detail. A combined B and I selected UBgRIJKs photometric catalog of 8753 objects in the FDF is presented and its properties are briefly discussed. The reduction of the z'-band and a special filter centered at 834 nm are also presented. The formal 50% completeness limits for point sources (AB system) are 26.5, 27.6, 26.9, 26.9, 26.8, ~ 25.5 , ~ 25.8 , 23.8, 22.6 in U, B, g, R, I, 834 nm, z, J and Ks, respectively. A comparison of the number counts in the FORS Deep Field with other deep field surveys is presented and shows very good agreement.

- In Chap. 3 we analyze a very homogeneous sample of about 5600 I-band selected galaxies in the FORS Deep Field down to a limiting magnitude of $I = 26.8 \text{ mag}$. We show that our I-band selected catalog is hardly affected by color bias. A comparison with the very deep K-selected catalog of Labbé *et al.* (2003) shows that more than 90 % of their objects are brighter than our limiting I-band magnitude. Therefore our scientific conclusions are not affected by this color bias.

Based on 9 filters we derive accurate photometric redshifts with $\Delta z / (z_{spec} + 1) \lesssim 0.03$ if compared with the spectroscopic sample of 362 objects. We calculate and present the luminosity functions in the UV (1500 Å and 2800 Å), u', B, and g' bands in the redshift range $0.15 < z < 5.0$. The error budget of the luminosity functions includes the photometric redshift error as well as the Poissonian error.

We show that the faint-end slope of the luminosity function does not have a large redshift evolution and is compatible within 2σ with a constant slope in most of the redshift bins and wavelengths considered here. Furthermore, the slopes in the 1500 Å, 2800 Å, and u' bands are very similar but differ from the slopes in the g' and B bands. We derive a best fitting slope of $\alpha = -1.07 \pm 0.04$ for the combined 1500 Å, 2800 Å and u' bands and $\alpha = -1.25 \pm 0.03$ for the combined g' and B bands. We find no evidence for a very steep slope ($\alpha \leq -1.6$) at $z \sim 3$ and 1700 Å rest wavelength as reported by other authors. From our data we can exclude a slope of $\alpha \leq -1.6$ at redshift $\langle z \rangle \sim 3.0$ and $\langle z \rangle \sim 4.0$ at least at the 2σ level.

We investigate the evolution of M^* and ϕ^* by means of a redshift parametrization of the form $M^*(z) = M_0^* + a \ln(1+z)$ and $\phi^*(z) = \phi_0^*(1+z)^b$. We find a substantial brightening of M^* and a decrease of ϕ^* with redshift in all analyzed wavelengths (UV \rightarrow g'). If we follow the evolution of the characteristic luminosity from $\langle z \rangle \sim 0.5$ to $\langle z \rangle \sim 5$, we find an increase of ~ 3.1 magnitudes in the UV, of ~ 2.6 magnitudes in the u' and of ~ 1.6 magnitudes in the g' and B band. The characteristic density decreases by about 80 % – 90 % simultaneously in all analyzed wavebands (UV \rightarrow g').

Moreover, we compare the luminosity function derived in the FDF with previous observational datasets, mostly based on photometric results, and discuss discrepancies. In general, we find good agreement at the bright end, where their samples are complete. Differences in the faint-end slope in some cases can be attributed to the shallower limiting magnitudes of most of the other surveys.

We also compare our results with predictions of semi-analytical models at various redshifts. The semi-analytical models predict luminosity functions which describe (by construction) the data at low redshift quite well, but show growing disagreement with increasing redshifts.

- In Chap. 4 we extend all the measurements of the blue bands presented in Chap. 3 to the red r', i', and z' bands. As in the blue bands the faint-end slope of the luminosity function does not show a large redshift evolution and is compatible within 2σ with a constant slope in most of the redshift bins and wavelengths considered here. Furthermore, the slopes in the r', i' and z' bands are very similar and follow the same trend already seen in the blue bands, i.e. the slope steepens for increasing wavebands (UV \rightarrow z'). We derive a best fitting slope of $\alpha = -1.33 \pm 0.03$ for the combined r', i' and z' bands. It is worth noting that in the NIR (K-band) the faint-end slope of the Schechter function decreases again (see e.g. Cole *et al.*, 2001).

We investigate the evolution of M^* and ϕ^* by means of the same redshift parametrization as introduced in Chap. 3. We find only a mild brightening of M^* and decrease of ϕ^* with increasing redshifts in all three analyzed wavebands. If we follow the evolution of the characteristic luminosity from $\langle z \rangle \sim 0.5$ to $\langle z \rangle \sim 3$, we find an increase of ~ 1.1 magnitudes in the r', of ~ 0.9 magnitudes in the i' and of ~ 0.7 magnitudes in the z' band. Simultaneously the characteristic density decreases by about 50 % in all analyzed wavebands.

Moreover, we compare the luminosity functions with previous observational datasets and discuss discrepancies. As for the blue bands, we find in general good agreement at the bright end. Differences in the faint-end slope in some cases can be attributed to the shallower limiting magnitudes of most of the other surveys.

We also compare our results in the red bands with predictions of semi-analytical models at various redshifts. The semi-analytical models predict luminosity functions which describe the data at low redshift very well, but following the trend already seen in the blue bands, they show growing disagreement with increasing redshifts. Unfortunately, the models only predict luminosities for massive galaxies and therefore, a comparison between the predicted and observed galaxy number

densities for low luminosity galaxies ($L \lesssim L^*$) could not be done.

- In Chap. 5 we subdivide our galaxy sample into 4 different SED types and analyze the type-dependent LF evolution at all wavebands (UV \rightarrow z'). This allows us to determine the contribution of a typical SED type to the total LF (as derived in Chap. 3 and Chap. 4). Furthermore, it also allows us to build up the shape of the total LF and give a reasonable explanation of the different slopes α seen in the different wavebands.

We also show that there is a good correlation between our 4 main SED types and the Sérsic index, i.e. the 4 SED types of the galaxies in the FDF are also related to different galaxy morphology types: (SED type 1 \rightarrow SED type 4) $\hat{=}$ (“early-type galaxies” \rightarrow “starburst galaxies”).

We find that independent of the waveband the SED type 1 and type 2 do not contribute at all to the LF for redshifts larger than $z \sim 1.9$. As the depth of the FDF allows us to detect early-type galaxies down to $M_B \lesssim -20.5$ at $z \sim 1.9$, the absence of those galaxies at higher redshifts is most probably real and not due to a selection effect (provided their dust extinction is not exceedingly large). On the other hand this is not a surprise, as the universe at $z \gtrsim 1.9$ is too young for old stellar populations (dominating early-type galaxies) to have formed.

Furthermore for SED type 1/2 in the redshift range $0.45 < z \leq 0.85$ and $0.85 < z \leq 1.31$ we see in the optical bands nearly the same number density for bright and faint galaxies. We derive a mean value of ≈ 0.00034 galaxies per magnitude per Mpc^3 with a typical error of 20% in every waveband for the redshift bin $0.45 < z \leq 0.85$.

The relative contribution of type 1/2 and type 3/4 SEDs to the total LF may also explain the steeper LF slope in the red bands if compared to the blue bands (see Fig. 5.10). For the UV bands the bright end of the LF is dominated by the SED of type 3 and type 4. For increasing wavebands ($u' \rightarrow g' \rightarrow r' \rightarrow i' \rightarrow z'$) the bright end of the LF is more and more dominated by SED of type 1 and type 2. On the other hand bright galaxies of SED type 4 decrease in number density very fast for increasing wavebands ($u' \rightarrow z'$). This decrease can hardly be compensated for by the other SED types thus the slope of the total luminosity function steepens for increasing wavebands ($u' \rightarrow g' \rightarrow r', i', z'$).

- In Chap. 6 we measure the SFR of the universe up to $\langle z \rangle \approx 4.5$ with unprecedented accuracy from the FORS Deep Field and the GOODS-South Field having a total area of about 90 arcmin^2 .

We demonstrate that the cosmic variance in the SFR history between the FDF and GOODS-South field is negligibly small. We show that the SFR of galaxies brighter than L_*^I is the same in the FDF B, I, (I+B) and GOODS K selected catalogs. This indicates that present optical and NIR surveys have unlikely missed a substantial population of massive star forming objects, with the possible exception of heavily dust-enshrouded starbursts which may escape detection in both optical and NIR surveys.

Furthermore we show that the total SFR integrated over all galaxy luminosities is the same in the B, I, and (I+B) selected catalogs and is lower in the K-selected catalog by ~ 0.2 dex. This difference originates at luminosities lower than L_* which implies that K-selected surveys miss a significant fraction of star-forming lower-luminosity galaxies. We find that at all redshifts, luminous galaxies ($L > L_*$) contribute only $\sim \frac{1}{3}$ to the total SFR, i.e. the integrated SFR of $L < L_*$ galaxies is a factor of ~ 2 higher than the one of $L > L_*$ galaxies. Moreover past determinations likely have overestimated the faint-end slope of the UV-LF, and therefore the SFR by a factor 2.

Finally we show that the SFR is approximately constant for $1 \leq z \leq 4$ and drops by about 50% around $\langle z \rangle = 4.5$, if dust corrections constant with redshift are assumed.

- In Chap. 7 we compare the stellar mass density derived from measurements which are only negligibly affected by dust extinction with the mass density computed from the star formation rate history in the redshift range $0.5 < z < 5$. We show that the stellar mass density derived from the star formation rate history uncorrected for dust extinction is lower by 0.4 dex when compared with mass density estimates in the literature at redshifts $0 < z < 2$.

We investigate the evolution of the stellar mass density by means of a redshift parametrization of the form $\log(\rho_*) = \log(\rho_*^0) + \beta z$ which very well describes the measured values in the FDF resulting in a reduced χ^2 of 1.08. For the mass density derived without dust correction the best fitting values read $\beta = -0.29 \pm 0.02$ and $\log(\rho_*^0) = 8.36 \pm 0.02 \mathcal{M}_\odot \text{Mpc}^{-3}$.

Furthermore we constrain the amount of UV flux absorbed by dust and re-emitted in the FIR. A dust corrected SFR is able to describe the stellar mass density (derived from measurements only negligibly affected by dust extinction) only if at all redshifts a mean correction factor of 2.50 ± 0.2 is applied to the measured SFR.

8.2 Concluding synthesis

To complete the picture of galaxy evolution with redshifts, in this section we visualize evolutionary results derived in this thesis supplemented by results based on the K-selected GOODS-South Field (Salvato *et al.* 2004, see also Chap. 6) as well as results derived in the thesis of Feulner (2004) based on the I-selected MUNICS catalog. MUNICS is a wide-field medium-deep survey covering about 0.35 deg^2 in K' , J , I , R , V , and B . Although the MUNICS catalog is shallower than the FDF and GOODS-South its area is about 25 times larger. Thus the results are able to reduce significantly cosmic variance at redshift $z \lesssim 1$. Furthermore the accuracy of the photometric redshifts are $\Delta z / (z_{spec} + 1) \leq 0.055$ and thus comparable with those derived for the GOODS-South. The two fields make it possible to extend the results derived in the FDF to the near-infrared K-Band.

In Fig. 8.1 we show the evolution of the luminosity function in the UV (1500 \AA , upper left panel), g' (upper right panel), i' (lower left panel), and K (lower right panel) bands. The dotted line represents the local LF whereas the filled (open) symbols show the luminosity function at $\langle z \rangle = 2.26$ corrected (uncorrected) for V/V_{max} . For the UV the local LF is taken from Table 3.4, whereas for the g' and i' bands the local SDSS luminosity function of Blanton *et al.* (2001) is used. The dotted line for the K-band represents the local luminosity function derived by Kochanek *et al.* (2001). The LF in the restframe UV, g' , and i' bands are calculated from the FDF I-selected catalog while for the restframe K-band the observerframe K-band selected catalog of GOODS-South has been used. Even without fitting Schechter functions to the data, it is obvious that there is strong evolution in the characteristic luminosity and number density in the UV band. Furthermore it is also visible that the evolution decreases for increasing wavebands ($UV \rightarrow g' \rightarrow i' \rightarrow K$).

In Fig. 8.2 we show the evolution parameters a (left panel) and b (right panel) introduced in Sect. 3.6 as a function of waveband. The assumed parametrization for $M^*(z)$ and $\phi^*(z)$ is $M^*(z) = M_0^* + a \ln(1+z)$ and $\phi^*(z) = \phi_0^* (1+z)^b$, respectively. The filled symbols are derived from the FDF whereas the open symbols are taken from Feulner (2004). The results of Feulner (2004) are derived in the redshift range $0.4 < z < 1.2$ using the same redshift parametrization as in the FDF. For the blue FDF bands a and b are derived in the redshift range $0.45 < z < 5.0$. For the red bands the FDF luminosity functions between redshift $\langle z \rangle \sim 0.65$ and $\langle z \rangle \sim 2.26$ as well as the local luminosity

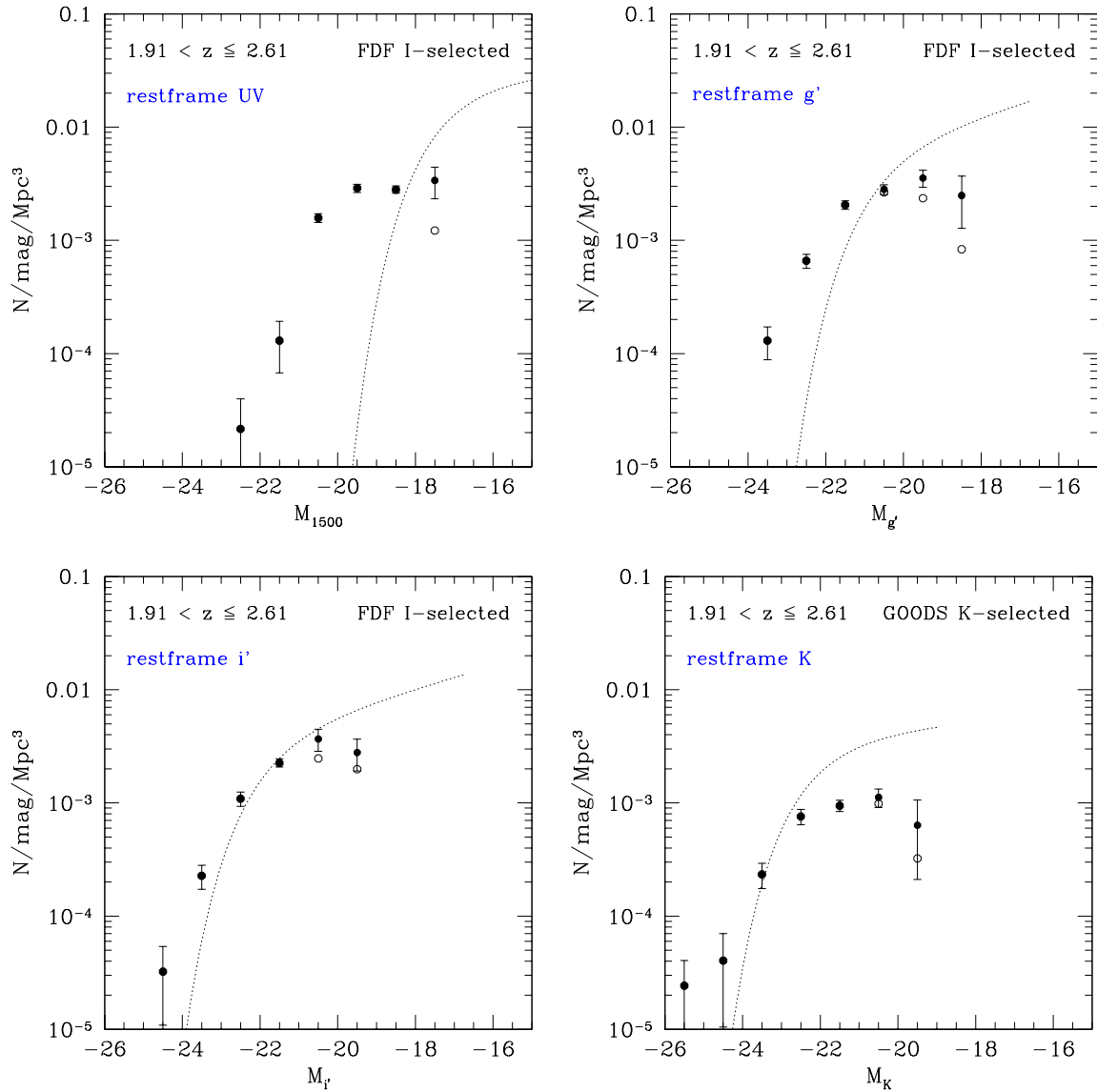


Figure 8.1: Comparison of the luminosity function in the UV (1500 \AA , upper left panel), g' (upper right panel), i' (lower left panel), and K (lower right panel) bands. The dotted line represents the local LF whereas the filled (open) symbols show the luminosity function at $\langle z \rangle = 2.26$ corrected (uncorrected) for V/V_{max} . For the UV the local LF is taken from Table 3.4, whereas for the g' and i' bands the local SDSS luminosity function of Blanton *et al.* (2001) is used. The dotted line for the K-band represents the local luminosity function derived by Kochanek *et al.* (2001). The LF in the restframe UV, g' , and i' bands are calculated from the FDF I-selected catalog while for the restframe K-band the observerframe K-band selected catalog of GOODS-South has been used.

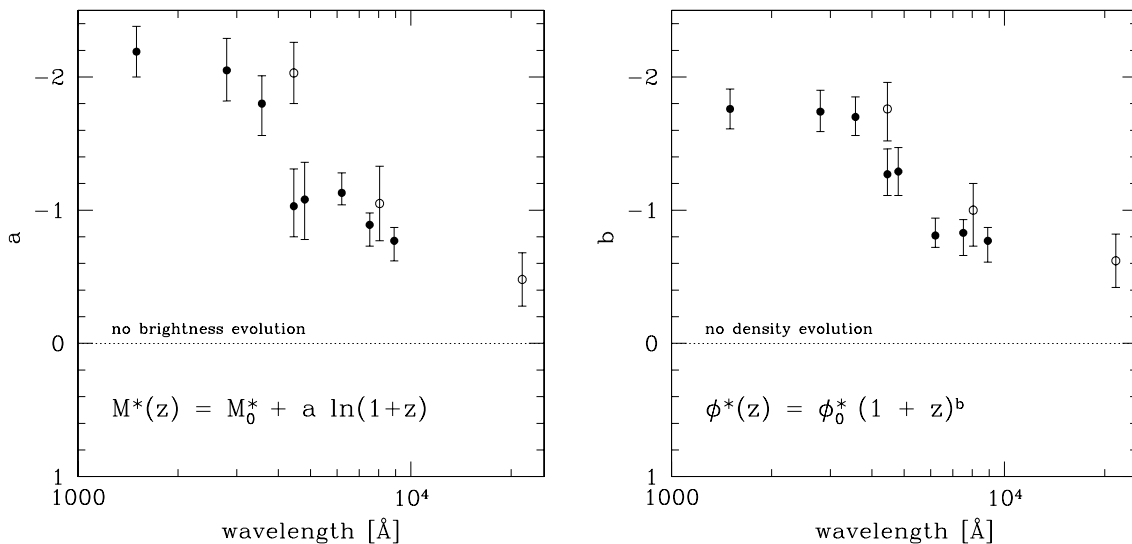


Figure 8.2: Evolution parameters a (left panel) and b (right panel) as a function of waveband. The filled symbols are derived from the FDF whereas the open symbols are results of Feulner (2004) (see text for details).

function of Blanton *et al.* (2001) are used to constrain a and b . The results of FDF and MUNICS agree very well for the I-band but are slightly different in the B-band (although they are compatible within $\sim 2\sigma$ also in the B-band). Please note that for the MUNICS survey the evolutionary parameters a and b are mainly constrained from the low to intermediate redshift regime ($0.4 \lesssim z \lesssim 1.2$), while for the FDF the evolutionary parameters are determined in the high redshift regime ($1 < z < 5$). This may result in different evolutionary parameters as at redshift $z \sim 1$ the evolution of the luminosity density changes (see e.g. Fig. 8.3 (left panel) for the luminosity density in the UV and Fig. 8.4 for the luminosity density in the K-band). Furthermore, as can be seen from Fig. 3.9 the FDF evolutionary parameters do not perfectly describe the evolution of M^* and ϕ^* below redshift $z \sim 1$ but are mainly determined by the evolution above redshift $z \sim 1$. Nevertheless all results exclude a model with no density evolution ($a = 0$) or no brightness evolution ($b = 0$) on at least 2σ . This holds not only for the blue and red bands (FDF & MUNICS) but also for the near-infrared K-band (MUNICS up to $z \sim 1.2$).

As described in Sect. 1.3.2 the total luminosity density produced by integrating over the luminosity function is given by $\mathcal{L} = \phi^* \times L^* \times \Gamma(2 - \alpha)$. Furthermore parametrizing $M^*(z) = M_0^* + a \ln(1+z)$ is equivalent to assuming a dependence of $L^*(z) = L_0^* (1+z)^\xi$ with $\xi = -0.4 \ln(10) a \approx -0.921 a$ (see also Sect. 3.6). This implies that the redshift evolution of the luminosity density is given by: $\mathcal{L} \propto (1+z)^{(b+\xi)}$. It is therefore straightforward to compute from the evolutionary parameter a and b the redshift evolution of the luminosity density. Please note that this method implies that the luminosity function can be perfectly described by a Schechter function. As this may not always be true the errors introduced by this method are usually larger than in the direct approach, i.e. summing up the luminosity of each single galaxy in the redshift bin. Nevertheless by integrating the Schechter function one can correct missing light from galaxies beyond the detection limit.

In Fig. 8.3 (left panel) we show the evolution parameters b and ξ . The filled symbols are de-

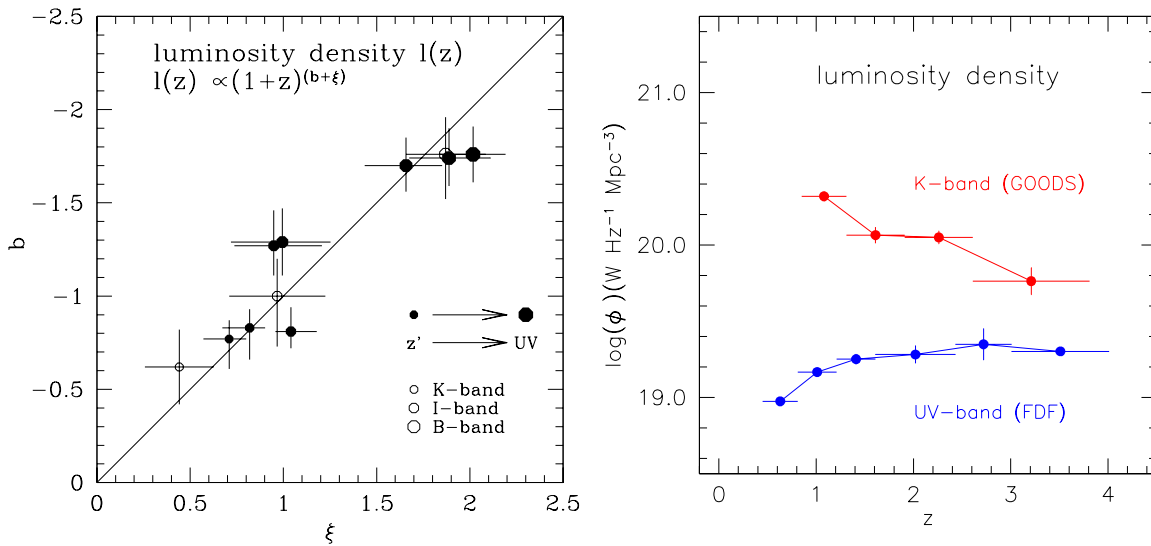


Figure 8.3: Left panel: Evolution parameters b and ξ . The filled symbols are derived from the FDF whereas the open symbols show the results of Feulner (2004). Waveband informations are coded in the symbol size, i.e. the largest symbol corresponds to the UV band and the smallest symbol to the K-band (see text for details). The solid line corresponds to $b = -\xi$ implying no redshift evolution of the luminosity density. Right panel: Luminosity density at 1500 \AA (blue symbols) derived from the I-band selected FDF as well as the restframe K-band luminosity density (red) derived from the K-band selected GOODS-South catalog.

rived from the FDF whereas the open symbols show the results of Feulner (2004). Waveband information is coded in the symbol size, i.e. the largest symbol corresponds to the UV band (1500 \AA) and the smallest symbol to the K-band. For the FDF the (filled) symbols follow the sequence $1500 \text{ \AA} \rightarrow 2800 \text{ \AA} \rightarrow u' \rightarrow g' \rightarrow B \rightarrow r' \rightarrow i' \rightarrow z'$, whereas for MUNICS the (open) symbols follow the sequence $B \rightarrow I \rightarrow K$. The solid line corresponds to $b = -\xi$ implying no redshift evolution of the stellar luminosity density. Within the errorbars nearly all wavebands are compatible with a luminosity density constant with redshift (at least out to $z \sim 4.5$ for the FDF and $z \sim 1.2$ for MUNICS).

The increase of the characteristic luminosity L^* and the simultaneous decrease of the characteristic density ϕ^* (for increasing redshift) cancel, resulting in a nearly constant luminosity density. On the other hand there seems to be a slight increase in the 1500 \AA luminosity density and a decrease in the K-band luminosity density for increasing redshift. As the MUNICS results are based on galaxies out to redshift of $z \sim 1.2$, we also derive the restframe K-band luminosity density from the deep K-band selected GOODS-South catalog. The procedure follows the method already described in Sect. 6.3. First, we derive \mathcal{L} at a given redshift by summing the V/V_{max} corrected LFs up to the absolute magnitude limits. Second, we apply a completeness correction (to zero galaxy luminosity) to take into account the missing contribution to the luminosity density of the fainter galaxies. To this end we use the best-fitting Schechter function with a fixed slope (see below).

In Fig. 8.3 (right panel) we show the 1500 \AA luminosity density (blue) derived from the I-band selected FDF as well as the restframe K-band luminosity density (red) derived from the K-band selected

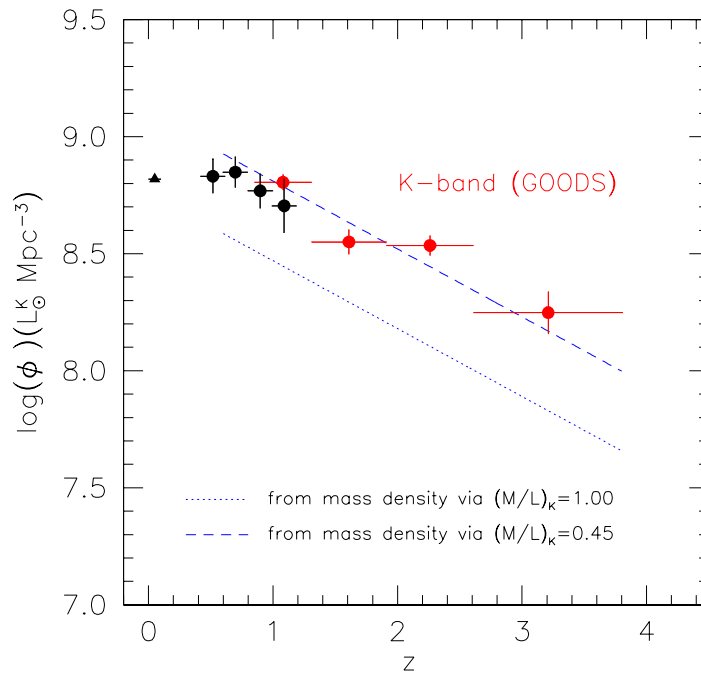


Figure 8.4: Restframe K-band luminosity density in solar units. The filled red points are derived from the observerframe K-band selected GOODS-South catalog, the filled black points are derived from the the MUNICS I-selected catalog by Feulner (2004), and the filled black triangle represents the local value as derived in Feulner (2004) using data from the 6dF field (Jones *et al.*, 2004). The dotted blue line represents the stellar mass density (converted into K-band flux) as derived from the FDF SFR after a mean dust correction of a factor of 2.50 has been applied to fit the mass densities from the literature (see dotted blue line in Fig. 7.2). A K-band mass-to-light ratio of unity has been assumed to convert the mass density into K-band flux. For the dashed line a K-band mass-to-light ratio of 0.45 is assumed to convert the mass density into K-band flux.

GOODS-South catalog. The error budget of the luminosity densities include the photometric redshift error as well as the Poissonian error (see also Sect. 6.3) and all symbols are completeness corrected assuming a fixed slope of $\alpha_K = -1.16$ (Cole *et al.*, 2001) and $\alpha_{UV} = -1.07$ (Gabasch *et al.*, 2004b) for the LFs. The figure shows a trend for the UV luminosity density to slightly increase with increasing redshift. On the other hand the K-band luminosity density clearly decreases. This can be partly due to the extrapolation, as the observerframe K-band at high redshifts traces bluer restframe wavebands and the restframe K-band luminosity density is derived by *extrapolating the best fitting SED*. Nevertheless, this trend should be verified or falsified very soon by upcoming Spitzer observations.

Last but not least we show in Fig. 8.4 the restframe K-band luminosity density in solar units. The filled red points are derived from the observerframe K-band selected GOODS-South catalog, the filled black points are derived from the MUNICS I-selected catalog by Feulner (2004), and the filled black triangle represents the local value as derived in Feulner (2004) using data from the 6dF field (Jones *et al.*, 2004). Furthermore the dotted blue line represents the stellar mass density (converted

into K-band flux) as derived from the FDF SFR after a mean dust correction of a factor of 2.50 has been applied to fit the mass densities from the literature (see also dotted blue line in Fig. 7.2). A K-band mass-to-light ratio of unity has been assumed to convert the mass density into K-band flux. As is clearly visible, the dotted blue line is lower by ~ 0.3 dex when compared to the filled red and black points. On the other hand if a K-band mass-to-light ratio of 0.45 is assumed (dashed blue line) there is a very good agreement concerning the K-band luminosity density at all redshifts $z \gtrsim 0.8$. Cole *et al.* (2001) estimated a local average K-band mass-to-light ratio of about unity. Drory *et al.* (2004) derived the evolution of the K-band mass-to-light ratio out to redshift $z \sim 1$ and found a decrease with increasing redshift. The K-band mass-to-light ratio at redshift $0.5 \rightarrow 0.7 \rightarrow 0.9 \rightarrow 1.1$ is $0.7 \rightarrow 0.6 \rightarrow 0.55 \rightarrow 0.45$. This is in very good agreement with our average K-band mass-to-light ratio of 0.45 for $z \gtrsim 0.8$ (dashed blue line in Fig. 8.4).

For redshift $z \lesssim 0.8$ the evolution of the measured K-band luminosity density decreases with time (see Fig. 8.4). Although the stellar mass density as derived from the integrated and dust-corrected FDF SFR is able to perfectly describe the local stellar mass density of Cole *et al.* (2001) (see Fig. 7.2), an extrapolation of the dashed blue line in Fig. 8.4 to redshift $z \sim 0$ would clearly overpredict the local K-band luminosity density by about 0.3 dex. On the other hand, it is possible to reconcile the dashed blue line with local K-band luminosity density if the K-band mass-to-light ratio changes by about a factor of 2 between $z \sim 1$ and $z \sim 0$ (i.e., increasing from ~ 0.45 to ~ 0.9). This agrees very well with the estimated local average K-band mass-to-light ratio of about unity of Cole *et al.* (2001).

Hierarchical clustering vs. Monolithic collapse model

As already introduced and discussed in Sect. 1.3.1 there are two competing scenarios which try to describe the formation and evolution of galaxies: the *monolithic collapse model* and the model based on *hierarchical clustering*. At this point the question arises, if, with the data presented in this thesis, it is possible to disentangle the two scenarios. For that purpose we compare in Fig. 8.5 model predictions presented in Calura *et al.* (2004) with observational data derived in the FDF. Calura *et al.* (2004) studies the evolution of the luminosity density as well as the mass density using the pure luminosity evolution (PLE) model of Calura & Matteucci (2003) and the semi-analytical model of hierarchical galaxy formation (SAM) of Menci *et al.* (2002) (see also Sect. 3.8).

In Fig. 8.5 (left panel) we show the redshift evolution of the stellar mass density already presented in Sect. 7.3. The dotted blue line represents the mass density derived from the FDF SFR after a mean dust correction of a factor of 2.50 has been applied. The two red lines show maximal (2.89) and minimal (2.14) dust corrections compatible with the data on a 3σ level. The solid black line describes the redshift evolution of the mass density as predicted by the semi-analytical model of hierarchical galaxy formation whereas the dashed black line shows the prediction of the PLE model (see Fig. 6 upper panel in Calura *et al.* 2004). While the SAM-model traces the observed mass density up to redshift $z \sim 3$ there is a huge discrepancy between the PLE model and the observed values. According to the PLE about half of the stars observable at very low redshift have already assembled at $z \sim 4$. This is due to the stellar mass produced in spheroids formed within a very short time at $z_f \sim 5$. In contrast, within the hierarchical framework massive spheroids are formed more gradually from merging episodes reaching their final mass at lower redshifts. Although the SAM is highly favored by the observed data, one has to keep in mind that the latter has been derived by assuming a constant mean dust extinction of 2.5 at all redshifts. On the other hand we show in Fig. 7.2 that at least out to $z \sim 2$ the stellar mass density derived from the dust corrected SFR very well describes the redshift evolution of the literature stellar mass density.

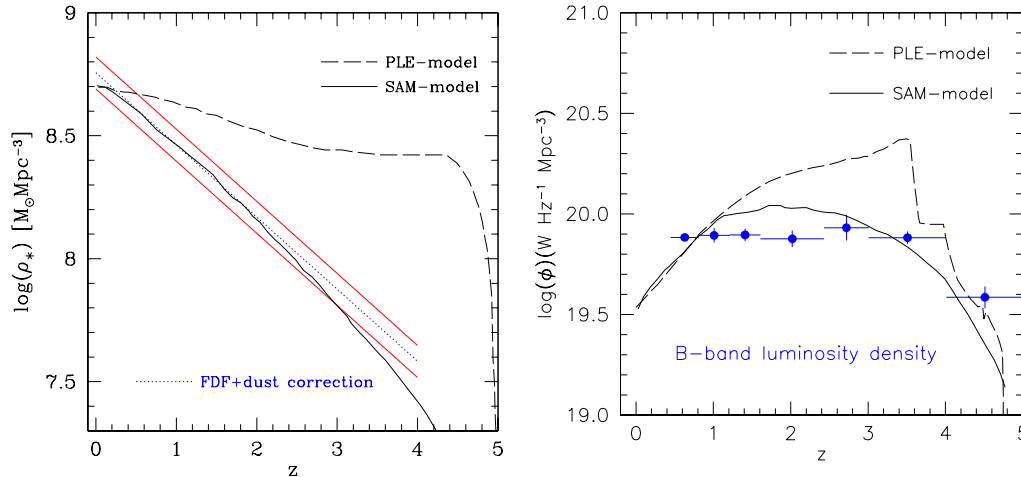


Figure 8.5: Left panel: Redshift evolution of the total mass fraction in stars. As in Fig. 7.2 the dotted blue line represents the mass density as derived from the FDF SFR after a mean dust correction of a factor of 2.5 has been applied (a dust correction by a factor of 2.5 best matches the literature mass densities; see Fig. 7.2). The two red lines show maximal (2.89) and minimal (2.14) dust corrections (3σ). The solid black line describes the redshift evolution of the mass density as predicted by a semi-analytical model of hierarchical galaxy formation whereas the dashed black line shows the prediction of a PLE model (see text for details). Right panel: Restframe B-band luminosity density (filled blue points) as derived from the I-band selected FDF catalog. All values are completeness corrected following the same recipe as in Sect. 6.3. The solid black line describes the redshift evolution of the B-band luminosity density as predicted by a semi-analytical model of hierarchical galaxy formation whereas the dashed black line shows the prediction of a PLE model (see text for details).

In addition we compare in Fig. 8.5 (right panel) the restframe B-band luminosity density (filled blue points) as derived from the I-band selected FDF catalog with the prediction of the PLE-model (black dashed line) as well as with the SAM-model (black solid line) taken from Fig. 3 (lower right panel) in Calura *et al.* (2004). All blue points are completeness corrected following the same recipe as in Sect. 6.3, i.e. using a V/V_{max} correction as well as applying a further correction (to zero galaxy luminosity), to take into account the missing contribution to the luminosity density of the fainter galaxies. Although neither model is able to reproduce the observed luminosity densities at all redshifts the SAM follows the flat luminosity density derived in the FDF better than the PLE. At low redshift ($z \lesssim 1$) both models predict nearly the same luminosity density in agreement with the measured values. In the redshift range $1 < z < 3.5$ the PLE model shows growing disagreement with increasing redshifts. At $z \sim 3$ the PLE overpredicts the observed luminosity density by 0.4 dex while the SAM traces the FDF results very well. The analysis presented in Fig. 8.5 clearly favors the semi-analytical galaxy formation model based on hierarchical clustering. The PLE model is able to reproduce neither the stellar mass density nor the B-band luminosity density in the redshift range $1. < z < 3.5$.

We also compared in Sect. 3.8 and Sect. 4.5 the luminosity function in different redshift bins and different bands with model predictions of Kauffmann *et al.* (1999) and Menci *et al.* (2002), both

based on the semi-analytical galaxy formation model. There seems to be reasonably good agreement between the models and the luminosity functions derived in the FDF up to redshift $\langle z \rangle \sim 2$ (of course at $z \approx 0$ the models are tuned to reproduce the data). On the other hand the discrepancy increases for larger redshifts.

Unfortunately not all physical processes involved in galaxy formation are perfectly understood and therefore model-predictions often have to rely on semi-empirical and simplified recipes. For this reason, although they are able to reproduce global (integrated) quantities like the luminosity and the mass density they often fail or do not yet have the numerical resolution (see e.g. Fig 3.12) to follow detailed quantities like the shape of the luminosity function. This can be seen best if one compares the predicted B-band luminosity function (Fig. 3.13) and the predicted luminosity density (Fig. 8.5, right panel) of Menci *et al.* (2002) with observations. In the redshift range $2.5 \lesssim z \lesssim 5.0$ the model predictions are not able to follow the observed brightening of the luminosity function and also the number density is much higher when compared to observations. On the other hand the luminosity density (derived by integrating over the Schechter or luminosity function; see Eq. 1.19) is able to reproduce the observed values (Fig. 8.5, right panel). The missing bright galaxies (in the model) are compensated by the large number density of faint galaxies resulting in the observed luminosity density. Therefore, as mentioned in Sect. 4.1, to constrain theoretical models it is very important to compare their theoretical predictions with as many observational results as possible. Ideally this should be done simultaneously for all wavebands (UV, optical, NIR) and for different redshift slices.

Bibliography

- Adelberger, K. L. & Steidel, C. C. 2000: *Multiwavelength Observations of Dusty Star Formation at Low and High Redshift*, ApJ, 544, 218
- Andreon, S. 2004: *Galaxy luminosity evolution: How much is due to model choice?*, A&A, 416, 865
- Appenzeller, I., Bender, R., Böhm, A., Drory, N., Fricke, K., Hafner, R., Heidt, J., Hopp, U., Jager, K., Kummel, M., Mehlert, D., et al. 2000: *The FORS Deep Field*, The Messenger, 100, 44
- Appenzeller, I., Fricke, K., Furtig, W., Gassler, W., Hafner, R., Harkl, R., Hess, H.-J., Hummel, W., Jurgens, P., Kudritzki, R.-P., Mantel, K.-H., et al. 1998: *Successful commissioning of FORS1 - the First Optical Instrument on the VLT*, The Messenger, 94, 1
- Arimoto, N. & Yoshii, Y. 1987: *Chemical and photometric properties of a galactic wind model for elliptical galaxies*, A&A, 173, 23
- Arnouts, S., Cristiani, S., Moscardini, L., Matarrese, S., Lucchin, F., Fontana, A., & Giallongo, E. 1999a: *Measuring and modelling the redshift evolution of clustering: the Hubble Deep Field North*, MNRAS, 310, 540
- Arnouts, S., D'Odorico, S., Cristiani, S., Zaggia, S., Fontana, A., & Giallongo, E. 1999b: *The NTT SUSI deep field*, A&A, 341, 641
- Arnouts, S., Vandame, B., Benoist, C., Groenewegen, M. A. T., da Costa, L., Schirmer, M., Mignani, R. P., Slijkhuis, R., Hatziminaoglou, E., Hook, R., Madejsky, R., et al. 2001: *ESO imaging survey. Deep public survey: Multi-color optical data for the Chandra Deep Field South*, A&A, 379, 740
- Böhm, A., Ziegler, B. L., Saglia, R. P., Bender, R., Fricke, K. J., Gabasch, A., Heidt, J., Mehlert, D., Noll, S., & Seitz, S. 2004: *The Tully-Fisher relation at intermediate redshift*, A&A, 420, 97
- Balogh, M. L., Christlein, D., Zabludoff, A. I., & Zaritsky, D. 2001: *The Environmental Dependence of the Infrared Luminosity and Stellar Mass Functions*, ApJ, 557, 117
- Barkana, R. & Loeb, A. 2001: *In the beginning: the first sources of light and the reionization of the universe*, Physics Reports, 349, 125
- Baugh, C. M., Cole, S., Frenk, C. S., & Lacey, C. G. 1998: *The Epoch of Galaxy Formation*, ApJ, 498, 504
- Baum, W. A. 1962: *Photoelectric Magnitudes and Red-Shifts*, in IAU Symp. 15: Problems of Extra-Galactic Research, Vol. 15, 390

- Bell, E. F., McIntosh, D. H., Katz, N., & Weinberg, M. D. 2003: *The Optical and Near-Infrared Properties of Galaxies. I. Luminosity and Stellar Mass Functions*, ApJS, 149, 289
- Bell, E. F., Wolf, C., Meisenheimer, K., Rix, H., Borch, A., Dye, S., Kleinheinrich, M., Wisotzki, L., & McIntosh, D. H. 2004: *Nearly 5000 Distant Early-Type Galaxies in COMBO-17: A Red Sequence and Its Evolution since $z \sim 1$* , ApJ, 608, 752
- Bender, R. et al. 2001: *The FORS Deep Field: Photometric Data and Photometric Redshifts*, in ESO/ECF/STScI Workshop on Deep Fields, ed. S. Christiani (Berlin: Springer), 96
- Benítez, N. 2000: *Bayesian Photometric Redshift Estimation*, ApJ, 536, 571
- Benson, A. J., Bower, R. G., Frenk, C. S., Lacey, C. G., Baugh, C. M., & Cole, S. 2003: *What Shapes the Luminosity Function of Galaxies?*, ApJ, 599, 38
- Benson, A. J., Pearce, F. R., Frenk, C. S., Baugh, C. M., & Jenkins, A. 2001: *A comparison of semi-analytic and smoothed particle hydrodynamics galaxy formation*, MNRAS, 320, 261
- Bertin, E. & Arnouts, S. 1996: *SExtractor: Software for source extraction.*, A&AS, 117, 393
- Blaizot, J., Guiderdoni, B., Devriendt, J. E. G., Bouchet, F. R., Hatton, S. J., & Stoehr, F. 2004: *GALICS- III. Properties of Lyman-break galaxies at a redshift of 3*, MNRAS, 352, 571
- Blanton, M. R., Dalcanton, J., Eisenstein, D., Loveday, J., Strauss, M. A., SubbaRao, M., Weinberg, D. H., Anderson, J. E., Annis, J., Bahcall, N. A., Bernardi, M., et al. 2001: *The Luminosity Function of Galaxies in SDSS Commissioning Data*, AJ, 121, 2358
- Blanton, M. R., Hogg, D. W., Bahcall, N. A., Brinkmann, J., Britton, M., Connolly, A. J., Csabai, I., Fukugita, M., Loveday, J., Meiksin, A., Munn, J. A., et al. 2003: *The Galaxy Luminosity Function and Luminosity Density at Redshift $z = 0.1$* , ApJ, 592, 819
- Bouwens, R. J., Broadhurst, T., & Illingworth, G. 2003a: *Cloning Dropouts: Implications for Galaxy Evolution at High Redshift*, ApJ, 593, 640
- Bouwens, R. J., Illingworth, G. D., Rosati, P., Lidman, C., Broadhurst, T., Franx, M., Ford, H. C., Magee, D., Benítez, N., Blakeslee, J. P., Meurer, G. R., et al. 2003b: *Star Formation at $z \sim 6$: i -Dropouts in the Advanced Camera for Surveys Guaranteed Time Observation Fields*, ApJ, 595, 589
- Bouwens, R. J., Illingworth, G. D., Thompson, R. I., Blakeslee, J. P., Dickinson, M. E., Broadhurst, T. J., Eisenstein, D. J., Fan, X., Franx, M., Meurer, G., & van Dokkum, P. 2004: *Star Formation at $z \sim 6$: The Hubble Ultra Deep Parallel Fields*, ApJ, 606, L25
- Bromm, V., Coppi, P. S., & Larson, R. B. 1999: *Forming the First Stars in the Universe: The Fragmentation of Primordial Gas*, ApJ, 527, L5
- Bromm, V., Kudritzki, R. P., & Loeb, A. 2001: *Generic Spectrum and Ionization Efficiency of a Heavy Initial Mass Function for the First Stars*, ApJ, 552, 464
- Bromm, V. & Larson, R. B. 2004: *The First Stars*, ARA&A, 42

- Brown, W. R., Geller, M. J., Fabricant, D. G., & Kurtz, M. J. 2001: *V- and R-band Galaxy Luminosity Functions and Low Surface Brightness Galaxies in the Century Survey*, AJ, 122, 714
- Brunner, R. J., Connolly, A. J., & Szalay, A. S. 1999: *The Statistical Approach to Quantifying Galaxy Evolution*, ApJ, 516, 563
- Bruzual, G. & Charlot, S. 1993: *Spectral evolution of stellar populations using isochrone synthesis*, ApJ, 405, 538
- Bunker, A. J., Stanway, E. R., Ellis, R. S., & McMahon, R. G. 2004: *The star formation rate of the Universe at $z \sim 6$ from the Hubble Ultra-Deep Field*, MNRAS, 450
- Burstein, D. & Heiles, C. 1982: *Reddenings derived from HI and galaxy counts - Accuracy and maps*, AJ, 87, 1165
- Calura, F. & Matteucci, F. 2003: *The Cosmic Evolution of the Galaxy Luminosity Density*, ApJ, 596, 734
- Calura, F., Matteucci, F., & Menci, N. 2004: *Cosmic star formation: constraints on the galaxy formation models*, MNRAS, 260
- Cardelli, J. A., Clayton, G. C., & Mathis, J. S. 1989: *The relationship between infrared, optical, and ultraviolet extinction*, ApJ, 345, 245
- Casertano, S., de Mello, D., Dickinson, M., Ferguson, H. C., Fruchter, A. S., Gonzalez-Lopezlira, R. A., Heyer, I., Hook, R. N., Levay, Z., Lucas, R. A., Mack, J., et al. 2000: *WFPC2 Observations of the Hubble Deep Field South*, AJ, 120, 2747
- Chen, H., Marzke, R. O., McCarthy, P. J., Martini, P., Carlberg, R. G., Persson, S. E., Bunker, A., Bridge, C. R., & Abraham, R. G. 2003: *The Las Campanas Infrared Survey. IV. The Photometric Redshift Survey and the Rest-Frame R-Band Galaxy Luminosity Function at $0.5 < z < 1.5$* , ApJ, 586, 745
- Cimatti, A., Mignoli, M., Daddi, E., Pozzetti, L., Fontana, A., Saracco, P., Poli, F., Renzini, A., Zamorani, G., Broadhurst, T., Cristiani, S., et al. 2002a: *The K20 survey. III. Photometric and spectroscopic properties of the sample*, A&A, 392, 395
- Cimatti, A., Pozzetti, L., Mignoli, M., Daddi, E., Menci, N., Poli, F., Fontana, A., Renzini, A., Zamorani, G., Broadhurst, T., Cristiani, S., et al. 2002b: *The K20 survey. IV. The redshift distribution of $K_s < 20$ galaxies: A test of galaxy formation models*, A&A, 391, L1
- Cohen, J. G. 1998: *Redshift Clustering in the Hubble Deep Field*, in The Hubble Deep Field, 52
- Cohen, J. G. 2002: *Caltech Faint Galaxy Redshift Survey. XVI. The Luminosity Function for Galaxies in the Region of the Hubble Deep Field-North to $z=1.5$* , ApJ, 567, 672
- Cohen, J. G., Hogg, D. W., Blandford, R., Cowie, L. L., Hu, E., Songaila, A., Shopbell, P., & Richberg, K. 2000: *Caltech Faint Galaxy Redshift Survey. X. A Redshift Survey in the Region of the Hubble Deep Field North*, ApJ, 538, 29

- Cole, S., Aragon-Salamanca, A., Frenk, C. S., Navarro, J. F., & Zepf, S. E. 1994: *A Recipe for Galaxy Formation*, MNRAS, 271, 781
- Cole, S., Lacey, C. G., Baugh, C. M., & Frenk, C. S. 2000: *Hierarchical galaxy formation*, MNRAS, 319, 168
- Cole, S., Norberg, P., Baugh, C. M., Frenk, C. S., Bland-Hawthorn, J., Bridges, T., Cannon, R., Colless, M., Collins, C., Couch, W., Cross, N., et al. 2001: *The 2dF galaxy redshift survey: near-infrared galaxy luminosity functions*, MNRAS, 326, 255
- Colless, M., Dalton, G., Maddox, S., Sutherland, W., Norberg, P., Cole, S., Bland-Hawthorn, J., Bridges, T., Cannon, R., Collins, C., Couch, W., et al. 2001: *The 2dF Galaxy Redshift Survey: spectra and redshifts*, MNRAS, 328, 1039
- Condon, J. J., Cotton, W. D., & Broderick, J. J. 2002: *Radio Sources and Star Formation in the Local Universe*, AJ, 124, 675
- Couchman, H. M. P. & Rees, M. J. 1986: *Pregalactic evolution in cosmologies with cold dark matter*, MNRAS, 221, 53
- Cowie, L. L., Songaila, A., & Barger, A. J. 1999: *Evidence for a Gradual Decline in the Universal Rest-Frame Ultraviolet Luminosity Density for $z < 1$* , AJ, 118, 603
- Cross, N. & Driver, S. P. 2002: *The bivariate brightness function of galaxies and a demonstration of the impact of surface brightness selection effects on luminosity function estimations*, MNRAS, 329, 579
- Davé, R., Hernquist, L., Katz, N., & Weinberg, D. H. 1999: *The Low-Redshift Ly α Forest in Cold Dark Matter Cosmologies*, ApJ, 511, 521
- de Lapparent, V., Galaz, G., Bardelli, S., & Arnouts, S. 2003: *The ESO-Sculptor Survey: Luminosity functions of galaxies per spectral type at redshifts 0.1-0.5*, A&A, 404, 831
- de Vaucouleurs, G. 1948: *Recherches sur les Nebuleuses Extragalactiques*, Annales d'Astrophysique, 11, 247
- Drory, N. 2003: *Yet another object detection application (YODA). Object detection and photometry for multi-band imaging data*, A&A, 397, 371
- Drory, N., Bender, R., Feulner, G., Hopp, U., Maraston, C., Snigula, J., & Hill, G. J. 2003: *The Munich Near-Infrared Cluster Survey. II. The K-Band Luminosity Function of Field Galaxies to $z \sim 1.2$* , ApJ, 595, 698
- Drory, N., Bender, R., Feulner, G., Hopp, U., Maraston, C., Snigula, J., & Hill, G. J. 2004: *The Munich Near-Infrared Cluster Survey (MUNICS). VI. The Stellar Masses of K-Band-selected Field Galaxies to $z \sim 1.2$* , ApJ, 608, 742
- Drory, N., Feulner, G., Bender, R., Botzler, C. S., Hopp, U., Maraston, C., Mendes de Oliveira, C., & Snigula, J. 2001: *The Munich Near-Infrared Cluster Survey - I. Field selection, object extraction and photometry*, MNRAS, 325, 550

- Egami, E., Dole, H., Huang, J.-S., Pérez-Gonzalez, P., Le Floc'h, E., Papovich, C., Barmby, P., Ivison, R. J., Serjeant, S., Mortier, A., Frayer, D. T., et al. 2004: *Spitzer Observations of the SCUBA/VLA Sources in the Lockman Hole: Star Formation History of Infrared-Luminous Galaxies*, ApJS, 154, 130
- Eggen, O. J., Lynden-Bell, D., & Sandage, A. R. 1962: *Evidence from the motions of old stars that the Galaxy collapsed.*, ApJ, 136, 748
- Ellis, R. S., Colless, M., Broadhurst, T., Heyl, J., & Glazebrook, K. 1996: *Autofib Redshift Survey - I. Evolution of the galaxy luminosity function*, MNRAS, 280, 235
- Fanson, J. L., Fazio, G. G., Houck, J. R., Kelly, T., Rieke, G. H., Tenerelli, D. J., & Whitten, M. 1998: *Space Infrared Telescope Facility (SIRTF)*, in Proc. SPIE Vol. 3356, p. 478-491, Space Telescopes and Instruments V, Pierre Y. Bely; James B. Breckinridge; Eds., 478-491
- Ferguson, H. C., Dickinson, M., & Williams, R. 2000: *The Hubble Deep Fields*, ARA&A, 38, 667
- Fernández-Soto, A., Lanzetta, K. M., & Yahil, A. 1999: *A New Catalog of Photometric Redshifts in the Hubble Deep Field*, ApJ, 513, 34
- Feulner, G. 2004: *A Near-Infrared Selected Galaxy Redshift Survey*, PhD thesis, Ludwig-Maximilians-Universität München
- Feulner, G., Bender, R., Drory, N., Hopp, U., Snigula, J., & Hill, G. J. 2003: *The Munich Near-Infrared Cluster Survey - V. The evolution of the rest-frame K- and J-band galaxy luminosity functions to $z \sim 0.7$* , MNRAS, 342, 605
- Firth, A. E., Lahav, O., & Somerville, R. S. 2003: *Estimating photometric redshifts with artificial neural networks*, MNRAS, 339, 1195
- Fixsen, D. J., Cheng, E. S., Gales, J. M., Mather, J. C., Shafer, R. A., & Wright, E. L. 1996: *The Cosmic Microwave Background Spectrum from the Full COBE FIRAS Data Set*, ApJ, 473, 576
- Fontana, A., Poli, F., Menci, N., Nonino, M., Giallongo, E., Cristiani, S., & D'Odorico, S. 2003: *A European Southern Observatory Very Large Telescope Survey of Near-Infrared ($z \leq 25$) Selected Galaxies at Redshifts $4.5 < z < 6$: Constraining the Cosmic Star Formation Rate near the Reionization Epoch*, ApJ, 587, 544
- Fontana, A., Pozzetti, L., Donnarumma, I., Renzini, A., Cimatti, A., Zamorani, G., Menci, N., Daddi, E., Giallongo, E., Mignoli, M., Perna, C., et al. 2004: *The K20 survey. VI. The distribution of the stellar masses in galaxies up to $z \sim 2$* , A&A, 424, 23
- Franx, M., Labbé, I., Rudnick, G., van Dokkum, P. G., Daddi, E., Förster Schreiber, N. M., Moorwood, A., Rix, H., Röttgering, H., van de Wel, A., van der Werf, P., et al. 2003: *A Significant Population of Red, Near-Infrared-selected High-Redshift Galaxies*, ApJ, 587, L79
- Fried, J. W., von Kuhlmann, B., Meisenheimer, K., Rix, H.-W., Wolf, C., Hippelein, H. H., Kümmel, M., Phleps, S., Röser, H. J., Thierring, I., & Maier, C. 2001: *The luminosity function of field galaxies and its evolution since $z=1$* , A&A, 367, 788

- Fukugita, M., Ichikawa, T., Gunn, J. E., Doi, M., Shimasaku, K., & Schneider, D. P. 1996: *The Sloan Digital Sky Survey Photometric System*, AJ, 111, 1748
- Gössl, C. A. & Riffeser, A. 2002: *Image reduction pipeline for the detection of variable sources in highly crowded fields*, A&A, 381, 1095
- Gabasch, A., Bender, R., Hopp, U., Saglia, R. P., Seitz, S., Snigula, S., Appenzeller, I., Heidt, J., Mehlert, D., Noll, S., Böhm, A., et al. 2004a: *Evolution of the Galaxy Luminosity Function in the FORS Deep Field (FDF)*, in Multiwavelength Cosmology, Proceedings of the Multiwavelength Cosmology Conference, held on Mykonos Island, Greece, 17-20 June 2003
- Gabasch, A., Bender, R., Seitz, S., Hopp, U., Saglia, R. P., Feulner, G., Snigula, J., Drory, N., Appenzeller, I., Heidt, J., Mehlert, D., et al. 2004b: *The evolution of the luminosity functions in the FORS Deep Field from low to high redshift. I. The blue bands*, A&A, 421, 41
- Gabasch, A., Salvato, M., Saglia, R. P., Bender, R., Hopp, U., Seitz, S., Feulner, G., Pannella, M., Drory, N., Schirmer, M., & Erben, T. 2004c: *The Star Formation Rate History in the FORS Deep and GOODS-South Fields*, ApJ, 616, L83
- Geller, M. J., Kurtz, M. J., Wegner, G., Thorstensen, J. R., Fabricant, D. G., Marzke, R. O., Huchra, J. P., Schild, R. E., & Falco, E. E. 1997: *The Century Survey: A Deeper Slice of the Universe*, AJ, 114, 2205
- Genzel, R., Tacconi, L. J., Rigopoulou, D., Lutz, D., & Tecza, M. 2001: *Ultraluminous Infrared Mergers: Elliptical Galaxies in Formation?*, ApJ, 563, 527
- Giavalisco, M. 2002: *Lyman-Break Galaxies*, ARA&A, 40, 579
- Giavalisco, M. & Dickinson, M. 2001: *Clustering Segregation with Ultraviolet Luminosity in Lyman Break Galaxies at $z \sim 3$ and Its Implications*, ApJ, 550, 177
- Giavalisco, M., Dickinson, M., Ferguson, H. C., Ravindranath, S., Kretchmer, C., Moustakas, L. A., Madau, P., Fall, S. M., Gardner, J. P., Livio, M., Papovich, C., et al. 2004a: *The Rest-Frame Ultraviolet Luminosity Density of Star-forming Galaxies at Redshifts $z < 3.5$* , ApJ, 600, L103
- Giavalisco, M., Ferguson, H. C., Koekemoer, A. M., Dickinson, M., Alexander, D. M., Bauer, F. E., Bergeron, J., Biagetti, C., Brandt, W. N., Casertano, S., Cesarsky, C., et al. 2004b: *The Great Observatories Origins Deep Survey: Initial Results from Optical and Near-Infrared Imaging*, ApJ, 600, L93
- Giavalisco, M., Steidel, C. C., Adelberger, K. L., Dickinson, M. E., Pettini, M., & Kellogg, M. 1998: *The Angular Clustering of Lyman-Break Galaxies at Redshift Z approximately 3*, ApJ, 503, 543
- Heidt, J., Appenzeller, I., Bender, R., Böhm, A., Drory, N., Fricke, K. J., Gabasch, A., Hopp, U., Jäger, K., Kümmel, M., Mehlert, D., et al. 2001: *The FORS Deep Field*, Reviews of Modern Astronomy, 14, 209
- Heidt, J., Appenzeller, I., Gabasch, A., Jäger, K., Seitz, S., Bender, R., Böhm, A., Snigula, J., Fricke, K. J., Hopp, U., Kümmel, M., et al. 2003: *The FORS Deep Field: Field selection, photometric observations and photometric catalog*, A&A, 398, 49

- Hernquist, L. & Springel, V. 2003: *An analytical model for the history of cosmic star formation*, MNRAS, 341, 1253
- Heyl, J., Colless, M., Ellis, R. S., & Broadhurst, T. 1997: *Autofib Redshift Survey - II. Evolution of the galaxy luminosity function by spectral type*, MNRAS, 285, 613
- Hogg, D. W., Cohen, J. G., Blandford, R., & Pahre, M. A. 1998: *The O II Luminosity Density of the Universe*, ApJ, 504, 622
- Hogg, D. W., Pahre, M. A., McCarthy, J. K., Cohen, J. G., Blandford, R., Smail, I., & Soifer, B. T. 1997: *Counts and colours of faint galaxies in the U and R bands*, MNRAS, 288, 404
- Hopkins, A. 2004: *On the evolution of star forming galaxies*, astro-ph/0407170
- Hopkins, A. M., Connolly, A. J., Haarsma, D. B., & Cram, L. E. 2001: *Toward a Resolution of the Discrepancy between Different Estimators of Star Formation Rate*, AJ, 122, 288
- Hopkins, A. M., Connolly, A. J., & Szalay, A. S. 2000: *Star Formation in Galaxies between Redshifts of 0.7 and 1.8*, AJ, 120, 2843
- Huang, J., Cowie, L. L., & Luppino, G. A. 1998: *Morphological Classification of the Local I- and K-Band Galaxy Sample*, ApJ, 496, 31
- Huang, J.-S., Glazebrook, K., Cowie, L. L., & Tinney, C. 2003: *The Hawaii+Anglo-Australian Observatory K-Band Galaxy Redshift Survey. I. The Local K-Band Luminosity Function*, ApJ, 584, 203
- Hughes, D. H., Serjeant, S., Dunlop, J., Rowan-Robinson, M., Blain, A., Mann, R. G., Ivison, R., Peacock, J., Efstathiou, A., Gear, W., Oliver, S., et al. 1998: *High-redshift star formation in the Hubble Deep Field revealed by a submillimetre-wavelength survey.*, Nat, 394, 241
- Hunter, D. A., Gallagher, J. S., & Rautenkranz, D. 1982: *Global properties of irregular galaxies*, ApJS, 49, 53
- Ilbert, O., Tresse, L., Arnouts, S., Zucca, E., Bardelli, S., Zamorani, G., Adami, C., Cappi, A., Garilli, B., Le Fèvre, O., Maccagni, D., et al. 2004: *Bias in the estimation of global luminosity functions*, MNRAS, 351, 541
- Im, M., Simard, L., Faber, S. M., Koo, D. C., Gebhardt, K., Willmer, C. N. A., Phillips, A., Illingworth, G., Vogt, N. P., & Sarajedini, V. L. 2002: *The DEEP Groth Strip Survey. X. Number Density and Luminosity Function of Field E/S0 Galaxies at $z < 1$* , ApJ, 571, 136
- Iwata, I., Ohta, K., Tamura, N., Ando, M., Wada, S., Watanabe, C., Akiyama, M., & Aoki, K. 2003: *Lyman Break Galaxies at $z \sim 5$: Luminosity Function*, PASJ, 55, 415
- Jäger, K., Heidt, J., Appenzeller, I., Bender, R., Fricke, K. J., & FDF-Team. 1999: *The FORS Deep Field (FDF): Selection and first impressions*, in Astronomische Gesellschaft Meeting Abstracts, 9
- Jarrett, T. H., Chester, T., Cutri, R., Schneider, S., Skrutskie, M., & Huchra, J. P. 2000: *2MASS Extended Source Catalog: Overview and Algorithms*, AJ, 119, 2498

- Jing, Y. P., Börner, G., & Suto, Y. 2002: *Spatial Correlation Functions and the Pairwise Peculiar Velocity Dispersion of Galaxies in the Point Source Catalog Redshift Survey: Implications for the Galaxy Biasing in Cold Dark Matter Models*, ApJ, 564, 15
- Jones, D. H., Saunders, W., Colless, M., Read, M. A., Parker, Q. A., Watson, F. G., Campbell, L. A., Burkey, D., Mauch, T., Moore, L., Hartley, M., et al. 2004: *The 6dF Galaxy Survey: samples, observational techniques and the first data release*, MNRAS, 482
- Jorgensen, I. 1994: *Secondary photometric standard stars for the Thuan-Gunn and Johnson-Kron-Cousins systems*, PASP, 106, 967
- Kümmel, M. W. & Wagner, S. J. 2001: *A wide field survey at the Northern Ecliptic Pole. II. Number counts and galaxy colours in B_r, R, and K*, A&A, 370, 384
- Kajisawa, M. & Yamada, T. 2001: *When Did the Hubble Sequence Appear?: Morphology, Color, and Number-Density Evolution of the Galaxies in the Hubble Deep Field North*, PASJ, 53, 833
- Kashikawa, N., Takata, T., Ohyama, Y., Yoshida, M., Maihara, T., Iwamuro, F., Motohara, K., Totani, T., Nagashima, M., Shimasaku, K., Furusawa, H., et al. 2003: *Subaru Deep Survey. III. Evolution of Rest-Frame Luminosity Functions Based on the Photometric Redshifts for a K'-Band-Selected Galaxy Sample*, AJ, 125, 53
- Kauffmann, G., Colberg, J. M., Diaferio, A., & White, S. D. M. 1999: *Clustering of galaxies in a hierarchical universe - I. Methods and results at z=0*, MNRAS, 303, 188
- Kauffmann, G., Heckman, T. M., White, S. D. M., Charlot, S., Tremonti, C., Brinchmann, J., Bruzual, G., Peng, E. W., Seibert, M., Bernardi, M., Blanton, M., et al. 2003: *Stellar masses and star formation histories for 10⁵ galaxies from the Sloan Digital Sky Survey*, MNRAS, 341, 33
- Kauffmann, G., White, S. D. M., & Guiderdoni, B. 1993: *The Formation and Evolution of Galaxies Within Merging Dark Matter Haloes*, MNRAS, 264, 201
- Kinney, A. L., Calzetti, D., Bica, E., & Storchi-Bergmann, T. 1994: *The Reddening law outside the local group galaxies: The case of NGC 7552 and NGC 5236*, ApJ, 429, 172
- Kinney, A. L., Calzetti, D., Bohlin, R. C., McQuade, K., Storchi-Bergmann, T., & Schmitt, H. R. 1996: *Template Ultraviolet to Near-Infrared Spectra of Star-forming Galaxies and Their Application to K-Corrections*, ApJ, 467, 38
- Kochanek, C. S., Pahre, M. A., Falco, E. E., Huchra, J. P., Mader, J., Jarrett, T. H., Chester, T., Cutri, R., & Schneider, S. E. 2001: *The K-Band Galaxy Luminosity Function*, ApJ, 560, 566
- Kolb, E. W. & Turner, M. S. 1990, *The early universe* (Frontiers in Physics, Reading, MA: Addison-Wesley, 1988, 1990)
- Koo, D. C. 1985: *Optical multicolors - A poor person's Z machine for galaxies*, AJ, 90, 418
- Kron, R. G. 1980: *Photometry of a complete sample of faint galaxies*, ApJS, 43, 305

- Labbé, I., Franx, M., Rudnick, G., Schreiber, N. M. F., Rix, H., Moorwood, A., van Dokkum, P. G., van der Werf, P., Röttgering, H., van Starckenburg, L., van de Wel, A., et al. 2003: *Ultradeep Near-Infrared ISAAC Observations of the Hubble Deep Field South: Observations, Reduction, Multicolor Catalog, and Photometric Redshifts*, AJ, 125, 1107
- Landolt, A. U. 1992: *UBVRI photometric standard stars in the magnitude range 11.5-16.0 around the celestial equator*, AJ, 104, 340
- Le Borgne, D. & Rocca-Volmerange, B. 2002: *Photometric redshifts from evolutionary synthesis with PEGASE: The code Z-PEG and the $z=0$ age constraint*, A&A, 386, 446
- Le Fevre, O., Vettolani, G., Paltani, S., Tresse, L., Zamorani, G., Le Brun, V., Moreau, C., & VIMOS VLT Deep Survey team. 2004: *The VIMOS VLT Deep Survey: Public release of 1599 redshifts to $IAB \leq 24$ across the Chandra Deep Field South*, A&A submitted (astro-ph/0403628)
- Lilly, S. J., Le Fevre, O., Crampton, D., Hammer, F., & Tresse, L. 1995a: *The Canada-France Redshift Survey. I. Introduction to the Survey, Photometric Catalogs, and Surface Brightness Selection Effects*, ApJ, 455, 50
- Lilly, S. J., Le Fevre, O., Hammer, F., & Crampton, D. 1996: *The Canada-France Redshift Survey: The Luminosity Density and Star Formation History of the Universe to Z approximately 1*, ApJ, 460, L1
- Lilly, S. J., Tresse, L., Hammer, F., Crampton, D., & Le Fevre, O. 1995b: *The Canada-France Redshift Survey. VI. Evolution of the Galaxy Luminosity Function to Z approximately 1*, ApJ, 455, 108
- Lin, H., Kirshner, R. P., Shectman, S. A., Landy, S. D., Oemler, A., Tucker, D. L., & Schechter, P. L. 1996: *The Luminosity Function of Galaxies in the Las Campanas Redshift Survey*, ApJ, 464, 60
- Lin, H., Yee, H. K. C., Carlberg, R. G., & Ellingson, E. 1997: *The Luminosity Function of Field Galaxies in the CNOC1 Redshift Survey*, ApJ, 475, 494
- Liske, J., Lemon, D. J., Driver, S. P., Cross, N. J. G., & Couch, W. J. 2003: *The Millennium Galaxy Catalogue: $16 < B_{MGC} < 24$ galaxy counts and the calibration of the local galaxy luminosity function*, MNRAS, 344, 307
- Loveday, J. 2000: *The K-band luminosity function of nearby field galaxies*, MNRAS, 312, 557
- Loveday, J., Tresse, L., & Maddox, S. 1999: *Spectral analysis of the Stromlo-APM Survey - II. Galaxy luminosity function and clustering by spectral type*, MNRAS, 310, 281
- Madau, P. 1995: *Radiative transfer in a clumpy universe: The colors of high-redshift galaxies*, ApJ, 441, 18
- Madau, P., Ferguson, H. C., Dickinson, M. E., Giavalisco, M., Steidel, C. C., & Fruchter, A. 1996: *High-redshift galaxies in the Hubble Deep Field: colour selection and star formation history to $z \sim 4$* , MNRAS, 283, 1388
- Madau, P., Pozzetti, L., & Dickinson, M. 1998: *The Star Formation History of Field Galaxies*, ApJ, 498, 106

- Maihara, T., Iwamuro, F., Tanabe, H., Taguchi, T., Hata, R., Oya, S., Kashikawa, N., Iye, M., Miyazaki, S., Karoji, H., Yoshida, M., et al. 2001: *Subaru Deep Survey I. Near-Infrared Observations*, PASJ, 53, 25
- Mannucci, F., Basile, F., Poggianti, B. M., Cimatti, A., Daddi, E., Pozzetti, L., & Vanzi, L. 2001: *Near-infrared template spectra of normal galaxies: k-corrections, galaxy models and stellar populations*, MNRAS, 326, 745
- Maraston, C. 1998: *Evolutionary synthesis of stellar populations: a modular tool*, MNRAS, 300, 872
- Marinoni, C., Hudson, M. J., & Giuricin, G. 2002: *The Optical Luminosity Function of Virialized Systems*, ApJ, 569, 91
- Marinoni, C., Monaco, P., Giuricin, G., & Costantini, B. 1999: *The Nearby Optical Galaxy Sample: The Local Galaxy Luminosity Function*, ApJ, 521, 50
- Marzke, R., McCarthy, P. J., Persson, E., Oemler, A., Dressler, A., Yan, M. B. L., Carlberg, R., Abraham, R., Ellis, R., Firth, A., Mackay, C., et al. 1999: *The Las Campanas Infrared Survey*, in ASP Conf. Ser. 191: Photometric Redshifts and the Detection of High Redshift Galaxies, 148
- Matteucci, F. 1994: *Abundance ratios in ellipticals and galaxy formation*, A&A, 288, 57
- McCarthy, P. J., Carlberg, R. G., Chen, H.-W., Marzke, R. O., Firth, A. E., Ellis, R. S., Persson, S. E., McMahon, R. G., Lahav, O., Wilson, J., Martini, P., et al. 2001: *The Las Campanas Infrared Survey: Early-Type Galaxy Progenitors beyond $z=1$* , ApJ, 560, L131
- McCracken, H. J., Metcalfe, N., Shanks, T., Campos, A., Gardner, J. P., & Fong, R. 2000: *Galaxy number counts - IV. Surveying the Herschel Deep Field in the near-infrared*, MNRAS, 311, 707
- Mehlert, D., Noll, S., Appenzeller, I., Bender, R., Seitz, S., & FDF Team. 2001: *The FORS Deep Field: First Spectroscopic Results*, in Deep Fields, 162
- Mehlert, D., Noll, S., Appenzeller, I., Saglia, R. P., Bender, R., Böhm, A., Drory, N., Fricke, K., Gabasch, A., Heidt, J., Hopp, U., et al. 2002: *Evidence for chemical evolution in the spectra of high redshift galaxies*, A&A, 393, 809
- Meisenheimer, K., Beckwith, S., Fockenbrock, H., Fried, J., Hippelein, H., Huang, J., Leinert, C., Phleps, S., Roser, H.-J., Thommes, E., Thompson, D., et al. 1998: *The Calar Alto Deep Imaging Survey for Galaxies and Quasars at $Z > 5$* , in ASP Conf. Ser. 146: The Young Universe: Galaxy Formation and Evolution at Intermediate and High Redshift, 134
- Menci, N., Cavaliere, A., Fontana, A., Giallongo, E., & Poli, F. 2002: *Binary Aggregations in Hierarchical Galaxy Formation: The Evolution of the Galaxy Luminosity Function*, ApJ, 575, 18
- Menci, N., Cavaliere, A., Fontana, A., Giallongo, E., Poli, F., & Vittorini, V. 2004: *Early Hierarchical Formation of Massive Galaxies Triggered by Interactions*, ApJ, 604, 12
- Metcalfe, N., Shanks, T., Campos, A., McCracken, H. J., & Fong, R. 2001: *Galaxy number counts - V. Ultradeep counts: the Herschel and Hubble Deep Fields*, MNRAS, 323, 795

- Miralda-Escudé, J. 2003: *The Dark Age of the Universe*, Science, 300, 1904
- Mobasher, B., Idzi, R., Benítez, N., Cimatti, A., Cristiani, S., Daddi, E., Dahlen, T., Dickinson, M., Erben, T., Ferguson, H. C., Giavalisco, M., et al. 2004: *Photometric Redshifts for Galaxies in the GOODS Southern Field*, ApJ, 600, L167
- Monet, D. G. 1998: *The 526,280,881 Objects In The USNO-A2.0 Catalog*, Bulletin of the American Astronomical Society, 30, 1427
- Nagamine, K. 2002: *Lyman Break Galaxies: Their Progenitors and Descendants*, ApJ, 564, 73
- Nagamine, K., Springel, V., Hernquist, L., & Machacek, M. 2004: *Photometric properties of Lyman-break galaxies at $z = 3$ in cosmological SPH simulations*, MNRAS, 350, 385
- Narlikar, J. V. & Padmanabhan, T. 2001: *Standard Cosmology and Alternatives: A Critical Appraisal*, ARA&A, 39, 211
- Noll, S., Mehlert, D., Appenzeller, I., Bender, R., Böhm, A., Gabasch, A., Heidt, J., Hopp, U., Jäger, K., Seitz, S., Stahl, O., et al. 2004: *The FORS Deep Field spectroscopic survey*, A&A, 418, 885
- Noll, S., Mehlert, D., Appenzeller, I., & The FDF-Team. 2001: *Spectroscopy in the FORS Deep Field*, in Astronomische Gesellschaft Meeting Abstracts, 532
- Norberg, P., Baugh, C. M., Hawkins, E., Maddox, S., Peacock, J. A., Cole, S., Frenk, C. S., Bland-Hawthorn, J., Bridges, T., Cannon, R., Colless, M., et al. 2001: *The 2dF Galaxy Redshift Survey: luminosity dependence of galaxy clustering*, MNRAS, 328, 64
- Norberg, P., Cole, S., Baugh, C. M., Frenk, C. S., Baldry, I., Bland-Hawthorn, J., Bridges, T., Cannon, R., Colless, M., Collins, C., Couch, W., et al. 2002: *The 2dF Galaxy Redshift Survey: the b_j -band galaxy luminosity function and survey selection function*, MNRAS, 336, 907
- Oh, S. P. & Haiman, Z. 2002: *Second-Generation Objects in the Universe: Radiative Cooling and Collapse of Halos with Virial Temperatures above $10^4 K$* , ApJ, 569, 558
- Ouchi, M., Shimasaku, K., Furusawa, H., Miyazaki, M., Doi, M., Hamabe, M., Hayashino, T., Kimura, M., Kodaira, K., Komiyama, Y., Matsuda, Y., et al. 2003: *Subaru Deep Survey. II. Luminosity Functions and Clustering Properties of Ly α Emitters at $z=4.86$ in the Subaru Deep Field*, ApJ, 582, 60
- Ouchi, M., Shimasaku, K., Okamura, S., Doi, M., Furusawa, H., Hamabe, M., Kimura, M., Komiyama, Y., Miyazaki, M., Miyazaki, S., Nakata, F., et al. 2001: *Statistical Properties of Lyman Break Galaxies at $z \approx 4$* , in Cosmology conference Where's the matter?, ed. L. Tresse & M. Treyer, 186
- Ouchi, M., Shimasaku, K., Okamura, S., Furusawa, H., Kashikawa, N., Ota, K., Doi, M., Hamabe, M., Kimura, M., Komiyama, Y., Miyazaki, M., et al. 2004a: *Subaru Deep Survey. V. A Census of Lyman Break Galaxies at $z \simeq 4$ and 5 in the Subaru Deep Fields: Photometric Properties*, ApJ, 611, 660

- Ouchi, M., Shimasaku, K., Okamura, S., Furusawa, H., Kashikawa, N., Ota, K., Doi, M., Hamabe, M., Kimura, M., Komiyama, Y., Miyazaki, M., et al. 2004b: *Subaru Deep Survey. VI. A Census of Lyman Break Galaxies at $z \simeq 4$ and 5 in the Subaru Deep Fields: Clustering Properties*, ApJ, 611, 685
- Pérez-González, P. G., Gallego, J., Zamorano, J., Alonso-Herrero, A., de Paz, A. G., & Aragón-Salamanca, A. 2003a: *Luminosity and Stellar Mass Functions of Local Star-forming Galaxies*, ApJ, 587, L27
- Pérez-González, P. G., Zamorano, J., Gallego, J., Aragón-Salamanca, A., & Gil de Paz, A. 2003b: *Spatial Analysis of the H α Emission in the Local Star-forming UCM Galaxies*, ApJ, 591, 827
- Padmanabhan, T. 1993, *Structure formation in the universe* (Cambridge, UK: Cambridge University Press, —c1993)
- Pannella, M., Hopp, U., Saglia, R., Bender, R., Feulner, G., Gabasch, A., Salvato, M., & Seitz, S. 2004: *"Morphology evolution in the GOODS South and Fors Deep Fields"*, in preparation
- Pascarelle, S. M., Lanzetta, K. M., & Fernández-Soto, A. 1998: *The Ultraviolet Luminosity Density of the Universe from Photometric Redshifts of Galaxies in the Hubble Deep Field*, ApJ, 508, L1
- Peacock, J. A. 1999, *Cosmological physics* (Cambridge University Press)
- Pearce, F. R., Jenkins, A., Frenk, C. S., Colberg, J. M., White, S. D. M., Thomas, P. A., Couchman, H. M. P., Peacock, J. A., Efstathiou, G., & The Virgo Consortium. 1999: *A Simulation of Galaxy Formation and Clustering*, ApJ, 521, L99
- Peebles, P. J. E. 1993, *Principles of physical cosmology* (Princeton Series in Physics, Princeton, NJ: Princeton University Press, —c1993)
- Penzias, A. A. & Wilson, R. W. 1965: *A Measurement of Excess Antenna Temperature at 4080 Mc/s.*, ApJ, 142, 419
- Persson, S. E., Murphy, D. C., Krzeminski, W., Roth, M., & Rieke, M. J. 1998: *A New System of Faint Near-Infrared Standard Stars*, AJ, 116, 2475
- Pickles, A. J. 1998: *A Stellar Spectral Flux Library: 1150-25000 Å*, PASP, 110, 863
- Poli, F., Giallongo, E., Fontana, A., Menci, N., Zamorani, G., Nonino, M., Saracco, P., Vanzella, E., Donnarumma, I., Salimbeni, S., Cimatti, A., et al. 2003: *The Evolution of the Galaxy Luminosity Function in the Rest-Frame Blue Band up to $z=3.5$* , ApJ, 593, L1
- Poli, F., Giallongo, E., Menci, N., D'Odorico, S., & Fontana, A. 1999: *The Evolution of the Galaxy Sizes in the New Technology Telescope Deep Field: A Comparison with Cold Dark Matter Models*, ApJ, 527, 662
- Poli, F., Menci, N., Giallongo, E., Fontana, A., Cristiani, S., & D'Odorico, S. 2001: *The Evolution of the Luminosity Function in Deep Fields: A Comparison with Cold Dark Matter Models*, ApJ, 551, L45

- Pozzetti, L., Bruzual A., G., & Zamorani, G. 1996: *Pure luminosity evolution for faint field galaxy samples*, MNRAS, 281, 953
- Pozzetti, L., Cimatti, A., Zamorani, G., Daddi, E., Menci, N., Fontana, A., Renzini, A., Mignoli, M., Poli, F., Saracco, P., Broadhurst, T., et al. 2003: *The K20 survey. V. The evolution of the near-IR Luminosity Function*, A&A, 402, 837
- Pozzetti, L., Madau, P., Zamorani, G., Ferguson, H. C., & Bruzual A., G. 1998: *High-redshift galaxies in the Hubble Deep Field - II. Colours and number counts*, MNRAS, 298, 1133
- Press, W. H. & Schechter, P. 1974: *Formation of Galaxies and Clusters of Galaxies by Self-Similar Gravitational Condensation*, ApJ, 187, 425
- Riffeser, A., Fliri, J., Gössl, C. A., Bender, R., Hopp, U., Bärnbantner, O., Ries, C., Barwig, H., Seitz, S., & Mitsch, W. 2001: *WeCAPP - Wendelstein Calar Alto pixellensing project I. Tracing dark and bright matter in M 31*, A&A, 379, 362
- Rowan-Robinson, M. 2003: *Photometric redshifts in the Hubble Deep Fields: evolution of extinction and the star formation rate*, MNRAS, 345, 819
- Rudnick, G., Rix, H., Franx, M., Labbé, I., Blanton, M., Daddi, E., Förster Schreiber, N. M., Moorwood, A., Röttgering, H., Trujillo, I., van de Wel, A., et al. 2003: *The Rest-Frame Optical Luminosity Density, Color, and Stellar Mass Density of the Universe from $z = 0$ to $z = 3$* , ApJ, 599, 847
- Sadler, E. M., Jackson, C. A., Cannon, R. D., McIntyre, V. J., Murphy, T., Bland-Hawthorn, J., Bridges, T., Cole, S., Colless, M., Collins, C., Couch, W., et al. 2002: *Radio sources in the 2dF Galaxy Redshift Survey - II. Local radio luminosity functions for AGN and star-forming galaxies at 1.4 GHz*, MNRAS, 329, 227
- Salvato, M. *et al.* 2004 in preparation
- Sandage, A. 1986: *Star formation rates, galaxy morphology, and the Hubble sequence*, A&A, 161, 89
- Sandage, A. 1990: *On the formation and age of the Galaxy*, J. R. Astron. Soc. Can., 84, 70
- Saracco, P., D'Odorico, S., Moorwood, A., Buzzoni, A., Cuby, J.-G., & Lidman, C. 1999: *IR colors and sizes of faint galaxies*, A&A, 349, 751
- Sawicki, M. J., Lin, H., & Yee, H. K. C. 1997: *Evolution of the Galaxy Population Based on Photometric Redshifts in the Hubble Deep Field*, AJ, 113, 1
- Schechter, P. 1976: *An analytic expression for the luminosity function for galaxies.*, ApJ, 203, 297
- Schirmer, M., Erben, T., Schneider, P., Pietrzynski, G., Gieren, W., Carpano, S., Micol, A., & Pierfederici, F. 2003: *GaBoDS: The Garching-Bonn Deep Survey. I. Anatomy of galaxy clusters in the background of NGC 300*, A&A, 407, 869
- Schmidt, M. 1968: *Space Distribution and Luminosity Functions of Quasi-Stellar Radio Sources*, ApJ, 151, 393

- Sérsic, J. L. 1968, Atlas de galaxias australes (Cordoba, Argentina: Observatorio Astronomico, 1968)
- Shapley, A. E., Steidel, C. C., Adelberger, K. L., Dickinson, M., Giavalisco, M., & Pettini, M. 2001: *The Rest-Frame Optical Properties of $z \sim 3$ Galaxies*, ApJ, 562, 95
- Small, T. A., Sargent, W. L. W., & Hamilton, D. 1997: *The Norris Survey of the Corona Borealis Supercluster. II. Galaxy Evolution with Redshift and Environment*, ApJ, 487, 512
- Snigula, J., Drory, N., Bender, R., Botzler, C. S., Feulner, G., & Hopp, U. 2002: *The Munich Near-Infrared Cluster Survey - IV. Biases in the completeness of near-infrared imaging data*, MNRAS, 336, 1329
- Somerville, R. S., Lee, K., Ferguson, H. C., Gardner, J. P., Moustakas, L. A., & Giavalisco, M. 2004: *Cosmic Variance in the Great Observatories Origins Deep Survey*, ApJ, 600, L171
- Somerville, R. S. & Primack, J. R. 1999: *Semi-analytic modelling of galaxy formation: the local Universe*, MNRAS, 310, 1087
- Somerville, R. S., Primack, J. R., & Faber, S. M. 2001: *The nature of high-redshift galaxies*, MNRAS, 320, 504
- Spiegel, D. N., Verde, L., Peiris, H. V., Komatsu, E., Nolte, M. R., Bennett, C. L., Halpern, M., Hinshaw, G., Jarosik, N., Kogut, A., Limon, M., et al. 2003: *First-Year Wilkinson Microwave Anisotropy Probe (WMAP) Observations: Determination of Cosmological Parameters*, ApJS, 148, 175
- Steidel, C. C., Adelberger, K. L., Giavalisco, M., Dickinson, M., & Pettini, M. 1999: *Lyman-Break Galaxies at $z < \sim 4$ and the Evolution of the Ultraviolet Luminosity Density at High Redshift*, ApJ, 519, 1
- Steidel, C. C., Giavalisco, M., Dickinson, M., & Adelberger, K. L. 1996: *Spectroscopy of Lyman Break Galaxies in the Hubble Deep Field*, AJ, 112, 352
- Steidel, C. C. & Hamilton, D. 1993: *Deep imaging of high redshift QSO fields below the Lyman limit. II - Number counts and colors of field galaxies*, AJ, 105, 2017
- Steidel, C. C., Pettini, M., & Hamilton, D. 1995: *Lyman Imaging of High-Redshift Galaxies. III. New Observations of Four QSO Fields*, AJ, 110, 2519
- Steidel, C. C., Shapley, A. E., Pettini, M., Adelberger, K. L., Erb, D. K., Reddy, N. A., & Hunt, M. P. 2004: *A Survey of Star-forming Galaxies in the $1.4 < z < 2.5$ Redshift Desert: Overview*, ApJ, 604, 534
- Stoughton, C., Lupton, R. H., Bernardi, M., Blanton, M. R., Burles, S., Castander, F. J., Connolly, A. J., Eisenstein, D. J., Frieman, J. A., Hennessy, G. S., Hindsley, R. B., et al. 2002: *Sloan Digital Sky Survey: Early Data Release*, AJ, 123, 485
- Sullivan, M., Treyer, M. A., Ellis, R. S., Bridges, T. J., Milliard, B., & Donas, J. 2000: *An ultraviolet-selected galaxy redshift survey - II. The physical nature of star formation in an enlarged sample*, MNRAS, 312, 442

- Szokoly, G. P., Bergeron, J., Hasinger, G., Lehmann, I., Kewley, L., Mainieri, V., Nonino, M., Rosati, P., Giacconi, R., Gilli, R., Gilmozzi, R., et al. 2003: *The Chandra Deep Field South: Optical Spectroscopy I*, ApJ submitted (astro-ph/0312324)
- Teplitz, H. I., Collins, N. R., Gardner, J. P., Hill, R. S., & Rhodes, J. 2003: *Emission-Line Galaxies in the STIS Parallel Survey. II. Star Formation Density*, ApJ, 589, 704
- Teplitz, H. I., McLean, I. S., & Malkan, M. A. 1999: *Near-Infrared Observations of the Environments of Radio-quiet QSOS at $z < 1$* , ApJ, 520, 469
- Tinsley, B. M. 1980: *Evolution of the Stars and Gas in Galaxies*, Fundamentals of Cosmic Physics, 5, 287
- Tresse, L., Maddox, S. J., Le Fèvre, O., & Cuby, J.-G. 2002: *The $H\alpha$ luminosity function and star formation rate up to $z \sim 1$* , MNRAS, 337, 369
- Treyer, M. A., Ellis, R. S., Milliard, B., Donas, J., & Bridges, T. J. 1998: *An ultraviolet-selected galaxy redshift survey: new estimates of the local star formation rate*, MNRAS, 300, 303
- Tyson, J. A. 1988: *Deep CCD survey - Galaxy luminosity and color evolution*, AJ, 96, 1
- van Dokkum, P. G., Förster Schreiber, N. M., Franx, M., Daddi, E., Illingworth, G. D., Labbé, I., Moorwood, A., Rix, H., Röttgering, H., Rudnick, G., van der Wel, A., et al. 2003: *Spectroscopic Confirmation of a Substantial Population of Luminous Red Galaxies at Redshifts $z < 2$* , ApJ, 587, L83
- Veron-Cetty, M.-P. & Veron, P. 1996, A Catalogue of quasars and active nuclei (ESO Scientific Report, Garching: European Southern Observatory (ESO), —c1996, 7th ed.)
- Warren, S. J., Hewett, P. C., & Osmer, P. S. 1991: *A wide-field multicolor survey for high-redshift quasars, Z above 2.2. II - The quasar catalog*, ApJS, 76, 23
- Weinberg, D. H., Davé, R., Katz, N., & Hernquist, L. 2004: *Galaxy Clustering and Galaxy Bias in a Λ CDM Universe*, ApJ, 601, 1
- Weinberg, D. H., Hernquist, L., & Katz, N. 2002: *High-Redshift Galaxies in Cold Dark Matter Models*, ApJ, 571, 15
- White, R. L., Becker, R. H., Fan, X., & Strauss, M. A. 2003: *Probing the Ionization State of the Universe at $z > 6$* , AJ, 126, 1
- White, S. D. M. & Rees, M. J. 1978: *Core condensation in heavy halos - A two-stage theory for galaxy formation and clustering*, MNRAS, 183, 341
- Williams, R. E., Baum, S., Bergeron, L. E., Bernstein, N., Blacker, B. S., Boyle, B. J., Brown, T. M., Carollo, C. M., Casertano, S., Covarrubias, R., de Mello, D. . F., et al. 2000: *The Hubble Deep Field South: Formulation of the Observing Campaign*, AJ, 120, 2735
- Williams, R. E., Blacker, B., Dickinson, M., Dixon, W. V. D., Ferguson, H. C., Fruchter, A. S., Giavalisco, M., Gilliland, R. L., Heyer, I., Katsanis, R., Levay, Z., et al. 1996: *The Hubble Deep Field: Observations, Data Reduction, and Galaxy Photometry*, AJ, 112, 1335

- Wilson, G., Cowie, L. L., Barger, A. J., & Burke, D. J. 2002: *Star Formation History since $z = 1.5$ as Inferred from Rest-Frame Ultraviolet Luminosity Density Evolution*, AJ, 124, 1258
- Wolf, C., Meisenheimer, K., Kleinheinrich, M., Borch, A., Dye, S., Gray, M., Wisotzki, L., Bell, E. F., Rix, H.-W., Cimatti, A., Hasinger, G., et al. 2004: *A catalogue of the Chandra Deep Field South with multi-colour classification and photometric redshifts from COMBO-17*, A&A, 421, 913
- Wolf, C., Meisenheimer, K., Rix, H.-W., Borch, A., Dye, S., & Kleinheinrich, M. 2003: *The COMBO-17 survey: Evolution of the galaxy luminosity function from 25 000 galaxies with $0.2 < z < 1.2$* , A&A, 401, 73
- Wu, K. K. S., Fabian, A. C., & Nulsen, P. E. J. 2000: *Non-gravitational heating in the hierarchical formation of X-ray clusters*, MNRAS, 318, 889
- Yan, H. & Windhorst, R. A. 2004a: *Candidates of $z \sim 5.5 - 7$ Galaxies in the Hubble Space Telescope Ultra Deep Field*, ApJ, 612, L93
- Yan, H. & Windhorst, R. A. 2004b: *The Major Sources of the Cosmic Reionizing Background at $z \simeq 6$* , ApJ, 600, L1
- Yee, H. K. C., Ellingson, E., & Carlberg, R. G. 1996: *The CNOC Cluster Redshift Survey Catalogs. I. Observational Strategy and Data Reduction Techniques*, ApJS, 102, 269
- Yoshida, N., Abel, T., Hernquist, L., & Sugiyama, N. 2003: *Simulations of Early Structure Formation: Primordial Gas Clouds*, ApJ, 592, 645
- Zehavi, I., Blanton, M. R., Frieman, J. A., Weinberg, D. H., Mo, H. J., Strauss, M. A., Anderson, S. F., Annis, J., Bahcall, N. A., Bernardi, M., Briggs, J. W., et al. 2002: *Galaxy Clustering in Early Sloan Digital Sky Survey Redshift Data*, ApJ, 571, 172
- Ziegler, B. L., Böhm, A., Fricke, K. J., Jäger, K., Nicklas, H., Bender, R., Drory, N., Gabasch, A., Saglia, R. P., Seitz, S., Heidt, J., et al. 2002: *The Evolution of the Tully-Fisher Relation of Spiral Galaxies*, ApJ, 564, L69
- Zucca, E., Zamorani, G., Vettolani, G., Cappi, A., Merighi, R., Mignoli, M., Stirpe, G. M., MacGillivray, H., Collins, C., Balkowski, C., Cayatte, V., et al. 1997: *The ESO Slice Project (ESP) galaxy redshift survey. II. The luminosity function and mean galaxy density.*, A&A, 326, 477

Acknowledgments / Danksagung

First of all I owe thanks to my thesis advisor Ralf Bender for his support during the last years, for always motivating me, giving suggestions to overcome problems, and for always being available for questions and discussions no matter how busy he was.

Also Ulrich Hopp deserves my deeply felt gratitude for many hours of discussions, for sharing his large experience with all of us and last but not least for his disarming honesty. Keep on like this.

I am indebted to Roberto Saglia for discussions, helpful suggestions and his very unique way of phrasing difficult topics in order to sell results effectively.

I owe no less gratitude to Harald Lesch for his enthusiasm as well as for the many very interesting lunch talks. He taught me a lot and showed me the world from a different perspective.

Special thanks go to Georg Feulner and Jürgen Fliri for bearing me all this years and becoming good friends. The hours spent in discussing, analyzing and last but not least in joking and laughing were wonderful. I want also to thank them for sharing my interest of ancient history and attending Greek History with me. The excellent atmosphere at the USM is unthinkable without you.

I am grateful to Jan Snigula for his very productive discussions and for keeping my computer alive. Although I gave my best, it was hard to find computer problems which he was not able to solve. He also motivated me to learn different computer languages so that in the end my computer skills improved considerably .

Very warm thanks go also to Aleksi Halkola and Veronika Junk for the excellent atmosphere in our room. The relaxing discussions helped a lot to overcome boring hours and re-motivate me. Especially I have to thank Aleksi for correcting and improving my English. A special thank goes also to Veronika Junk for her idealism. Keep it on as long as possible.

It is also a pleasure to thank Claudia Maraston. She always helped me and encouraged me to practice my Italian more often and to improve it (at least I hope so). Ti ringrazio soprattutto per tutti i buoni consigli che mi hai dato riguardanti il lavoro scientifico ma anche per avere analizzato e migliorato le mie presentazioni orali. È un piacere discutere con te e il tuo entusiasmo è stato sempre travolgente e lo è ancora. Resta come sei.

For their advice and comments connected to my thesis my gratitude and respect goes to the staff members of the different groups at the USM and MPE in particular Stella Seitz, Mara Salvato, Mark Neeser, Bo Milvang-Jensen, Daniel Thomas, Daniele Pierini and Elena D'Onghia.

Thanks go to all my fellow students at the Sternwarte and at the MPE. In particular Arno Riffeser, Christine Botzler, Claus Gössl, Johannes Koppenhöfer, Sarah Bühler, Yulia Goranova, Jens Thomas, Maurilio Pannella and Thomas Puzia. Thank you all for many nice discussions and interesting talks.

I furthermore would like to thank Immo Appenzeller, Laura Greggio, Jochen Heidt and Regina Schulte-Ladbeck. Their comments about my work were always highly valued and constructive.

I would also like to explicitly thank the Sonderforschungsbereich 375 - Astroteilchenphysik of the Deutsche Forschungsgesellschaft as well as the Max Planck Institute for Extraterrestrial Physics for supporting my work.

Last but definitely not least, my deepest thanks go to my parents, my brother and sister. Einen speziellen Dank möchte ich sowohl meinen Eltern Gabriella und Josef als auch meinem Bruder Harald und meiner Schwester Tamara für ihre Unterstützung während meiner gesamten Studienzeit aussprechen. Ohne unseren Zusammenhalt wäre ich wohl nie so weit gekommen.

CURRICULUM VITAE

Name: Armin Gabasch
Born: February the 7th, 1973, Bozen, Italy
Marital Status: Single
Citizenship: Italian
Home: Koflweg 10, 39040 Kurtatsch, Italy
Sperlingweg 12, 80937 Munich, Germany

Education

1979 – 1987	Elementary School Student in Kurtatsch and Tramin
1987 – 1992	High-School Student, Realgymnasium, Bozen
1992	Abitur, Realgymnasium, Bozen
1992 – 1993	Diploma Student, Physics, LMU Munich
1993 – 1994	Military service, Italy
1994 – 2000	Diploma Student, Physics, LMU Munich
1999 – 2000	Diploma Thesis, Physics, LMU Munich
2000	Physics Diploma, LMU Munich
2000 – 2004	Ph.D. Student, Astronomy & Astrophysics, LMU Munich